



**ESS**  
**BILBAO**

# Technical Design Report: ESS-BILBAO RFQ

Editors:  
I. Bustinduy  
J. L. Muñoz

June 12, 2015





ESS-Bilbao RFQ  
Technical Design Report

ESS-Bilbao Consortium Report Series  
ESSB-Rep-2015-10

June, 2015

ISBN-13: 978-84-616-5445-1  
Depósito legal: BI-1070-2015  
Printed in Spain

Technical Design Report:  
ESS-Bilbao RFQ



**Scientific Editor:** Prof. F. J. Bermejo (2013 edition)

José Luis Martínez (2015 edition)

**Structural Editor and Project Manager:** I. Bustinduy (2013 edition)

J.L. Muñoz (2015 edition)

**Layout & typesetting:** Z. Izaola

**Contributors:** D. Belver<sup>1</sup>, I. Bustinduy<sup>2</sup>, D. de Cos<sup>3</sup>, J. Feuchtwanger<sup>4</sup>,  
N. Garmendia<sup>5</sup>, A. Ghiglinò<sup>6</sup>, O. González<sup>7</sup>, P. González<sup>8</sup>, Z. Izaola<sup>9</sup>,  
I. Madariaga<sup>10</sup>, C. Martínez de Marigorta<sup>11</sup>, J.L. Muñoz<sup>12</sup>, I. Rueda<sup>13</sup>,  
A. Vélez<sup>14</sup>, A. Zugazaga<sup>15</sup>

**Collaborators:**

**ESS-BILBAO:** I. Arredondo, E. Abad, G. Bakedano, J. Bilbao,  
D. Cortazar, M. Eguiraun, G. Harper, M. Huerta, A. Kaftoosian,  
G. Larrea, R. Martínez, G. Mugika, X. González, I. López,  
M. Magán, F. Martínez, A. Megia, L. Muguira, T. Poggi,  
F. Sordo, S. Terrón, S. Varnasseri, J.P. de Vicente, A. Vizcaíno

**EHU/UPV:** V. Etxebarria, J. Jugo, F. Legarda, J. Portilla.

**UPM:** M. Perlado.

**Industry Partners (design & prototyping phase):**

**AVS, Elgoibar** Tech. support.

**SWISSLAN, Elgoibar** OHFC Weld Test Models.

**ZEISS, Elgoibar** Metrology.

**MECANIZADOS MANDRINADOS MANCISIDOR, Elgoibar**  
Al Cold Model.

**ARILAN, Elgoibar** Al Cold Model vane profile.

**ERAKI, Astigarraga** Bead pull cradle.

**EDWARDS IBERICA, Madrid** Turbo pump.

**AEROTXURI, Elgoibar** Ancillaries.

**JUMAR, Vitoria-Gasteiz** Ancillaries.

**TTI, Santander** Coupler.

**TECNALIA, Derio** Brazing technical support.

<sup>1</sup> Chapters: 8    <sup>2</sup> Chapters: 1, 2, 3, 7, A, V    <sup>3</sup> Chapters: 2, 3, V    <sup>4</sup> Chapters: 6, 7

<sup>5</sup> Chapters: 5, V    <sup>6</sup> Chapters: 6, V    <sup>7</sup> Chapters: 4, 5, V    <sup>8</sup> Chapters: 5, V    <sup>9</sup> Chapters: 8, V

<sup>10</sup> Chapters: 7, V    <sup>11</sup> Chapters: 7, V    <sup>12</sup> Chapters: 3, 4, 6, V    <sup>13</sup> Chapters: V

<sup>14</sup> Chapters: 2, 4, 5    <sup>15</sup> Chapters: V

**The ESS-Bilbao Technical Advisory Committee (TAC)**

- James Stovall – Linear Accelerators LLC, USA
- Alan Letchford – Rutherford Appleton Laboratory, UK
- Maurizio Vretenar – CERN, Switzerland
- Robin Ferdinand – IPN-Orsay, France
- Peter Ostroumov – Argonne National Laboratory, USA (*in absentia*)
- John Staples – Berkeley National Laboratory, USA (*in absentia*)

# Contents

<b>1</b>	<b>Introduction</b>	<b>1</b>
1.1	Preface	1
1.1.1	Purpose	1
1.1.2	Brief Description of the Facility	1
1.2	Functional Description	3
1.2.1	Sections	8
1.3	Design Options	9
1.3.1	RFQ Design Options and Trade-offs	11
1.3.2	A note from the Editor	17
<b>I</b>	<b>Design Procedure</b>	<b>19</b>
<b>2</b>	<b>Vane modulation</b>	<b>21</b>
2.1	Modulation design	21
2.1.1	RFQSIM	22
2.1.2	Kilpatrick simulations	24
2.1.3	Modulation selected for the ESS-Bilbao RFQ	25
2.1.4	Input/output radial matching sections	28
2.2	Particle tracking simulations	29
2.2.1	Simulation codes	30
2.2.2	Results and discussion	31
2.3	Modulation robustness and stability	35
2.3.1	Variation of the input beam characteristics	35

2.3.2	Variations of the electric field amplitude . . . . .	38
2.3.3	Effects of the vane machining/assembly errors on the beam dynamics . . . . .	40
2.4	Conclusions . . . . .	42
<b>3</b>	<b>RFQ Segments</b>	<b>45</b>
3.1	Introduction . . . . .	45
3.1.1	Number of Sections: A discussion . . . . .	45
3.2	Particle Tracking Simulations . . . . .	50
3.3	FEM simulations . . . . .	50
3.3.1	Power dissipation . . . . .	51
3.3.2	Gap surface electric field . . . . .	53
3.4	Robustness study . . . . .	54
3.4.1	Static Error Study . . . . .	56
3.4.2	Input Beam Error Study . . . . .	58
3.5	Summary . . . . .	59
<b>II</b>	<b>Engineering Design</b>	<b>61</b>
<b>4</b>	<b>Electro-Magnetic Design</b>	<b>63</b>
4.1	Introduction . . . . .	63
4.1.1	RFQ Geometry Design and Simulation . . . . .	64
4.2	RFQ cavity geometry design . . . . .	66
4.2.1	Transverse cross section . . . . .	66
4.2.2	3D model . . . . .	67
<b>5</b>	<b>RF Design</b>	<b>77</b>
5.1	RF Power Coupler Design . . . . .	77
5.1.1	Electromagnetic Design . . . . .	78
5.1.2	The Drum-like Coupler . . . . .	83
5.1.3	The Nose-Cone Coupler . . . . .	86
5.2	RF Transmitter . . . . .	96
5.2.1	Klystron . . . . .	98
5.2.2	Modulator . . . . .	99
5.2.3	Circulator and Water Load . . . . .	99

5.2.4	Low Level RF System	100
5.3	RF Seals	104
5.3.1	Coupler, pick-up probe and tuner ports	105
5.3.2	Transverse joints	105
5.3.3	Longitudinal joints	106
5.4	Cold Model RF Measurements	106
5.4.1	Introduction	106
5.4.2	Resonant Frequency Modes	108
5.4.3	Dipole Stabiliser Rods	110
5.4.4	Pick-up Coupling Factor	113
5.4.5	Coupling Factor	113
5.4.6	Quality Factor	113
5.4.7	Frequency Tuning System	115
5.4.8	Accelerating Field Flatness	118
5.4.9	Low Level RF System	119
<b>6</b>	<b>Cooling Requirements &amp; Design</b>	<b>123</b>
6.1	Heat losses	123
6.2	Comparison between baffles and drilled options	126
6.2.1	Introduction	126
6.2.2	Calculation Procedure	127
6.3	Baffle design	128
6.3.1	Drilled design	133
6.3.2	Conclusions	137
6.4	Water temperature sensitivity	138
<b>III</b>	<b>Mechanical Design</b>	<b>141</b>
<b>7</b>	<b>Mechanical &amp; Vacuum Engineering</b>	<b>143</b>
7.1	Supports	143
7.1.1	CERN designed Jacks	144
7.1.2	Our design for the support	145
7.1.3	Girder	147
7.1.4	Conclusions of the support design	147

7.2	Ancillaries . . . . .	149
7.3	Vane assembly . . . . .	149
7.4	Alignment . . . . .	153
7.4.1	RFQ alignment with respect to the beam axis . . . . .	153
7.4.2	Segment to segment alignment . . . . .	154
7.5	Prototypes . . . . .	155
7.5.1	AI Cold Model . . . . .	156
7.5.2	Metrology . . . . .	159
7.5.3	OHFC Weld test Models . . . . .	163
7.6	Vacuum requirements & design . . . . .	166
7.6.1	Introduction . . . . .	166
7.6.2	Calculations . . . . .	168
7.6.3	Conclusions . . . . .	170
<b>IV Diagnostics</b>		<b>173</b>
<b>8</b>	<b>Mobile Test Stand</b>	<b>175</b>
8.1	Beam parameters . . . . .	175
8.2	Diagnostic instruments and layout . . . . .	177
8.2.1	Position Monitors . . . . .	179
8.2.2	Current Monitors . . . . .	180
8.2.3	SEM Grid . . . . .	182
8.2.4	Beam Shape Monitor . . . . .	183
8.3	Diagnostics Control system . . . . .	184
8.3.1	Position Monitors . . . . .	185
8.3.2	Current Monitors . . . . .	185
8.3.3	Slit . . . . .	186
8.3.4	SEM Grid . . . . .	186
8.3.5	Beam Shape Monitor . . . . .	186
<b>V Design Update 2015</b>		<b>187</b>
<b>9</b>	<b>Introduction and scope of the design update</b>	<b>189</b>

9.1	Summary of the technical aspects recommended by the Technical Advisory Committee . . . . .	190
<b>10</b>	<b>Modulation design and beam dynamics</b>	<b>193</b>
10.1	Characteristics of the previous design . . . . .	193
10.2	Recommendations of the review Committee and changes implemented . . . . .	194
10.2.1	Injection energy . . . . .	195
10.2.2	Modulation length . . . . .	196
10.2.3	Modulation shape . . . . .	198
10.3	New design: modulation 15.7.3.19 . . . . .	199
10.4	Beam dynamics results . . . . .	203
10.5	Beam dynamics under non ideal conditions . . . . .	205
10.6	Conclusions . . . . .	209
<b>11</b>	<b>Cavity design</b>	<b>211</b>
11.1	Electromagnetic design, 2D cross section . . . . .	211
11.1.1	RFQ-2014 design . . . . .	214
11.2	Electromagnetic design, 3D design . . . . .	214
11.2.1	Input and output sections . . . . .	216
11.2.2	Full length simulations . . . . .	220
11.2.3	Vacuum grid detuning compensation . . . . .	220
11.3	Cavity modes spectrum . . . . .	221
<b>12</b>	<b>Cavity static tuning</b>	<b>225</b>
12.1	Number and position of tuners . . . . .	225
12.2	Frequency profile along RFQ length . . . . .	227
12.3	Frequency tuning effect of plunger tuners . . . . .	227
12.4	Field profile effect of static tuners . . . . .	228
12.4.1	Finite element model . . . . .	228
12.4.2	Transmission line perturbation model . . . . .	230
12.4.3	Application of perturbation model to RFQ tuning . . . . .	232
12.5	Proposed static RFQ tuning strategy . . . . .	233

<b>13</b>	<b>235</b>
13.1 Power loss . . . . .	235
13.2 General cooling strategy . . . . .	237
13.2.1 Water temperature . . . . .	238
13.3 General results . . . . .	238
13.3.1 Deformation of fields . . . . .	239
13.4 Tuning of cavity frequency with water temperature . . . . .	239
13.4.1 Effect of vane cooling water temperature on cavity frequency . . . . .	243
13.4.2 Effect of duty cycle on cavity frequency . . . . .	243
13.4.3 Application to cavity dynamic tuning . . . . .	245
<b>14 Cavity assembly, support and vacuum strategy</b>	<b>247</b>
14.1 Support . . . . .	248
14.2 Vanes assembly . . . . .	250
14.3 Alignment . . . . .	252
14.3.1 Vane assembly and alignment . . . . .	254
14.3.2 Segment to segment alignment . . . . .	255
14.3.3 RFQ alignment with respect to the beam axis . . . . .	256
14.4 Aluminium model for vacuum tests . . . . .	256
<b>15 Commissioning plan</b>	<b>261</b>
15.1 Beam Operation Modes . . . . .	262
15.2 RFQ fundamental characterisation . . . . .	262
15.3 RFQ additional characterisation . . . . .	264
15.4 Beam diagnostic techniques and devices . . . . .	264
15.5 LEBT: a preparatory phase . . . . .	269
15.5.1 LEBT #0 . . . . .	270
15.5.2 LEBT #1 . . . . .	270
15.5.3 LEBT #2 . . . . .	276
<b>16 Open questions and future steps</b>	<b>277</b>
<b>17 Overall conclusions</b>	<b>279</b>

<b>VI Appendices</b>	<b>281</b>
<b>A Budget (2013)</b>	<b>283</b>
A.1 Schedule . . . . .	283
A.2 Budget . . . . .	285
<b>B ESS-Bilbao RFQ Technical Design Review Report (2015)</b>	<b>287</b>
B.1 Modulation and Beam Dynamics . . . . .	289
B.2 Electromagnetic Cavity Design . . . . .	292
B.3 Mechanical Design . . . . .	294
<b>C ESS-Bilbao RFQ Technical Design Review Report (2013)</b>	<b>299</b>
C.1 Conceptual Design . . . . .	302
C.2 Electromagnetic Design . . . . .	304
C.3 Modulation & Segmentation . . . . .	308
C.4 Coupler Design & RF Transmission . . . . .	308
C.5 RFQ Cold Model . . . . .	310
C.6 Cooling Design . . . . .	311
C.7 Mechanical & Vacuum . . . . .	314
C.8 Test Stand . . . . .	317
C.9 Budget & Schedule . . . . .	320
<b>Bibliography</b>	<b>323</b>



# Chapter 1

## Introduction

### 1.1 Preface

#### 1.1.1 Purpose

This Technical Design Report (TDR) is edited to provide a reasonably complete technical description of the the accelerator structure for the ESS-Bilbao Light Ions Accelerator Facility, which is in the sequel will be referred to as the Radio-Frequency-Quadrupole (RFQ). The report is written to assemble within a single document the results of design efforts carried out by several work groups within our organisation together with those resulting from the action of ongoing international collaborations. On the other hand, the resulting document is also meant for the scrutiny of an ad-hoc accelerator technical advisory committee (TAC), which has agreed to review the technical aspects of the accelerating structure as well as to assess the critical choices adopted for our final design.

#### 1.1.2 Brief Description of the Facility

At the time of writing the facility so designed comprises a 50 MeV linac composed by two room-temperature accelerator structures, namely a Radio-Frequency-Quadrupole and a Drift-Tube-Linac together with match-

Table 1.1: The parameters refer to the final design options. The structure is to be built with oxygen-free copper (OHFC) and should be machined to match its main acceleration mode to the required value of 352.2 MHz.

<b>Parameter</b>	<b>Value</b>
Type	4-vane
RF Frequency	352.2 MHz
Inter-vane Voltage	85 kV
Material	OHFC
Specimen	$H^+ / H^-$
Input Energy	75 keV
Output Energy	3 MeV
Max. Current	75 mA
Pulse Length	Up-to 1.8 ms
Repetition rate	50 Hz
Total length	3.8767 m
Number of coupling cells	0
Number of resonating segments	1
Electrical length	$< 5\lambda$
Number of cells	282
Modulation	1-1.7219 m
$r_0$	3.4726-3.4848 mm
Gap distance	0.2 mm
Front-end Gap	15 mm
Power in copper (COMSOL 3D)	397 kW
Beam power	219 kW
$Q_0$	10 786

ing sections such as the Low Energy Beam Transport and Medium Energy Beam Transport. The 50 MeV proton beams from the linac are then transported into applications laboratories devoted to the studies of proton radiation effects on a variety of systems and devices as well as a neutron production target based upon direct (p,n) reactions on Be targets.

A very first phase of the project for which all the relevant subsystems have either been built or are under an advanced state of development comprises a low energy —although high proton current— linac able to deliver beams with a final energy of 3 MeV into some selected applications laboratories. Such beams are the result of particle bunching, focusing and acceleration processes being carried out within the structure referred to as the RFQ. The structure which constitutes a resonating radio-frequency cavity takes proton or  $H^-$  pulses of 75 keV fed from the electrostatic accelerator column at the end of the ion sources stretching up to 1.8 ms of duration and transforms them into a sequence of micropulses within the nanoseconds range to match the frequency and period of the externally injected radio-frequency (RF) field. The basic parameters which characterise the structure just referred to are listed below.

## 1.2 Functional Description

As briefly referred to above, the RFQ is a device used in the low energy section of most of the modern linear accelerators (linacs) thus substituting the often used Cockcroft-Walton voltage multipliers as first injection steps. Such structures basically consisted on a ladder network of capacitors and diodes able to provide an electrical potential up to a few MV and thus provide initial electrostatic acceleration to a beam coming out of the ion source. Their main drawbacks which ditch its use in present day machines were the relatively low beam currents which could be handled with such structures as well as an inherent limitation if too many stages were used due to the mounting AC impedance of the capacitors in the lower stages which lead to strong voltage ripple. The RFQ not only effectively circumvents these problems and also constitutes a far less bulkier structure, but also provides a beam with a time structure fully prepared for acceleration by RF fields within further accelerator segments. This structure thus has

as its tasks bunching the initially DC beam, provide initial acceleration to such a beam and also to keep it focused within both transverse and longitudinal directions. Alternatively, the structure can also be used in some applications to decelerate beams of particles resulting from higher energy processes such as antiprotons, from a few MeV down to the keV range. In what follows we will restrict our description to applications involving the generation of light ( $A = 1$ ) ions with charge states  $q/A = +1, -1$  to be accelerated once adequately focused and transported by the structure here under consideration. Typical accelerations achievable with present day RFQ's reach a few MeV per nucleon.

The concept for such an instrument was first proposed by Kapchinskiy and Teplyakov [1] in 1970 in the USSR who apart from the basic concept also provided the closed form equations needed to model the electromagnetic field dynamics within the resonator. However, it was not until 1980 that the first RFQ was built and run in the western world which was at the time named POP (Proof Of Principle) [2]. Such groundbreaking developments took place at Los Alamos Natl. Lab., and indeed constituted a fundamental milestone in the development of the low energy structures for linear accelerators.

The main processes which take place inside a RFQ as employed in applications where its main task is to increase the energy of an input beam are first, to form bunches from an initial *macro-pulse* typically a few  $\sim$ ms of duration into a train of  $\sim$  ns *micro-pulses* or bunches which thus form the temporal structure of the beam pulse to be accelerated.<sup>1</sup> The structure then focuses and accelerates such bunches up to velocities typically  $\beta \simeq 0.06$  times the speed of light. Both acceleration and focusing within this structure are thus provided by the field components of the injected Radio Frequency power (see chapter 5).

The quadrupole is basically a resonant structure that needs to be manufactured with high mechanical accuracy since its resonant frequency must match that provided by the external RF source (352.2 MHz in our current design) and also, the bunches once formed have to be distributed along the accelerator main axis with a separation in time that matches the in-

---

<sup>1</sup> It goes without saying that several other types of acceleration devices based on pure electrostatics, induction machines etc. do not require the input beam to be decomposed into ns bunches.

verse of such a frequency. To such an avail, four electrodes with a very precise modulation made to have a strict relationship to the injected RF field, are designed for the task of creating electric field lines that push the particles in a synchronous way. Such electrodes which may have different shapes, are placed within the RFQ cavity fulfilling quadrupolar symmetry around the longitudinal (main) axis. This particular geometry of such electrodes focuses the beam transversely ( $x, y$  directions) once excited by the RF power. Such focusing works against the basic electrostatic repulsion generated by a packet of equal charge particles which tend to defocus the beam, an effect known as *self space charge*, which becomes strong because of the effects of the Lorentz force at low particle velocities vanishes but becomes dominant as  $\beta \rightarrow 1$ . In addition to focusing due to the quadrupolar symmetry, an effect which does not depend upon particle velocities, the RF power creates an alternating field, which combines transversal focusing with longitudinal acceleration (including bunching) making the process stable.

To generate a field along the main cavity axis able to accelerate particles one needs to make the electrodes with a given modulation and also to shift the modulation of two of them (say, at the vertical positions) with respect to that imprinted on the other two (i.e. their horizontal counterparts). This has to be done in order to generate a longitudinal component that will result in a strong enough field in the main axis. Retaining full quadrupolar symmetry for all electrodes will result otherwise in a vanishing field at the main axis.

What *longitudinal modulation* stands for is a spatial pattern made by varying the distance from the axis to the electrode with a period of  $\lambda\beta$ , where  $\lambda$  is the RF wavelength and  $\beta$  the particle normalised velocity. This results in an axial field that changes sign every half period. In such a way, instability zones are created where the field decelerates the particles (notice that these zones are not static but they move with the beam). All the particles tend to abandon these zones and join those where the forces are accelerating, hence the beam is shaped into bunches of particles. However some particles never join a bunch; these particles are eventually lost because they do not gain enough velocity to be captured by the following accelerating elements of the linac. The RFQ is built up of cells of length  $\lambda\beta/2$ , each cell having a minimum and a maximum distance from axis

to electrode. The minimum radius is called the aperture  $a$ , and the ratio between maximum and minimum is the modulation factor,  $m$ .

If we focus onto a given point on axis, we will see a field that increases up to a maximum and then decreases until it vanishes and changes sign. After that, the field pattern will be the same but in the opposite direction and then the cycle will start again. When the field is negative the forces are decelerating (for a positive particle) and no particle should be at that point of the axis if the beam is already bunched. But when the forces are accelerating, particles can arrive at different moments and thus experience different forces. Let's suppose that particles always arrive while the field is increasing. Those particles arriving early will see a weaker force than those arriving late. Therefore, those particles that arrived early will now get late to the next period and those ones that were late will arrive early, changing their role. Thus the particles tend to oscillate longitudinally around a reference particle which we call the *synchronous particle*. The phase between the synchronous particle at the beginning of a cell and the RF is called the *synchronous phase*.

The RFQ is thus built up from cells of length  $\lambda\beta/2$  for the synchronous phase to be the same after a RF period. In fact, this is not exact; the length of the cells is made usually a bit longer in order to increase the synchronous phase as we want. Thus the synchronous phase somewhat varies along the RFQ. So we can now define the synchronous particle as the particle for which the RFQ is designed. In Figure 1.2, we can see the evolution of the phase density —of single bunch— along the entire structure. It is worth emphasising here that the synchronous phase sets the time structure for the beam for each subsequent accelerator structures.

The RFQ is thus designed for the synchronous particle (and thus the particles orbiting around it) to see an accelerating field every half period. A scheme of the motion of a bunch of particles through a period is shown in Figure 1.1.

Summarising, particles feel transverse focusing due to the quadrupolar symmetry. The accelerating force is consequence of the vertical vanes been shifted with respect to the horizontal ones by a phase of  $\lambda\beta/2$ , so the closer an electrode is to the axis the farther away is the adjacent one. This geometry is responsible for bunching the beam and accelerating these bunches as well as maintaining them focused.

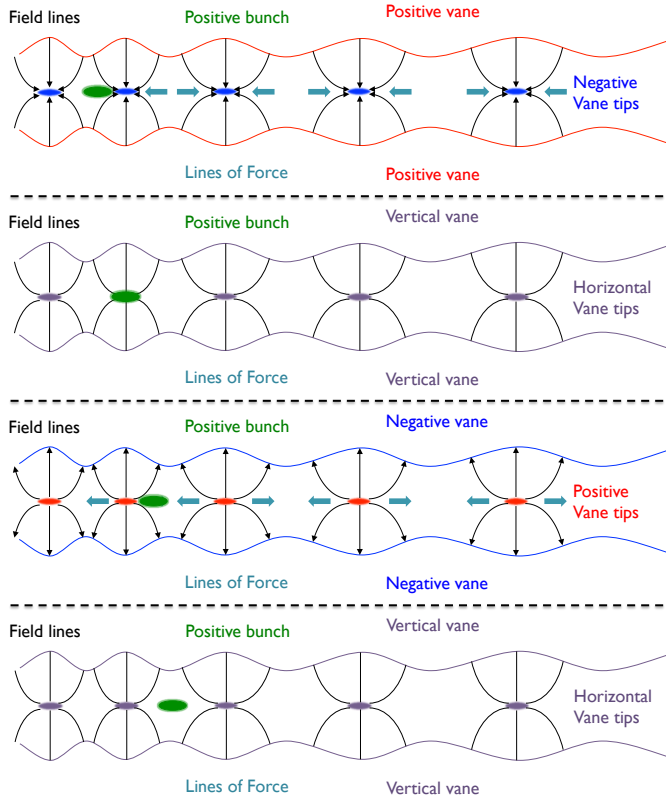


Figure 1.1: Sequence to show how the electrode modulations accelerate a particle bunch. Only vertical electrodes are shown. From top to bottom: **1)** Particle bunch feels an accelerating force. **2)**  $1/4$  RF Period later, the field drops to zero and the bunch feels no accelerating force. **3)** Another  $1/4$  RF Period later, the field is at a maximum again but the sign is reversed, the bunch feels an accelerating force. **4)** Another  $1/4$  RF Period later, the field drops to zero and the bunch feels no accelerating force once more. *Courtesy of Simon Jolly (UCL)*

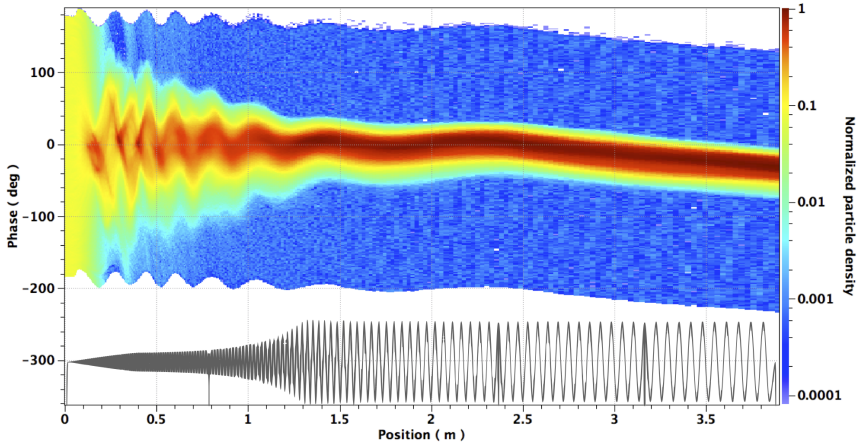


Figure 1.2: Particle phase density respect to the synchronous phase transport along the RFQ vertical vane profile design represented in black.

### 1.2.1 Sections

Most of the RFQs built so far are prototypes in the strict sense. This means that one can always find an exception to any generalisation we may use to describe their main features. With such a proviso in mind we will briefly describe the structures and purpose of the main RFQ sections as applicable to the majority of such structures built so far.

The RFQ is divided in 4 sections, each having a different purpose (see Figure 1.3). It starts with what is called the *Radial Matcher* which has the longitudinal shape of a quarter of a circle, thus starting with a large aperture and gradually decreasing it. Its main task is to direct the particles, which come with very crossed paths, into the RFQ. Once this is achieved, the beam enters the *Shaper*, which is mainly dedicated to focus the beam. The beam gets here some acceleration, while the synchronous phase is increased. However, the modulation is still very soft and therefore the acceleration is not too high.

After the Shaper comes the so called *Gentle Buncher*. This section is dedicated to separate the beam into bunches. A stronger field is needed in axis; so the aperture is decreased while the modulation factor slowly

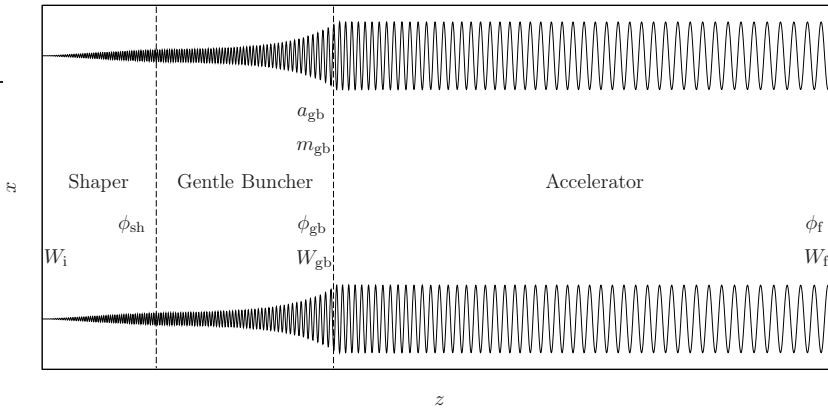


Figure 1.3: Sections and Parameters employed in the complete modulation design. Input and Output Radial matcher have not been included.

increases. Moreover, the synchronous phase continues to grow and the beam is accelerated.

The *Accelerator* is the last section and here is where main energy gain is achieved. The aperture and the modulation factor are kept constant within this section, whereas the synchronous phase can either be kept constant or be slightly increased. It is important to emphasise that all the sections (except the radial matcher) are modulated; therefore, although all sections accelerate, bunch and focus transversely, each section is dedicated to fulfil one of the tasks more dominantly over the rest.

The modulation design requires the use of specific computer codes, since the generated electric fields along the RFQ is described by equations complicated enough that makes them not amenable to a simple analytical solution.

### 1.3 Design Options

The task of the RFQ accelerator is, as referred to in the previous chapter, to efficiently accelerate a beam of given current from an initial energy to a

final energy once a definite time structure in the form of nanosecond-length micro-pulses has been generated within the first section of this structure. The aim is to do that efficiently, thus minimising the number of particles which are lost by striking the accelerator structure during this process, since they will cause a radioactivity buildup over time.

Most of the conventional intense RFQ designs are exemplified by several prototype designs such as the groundbreaking development at The Institute for High Energy Physics at Protvino (IHEP) in 1972 developing a Demo RFQ to accelerate a beam of 200 mA protons up to 620 keV at low duty or the Proof-of-Principle machines developed at LANL in 1980-1981. A number of machines were then built, including that to feed Linac1 at CERN and several others and, also very significant developments took place hidden from the public life within the Directed Energy Weapons programmes. The first prototype to be installed within a heavy duty machine was however the Low Energy Demonstrator Accelerator (LEDA) at LANL which was commissioned in 1999-2000 and was able to accelerate a 100 mA CW beam of protons from 76 keV to 6.7 MeV. Most of the design criteria nowadays in use owe a great deal to efforts carried out by the LEDA team.

The main design criteria used at those times mostly relied upon considerations on maximum beam-current-related achievable plus some recipe for assigning the synchronous phase. The whole linac is laid out keeping many parameters constant in the main accelerating section to ease manufacturing and tuning as understood at the time. Limited computing capabilities at the time meant that most design exercises relied upon measuring the performance at the output and then getting back to the design stage in case that the target transmission was not achieved. The beam acceleration was then simulated and the resulting transmission to the output is observed as the measure of successful performance.

Computer tools at hand these days enable us to understand in detail the cell-by-cell performance of the beam as it undergoes the very complicated process of forming a bunch from an initial macro-pulse and how acceleration proceeds bunch by bunch. This is nowadays performed using multi-particle simulation codes which are deemed to bear a high predictive capability. The concurrent use of such computational tools together with the basic field equations cast in analytical form by Profs. Il'ya Mikhailovich

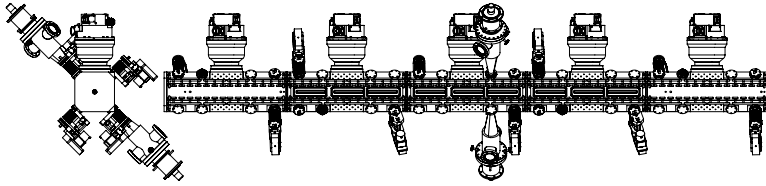


Figure 1.4: A side view of the 5 segment RFQ, accompanied by the expected five pumps, ten slug tuners and two couplers.

Kapchinski and Vladimir A. Teplyakov provide us with design tools not available a few decades ago.

A fairly basic design option was taken (see Table 1.1) at the outset of the current project looking for synergies with ongoing projects under advanced design or construction stages. Between those, a decision was taken to embark ourselves with our colleagues at ISIS-FETS on a common endeavour of building a new generation RFQ, avoiding known risks and possible mishaps. As remarked during the ESS-Bilbao Workshop in March 2009, the lack of common engineering practice employed in the manufacture of most existing high-power RFQs suggest that the ideal manufacturing processes are yet to be found. It was then decided that entering this two-sided collaboration will only result in clear benefits for both partners, basically on the basis of risk-sharing.

### 1.3.1 RFQ Design Options and Trade-offs

**Frequency** The frequency, output energy, and current were preselected for the RFQ design. The frequency was fixed at 352.2 MHz for the entire linac because of several reasons. First, concerns compatibility with ESS as well as several other ongoing projects. Second, since our main concern is to optimise beam stability and thus limit the emittance growth, the frequency had to be chosen as high as reasonably achievable, account made of the compatibility issue. At the time of writing a somewhat higher frequency such as 402.5 MHz as used at SNS would probably had been a better choice if we were to build the machine on a green field. The final energy was set to

3 MeV for compatibility reasons with both ESS and Linac4. The saga of the high currents envisaged within the 2003 ESS project (150 mA) is now touching ground and such project just updated a beam the peak current to 61 mA at the time of writing. The *current limit* should be set to twice the desired operating current.

**Input** Input beam characteristics are set by the current ion-sources and emittance increase introduced by the chosen low energy beam transport system. The estimated input normalized beam emittance values are given in chapter 2.

**The goal** for transmission through the RFQ was set at 95%, or better. Keeping relatively high transmission will obviously reduce the beam loss on the long term performance of the vane tips for such a relatively high power RFQ. Beam losses are to be kept as small as possible for energies above  $\approx 2$  MeV to avoid neutron production reactions.

**RF efficiency** Both the current machine as well as that being developed at ISIS-FETS for a close bunch frequency (324 MHz) are relatively efficient as far RF power consumption is concerned. The cost of RF power may otherwise overshadow the capital cost of the whole RFQ structure. The smooth shape of the cross-section has been chosen to achieve a significant increase in the quality factor, producing a decrease in the required RF power consumption, this unconventional rounded shape has also a significant impact on the heat load distribution.

The required input power to be provided by the RF coupler is the sum of the dissipated power in the RFQ  $P$ , the fraction delivered to the beam  $P_{\text{beam}}$ .<sup>2</sup>

For the 800 mm segments it has been estimated a dissipated peak power of 74 350 W per segment, and 397 484 W for the whole structure.<sup>3</sup> The fraction of the power that is transferred to the beam is

<sup>2</sup> The RF-klystron has to be also provide enough power to cope with the power losses in the waveguide, reflected power and the power dissipation in the RF generator itself

<sup>3</sup> Considering 16 Tuner ports and two vacuum ports per segment. In the final design, there are no pick-up ports: pick-ups will be placed in the same tuner ports during RF commissioning.

219 375 W following the formula:

$$P_{\text{beam}} = I_{\text{peak}} \times \Delta W/q. \quad (1.1)$$

In order to cope with the RF power requirements, installation of two couplers in parallel is envisaged to power the accelerating structure, with up to  $\sim 700$  kW total peak power at the required duty cycle.

**Electrode form** Because of the relatively high frequency chosen and the accelerated specimen, vane electrodes are the option most experts would recommend, since rod-type structures are better suited heavy ions and frequencies about 200 MHz or lower.

**Modulation shape** A sinusoidal shape was adopted to profit from synergies with ongoing developments at the new ISIS front end test stand. Other alternatives which could ease machining such as that trapezoidal in shape could also be an option. This type of modulation—originally proposed and adopted at IHEP-Protvino—produces more peaked longitudinal fields, increasing RFQ acceleration efficiency. Therefore, it leads to lower manufacture and operation cost. The only drawback is related with the increase of maximum field at vane surfaces.

**Total length and segments length** The equation that relates the local frequency variations  $\delta f_o$  with the deviation of the local field  $\delta E_o(z)/E_o$ , in a 4-vane RFQ, is given by:

$$\frac{\delta^2}{\delta z^2} \left( \frac{\delta E_o(z)}{E_o} \right) = \frac{8\pi^2}{\lambda^2} \left( \frac{\delta f_o(z)}{f_o} \right). \quad (1.2)$$

Field errors scale as the square of the length of the RFQ, restricting thus the practical length of the structure to  $\sim 5$  free space wavelengths. In this design, considerations of the beam acceleration quality and efficiency have guided the choice of keeping total length of about 4 m as optimal to accelerate the beam up to 3 MeV. The length of each segment has been chosen on the basis of ease of manufacturing. Keeping a maximum length per segment of some 800 mm will enable local manufacturers to reach mechanical accuracy up to some  $5 \mu\text{m}$  for the flatness of the reference surface.

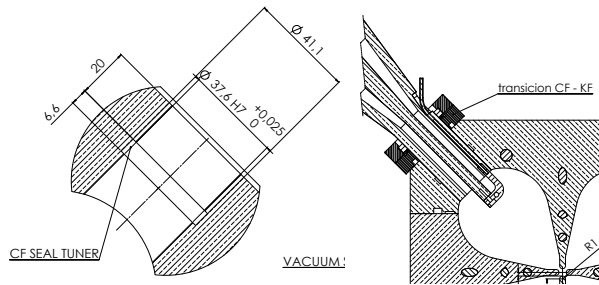


Figure 1.5: Tuner port dimensions. Right frame shows it can be used as coupler port.

**Peak Field** Far too high values will obviously result in sparking and performance degradation. Cannot relax much such parameter unless the total length is increased. The current design considers such fields using a bravery factor  $\leq 1.8$ . In order to prevent future electrical breakdown ( $\sim 33$  MV/m), a full electrostatic analysis by finite elements has been performed. This accurate field map includes the local perturbations in the gaps between segments.

**Tuning** The chosen option is to control resonance frequency excursions up to a few hundreds of kHz by mechanical means only. Use of the cooling water temperature as a handle to control the cavity frequency shifts was deemed to lead to complications which could be difficult to cope with. In the proposed design, 14 fixed and 2 movable tuners are envisaged per segment. In this design diameter ( $\text{Ø}37.6\text{H}7$ ) has been chosen as it matches the diameter used for the pick-ups and N-type RF power couplers (see Figure 1.5). As such, it will also be possible to inject RF power at the same location. Each tuner enters perpendicular to each of the RFQ lobes. The cavity has been designed at a slightly lower frequency and increase its resonant frequency by introducing the metal rods in the cavity, if required.

**A welding safety net** Past experience on several projects (IPHI, Linac<sub>4</sub>, Spiral<sub>2</sub>) have highlighted the dangers of manufacturing whole brazed structures. Some room to manoeuvre can be gained if the welding strategy is applied step-wise as proposed by the designers of ISIS-

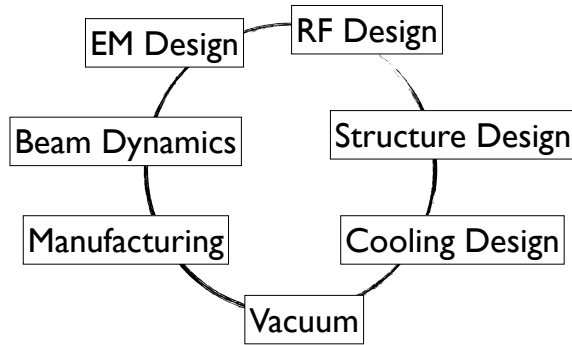


Figure 1.6: RFQ Design cycle.

FETS RFQ, leaving the full braze option as a last resort. Whenever possible, bolted options will be taken.

**Conventional Design** Based on the design process developed at the Los Alamos National Laboratory in 1978–1980 several parameters have been kept constant along the vanes to ease manufacturing complexity: the average aperture  $r_0$  between vanes, the vane tip transverse radius of curvature  $\rho$  and the voltage  $V$  between opposing vanes.

The RFQ Design process constitutes an entangled problem on its own nature, the cavity has to fulfil some specific requirements from the Electromagnetic point of view. The cavity has to be excited in a quasi- $TE_{210}$  electric quadrupole mode, in order to provide a time varying quadrupole focusing field on axis. The goal is to produce a flat field profile keeping the  $TE_{110}$  dipole modes away in frequency, while maximising the *effective shunt impedance* of the whole structure. Moreover, the desired fundamental mode (quadrupole) is required to be close to the final operating frequency of 352.2 MHz to match with the klystron and RF system.

End cells are carefully designed in order to obtain an optimum shape that guarantees the field flatness along the structure and ensures power deposition can be removed with the chosen cooling system. This power

deposition in OHFC will derive in expansion of the material leading to variation in the conditions of the resonator and also possible variations in the shape of the vane profile, affecting thus the quality of the accelerated beam. As a consequence, slug tuning rods must be added in order to adjust the RFQ resonant modes, and possibly correct some imperfections in the machining process. Along with the tuners, Electromagnetic optimisation process has to fulfil several other constraints imposed by the inherent manufacturing procedures, cooling, etc.

By its own nature within the RF resonant cavity a minimum pressure  $10^{-7}$  mbar has to be achieved to avoid spark phenomena due to the generated electromagnetic fields, as well as to avoid scattering particles out of the beam, which increases two phenomena, namely emittance and radiation hazard. It is therefore required to minimise the perturbation effects on the fields generated by the inclusion of pumping ports.

In chapters that follow, a brief introduction to the basic physics of such a structure is provided together with justification for the chosen final options. Also, on a more technical vein, the rest of chapters report on steps carried out within the current design effort. More into details, the relevant design options and trade offs are addressed in Chapter 1, and those pertaining to the final choosing of the electrode modulation parameters are described in Chapter 2. The main results of the electromagnetic design are given in Chapter 4, while the details of the chosen options of the main geometric parameters are given in Chapter 7 and the error studies detailed in Chapter 2. The full-fledged electromagnetic analysis is presented in Chapter 4 while details pertinent to the RF coupler as well as other aspects dealing with the RF engineering such as transmission, low-level RF controls etc. are given in Chapter 5. A detailed study of the effects of thermal disturbances is provided in Chapter 6. The subtleties involved in the different manufacturing processes and the vacuum requirements are described in Chapter 7.

The Chapter 7.5, gives an account of experiments and tests carried out on several prototypes and Cold Models in order to verify some of the calculation and simulation predictions and, finally a chapter detailing relevant information about project costs, schedule, commissioning strategy, envisioned so far.

### **1.3.2 A note from the Editor**

Since its very inception, the project has largely benefited from the ongoing collaboration with some of our international partners involved in similar developments such as the new ISIS front-end test stand, the SNS facility at Oak Ridge Natl. Lab. as well as the Linac4 project at CERN. As a result, the current document contains significant inputs originated in these facilities which are gratefully acknowledged.

In spite of all of the above decisions, there is still ample room left for critical issues that have to do with basic manufacturing techniques such as brazing as well as the development of tools and fixtures to guarantee that subsequent manufacturing stages do not lead to deformations beyond some acceptable limits.

The present document tries to assemble as much detail as we are able to recall at the time of writing. However, some relevant decisions are still pending and will be taken when a final validation of results derived from measurements on the cold models is finally made.



**Part I**

**Design Procedure**



# Chapter 2

## Vane modulation

This chapter explains the procedure followed to create a vane modulation for the ESS-Bilbao RFQ, performed using Alan Letchford's RFQSIM software. The modulation was designed to fulfil the design specification of the ESS-Bilbao RFQ [3], shown in Table 2.1.

The final design was selected among others in terms of different figures of merit, presenting very reasonable values both for physical parameters (total length, surface field) as well as beam dynamics results (e.g. emittance growth, transmission). The particle tracking performance of the design, as well as its stability under different conditions, are studied and evaluated in sections 2.2 and 2.3, respectively.

### 2.1 Modulation design

Designing the vane modulation demands using a computer program, since the Physics behind the electric fields in the RFQ is described by complex expressions that cannot be easily handled. There is a short number of programs that are able to calculate the electric field map of an RFQ and perform beam tracking simulations; and there is an even shorter number of codes that allows to *design* a working vane profile. One of the few codes that is able to carry out both tasks successfully is RFQSIM [4], written by

Table 2.1: RFQ design specification.

Type	4-vane
RF Frequency	352.2 MHz
Intervane voltage	85 kV (constant)
Species	Protons
Input Energy	75 keV
Output Energy	3 MeV
Max. current	75 mA
Peak surface field	$\leq 1.8 \times \text{Kilpatrick}$
Pulse length	Up to 2 ms
Repetition rate	Up to 50 Hz
Duty cycle	$< 8\%$
Total length	$< 4\text{ m}$
No. particles per pulse	$9e + 14$ (2 ms)
No. particles per bunch	$2 \times 10^8$

Alan Letchford, from ISIS (RAL), partner of ESS-Bilbao in the RFQ project. The RFQ design presented in this work has been performed with RFQSIM, as explained next.

### 2.1.1 RFQSIM

RFQSIM is a suite containing several codes that can generate an RFQ vane profile, as well as performing particle tracking simulations.

The vane modulation is calculated by RFQSIM as follows: first, the value of certain parameters at the end of the *Gentle Buncher* section must be set, which depend partly on the operation characteristics of the RFQ (such as the inter-vane voltage, maximum current to transport, etc). Once those parameters are set, RFQSIM can calculate the vane modulation all the way back to the *Radial Matching Section*, and forward to the end of the RFQ, following the design rules proposed by Kapchinskiy–Tepliakov.

This program demands that values of certain physical parameters are provided at different parts of the RFQ, such as the synchronous phases at the end of each section and the energy of the particles at the output of the

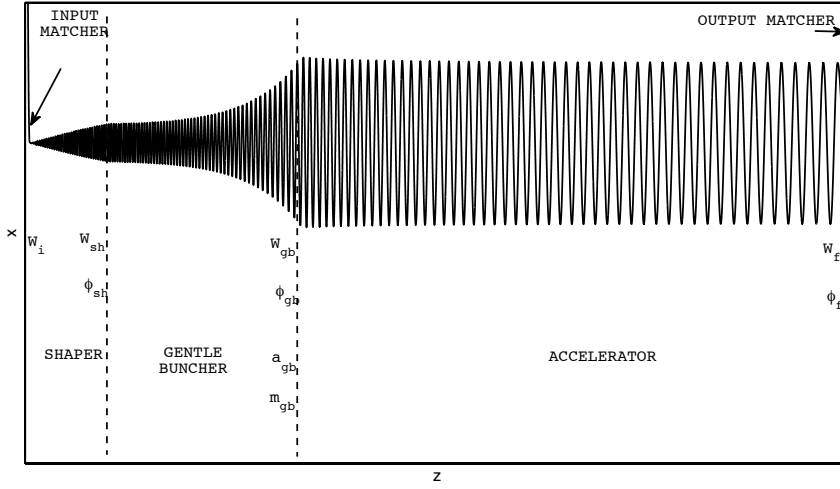


Figure 2.1: Representation of the amplitude of the positive horizontal vane, including the RFQ sections and the parameters used by RFQSIM to construct the full vane modulation.  $W_x$  stand for energies and  $\phi_x$  for synchronous phases. The amplitude and modulation factor at the end of the Gentle Buncher are represented by  $a_{gb}$  and  $m_{gb}$ , respectively.

*Gentle Buncher.* Therefore, the usual procedure is to perform several simulations using different designs in which the values of certain parameters are scanned, thus searching for the best configuration. A scheme with the parameters used by RFQSIM to define the full RFQ vane modulation is presented in Figure 2.1. The ratio between the pole radius of curvature and the mean vane aperture ( $\rho/R_0$ ) must be specified as well, but it is chosen to be constant along the full RFQ length.

The evaluation of the RFQ models created by this method was performed in terms of the following figures of merit:

- The length ( $L$ ) is the sum of the lengths of all the cells generated by RFQSIM. This includes the Input Matcher, but not the Output Matcher or any transition cells prior to it. Due to fabrication constraints, the vanes will be fabricated in five segments, each one less than 790 mm long. As a consequence, the parameter  $L$  is constrained

to be several centimetres below 3.95 m (preferably,  $< 3.90$  m).

- The *Bravery Factor* (BF) is the ratio between the maximum electrical field at the surface and the Kilpatrick limit ( $\sim 18.5$  MV/m for  $f = 352.2$  MHz). It is highly recommended that it remains below 1.8, in order to prevent electrical breakdown ( $\sim 33$  MV/m). The procedure is explained in more detail below, in section 2.1.2.
- The emittance growth ( $\Delta\varepsilon$ ) is calculated as the mean of the relative increases in  $\varepsilon_x$  and  $\varepsilon_y$ , both referred to input normalized rms emittances of  $0.25\pi$  mm mrad. Emittance growths of 10 % or lower are considered almost negligible in practical terms.
- The transmission percentage is calculated by discarding both the particles that impacted with the RFQ vanes and those that were not captured by a bunch (i.e., transmitted particles with an energy significantly lower than that of the synchronous particle). The energy threshold is placed at  $\Delta E < 0.1$  MeV.

### 2.1.2 Kilpatrick simulations

As explained above, one of the figures of merit taken into account in the modulation design has been the maximum surface field reached. To this end, electrostatic simulations have been carried out using the COMSOL (AC/DC) module. Thus, a parametrised 3D model of the full length RFQ vane region has been created. Electrostatics simulations using a constant inter-vane voltage difference of 85 KV and different vane modulation descriptions were then run. The field maps created were used to evaluate the suitability of the studied modulation, not only in terms of the Bravery Factor, but also in terms of beam dynamics results obtained by tracking particles through those field maps, as explained in Section 2.2.1.

Once the electrostatic design procedure is finished and a modulation candidate is selected, the design loop is finished. From this point and regarding the RF design, the 3D structure for the vanes including an input and output matcher will be considered as a closed item of the RFQ model, so the models for RF design must be built starting from the vane modulation solids (Figure 2.2).

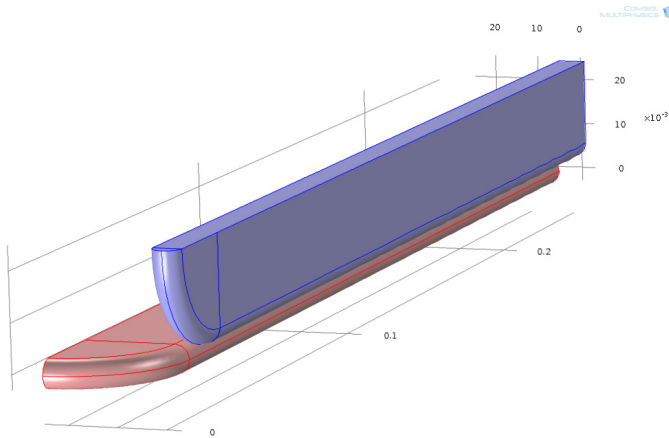


Figure 2.2: 3D model of the modulation vanes.

In Figure 2.3, the maximum value of the surface electric field along the RFQ length for different vane modulation designs is presented. To extract accurate values for the surface fields from FEM codes can be a very computationally intensive task. To overcome this difficulty, the solution chosen consisted on performing very detailed simulations of a portion of the RFQ length containing three cells and analysing the results only for the central cell. These simulations were done using the finest-grained meshes allowed by our computing facilities. In the figure, each point corresponds to the maximum of electric field for a particular modulation cell obtained using this procedure.

### 2.1.3 Modulation selected for the ESS-Bilbao RFQ

We have performed several attempts to find the best possible modulation for the ESS-Bilbao, resulting in a few provisional designs. As we implemented new characterisation tools (both for particle tracking and field calculation), it was found that those designs had to be eventually replaced by new improved ones. Although certain values were changed, most of

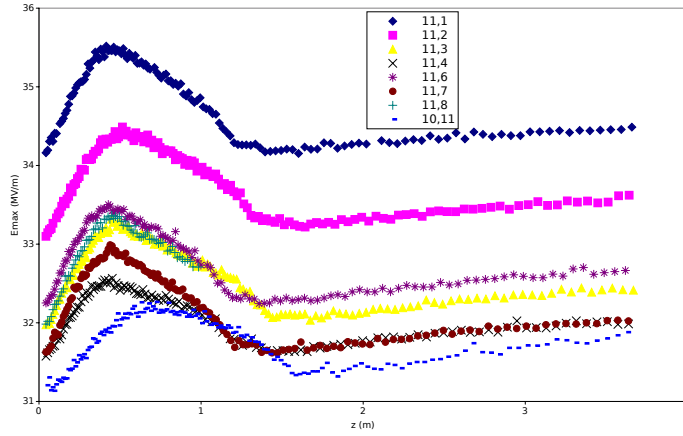


Figure 2.3: Maximum electric field values along RFQ vanes length for different modulation designs.

the best results are achieved when the design parameters are kept within quite narrow intervals, as shown in Table 2.2 (centre column).

The current working modulation, designated 11.4, was produced with the parameters addressed in the rightmost column of Table 2.2. This design has been tested with all the tools currently available to us, including several different methods to calculate the electric field distribution, as well as to perform particle tracking simulations. According to those tools, modulation 11.4 fulfils all the design specifications and displays notable results in all the figures of merit considered, with transmissions in the 90–95 % range, acceptable emittance growths and a Bravery Factor below 1.8. Sections 2.2 and 2.3 present the particle simulation results in greater detail.

Figure 2.4 shows the evolution of several parameters along the RFQ. The end of the Gentle Buncher and start of the Accelerator can be clearly identified at cell number 182.

Table 2.2: Design parameter values used in RFQSIM.

Design parameter	Typical values	Version 11.4
$W_{\text{sh}}$	80 to 90 keV	87 keV
$\phi_{\text{sh}}$	$-82^\circ$ to $-77^\circ$	$-78^\circ$
$W_{\text{gb}}$	0.4 to 0.6 MeV	0.525 MeV
$\phi_{\text{gb}}$	$-38^\circ$ to $-34^\circ$	$-35^\circ$
$a_{\text{gb}}$	2.5 to 2.7 mm	2.65 mm
$m_{\text{gb}}$	1.6 to 1.7	1.63
$\phi_{\text{f}}$	$\sim -30^\circ$	$-30^\circ$
$\rho/R_0$	0.8 to 0.85	0.85

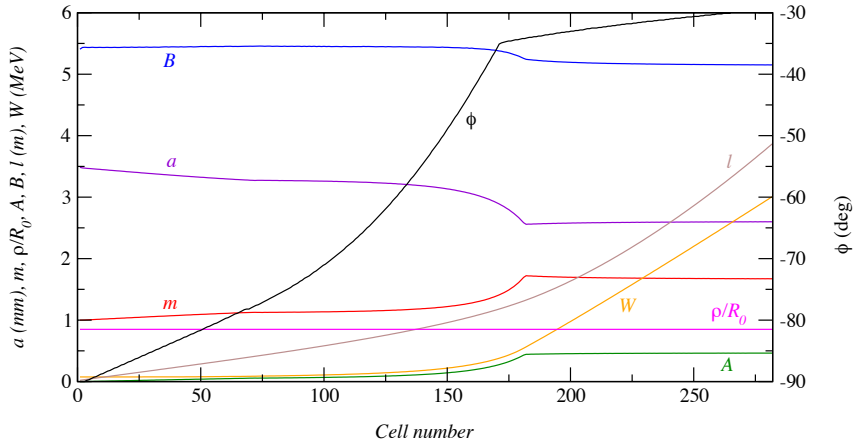
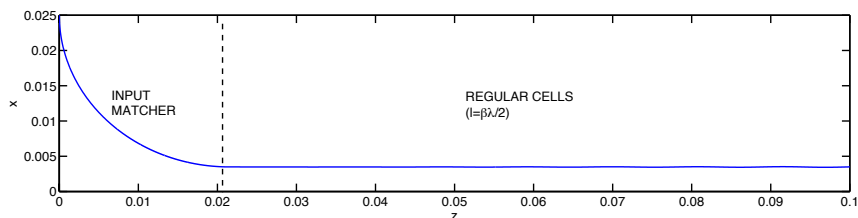
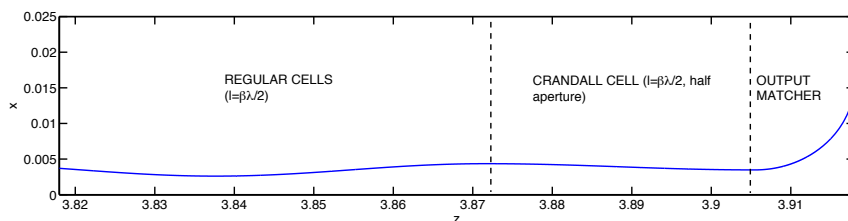


Figure 2.4: Evolution of several RFQ parameters as a function of the cell number.



(a) Low energy end.



(b) High energy end.

Figure 2.5: Side view of both ends of the positive horizontal vane.

### 2.1.4 Input/output radial matching sections

Radial matching sections are placed at the input and output of the modulation. Their profiles follow a constant radius sweeping from the vane ends (vertical) to the vane modulation (horizontal), thus completing  $90^\circ$  of a circle of the same transverse radius of curvature as the rest of the cells (see Figure 2.5). This profile, also followed by our partners ISIS in their own RFQ design, is capable of creating the quadrupolar fields needed to match the beam between the RFQ and the transport systems up- and downstream of it, while simplifying the RF design and the machining of the vanes.

Other relevant characteristics of the radial matchers are explained next:

**Input matcher:** Its length (i.e. radius) is set to  $2\beta\lambda$ , which is long enough to gradually increase the focusing strength without compromising the acceptance of the RFQ.

**Output matcher:** Since its main purpose is to match the beam into the MEFT, the length of the output matching section is basically deter-

ined by optical simulations. Additionally, a half aperture transition cell (also called Crandall cell [5]) needs to be placed between the last cell of the accelerating section (asymmetric) and the output matcher (of quadrupolar symmetry), in order to avoid discontinuities in the vane profile. The length of the transition cell can also be set as needed by the MEBT input beam requirements. In our case, the lengths of both elements were frozen after studying beam evolution downstream the MEBT and DTL; electing the solution that kept the transmission high and emittance increase low, which is: Transition cell =  $\beta\lambda/2$ , and Output matcher radius = 12.5 mm.

## 2.2 Particle tracking simulations

To accurately simulate the performance of an RFQ, two basic tools are needed:

- A procedure to estimate the electric field at any point inside the cavity, with especial accuracy in the region centred at the longitudinal axis and surrendered by the vane tips. This estimation can be obtained either by following an analytical approach or by performing an electrostatic simulation with computing methods.
- A computer code to track the movement of the particles inside the electric field addressed above. Other additional capabilities are usually required, such as calculating the space-charge forces (beam-to-beam interactions), and removing the particles that impact with the vanes from the simulation.

We have followed several different methods both to estimate the electric field of the ESS-Bilbao RFQ design and to simulate the movement of the particles along it. Those methods will be explained in this section, together with the results obtained with each of them.

In order to establish accurate comparisons, certain simulation parameters have been kept fixed in the different procedures, as summarised in Table 2.3.

Table 2.3: Common parameters used in the particle tracking simulations.

Parameter	Value
Particle	Proton
Number of macroparticles	10000
Input energy	75 keV
Input current	60 mA
Input beam C-S parameters:	
$\alpha_x$	0.769
$\beta_x$	0.0272 m/rad
$\alpha_y$	0.814
$\beta_y$	0.0317 m/rad
Input transverse emittance	$0.25 \pi$ mm mrad

The input beam Courant-Snyder parameters have been calculated with Trace2D [6]. They are supposed to be optimal (i.e. maximise transmission), although a brute-force search revealed that many sets of parameters in the same range of values ( $\alpha$ -s between 0.7 and 1.3,  $\beta$ -s between 0.035 and 0.045 mm/mrad) offer very similar results.

The number of macroparticles used in the simulations has been set to 10000, as it has been found to present the best compromise between accuracy and computing time consumption.

### 2.2.1 Simulation codes

The main characteristics of the particle tracking codes used in the simulations, including the field map calculation methods, are briefly explained below:

- RFQSIM, written by Alan Letchford (ISIS), is a suite of codes that allows both to design an RFQ modulation (see Section 2.1), calculate its electric field, and perform particle tracking simulations. The electric field inside the cavity is analytically approximated using an 8-term multipole expansion. RFQSIM also makes an estimation for the electrical surface field, although this value has been found to be underestimated by the other procedures, as explained below.

- TOUTATIS, written by Romuald Duperrier (CEA/SACLAY), is a computer code specialised in RFQ particle tracking. The RFQ is defined by providing certain parameter values for each cell, and the electric field is then calculated using the finite differences method [7]. TOUTATIS uses specific algorithms to calculate the effect of the beam on the RFQ field near the boundary walls, which takes special relevance when high currents are simulated [8].
- GPT (General Particle Tracer), written by Pulsar Physics, is a general purpose particle tracking code that uses on a 5<sup>th</sup> order Runge-Kutta algorithm [9]. Since GPT is not RFQ-oriented, it is necessary to use external tools to perform certain tasks, such as proper space-charge calculation and particle elimination. In addition, the RFQ field map must be generated externally, for which we have used two different procedures:
  - 8-term multipole analytical approximation, in which the multipole coefficients are provided by the RFQSIM’s expansion. Therefore, the field map provided to GPT is very similar to that used in the RFQSIM simulations.
  - Finite element simulation with the finite element software package COMSOL. A full CAD 3D model of the RFQ is built, and then an electrostatic analysis by finite elements is performed to obtain an accurate field map. This is a quite complicated system, which demanded heavy work in order to build an accurate model and optimise the meshing process, but eventually produces a very realistic description of the RFQ field distribution. Combined with GPT, this method probably offers the most accurate particle tracking results.

### 2.2.2 Results and discussion

Figure 2.6 presents some particle density plots at the output of the RFQ, obtained with RFQSIM. The successfully transmitted particles remain within a 2 mm radius from the RFQ axis, with 90 % of them found within a 1 mm radius, and 55 % of them within a 0.5 mm radius. The maximum particle inclinations are below  $\pm 30$  mrad. The energy dispersion is quite low, with

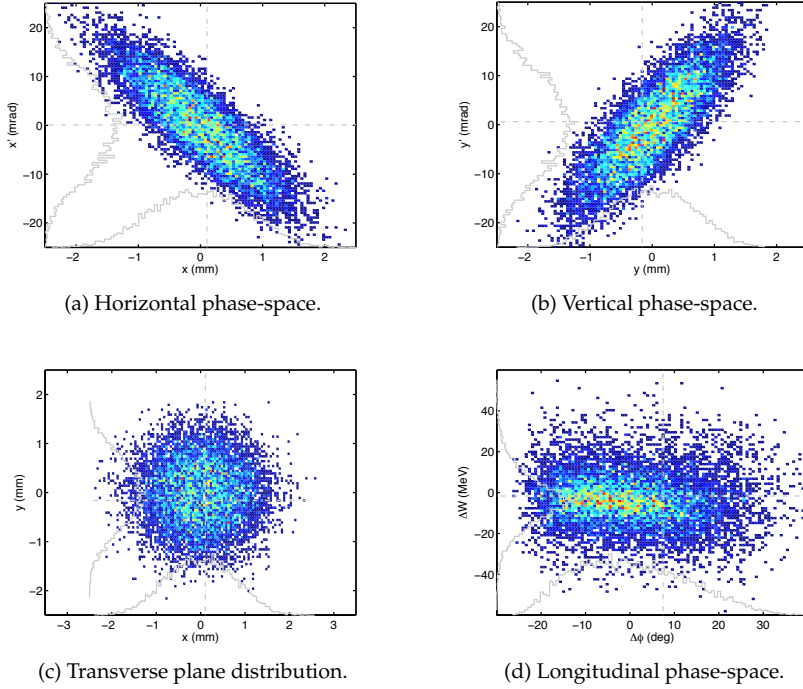


Figure 2.6: Particle density plots at the output of the RFQ.

90 % of the transmitted particles presenting energies below 30 keV about that of the synchronous particle (calculated to be 3.015 MeV).

As explained above, we have based our decision on the modulation design not only on the results obtained with RFQSIM. Table 2.4 shows the main RFQ figures of merit, as simulated with the methods described in Section 2.2.1, under the conditions stated in Table 2.3. The main conclusions are commented next:

- The transmission remains above 90 % in all cases, reaching values of  $\sim 95$  % when the more accurate geometry-based descriptions of the RFQ field are used (that is, TOUTATIS and COMSOL).

Table 2.4: Simulation results at the output of the RFQ for the four methods used. The figures of merit are: successful transmission (%), transverse normalised root mean square (*rms*) emittance ( $\pi$  mm mrad) calculated as the average between the horizontal and the vertical values, longitudinal rms emittance ( $\pi$  deg MeV) and maximum surface electric field (MV/m).

Simulation method	T	$\epsilon_t$	$\epsilon_z$	$E_s$
RFQSIM	90.8	0.273	0.167	30.0
TOUTATIS	94.4	0.321	0.186	31.9
GPT + Multipoles	92.7	0.284	0.183	30.0
GPT + COMSOL	95.3	0.307	0.177	32.6

- The transverse emittances are all close to  $0.30\pi$  mm mrad, with some variations probably due to the different transmissions achieved (having more particles transmitted increases the emittance).
- The longitudinal emittances obtained are quite similar values in the four methods, with values around  $0.17\pi$  deg MeV.
- The three<sup>1</sup> RFQ electrostatic field simulation methods yield maximum surface values lower than 33 MV/m. However, we consider the figure provided by COMSOL as the most accurate of the three by far, followed by TOUTATIS. In this scenario, the *Bravery Factor* of our RFQ probably lies at some value close to 1.75. This, together with the fact that ESS-Bilbao will be operating under a quite low duty cycle, gives us confidence that we should avoid heavy electrical breakdown problems.

In order to establish a more in depth comparison of the different simulation methods, we can analyse the successful transmission (particles accelerated to  $3.0 \pm 0.1$  MeV) at different input currents, as presented in Figure 2.7. Once again, the results are very similar between TOUTATIS and GPT + COMSOL, probably due to the fact that both use geometry-based field maps, as opposed to the multipole models. All the transmissions

<sup>1</sup> RFQSIM and GPT + Multipoles use the same analytical expression to estimate the surface field.

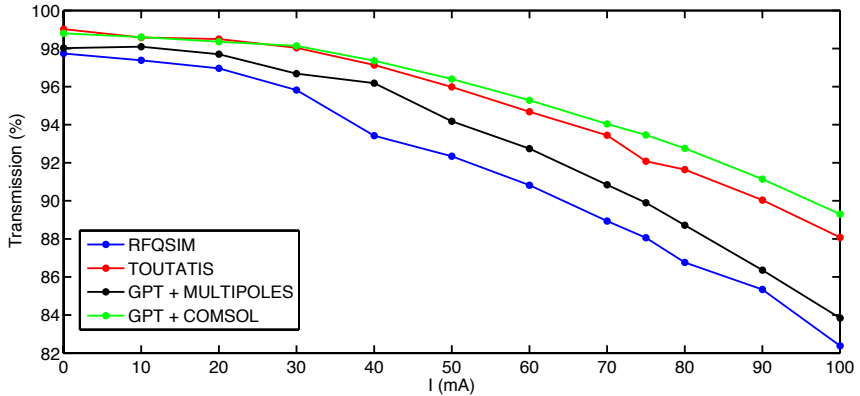


Figure 2.7: Transmission as a function of the beam current, simulated with four different methods.

remain above 90% at the range of interest (below 60–70 mA), with the two more accurate methods yielding transmissions above 95%, at medium currents, and above 98% for any current below 30 mA.

Finally, Figure 2.8 compares the transverse losses (due to particles impacting with the vanes) along the RFQ, by depicting the beam power lost per centimetre of length. The main region where particles are lost is the end of the Gentle Buncher, which is located at 1.3 m from the beginning of the RFQ. As depicted in Figure 2.4, there is a rapid decrease in the minimum aperture  $a$ , which creates a certain *bottleneck* that can strip some of the outer particles of the beam. The total power losses, displayed in the legend box, take different values due to the different transmission percentages obtained. However, all the methods show minimal losses at the last half meter, which is the region where the beam energy surpasses the copper activation threshold [10].

In summary, the results presented above prove the validity of the proposed vane modulation to reach the desirable beam transport performance, as tested with different particle tracking and field map calculating methods. However, it is also necessary to check the behaviour of the RFQ when certain parameters, either related to the beam characteristics, RFQ operating parameters, or vane machining accuracy, vary from the ideal conditions. Those studies are presented in the next section.

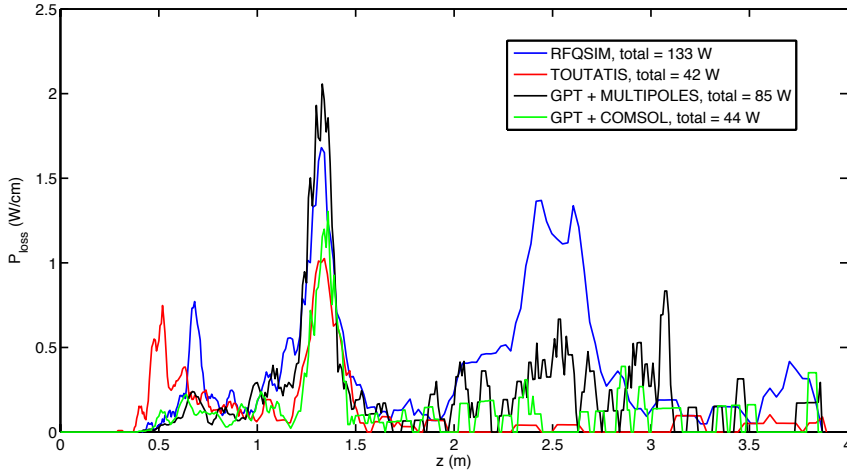


Figure 2.8: Beam power loss per centimetre of RFQ length, simulated with four different methods.

## 2.3 Modulation robustness and stability

In this section we examine the effects of varying certain simulation parameters, which allows us to predict the behaviour of the RFQ when operating under non ideal conditions.

### 2.3.1 Variation of the input beam characteristics

We have performed particle tracking simulations in which we sweep the values of the beam current, input energy, and transverse emittance. All the simulations in this section have been performed with the combination GPT + COMSOL (as particle tracking and field map simulation methods, respectively), since we consider it to be the most accurate tool available to us.

Figure 2.9 presents the particle transmission for different input currents. In addition to the information shown in Figure 2.7, in which only the particles captured by a bunch were included, we also plot the full transmission (i.e. particles that reached the end of the RFQ, regardless of

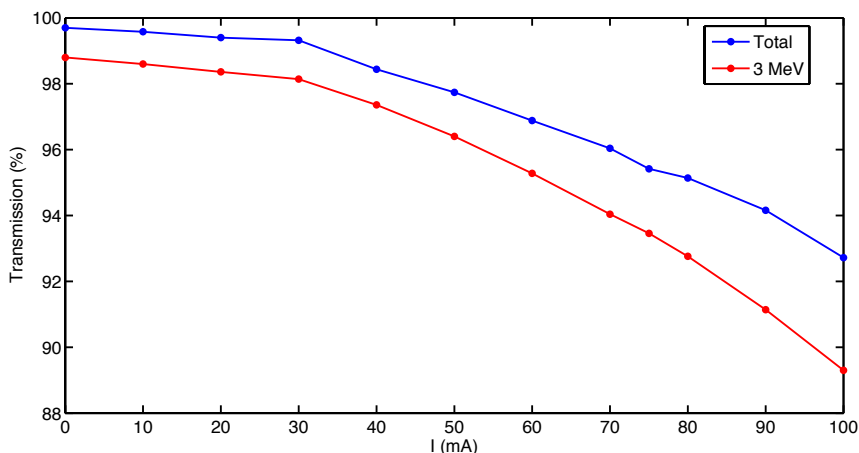


Figure 2.9: Total and 3 MeV transmissions as a function of the input beam current.

their energy). The captured transmission remains  $\sim 1\%$  below the full one for currents up to 50–60 mA, which demonstrates that the transmission drop with increasing currents occurs basically due to longitudinal losses.

In Figure 2.10 we plot the transmission (both total and captured) for different input beam energies. Although the transmission is maximised for the nominal 75 keV, the curve is pretty broad for an energy span of about  $\pm 3$  keV, dropping faster outside this energy range. In any case, the transmission drop should not be a problem, since the energy of the ion source is centred at 75 keV, with a dispersion of about 100 eV [11].

Finally, we have performed two transverse emittance related studies. In the first one, presented in Figure 2.11, we plot the transmission as a function of the input beam rms emittance. As expected, increasing the beam size mainly affects the transverse losses (i.e. particles hitting the vanes), as deduced from the fact that both curves are almost parallel. However, the transmission remains above 90% for input emittances below  $0.45\pi$  mm mrad, which leaves a considerable margin from the expected value for the input beam, even accounting for a certain emittance growth in the LEBT.

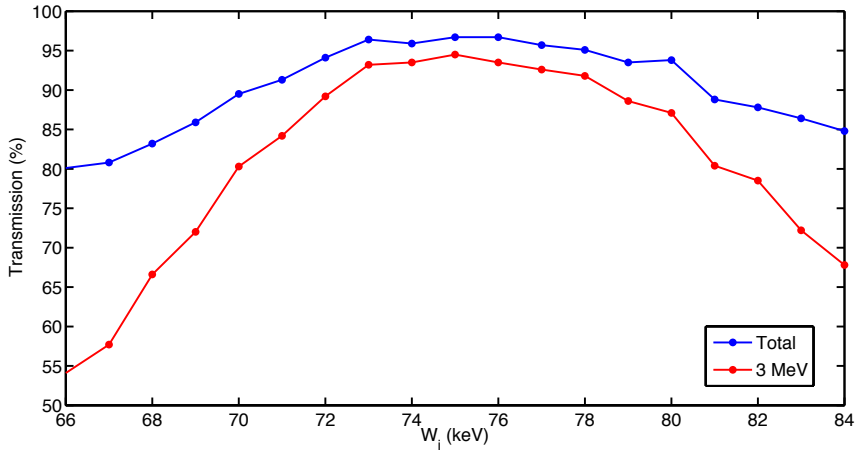


Figure 2.10: Total and 3 MeV transmissions as a function of the input beam energy.

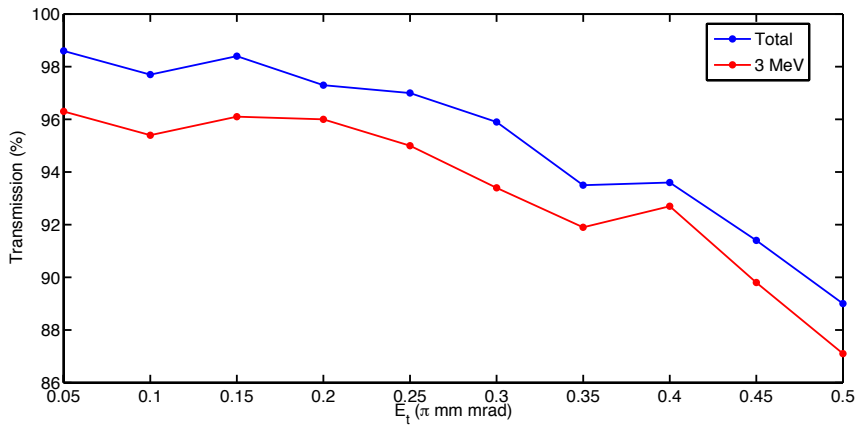


Figure 2.11: Total and 3 MeV transmissions as a function of the input beam transverse emittance.

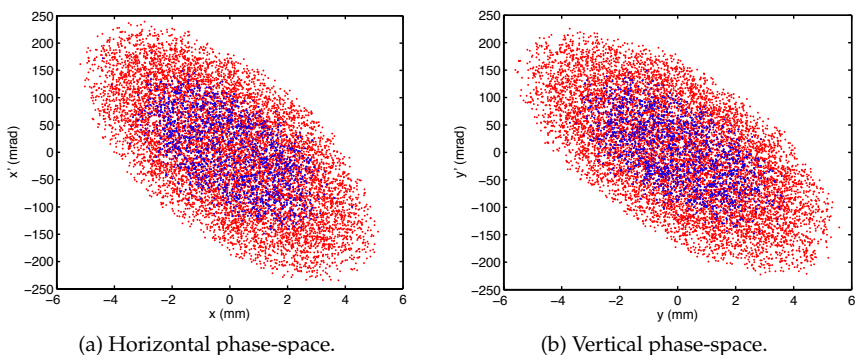


Figure 2.12: Particle density plots at the output of the RFQ.

In the second transverse emittance related study, we have investigated the zero current acceptance of the RFQ. This is the maximum size of the input beam that gets successfully transmitted when the particle-to-particle interactions are neglected. In order to do this, a very high emittance beam is used as input, only part of which will be transmitted. The emittance of those transmitted particles, calculated at the input of the RFQ, is defined as the zero-current acceptance. Figure 2.12 shows both the full input beam (red) and the part that gets transmitted (blue), plotted in the transverse phase spaces. The acceptances (rms emittances of the blue beam) are  $1.03$  and  $0.96\pi$  mm mrad for the horizontal and the vertical phase spaces, respectively. In principle, any beam contained in the blue regions of the figures should be transmitted, provided the current is very low. At non-negligible currents, space charge effects create transverse forces that result in an increased particle loss.

### 2.3.2 Variations of the electric field amplitude

Along with studying the response of the RFQ to different beam characteristics, it is useful to analyse its performance when the magnitude of the electric field is varied. The practical interest of this study lies in being able to predict the impact of such operating conditions in the focusing

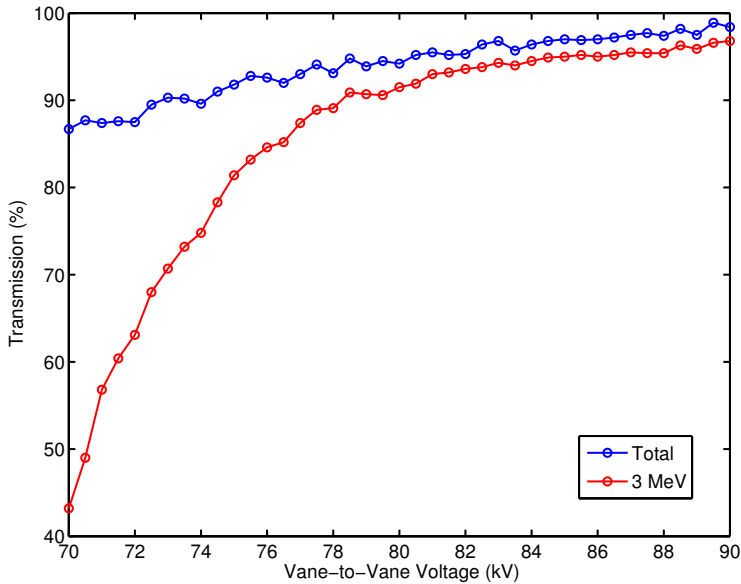


Figure 2.13: Total and 3 MeV transmissions as a function of the RFQ vane-to-vane voltage used in the electrostatic simulation.

and accelerating capabilities of the RFQ. Lowering the RF power might be needed in order to reduce electrical breakdowns, while increasing it should improve the particle transmission values.

Figure 2.13 presents the transmission as a function of the vane-to-vane voltage. This parameter is swept indirectly in the GPT simulations, where the electric field multiplication factor is used ( $E/E_0 = 1$  implies  $V = 85$  kV). The captured transmission remains above 90% for voltages higher than 79 kV, which leaves a certain margin to decrease the RF power if sparking phenomena are found. On the other hand, the simulations suggest that increasing the RF power should result in a slight improvement of the particle transmission figures.

Table 2.5: Simulations Setup

Parameter	Value
$dR$ , Longitudinal profile error	50 $\mu\text{m}$
$d$ , Transverse curvature of the electrode error	50 $\mu\text{m}$
$TEpe$ , Perpendicular tilt error by electrode	100 $\mu\text{m}$
$TEpa$ , Parallel tilt error by electrode	100 $\mu\text{m}$
$DEpe$ , Perpendicular displacement error by electrode	100 $\mu\text{m}$
$DEpa$ , Parallel displacement error by electrode	100 $\mu\text{m}$
$DELong$ , Longitudinal displacement error by electrode	100 $\mu\text{m}$

### 2.3.3 Effects of the vane machining/assembly errors on the beam dynamics

The RFQ structure will be made by segments  $\sim 800$  mm long; such elements will be flanged with a short longitudinal discontinuity ( $\sim 0.2$  mm). Those RFQ vane segments may be displaced in a particular direction, be tilted, or have a wrong field (phase and/or amplitude). In order to evaluate the robustness of the RFQ design as a whole with respect to fabrication and alignment errors, a number of simulations have to be performed. These simulations help establishing boundaries for the deformations due to thermal expansion and therefore affect cooling design (see Chapter 6). Due to the lack of parameters from the manufacturer the limits used to study the vane profile robustness have been taken from the literature [12]. For this first round of simulations, only *static* or time-independent errors have been considered. In other parts of the linac some effects of these kind of errors can be corrected, in the RFQ as a whole however there is no steerer we could use.

We consider the modulation mentioned in the previous section. The errors, represented by the TRACEWIN parameters (see Figure 2.14), have been uniformly distributed; each value expressed in the Table 2.5 expresses the maximum range for each type of which could affect the modulation. 200 different cases per fraction (see Figure 3.8) have been launched, with 200 000 particles each.

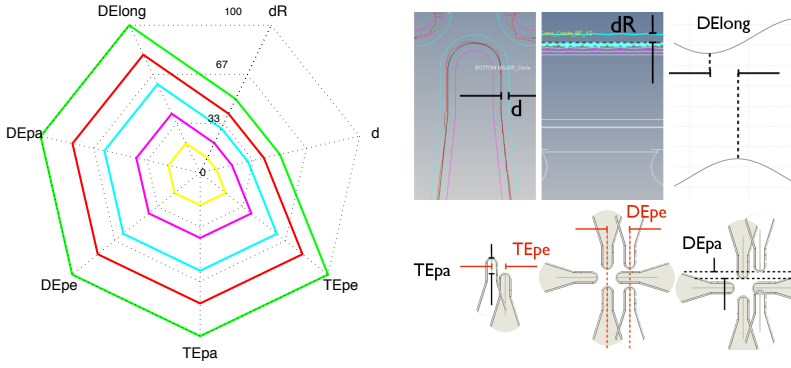


Figure 2.14: **Left:** Error setup for a statistical error study. Distances are given in  $\mu\text{m}$ , description of each parameter Table 2.5. **Right:** Parameter description.

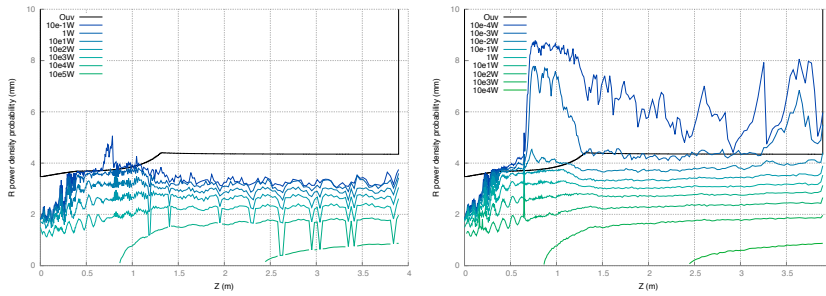


Figure 2.15: **Left:** Accumulated power density levels (W) for the  $\text{H}^+$  along the RFQ, with a 65 mA current for the nominal case. **Right:** accumulated density profile for the statistical error study.

For the conditions described before, Figure 2.15 compares the power density profile for the nominal case and the accumulated power density levels along the RFQ structure. The black line represents the aperture, i.e. all lines exceeding this boundary indicate the likelihood for losses according to the performed statistical study. In this case only below 0.1 W lines do cross the boundary, mainly in the *Gentle Buncher* critical region.

In the Figure 2.16 we can observe that in the worst case, in which all errors are combined with the 100 % values from Table 2.5, the mean value for the beam losses –when combining all types of errors– does not exceed 2% of the nominal case. Moreover, the emittance increase, in average, stays below 5% for both the transverse and longitudinal cases. see Chapter 3 for more details.

## 2.4 Conclusions

We have presented the procedure followed to design the ESS-Bilbao RFQ modulation, based on Alan Letchford's RFQSIM software. The proposed modulation, designated 11.4, fulfills all the imposed design constraints, with an acceptable length, a Bravery Factor below 1.8, and good results in particle tracking simulations, which were carried out with four different methods.

Additionally, we have studied the behaviour of the RFQ outside the nominal conditions. The proposed design should work with a wide range of input beam characteristics, and be tolerant of standard manufacturing errors.

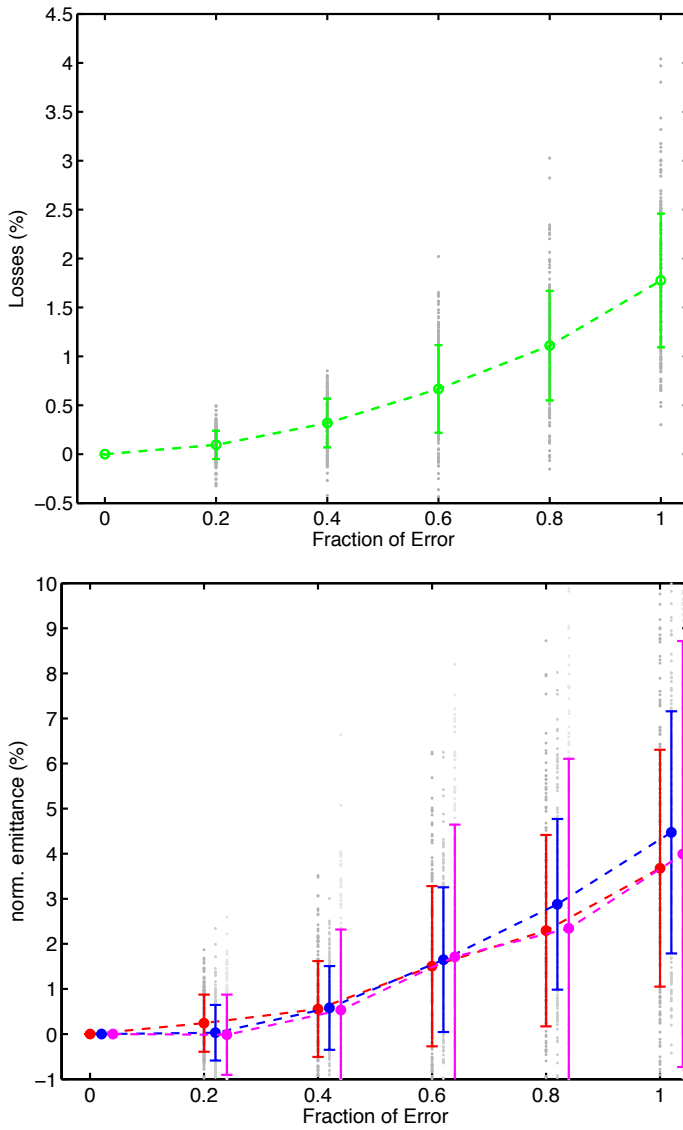


Figure 2.16: **Top:** Losses (%) **Bottom:** Transverse (red and blue) and Longitudinal (pink) emittance increase (%) respect to the nominal case.



# Chapter 3

## RFQ Segments

### 3.1 Introduction

For a certain  $L/\lambda$  ratio a *RF compensated* or *coupled* design [13] is recommended. In the coupled RFQ design, different sections are decoupled magnetically and the magnetic field rotates in each of the sections independently, making it possible to stabilise local decompensation (by tuners, for example) without affecting the rest of the structure, as well as a number of advantages associated with the tuning of the resonant modes. However, major disadvantages of this design are related to the complexity of the *coupling plates* design, and the derived long gaps ( $> 4$  mm) between sections.

#### 3.1.1 Number of Sections: A discussion

Along with our RFQ project, a survey among local workshops has been done, and it seems that the same people who made the OHFC WELD TEST MODELS ( $\sim 300$  mm long) are quite confident about the roughness ( $R_a = 0.4\text{--}0.5$   $\mu\text{m}$ ) and the tolerances they can achieve ( $\sim 5\text{--}10$   $\mu\text{m}$ ). But there is a shortcoming: in order to achieve such tolerances, we would need to shorten each RFQ section to  $\sim 800$  mm, so they can fit in their machine. As a direct consequence, we would move from 4 sections ( $\sim 1$  m long)

to 5 sections ( $\sim 800$  mm long). For the 1 m option they would offer an approximated value of  $R_a = 0.8 \mu\text{m}$  for the arithmetic average roughness, and  $20\text{--}35 \mu\text{m}$  for the tolerances, with big uncertainties, since they would need to use a machine they are not familiarised with. It seems clear that some parameters will get worse, such as the Q factor, since one more joining means one more transition. Moreover, in order to keep the symmetry in each section, one extra turbo pumps will be included (good for vacuum, not so much for the Q, and increasing the dipole mode component). Finally, if 16 tuners per section remain constant (now each section has 800 mm, so compared with the original 64 total tuner ports, we would have 80), this provides more tuning range and efficiency, but the Q will get worse.

From the IFMIF and TRASCO experience, when reducing the segments length, the number of tuners cannot kept the same due the lack of space: at the beginning and the end of any section one needs the same space for the flanges in any case, so the distance between tuners would be reduced, with the problem of space allocation for the tuner itself. If the number of sections is increased a more complicated water cooling circuit will also be required.

On the other hand, the ISIS experience tells us that the fewer sections the RFQ is made from, the better, but there is a compromise. The reduction in Q only really becomes an issue if you are limited on RF power or if the extra heat load is difficult to cool away, which does not seem to be our case (see Chapter 6). One suggestion was to reduce the number of tuners to 12 per section, for a total of 60, which may not compromise too much our ability to tune. Having an extra section will produce more assembly problems and there will be an extra vacuum joint, both of which would be interesting to avoid.

Finally, it is worth mentioning that both, previous experience from Los Alamos and INFN-Legnaro, have successfully built a machine using the later sections as short as 500 mm. They use wire EDM to cut out the pieces, then finish them in the milling machine prior to brazing. There should not be any degradation in the Q at the joints between segments. Since there is no current crossing the joints, there should not be any RF gaskets, just a small gap. If we put something like a helical wire seal there, the magnetic fields will excite currents in the wire and spoil the Q. For flanges, copper is recommended. After a lot of problems trying to braze

stainless flanges onto Cu cavities, they abandoned this idea and now they just use thick Cu flanges. Based on Young's experience [14], tolerances are much tighter in order to achieve the required RF fields. So if we can maintain a 10–35  $\mu\text{m}$  precision on the vane tip positions, that will allow to preserve the field distribution, and the beam dynamics should not be affected. Finally, they don't think it is necessary to maintain the symmetry by adding pumps. If the grill has been properly designed, it should have no effect on the field distribution, so extra tuners would probably be more valuable than symmetry.

In conclusion, in order to keep machining tolerances within an acceptable range, the RFQ structure will be divided in 5 different segments, each of them with a maximum length of 800 mm. In a non-coupled RFQ design, the magnetic field rotates only at the ends of the structure. As a consequence, there is no need for coupling-gaps; the gaps between the different sections are limited only by assembly limitations and the minimum distance to account for any thermal expansions in the OHFC. With this in mind, we have selected 0.2 mm as the length of the gaps between segments in cold<sup>1</sup> state. This length ( $d$ ) is expected to be  $\sim 2$ – $3$  times as long as the expected expansion at this point, so the gap will not fully (but nearly) close at full power.

Dividing the RFQ into segments presents an extra drawback: the surface electrical field will likely increase at the segment ends (Figure 3.5). As a first approximation based on cylindrical capacities, the field enhancement factor  $K$  is linked to the local curvature radius  $r$  and to the inter-vane half-distance  $d$  by:  $K \approx 1 + d/6r$  [15]. In the following sections of this chapter we will discuss the several approaches taken in order to overcome this undesired effect.

### Radius of curvature

There are two approaches that constitute a good reference of the state of the art: the IFMIF and the IPHI projects.

For the IFMIF RFQ (D+, 5 MeV, 130 mA, 175 MHz, CW) [16], the coupling gaps are very small: 0.1 mm; it constitutes the minimum distance mechanically possible between the 18 modules. Along with this gap dis-

---

<sup>1</sup> No power transmitted to the resonant cavity.

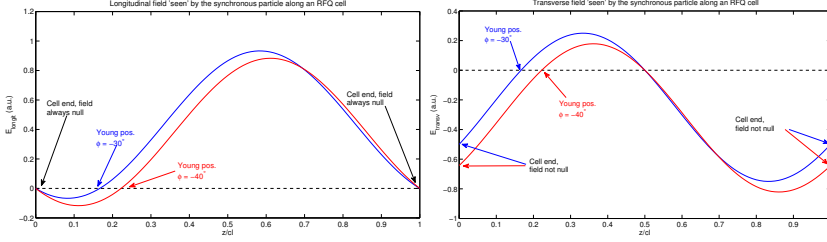


Figure 3.1: Longitudinal (left) and transverse (right) fields that synchronous particle sees on-axis along the RFQ.

tance the elected radius of curvature was a compromise ( $r = 0.5$  mm) between spark phenomena (smaller radius) and undesired effects on beam quality (larger radius).

According to the IPHI RFQ (5 MeV, 100 mA, 352.2 MHz, CW) experience [15], increasing  $r$  in order to obtain a reasonable peak field ( $K = 1.10$ ) leads to unrealistic radius values ( $r > 17$  mm). The solution to avoid this problem is to use an elliptical corner instead. The following half-axis parameters:  $a = 2$  mm,  $b = 0.75$  mm constitute a good compromise.

### Location for the cuts

On the other hand, such elliptical corners slightly enforces the on-axis field drop due to the coupling gap. Two positions were studied:

**Young:** To minimise the coupling gap perturbation, L. Young [13], from LANL, has put into practice a new technique consisting of locating the gap at the longitudinal position crossed by the bunch when the RF power is equal to zero. Applying this concept in a particular cell gives the law:

$$z = L_c \frac{\Phi_s}{\pi}, \quad (3.1)$$

for the position gap centre, where  $L_c$  is the cell length and  $\Phi_s$  is the synchronous phase. This way, the field vanishes when the bunch centre crosses the gap (see figures 3.1 to 3.3).

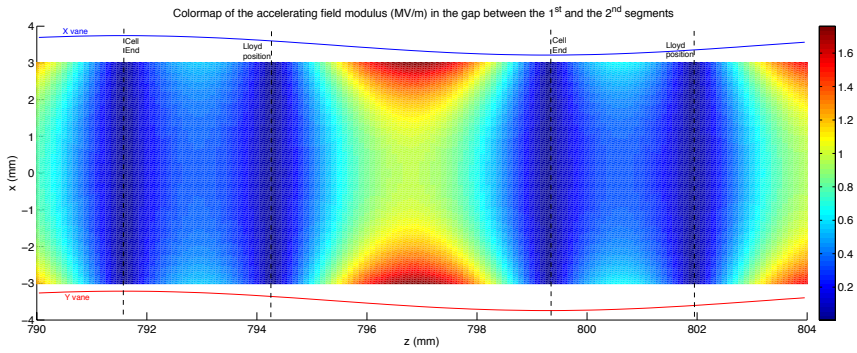


Figure 3.2: Accelerating field in the first gap region, with Cell-End and Young positions marked.

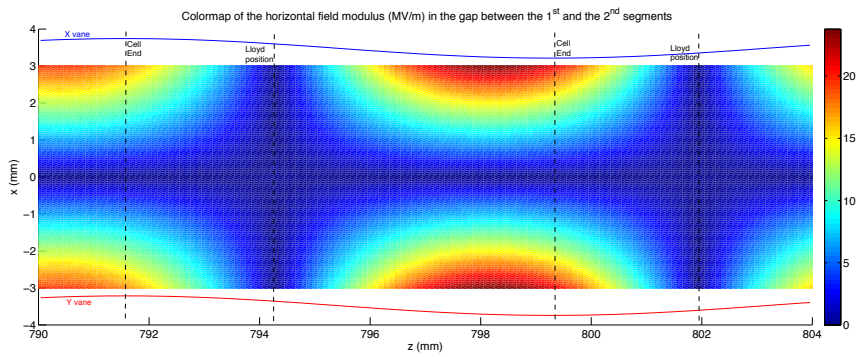


Figure 3.3: Horizontal field in the first gap region, with Cell-End and Young positions marked.

**Cell-End:** The other option would be to cut the vanes at the end of the corresponding cell. In this position, we assure that the accelerating component of the RF fields is equal to 0 for all particles, not only for the synchronous one. The transverse components, however will be  $\neq 0$  (see figures 3.1 to 3.3).

## 3.2 Particle Tracking Simulations

Several simulations, with the conditions —summarised in Table 3.1, have been carried out in order to evaluate the net effects of the perturbation introduced by the inclusion of these gaps on the ideally continuous vane shape profile.<sup>2</sup> The formerly proposed elliptical shaped curvature ( $a = 2$  mm,  $b = 0.75$  mm) [15] has also been included to use as a comparison with the standard  $r = 0.5$  mm curvature. As one can infer from Table 3.1, there is little difference from the beam dynamics point of view, so going to 5 segments as suggested by the manufacturer, should not represent a substantial worsening of the results. In order to adopt a solution FEM simulations would be a critical factor. Those FEM simulations will be detailed in the following section, and will serve to choose between curvature radius in order to minimise the maximum electric surface field.

## 3.3 FEM simulations

Two different aspects related to segmentation have been analysed. One is related to power losses: on one hand the dissipation is increased due to the additional vacuum port (a pair of which is installed in each segment) for 800 mm segments, but on the other hand a much better surface roughness finishing can be obtained for shorter segments, thus reducing losses. The other is related to the increase of surface electric field in the gap region, where it can rise above the 1.8 Kilpatrick criterion used for RFQ design. These aspects have been studied using FEM simulations (COMSOL Multiphysics) and Matlab scripts.

---

<sup>2</sup> These particular simulations have been done using the modulation coded 10.11, a previous design to the finally selected 11.4. Similar results are expected for both modulations.

Table 3.1: Output RMS characteristics of the beam for accelerated particles (transverse emittances in  $\pi$  mm mrad, longitudinal emittance in  $\pi$  deg MeV and transmission in %). The size of the gaps is  $d = 0.5$  mm. In the circular case the radius is  $r = 0.5$  mm and in the elliptical  $a = 2$  mm and  $b = 0.75$  mm.

Gaps	0	3		4		
		circular		elliptical		
		Young	Cell-End	Young	Cell-End	
$\epsilon_{xyp}$	0.25568	0.25531	0.24917	0.24878	0.24956	0.25358
$\epsilon_{yyp}$	0.25142	0.25247	0.24804	0.24833	0.24789	0.24988
$\epsilon_{zyp}$	0.1474	0.14976	0.13483	0.1359	0.13582	0.13798
T	95.32	95.44	95.20	95.31	95.31	95.22

Table 3.2: Power losses and other figures of merit for 800 mm or 1000 mm long RFQ segments, while  $f_Q$  is the frequency of the quadrupolar mode. Figures of merit are related to the quadrupolar mode.

Segment	$f_Q$ (MHz)	$P_{segment}$ (W)	$P_{total}$ (W)	Roughness ( $\mu$ m)	Q corrected for $R_p$
800 mm	351.9	74 350	397 484	0.4	11 249
1000 mm	352.0	94 435	404 506	0.8	11 159

### 3.3.1 Power dissipation

In order to estimate the overall power losses in the two configurations considered (4 segments of about 1 meter vs 5 segments of about 800 mm), two models have been solved (RF eigenfrequency solver). Electromagnetic field values have been then scaled in both models to provide the same accelerating field in order to compare results, and finally power loss and other magnitudes have been studied. Power loss can be seen in figures 3.4 top and 3.4 bottom. The estimation for the whole RFQ losses is done taking into account the first segment of the RFQ, containing an input matcher but no output matcher (so total losses are not just 4 times the losses of the 1000 mm segment, for example). Results are described in Table 3.2. There are no big differences, but with 800 mm segments a slightly better quality factor is obtained, due to the reduced surface roughness.

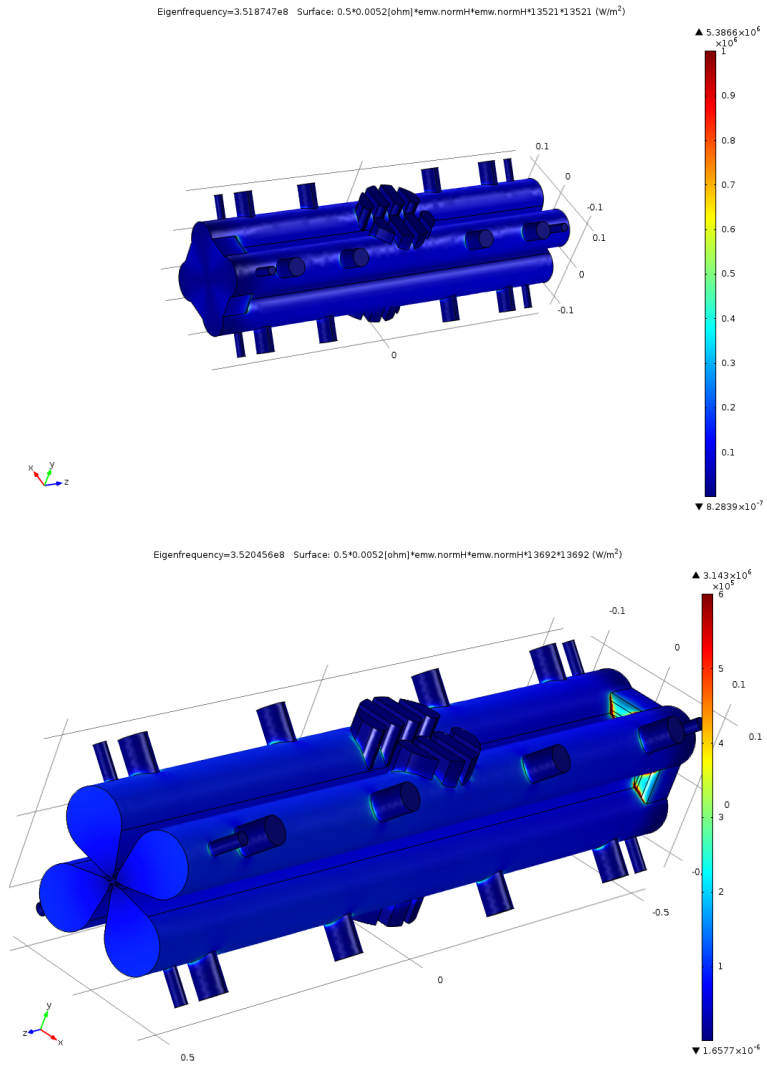


Figure 3.4: **Top:** Power loss in a half segment of 800 mm. **Bottom:** Power loss in a half segment of 1000 mm.

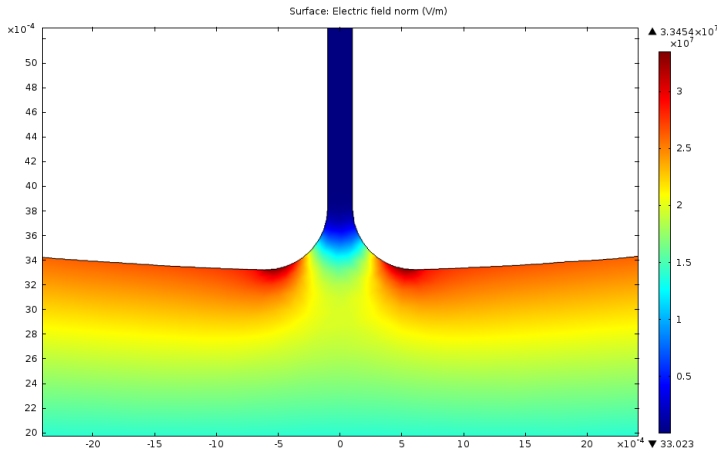


Figure 3.5: Normalised electric surface field 3D Electrostatic simulations with  $d = 0.2$  mm and  $r = 0.5$  mm. Although the cut plane indicates a maximum value of 33.45 MV/m, the maximum value found in the 3D simulation is 42.60 MV/m.

### 3.3.2 Gap surface electric field

The presence of a inter-segment gap increases the electric field locally above the considered threshold for the electric surface field ( $\sim 33$  MV/m). In order to reduce the field values, the shape of the gap is improved by rounding the corners with a circular (radius  $r$ ) or elliptical shape (major/minor semi-axis  $a/b$ ).

This was studied by electrostatic FEM calculations. In a first step, gap geometries were created using CAD software and imported in the electromagnetic simulator but CAD creation took a lot of time for quick gap geometry prototyping, so geometries were finally generated in the simulator. This procedure was also chosen for building the models for electromagnetic simulations, and it is described there. In the models, only the vacuum volume close to the gap in the vane tip region is selected for electrostatics calculations. To increase the accuracy of the maximum value of the surface electric field calculation, models are solved using cubic base functions and tailored meshes.

Table 3.3: Maximum surface field for the different inter-segment gaps. Gaps considered have a width of  $200 \mu\text{m}$ , and ellipse parameters of  $a = 2 \text{ mm}$  and  $b = 0.75 \text{ mm}$ .

Gap	$z_0$ (m)	$z_1$ (m)	$z_{ec}$ (m)	$z_{LL}$ (m)	$E_{\text{no gap}}$ (MV/m)	$E_{ec}$ (MV/m)	$E_{ll}$ (MV/m)
1	0.76879	0.83081	0.7916	0.7943	32.44	35.6	34.68
2	1.5049	1.6543	1.5775	1.5811	31.74	33.52	34.59
3	2.2876	2.4966	2.3645	2.3691	31.8	34.1	34.69
4	3.068	3.3148	3.1592	3.1339	31.89	34.29	34.83

Different gap lengths and geometries, as well as different gap centre positions (in the end of a modulation cell or in the Young position) are under consideration. The constant radius  $r = 0.5 \text{ mm}$  surface fields resulted in high surface fields  $E_{ec} = 40.6 \text{ MV/m}$ ,  $E_{ll} = 40.7 \text{ MV/m}$ , we therefore focused on elliptical shaped rounding.

The analysis has been done with modulation 11.4 (frozen modulation at the time of writing). The computed models correspond to a portion of RFQ inter-vane area. The increase of surface field is studied by comparison of the model solved without gap and with gaps in the Cell-End and Young positions. Maximum surface electric field is not an easy magnitude to obtain accurately. These results are summarised in Table 3.3.

Figure 3.7 represents the parametric study performed using different  $a$ ,  $b$  parameters of the ellipse in the fourth gap. The estimated perturbation introduced on-axis field was calculated using the following formula:

$$\delta f = \sqrt{\int (\mathbf{E}(z) - \mathbf{E}0(z))^2 dz}, \quad (3.2)$$

where  $\mathbf{E}0(z)$  stands for the accelerating field without any gap, and  $\mathbf{E}(z)$  is the perturbed accelerating field with the gap.

### 3.4 Robustness study

In order to take a decision on the optimal location for the segment cuts (*Young* or *Cell-End*), two types of error studies have been performed by means of TRACEWIN/TOUTATIS:

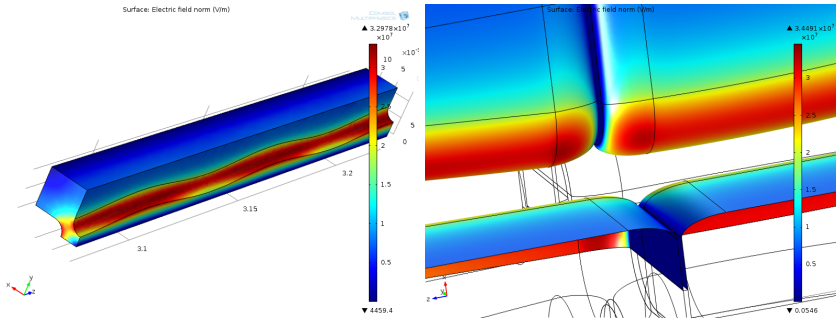


Figure 3.6: **Left:** Surface field in a portion of RFQ without a gap. **Right:** Surface electric field in a portion of RFQ with a gap. Gap width is  $200\ \mu\text{m}$  and is placed at the Young position in fourth gap between segments 4 and 5.

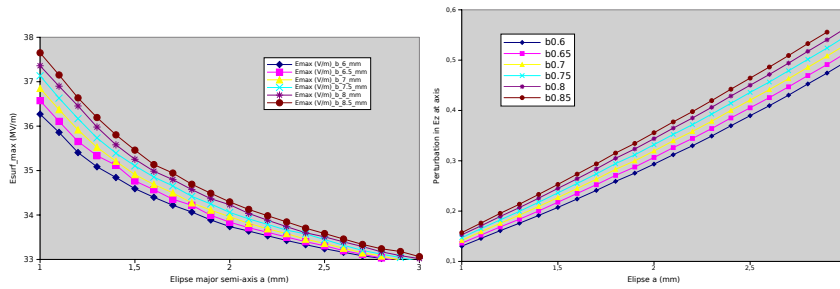


Figure 3.7: **Left:** Surface field values for different combinations of the ellipse parameters:  $a$  and  $b$ . **Right:** Introduced perturbation in the on-axis accelerating field map.

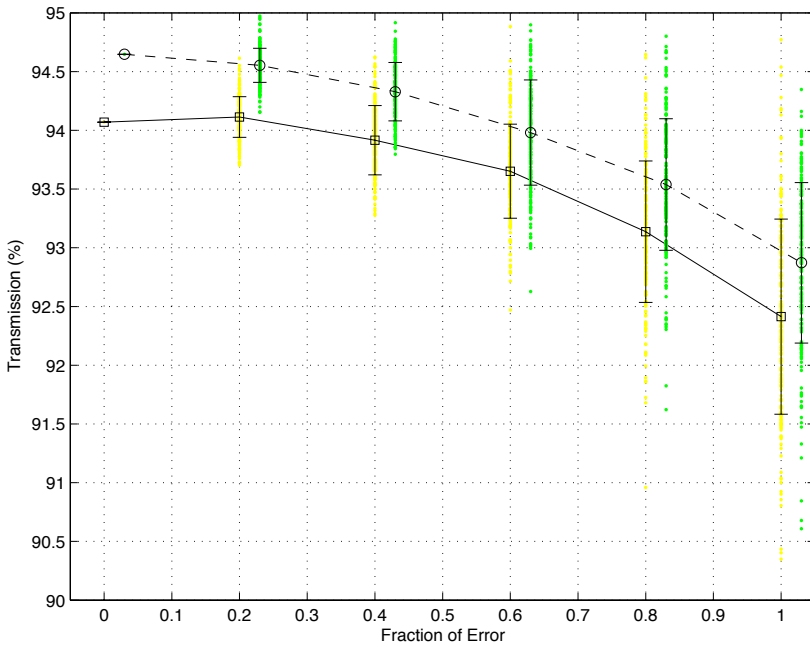


Figure 3.8: Transmission for two locations of cuts under study, for a statistical error study. Input conditions have been kept the same for both cases. *Young* in green ( $\circ$ ), *Cell-End* in yellow ( $\square$ ).

### 3.4.1 Static Error Study

A comparative time-independent error study has been performed. Here, 200 RFQs per error fraction have been simulated, i.e. 1000 RFQ per cut. Table 2.5 expresses the maximum considered errors introduced in the vane modulation. Those errors are combined uniformly in groups of fractions, so that we can evaluate statistically the possible effects of the machining, mounting and alignment in the most realistic scenario.

Figure 3.8 shows the obtained transmission values for the generated 2000 RFQs along with its correspondent *mean* and *standard deviation* values. In order to increase visibility of the data, the simulations corresponding to *Young* cuts –represented by green dots ( $\circ$ ), have been offset by a small frac-

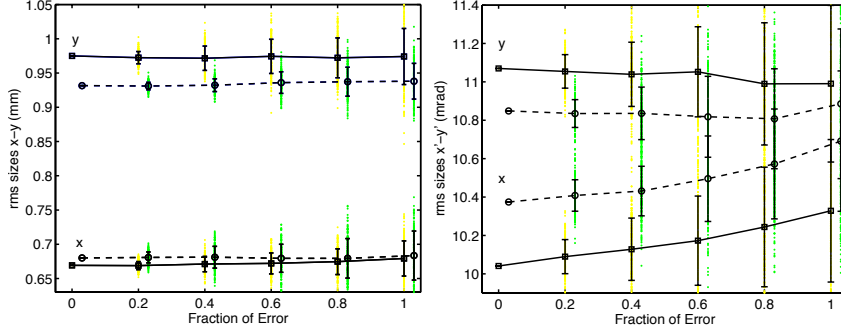


Figure 3.9: Transverse output for the statistical error study. **Left:** Average *RMS* size ( $x$  in blue,  $y$  in red). **Right:** Average *RMS* angle size ( $x'$  in blue,  $y'$  in red). Young cuts are expressed with *dashed lines* and *circles*, and Cell-End option is represented by *solid lines* and *squares*.

tion in the abscissa axis respect to the *Cell-End* cuts –represented by yellow dots ( $\square$ ). If we compare the transmissions against the ideal machining case for a 60 mA,  $0.25 \pi$  mm mrad normalised transverse emittance, 75 KeV input energy and  $2 \times 10^5$  particles, considering a 200  $\mu$ m gap distance, and a 15 mm gap distance for both RFQ ends. From here, it can be inferred that the Young cut seems a more robust option.

Figure 3.9 shows the output *rms* size in  $(x, y)$  and  $(x', y')$  space. From here we can infer that the projections of the bunch will not be affected compared to the angles. Although the mean values seem to evolve quite steadily, the spread of the each simulated combined errors indicate that  $\delta r / \delta z$  ( $r$  stands for either  $x$  or  $y$ ) seem to be more sensitive to any perturbation of the vane shape.

In Figure 3.10 we can see the output *rms* size in the longitudinal space. Although mean values indicate a steady evolution against the increase of error fraction, the standard deviation values indicate the unsteady results for each case. In our experience<sup>3</sup> an improvement for the energy spread value is usually accompanied with a worsening of the corresponding phase spread parameter.

<sup>3</sup> Single events could not be tracked back due to a limitation of the employed technique.

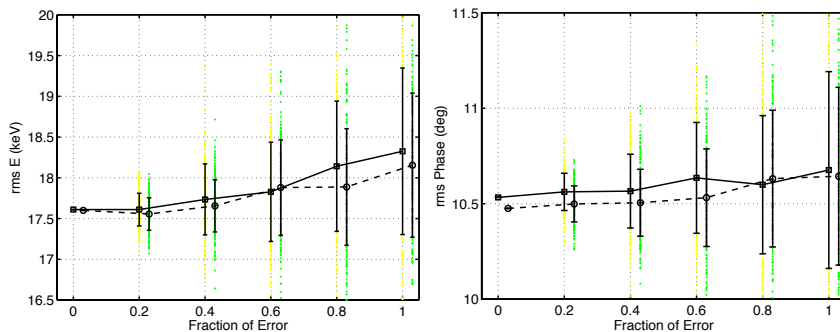


Figure 3.10: Longitudinal output for the statistical error study. **Left:** Average energy RMS spread (keV). **Right:** Average phase RMS spread (deg). Young cuts are expressed with *dashed lines and circles*, and Cell-End option is represented by *solid lines and squares*.

Inspecting both figures 3.9 and 3.10, we can infer that it is the longitudinal plane the one that is more vulnerable to fabrication and alignment errors: We can see that transverse displacement spread is more stable compared to momentum along the increment in the presence of errors.

In order to establish a fair comparison between *Young* and *Cell-End* options, results should be weighted by the obtained transmission for each step of statistical error: Collimated results tend to obtain better figures of merit at the expense of losses. With this in mind, it is difficult to have a clear winner observing transverse profiles, since both  $x$  and  $y$  results are complementary. The longitudinal study seems to show a slightly better performance for the *Young* case.

### 3.4.2 Input Beam Error Study

Figure 3.11 represents the transmission at the output of both types of RFQ, for the ideal machining case, when input conditions change. In this case, a linear scanning of the input beam current, transverse position and emittance mismatch condition is used. Again, Young option seems to obtain slightly better results.

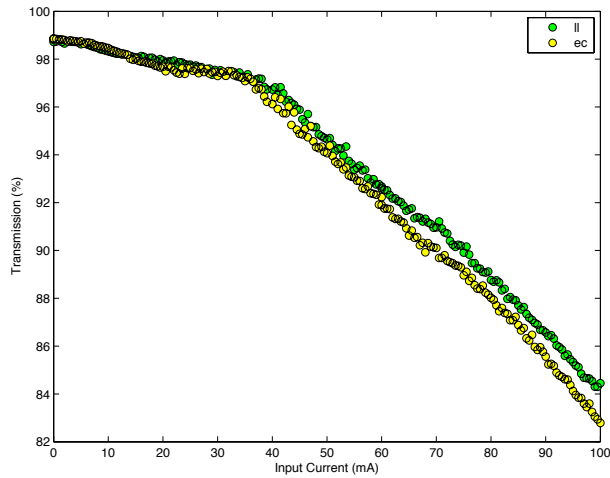


Figure 3.11: Transmission at the end of the RFQ for two locations of cuts under study for an input current variation. The input conditions have been kept the same in both cases.

### 3.5 Summary

After this study, we can conclude that an elliptical rounding offers better performance than the constant radius case. According to the simulations launched with TRACEWIN/TOUTATIS, beam quality is not been severely affected by this choice. Finally, the best possible location for cuts across the modulation was seek between the Cell-End and the Young option; the latter seemed more robust against both input and machining errors.



**Part II**

**Engineering Design**



# Chapter 4

## Electro-Magnetic Design

### 4.1 Introduction

In this chapter, the electro-magnetic conceptual design of the RFQ cavity will be presented. As it is well known, the RF power delivered into the RFQ excites resonant modes in the cavity corresponding to the fundamental mode and the higher order harmonics. The spectral frequency distribution of these modes depends exclusively on the cavity geometry. Within such a wide spectrum, one needs to select the mode desired for RFQ operation that is the quadrupole mode which corresponds to a quasi- $TE_{210}$  mode. It is precisely this resonant mode that generates the correct inter-vane voltage distribution in the cavity and hence inducing the proper accelerating potential.

Whereas vane modulation may be regarded as perhaps the most critical part of the design, one should bear in mind that the RFQ ought to be carefully designed as a whole taking into account all the elements present in the structure. That means to integrate the modulation responsible for particle acceleration, focusing and bunching with other very important elements such as radial matcher lobes (input and output) and tuners.

Regarding the RF design, lets recall that the main figures of merit are the frequency of the quadrupole mode (design frequency), together with

the distance between this mode and the adjacent dipole modes. Typically these structures show a characteristic close distance between quadrupole and dipole modes.

The excitation of resonant modes in cavities is relatively easy to calculate in the case of a structure amenable to analytical treatment such as a coaxial waveguide. These modes present in the guide and their frequencies depend on the guide cross-section parameters (inner and outer radius) and its total length. But in the case of the RFQ, its complex cross-section geometry makes the modal calculation almost impossible to be carried out by analytical means. To overcome this problem, 3D electromagnetic simulators are used.

The ESS-Bilbao RFQ operates at a frequency of 352.2 MHz for the fundamental mode. The design goal for our RFQ has been set to have a final quadrupole frequency of 351 MHz, separated by more than 5 MHz difference from the dipole modes. The 1 MHz margin is introduced to mitigate possible fabrication deviations and can be corrected afterwards by tuners. These initial specifications are detailed In this chapter.

### 4.1.1 RFQ Geometry Design and Simulation

A unified electrostatic/electromagnetic simulation tool has been used for the design process, being all the steps within the design procedure integrated in the same finite elements software tool (COMSOL Multiphysics). A fully parametrised model has been generated to describe the complex RFQ geometry. Any of these parameters can be easily modified to obtain a tailored geometry and subsequently perform the proper analysis. The results obtained have been also cross checked using other commercial software tools. For the final design stages, CAD models of the RFQ structure have been used as input geometry for simulations in order to be coordinated with the mechanical engineering activities. For a proper design, the COMSOL model is divided into two main tasks, namely the vanes design and the resonant cavity design. The design techniques used are different in both cases and will be discussed in the following sections.

Table 4.1: Tentative design parameters.

Parameter	Value
Name	FEB13_05
$r_{\text{vane}}$	2.95 mm
$y_{p1}$	16 mm
$x_{\text{circ}}$	55 mm
$r_{\text{lobe}}$	37.160 mm
$x_{30}$	8 mm
$y_{\text{mod}}$	3.485 mm (average for y mod.)
Modulation	11.4
$z_{\text{matcher}}$	18.57 + 34 mm
$\alpha$	45 deg
$x_{\text{matcher}}$	70 mm
freq (Quad) first segment	350.0 MHz
freq (Dip) first segment	342.1 MHz, 342.3 MHz
$Q_0$	10786
Power loss <sub>peak</sub>	75.7 kW (Segment 1, no tuners)

## 4.2 RFQ cavity geometry design

### 4.2.1 Transverse cross section

It was decided from the outset to base the 2D cross section for the RFQ upon a design pretty close to that developed for the ISIS RFQ. Lets recall at this point that the main figure of merit is the quadrupole mode design frequency (351 MHz), as well as a 5 MHz frequency separation with respect to the dipole modes. This is determined by the cross-section geometry. Thus, it is crucial to find a correct parametrised cross-section design able to be tailored as many times as needed in order to find an adequate distribution. The 2D cross section is here defined by the variables  $x_{\text{lobe}}$ ,  $y_{\text{lobe}}$ ,  $r_{\text{lobe}}$ , described in Figure 4.1. These parameters correspond to the centre of the circle defining the lobe and its radius, and it is straightforward to see that there will be a large number of values for this parameters satisfying the resonance frequency condition. Nevertheless, at this point we have three important restrictions, namely

1. The vane tip shape is determined by the modulation design.
2. The lines connecting the vanes top end with the circular lobe must be tangent to this one.
3. The dimensions of the copper block of the RFQ are selected to be of are 115 mm, and thus the maximum allowed value for parameter  $y_{\text{lobe}}$  is 115/2 mm.
4. Specifications for the cooling channels impose a minimum metal thickness of 15 mm at a vertical distance of 30 mm from the axis for each vane. That comes equal to the diameter of the cooling channel (7 mm) plus a safety distance of 4 mm at both sides.

According to these restrictions the set of parameters has been reduced to a few. The new set of parameter values was selected (as described in Table 4.1) after 2D electromagnetic analysis and optimisation. The selected parameters correspond to a resonant frequency of the quadrupolar mode of 351.6 MHz with a value of  $Q_0 = 10400$ .

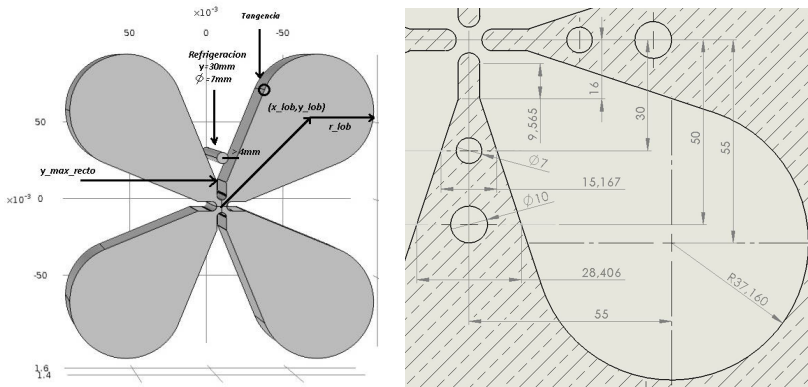


Figure 4.1: 2D model cross-section design parameters (left) and tentative values (right).

## 4.2.2 3D model

### Design strategy

Once a preliminary 2D model is built, a 3D model needs to be generated. Before embarking ourselves in such an endeavour, some consistency check for the simulation procedure is in order, since this substantially affects the 3D model generation. As it is well known, finite element solvers like COMSOL require a large amount of RAM memory for their calculations. In the particular case of COMSOL, the amount is even higher because it makes use of quadratic base functions inside the tetrahedrons (thus having 10 nodes instead of 4 for each tetrahedron). This, together with the automatic use of curvilinear elements in non-planar surfaces (as is the case for all surfaces of the RFQ) results in substantial memory and computation time requirements. In order to properly obtain the eigenvalues of a problem, the solver needs to store in memory the sparse problem matrices generated from the mesh and then operate with it. So in order to compute the whole 4 meters RFQ structure accurately a single machine calculation is not enough to solve the problem.

In our case, the proposed simulation approach consists on a approximation using magnetic walls (*slice by slice*), that allows to calculate reduced

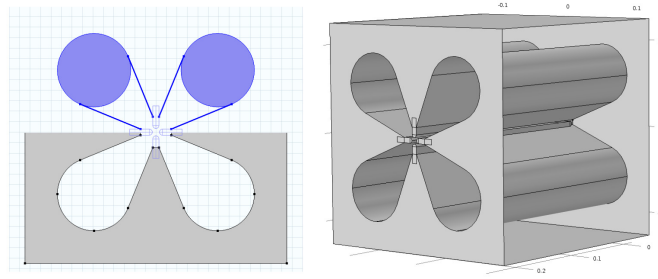


Figure 4.2: Transition 2D-3D model.

models in a local machine. The obtained results can then be extended for the whole RFQ to determine a slice by slice modal distribution. Since this approach is an approximation the results obtained can not be considered as exact for a whole model but rather, they represent the best chance in order to achieve the RFQ design. Nevertheless, further complex meshing developments have allowed us to perform highly precise simulations for 0.5m RFQ sections. As a consequence the effect of elements such as RFQ matcher lobes can be accurately predicted.

Once the 2D parameters are set, the generation of the 3D solid (without radial matcher lobes) is easily created by simply extruding the 2D cross section along the vanes (Figure 4.2) and adding the vane modulation solids. Nevertheless, those 2D parameters must be validated in 3D models. The way to determine the correct geometry for the desired resonant modes by means of the slice by slice technique has been set up by taking 20 mm slices. XY plane magnetic walls have been applied (being Z the RFQ length). Since the modulation is not constant along the RFQ, a frequency variation for the different quadrupole and dipole modes depending on the Z position is expected for any taken slice. In order to confirm it and to evaluate the effect of the modulation on the resonant frequency, many 20 mm slices along the 4 meters RFQ have been simulated. As predicted, the resonance frequency for the quadrupole mode slightly rises along the RFQ length. This effect can be understood from analysis of a resonant lumped equivalent circuit model for the quadrupole mode in a RFQ cavity. As it can be seen from

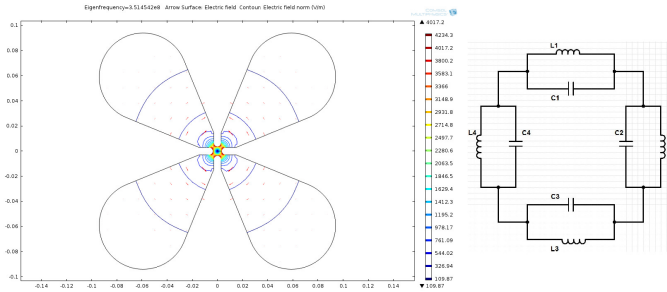


Figure 4.3: (a) 2D E-field representation for the Quadrupole mode. (b) Equivalent resonant circuit model for an RFQ cross section.

Figure 4.3 the RFQ quadrupole mode can be described as a resonant LC lumped circuit in which  $C'$  represents the capacitive coupling between the vanes.  $L'$  accounts for inductive metallic path between them and depends directly on the lobes external shape. Thus, as it is well known the resonance frequency of this circuit ( $\omega$ ) can be described by the formula:

$$\omega = \frac{1}{\sqrt{L'C'}} \quad (4.1)$$

As a matter of fact, larger modulations (amplitude increases with  $Z$ ) cause a reduction in the coupling force between vanes, thus if  $L'$  remains constant (unmodified lobe profile) an increase in the resonance frequency for the quadrupole mode results. This analysis can be done for any mode present in the structure by modifying the lumped circuit model.

In order to evaluate the frequency shift induced by the modulation, a parametric study taking slices (2 modulation cells) along the RFQ has been carried out. Although local resonance frequency changes, the total frequency shift from input to output is not larger than 3 MHz (from 349 MHz to 352 MHz), having an average resonance frequency for the quadrupole mode equal to 351 MHz.

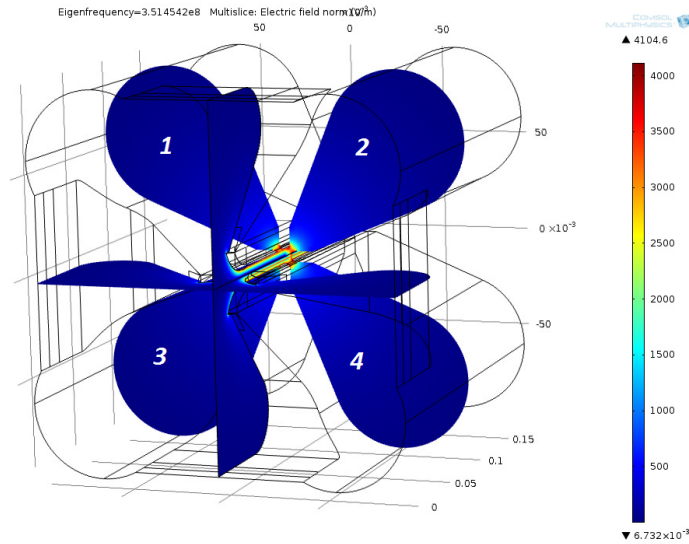


Figure 4.4: Electric field calculations for the quadrupole mode (3D layout).

### Input matchers section

At this point, even though most of the geometry elements are already set, there is a key aspect that still remains open, which concerns the radial matcher lobes. A 3D representation of a radial matcher lobe is depicted in Figure 4.4.

As it is known, magnetic field coupled through the coupler loops flows along RFQ lobes toward their ends. In the case of the quadrupole mode, the magnetic field on one lobe (1) must turn around to get into the adjacent lobes (2,3) thus, the RFQ vanes must be open on their ends. These apertures are the so called radial matcher lobes and have been also parametrised and included in the 3D model design. In the same way as in the cross-section profile there are two main restrictions to fulfil related to fabrication constraints. First of all, the line connecting the vane tip in the ends and the circle defining the area of the radial matcher lobe must be tangent (Figure 4.5).

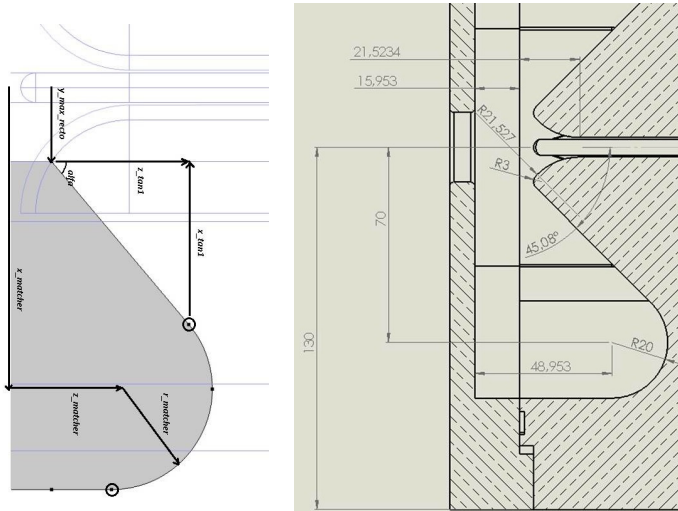


Figure 4.5: Radial matcher lobes design parameters 2D layout (left) and tentative parameters (right).

Also, due to the need of simplifying the drilling for cooling channels, the angle formed by the radial matcher lobe and the particle axis (alfa on Figure 4.5) must be  $> 45^\circ$ . On the basis of this new specification, the radial matcher lobes are parametrised and included in the final 3D model (Figure 4.6).

### Field flatness

At this point there is a final specification not imposed by post processing steps but by the need to provide a proper EM design. This refers to the so called field flatness. On radial matcher lobes, the magnetic field turns from lobe to lobe and the maximum  $H$  field concentration is found. Thus, the overall field distribution (field flatness) becomes highly influenced by the shape of the radial matchers lobes. Typically, the field flatness is a

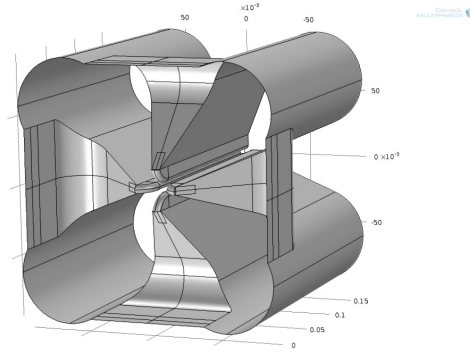


Figure 4.6: RFQ Input matcher lobes 3D layout.

normalised value defined in equations 4.2 and 4.3:

$$ff_E = \frac{E_{\min}}{E_{\max}}, \quad \text{and} \quad (4.2)$$

$$ff_H = \frac{H_{\min}}{H_{\max}} \quad (4.3)$$

In order to ensure adequate operation, the field flatness characteristics along the RFQ should be as constant as possible (typically above 0.97). Although this value can be tuned afterwards by means of mechanical elements such as tuners, the ideal scenario is to be able to specify it as low as possible by design. This task is complex and requires of a delicate and recursive work. The radial matcher lobes can be described with a lumped model based on a capacitive coupling between the vane tip and the RFQ covers and the metal inductive path described all along the lobe itself. Thus, it is clear to see that when the radial matcher lobe shape is tuned in order to obtain a better field flatness performance, we are also modifying the resonance frequency of the RFQ ends and therefore its quadrupole frequency response. After a careful study and several tested input lobe designs, this value has been optimised obtaining a final value of  $ff = 0.98$ . Figures 4.7 and 4.8 depict the electric and magnetic field responses for a 0.4 meter RFQ section at different distances from the Z axis.

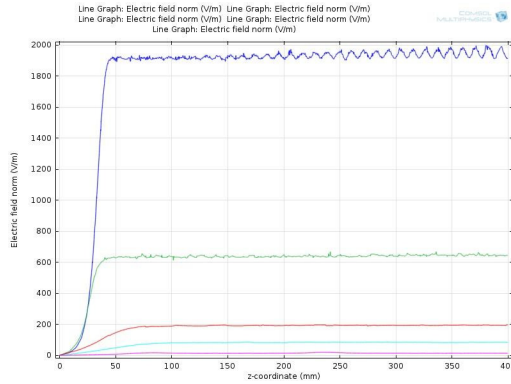


Figure 4.7: Longitudinal one lobe electric field representation. Points taken in the lobe axis at different distances from the propagation axis. Distances: 5 mm (dark blue), 10 mm (green), 30 mm (red), 50 mm (light blue) and 75 mm (purple). The effect of the vane modulation can be observed in the vicinity of the axis (5 mm).

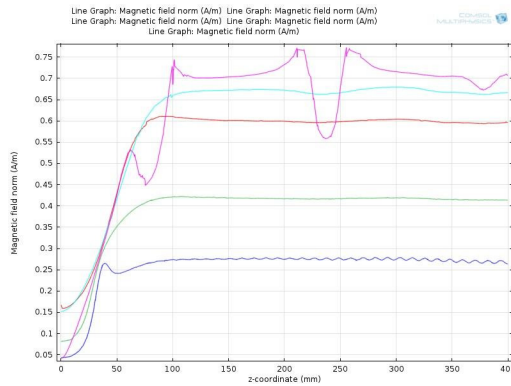


Figure 4.8: Longitudinal one lobe magnetic field representation. Points taken in the lobe axis at different distances from the propagation axis. Distances: 5 mm (dark blue), 10 mm (green), 30 mm (red), 50 mm (light blue) and 75 mm (purple). Field distortion can be observed in the vicinity of the tuners (75 mm).

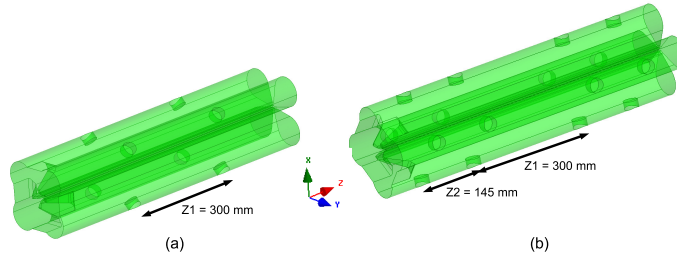


Figure 4.9: Electromagnetic model of the 800 mm segment of the RFQ including (a) 8 tuners and (b) 16 tuners. The slug diameter is set to  $D_{\text{tuner}} = 37.6$  mm.

### Some considerations concerning the Tuners

The 3D electromagnetic design has been done considering all tuners to be in flush position, that is 0 mm penetration inside the cavity. Nevertheless, a complete study for different tuner configuration and penetrations has been carried out. The ESS-Bilbao RFQ will be 4 m long and it will be manufactured into 5 different segments.

Figures 4.9-a and 4.9-b depict the RFQ segment loaded with 8 and 16 tuners, respectively. As shown in both figures, two different distances between tuners  $Z_1$  and  $Z_2$  have been defined. Moreover, since we have observed a little effect of  $D_{\text{tuner}}$ , this value is fixed to  $D_{\text{tuner}} = 37.6$  mm, and our study will focus on the effect of  $L_{\text{prof}}$  in the tuning range for the different configurations. We first consider that all the tuners are movable with a maximum penetration of  $L_{\text{prof}} = 50$  mm. Then, we consider the specific case where just one the tuners of each plane is movable. Finally, the effect of decreasing the distance  $Z_2$  is also studied. The results obtained are depicted in Table 4.2.

Recent tests performed with the RFQ cold model confirm a small frequency shift between simulation and tests for the RFQ modes (0.2 MHz). As it can be seen from tuning simulations, very short penetrations must be enough for frequency compensation. Therefore the design objective for the quadrupole mode was lowered from 352.2 MHz to 351 MHz.

Table 4.2: Study for the RFQ with 8 and 16 tuners, corresponding to Figure 4.9.

Number tuners/Number Movable	$\Delta f_{\text{quad}}$ , [MHz]
8/8	8
8/2	2.46
16/ 16 ( $Z_2 = 145$ mm)	15.54
16/ 4 ( $Z_2 = 145$ mm)	5.49
16/ 16 ( $Z_2 = 100$ mm)	15.63

### 3D constructive model and validation

At this point we can consider the EM procedure as completed. Nevertheless, it is mandatory to be able to export the complete set of parameters into a constructive model and validate the models obtained. Based on the experience gained during this whole process, this last step has been improved by means of the auto link tool with Solidworks provided by COMSOL. Thus, a Solidworks parametrized model has been developed from the initial set up extracted from COMSOL that allows us to directly perform slightly modifications on the final model as well (Figure 4.10). This procedure allows also to perform curved corners and chamfers to avoid sparking and therefore to be able to perform electromagnetic simulations easily. In addition, vacuum tubes are also included in the final model. Regarding these elements, our simulations have shown that these do not to induce a worse overall electromagnetic response. Final simulations show very good agreement between the results obtained from pure COMSOL models and SolidWorks/COMSOL models with rounded shapes in terms of frequency response. As it can be inferred from Figures 4.6 and 4.11 the quadrupole mode shift from between both models for the final design is equal to 0.3 MHz (351.4 MHz–351.7 MHz). Regarding the dipole modes, again the frequency shift is in good agreement (345.1 MHz COMSOL - 351.4 MHz SolidWorks). In addition, field flatness values obtained (0.98) seem to be very promising although they still need to be validated.

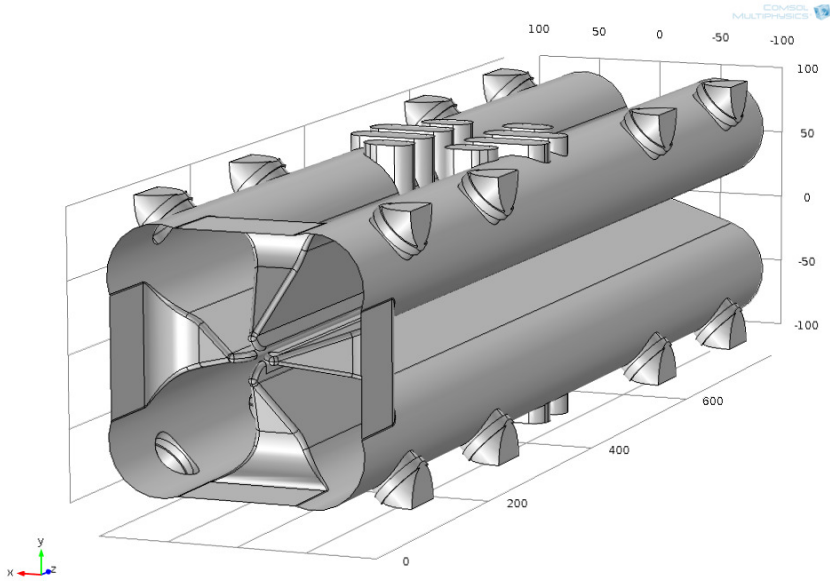


Figure 4.10: Final constructive SolidWorks Model.

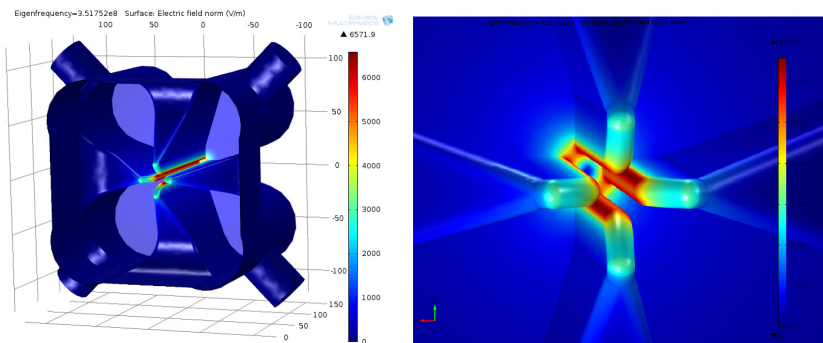


Figure 4.11: SolidWorks model Electromagnetic analysis.

# Chapter 5

## RF Design

In this chapter, several issues regarding the RF power system for the ESS-Bilbao RFQ will be covered. Specifically, some details will be presented about the high power RF transmitter, RF power coupler and RF seals. Finally low power RF characterisation of the RFQ cold model will be presented.

### 5.1 RF Power Coupler Design

Injection of RF power into the RFQ cavity is achieved by means of adequate RF input couplers. Such devices basically consist in a externally cooled coupling loop help by an adequate structure onto which the RF power generated by the transmitter is transported, usually by means of a coaxial guide, up to a window that serves to keep a decent vacuum level inside the RFQ.

Our first contact with a RF coupler of the kind here considered was enabled by the agreement reached between our institution and the group in charge of development of the new accelerator ISIS Front End Test Stand (FETS) geared towards the construction of a new injector for the ISIS Spallation Neutron Source located at Oxon, U.K. Within such an agreement we took responsibility for developing a coupler which could be used at

both installations. This brought forward a number of design constraints such as:

1. The coupler must be able to work in a wide frequency band, from 300 to 400 MHz, in order to fit with both ESS-Bilbao (352.2 MHz) and ISIS (324 MHz) operation frequencies.
2. The input coupler interface (this is the power coming from the Klystron) is a standard 4 1/16" flanged Rigid Coaxial.
3. The output coupler interface (vacuum flange inserted into the RFQ cavity) is a standard ConFlat (CF) 2 3/4" (DN 40) flange.

### 5.1.1 Electromagnetic Design

#### Starting Point: ISIS Coupler Models

The starting point for our study is the RF coupler models provided by ISIS and fully tested at the installation. To perform the electromagnetic design of the couplers, the coupling loop located at the output of the coupler has been removed and the Scattering (S) parameters of a variety of structures have been computed. All the couplers under study will be designed and analysed by Full-Wave electromagnetic simulators. Specifically, CST Microwave Studio (MWS), HFSS from Ansoft and COMSOL have been used. Both HFSS and COMSOL are frequency domain solvers which use the Finite Element Method (FEM) to solve Maxwell Equations. On the other hand, CST MWS can solve the problem either by a Frequency Domain Solver (FEM) or a Time Domain Solver (Finite Difference Time Domain Method or FDTD method).

#### ISIS Coupler at 200 MHz

The first ISIS coupler analysed is shown in figure 5.1-a. This coupler is currently in use on the ISIS accelerator. It operates at 200 MHz. As it can be seen in the figure, it is based on a coaxial geometry. Moreover, the ceramic window (structure with grey colour in the figure) separates the cavity vacuum from air.

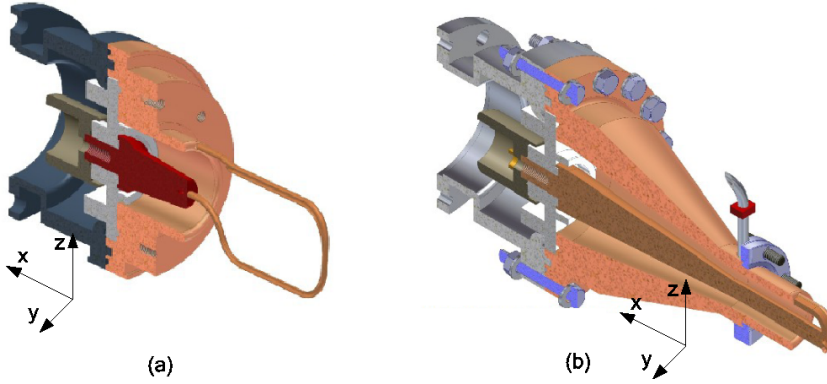


Figure 5.1: A view of the RF coupler as developed and tested at ISIS for operation at 200 MHz **(a)** and that originally developed at the Spallation Neutron Source at Oak Ridge Natl.Lab. **(b)**, later adapted at ISIS to work at a frequency of 324 MHz.

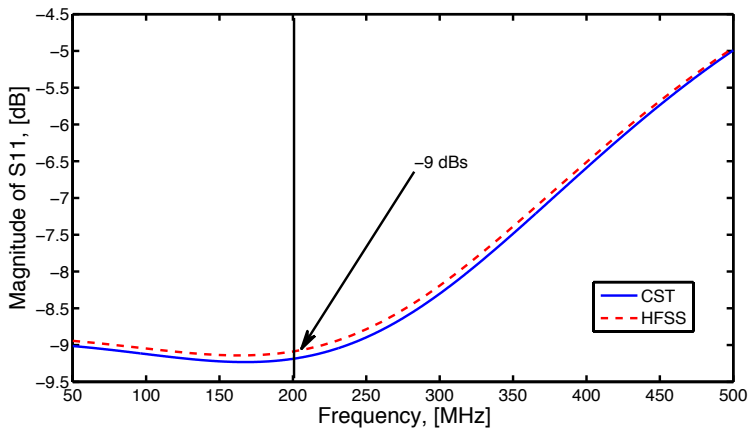


Figure 5.2:  $S_{11}$  obtained by HFSS and CST of the ISIS coupler shown in Figure 5.1-a.

**Simulation set up.** In order to analyse the coupler, 3D electromagnetic simulations have been carried out with both CST Microwave Studio and HFSS (Ansoft) commercial simulators.

1. Conductors were defined as Perfect Electric Conductors (PEC) and void space as vacuum. The most commonly used [17, 18] material is Alumina in different purity concentrations (typically from 99.99% to 95%) with a relative dielectric permittivity  $\epsilon_r$  varying from 9 to 9.9. Note that the higher the value of  $\epsilon_r$ , the greater the difference between the vacuum and the window impedances. This will imply that, in general, the performance of the coupler will get worse. Therefore, in order to consider the worst case scenario, an  $\epsilon_r = 9.9$  has been chosen for the simulations.
2. In addition, in order to run the simulations faster, some symmetries can be defined in the structure. Specifically, for the TEM propagating mode in the structure two Perfect Magnetic Walls (PMW) are defined lying on the XY and XZ planes (see Figure 5.1). In this way, the number of mesh cells needed to successfully simulate the structure is drastically reduced since only the 25% of the total structure is being simulated. Finally, two input and output 50  $\Omega$  ports are defined at the ends of the coupler.
3. Once the structure to simulate is completely defined, the frequency domain solver has been activated for both simulators. The structure is then meshed using tetrahedrons. The iterative solver finds the optimum number of cells (tetrahedrons) according to the desired accuracy. In our case, a maximum  $\Delta S = 0.0001$  is applied for both simulators.

**Results.** After performing the simulations, Figure 5.2 shows the  $S_{11}$  parameter (RF or return losses) obtained. On such grounds, two main conclusions must be pointed out:

1. The results obtained by both commercial simulators show good agreement.

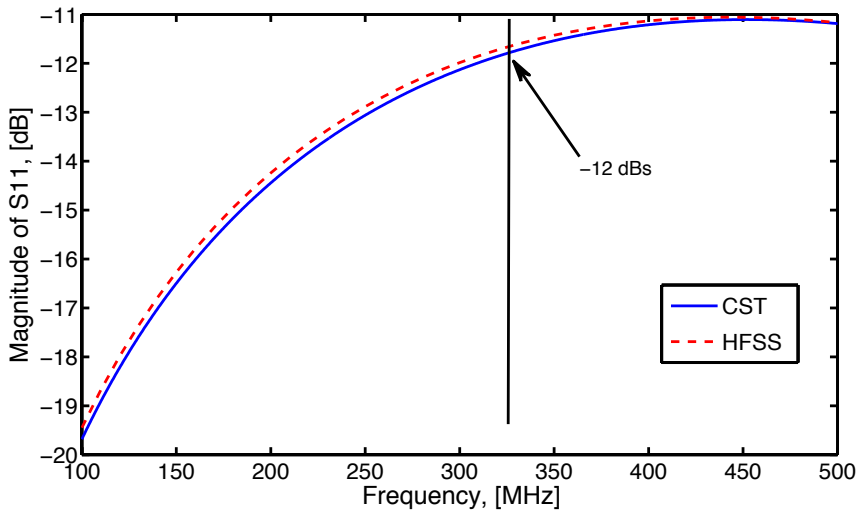


Figure 5.3:  $S_{11}$  obtained by HFSS and CST of the ISIS Coupler shown in Figure 5.1-b.

2. A poor matching ( $S_{11} \approx -9$  dBs) at the frequency of interest is observed. This result implies that more than a 10% of the input power is being reflected back to the circulator. Taking into account the considerable amount of power injected to these couplers, the goal is usually set to  $S_{11} \leq -30$  dB, which means that only the 0.1% of the power should be reflected.

### The SNS coupler as adapted to work at 324 MHz at ISIS

The second coupler which we refer to as *hybrid coupler* is shown in Figure 5.1-b and has also been provided by ISIS. This coupler, currently being designed and tested at ISIS facilities, is an adaptation of the coupler topology designed by the OAK Ridge National Laboratory (ORNL) for its Spallation Neutron Source (SNS) [19, 20]. It must operate at 324 MHz. The left-hand side of the structure has been copied from the 200 MHz coupler, while the output side has been adapted in order to fit in the new RFQ coupler port also being designed at ISIS. Therefore, as shown in Fig-

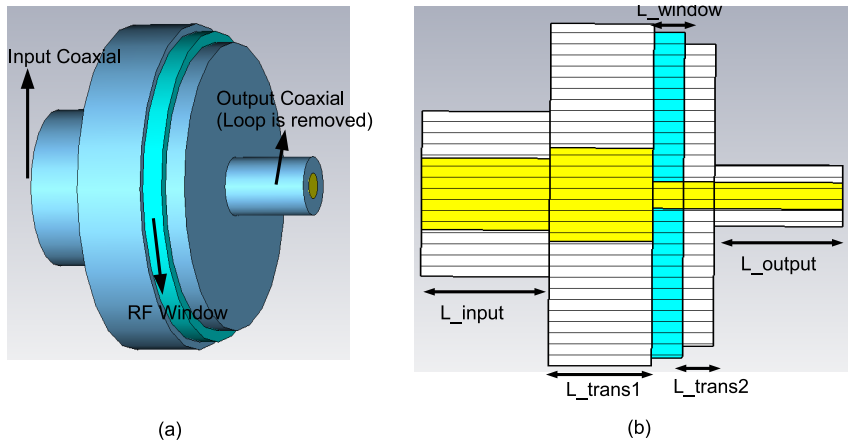


Figure 5.4: Drum-like coupler designed at ESS-Bilbao. (a) Full view; (b) Cut view with parameters.

ure 5.1-b, the ceramic window is exactly the same as the one designed for the 200 MHz coupler.

**Simulation set up.** To carry out a meaningful comparison, exactly the same steps followed for the 200 MHz coupler have been adopted for this hybrid coupler. This also includes the different material considerations.

**Results.** After performing the simulations, Figure 5.3 shows the  $S_{11}$  parameter (return losses) obtained. Under the light of these results, two main conclusions must be pointed out:

1. The results obtained by both commercial simulators show good agreement.
2. A poor matching ( $S_{11} \approx -12$  dB) at the frequency of interest is observed. This result implies that almost a 10% of the input power is being reflected back to the circulator.

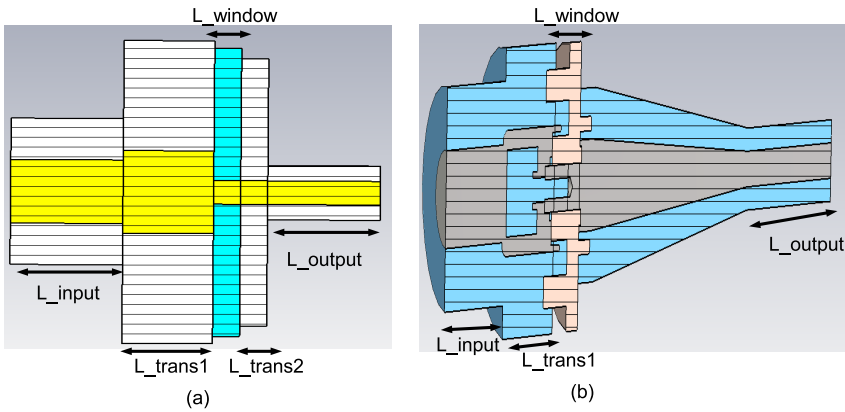


Figure 5.5: Cut views of the (a) Drum-like coupler designed at ESS-Bilbao and (b) Hybrid coupler of ISIS.

### 5.1.2 The Drum-like Coupler

#### Motivation

The rather poor results obtained for the initial ISIS designs lead us to deepen into two main questions, trying to understand,

1. Why is the matching obtained so poor?
2. Is it alumina the material used in the ISIS couplers? At the time of our study, ISIS could not provided us with the exact windows material used for their couplers.

It is clear that both questions are linked since the matching obtained drastically depends on the electrical properties of the chosen material. Generally speaking, by reducing the  $\epsilon_r$  of the material, the matching improves.

In summary, we seek to develop a robust topology for the RF coupler from an EM standpoint. In doing so we will search for a window material that exhibits adequate mechanical and thermal properties.

## Design

The designed coupler is shown in Figure 5.4-a. Besides the input, output, and coaxial window, two new transitions have been added. Each transition is located at one side of the ceramic window. Thus, once the length and the material for the window is chosen, by changing the dimensions of the transitions (both length and radius) and the window (radius), the required matching can be obtained. To this end, as depicted in Figure 5.4-b, some parameters have been defined in the model such as the length ( $L_{\text{Trans1}}$  and  $L_{\text{Trans2}}$ ) and both the internal and external radius ( $R_{\text{Trans1}}^{\text{ext}}$ ,  $R_{\text{Trans1}}^{\text{int}}$ ,  $R_{\text{Trans2}}^{\text{ext}}$  and  $R_{\text{Trans2}}^{\text{int}}$ ) of the transitions and the radius of the window ( $R_{\text{Window}}$ ).

## Drum-Like Versus Hybrid Coupler

In order to compare the topologies of both ESS-Bilbao and Hybrid couplers, Figure 5.5 is presented. The following aspects can be pointed out:

1. The input and output coaxial dimensions are the same for both couplers.
2. As a first approach, the ceramic window of the ESS-Bilbao coupler has been simplified with respect to the ISIS one. To this end the window topology has been fixed as a simple cylinder with similar dimensions than the ISIS one. Specifically a value of  $L_{\text{Window}} = 6$  mm has been chosen. However, this value can be changed at any time if needed since it is actually one more parameter in the model. Actually, the proposed model has been successfully tested up to  $L_{\text{Window}} = 35$  mm.
3. For the ESS-Bilbao coupler two parametrized transitions have been clearly defined. As stated before, this will allow us to properly match the coupler. In the ISIS coupler, however, only one transition stage is defined.

## Ceramic Window Materials

As mentioned above, the choice of material for the ceramic window represents a very important issue and, therefore we have paid due attention to it.

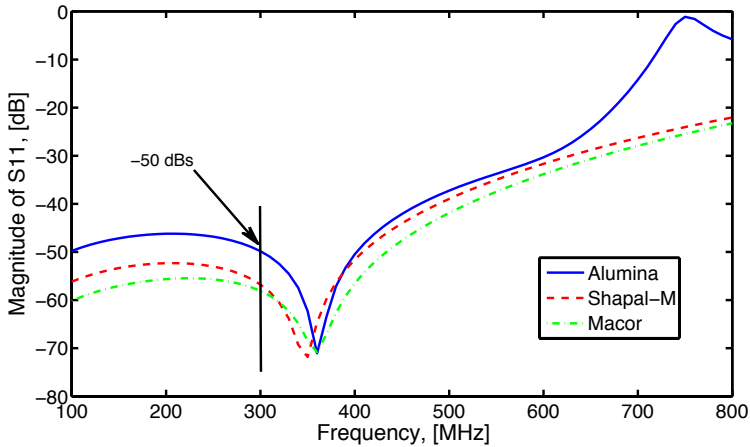


Figure 5.6:  $S_{11}$  obtained by HFSS of the Drum-like Coupler shown in Figure 5.4.

From the outset we have taken into consideration three different kinds of materials:

**Alumina:** this is the material most commonly used in the bibliography. Its dielectric constant  $\epsilon_r$  varies from 9 to 9.9 depending on the purity. In this work, HA-95 Alumina with  $\epsilon_r = 9.2$  and a dielectric loss tangent  $\tan \delta = 3 \times 10^{-4}$  has been chosen.

**Shapal-M:** this is a machinable grade of Aluminium Nitride. According to the documentation, Shapal-M can be machined into complex shapes with high precision. The thermal conductivity is five times larger than that of alumina while the mechanical strength is comparable. The dielectric constant is  $\epsilon_r = 7.1$  and the dielectric strength of 40 KV/mm (AC, 1 mm thickness) The main applications of this material are related to vacuum parts.

**Macor:** Macor MGC (machinable glass ceramic) is a white, odourless, porcelain-like material composed of 55% fluorophlogopite mica and 45% borosilicate glass. According to the data sheet, this material is the choice when you need the performance of a technical

ceramic: high use temperature, electrical resistivity, zero porosity. Besides, it will lower costs and substantially reduce the time between design and actual use. The main electrical properties are  $\epsilon_r = 5.8$  (at around 352 MHz),  $\tan \delta = 0.006$  and a dielectric strength at 25 °C of 9.4 KV/mm (AC, 12 mm thickness). There is a wide variety of applications for this material including constant vacuum techniques.

## Results

Taking into account all the information detailed above, a fair number of simulations using HFSS have been performed. For each one of the window materials described in the previous section, an optimisation of the parameters of the model has been carried out. In all the simulations, the dimensions of both the input and output coaxial as well as the length of the window ( $L_{\text{window}} = 6$  mm) have been fixed. Moreover, copper is assumed for the internal conductors of the model. The optimisation goal has been set to obtain  $S_{11} < -50$  dBs (much better than the usually considered 30 dB) in a wide frequency band (300–400 MHz).

The results obtained are shown in Figure 5.6. As it can be seen, an outstanding performance of the coupler from a matching point of view is obtained.

### 5.1.3 The Nose-Cone Coupler

#### Motivation

Although the Drum-like coupler exhibits an outstanding performance from a matching point of view, its behaviour in terms of multipacting can be a crucial issue. Since these side effects sometimes occur when sharp transitions exist in the structures under analysis, it could be mandatory to avoid such transitions from the model.

Keeping this in mind, in recent times, an alternative topology for the coupler has been investigated in order to avoid such sharp transitions but keeping the outstanding electrical behaviour of its predecessor. This topology has been developed in collaboration with an external company [21]. The topology of this coupler is inspired on the SNS coupler [19, 20].

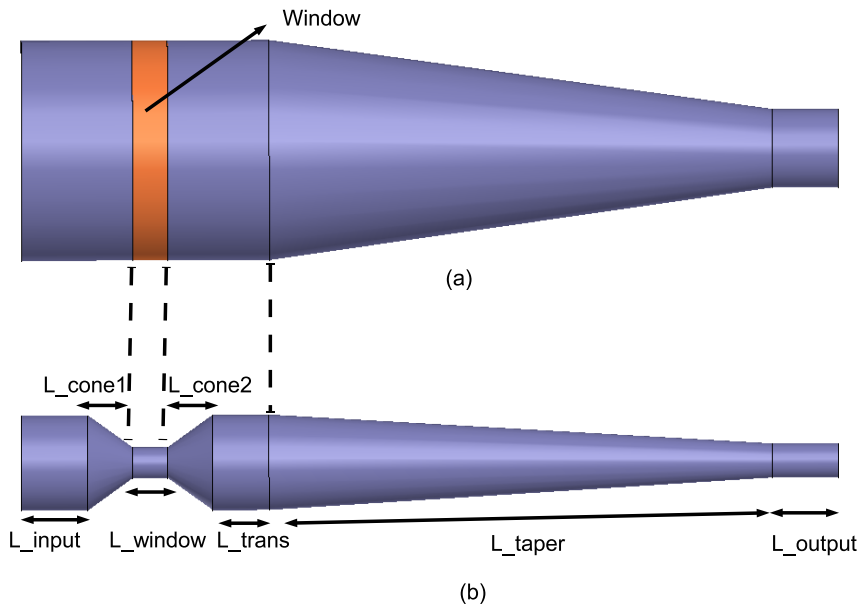


Figure 5.7: Nose-cone coupler designed at ESS-Bilbao. (a) Outer conductor and window view; (b) Inner conductor.

## Design

The designed coupler is shown in Figure 5.7. Compared to the drum-like coupler, the sharp transitions in the outer conductors have been removed. The matching is now achieved by smoothly changing the dimensions of the inner conductors. As it can be seen, two conical sections ( $L_{\text{cone1}}$  and  $L_{\text{cone2}}$ ), a transition ( $L_{\text{trans}}$ ) and a taper ( $L_{\text{taper}}$ ) have been defined. By properly changing the dimensions of the previous parameters, the required matching can be obtained.

The following aspects can be pointed out:

1. The input and output coaxial dimensions, chosen to guarantee a characteristic impedance of  $Z_0 = 50 \Omega$ , are the same that for the drum-like coupler imposed by the input and output interfaces described in the introduction section of this report.
2. The window topology has been kept as a simple cylinder of length  $L_{\text{window}} = 6 \text{ mm}$ . However, as in the drum-like coupler, this value can be changed at any time if needed since it is actually one more parameter in the model. The proposed model has been successfully tested up to  $L_{\text{window}} = 35 \text{ mm}$ .
3. For the nose-cone coupler, several parameterised transitions have been defined. As stated before, this will allow us to properly match the coupler

## Ceramic Window Materials

The choice of material for the ceramic window is a key issue. Specifically, HA-95 Alumina ( $\epsilon_r = 9.2$ ,  $\tan \delta = 3 \times 10^{-4}$ ) has been chosen for the simulations since it is the most restrictive material from an electrical view point.

## Results

Taking into account all the information detailed above, an optimisation of the proposed coupler has been performed by using HFSS. The results obtained are shown in Figure 5.8. As it can be seen, an outstanding

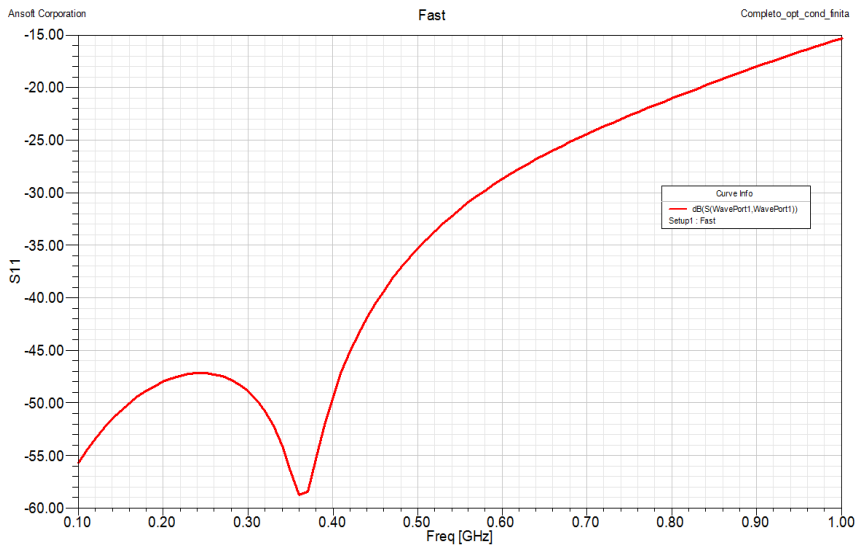


Figure 5.8: S11 obtained for the coupler shown in Figure 5.7

performance of the coupler from a matching point of view is once more obtained.

### Mechanical Design of the Nose Cone Coupler

In this section, the mechanical design of the Nose Cone Coupler is carefully addressed. Special attention is paid to the flanges, the input and output interfaces, the ceramic window structure, the vacuum and control ports, and the loop design.

### From the Electromagnetic to the Mechanical Model

Figure 5.9 shows the electromagnetic model of the designed nose cone coupler. From this model, the mechanical design of the coupler developed in CATIA is presented in Figure 5.10. In the following, we will analyse each of the parts of the coupler independently.

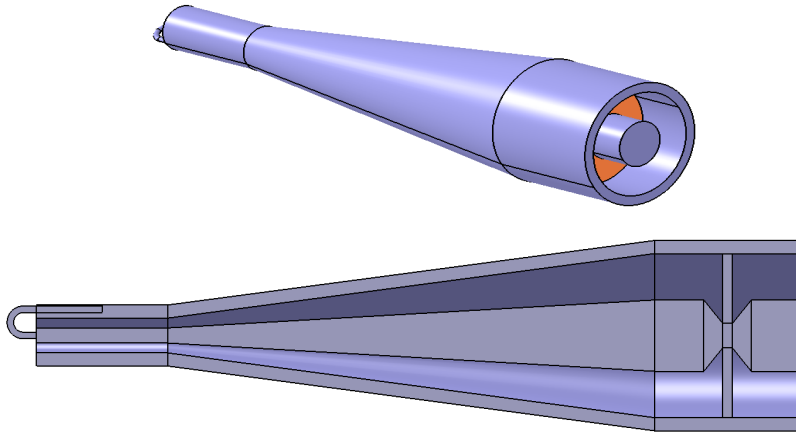


Figure 5.9: Electromagnetic model of the Nose Cone Coupler.

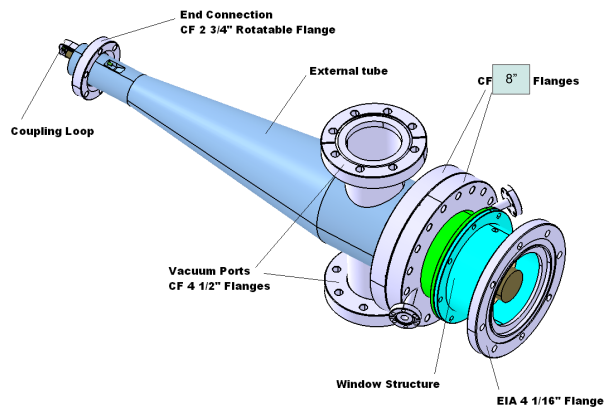


Figure 5.10: Mechanical Design of the Nose Cone Coupler developed in CATIA.

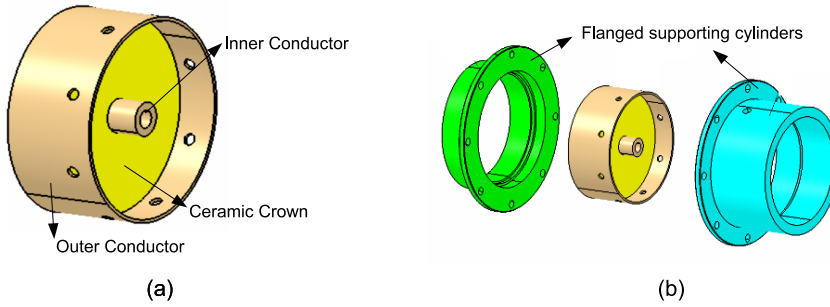


Figure 5.11: Mechanical design of the window for the nose cone coupler of figure 5.10. (a) Ceramic window; (b) Assembly of the ceramic window with flanged supporting cylinders.

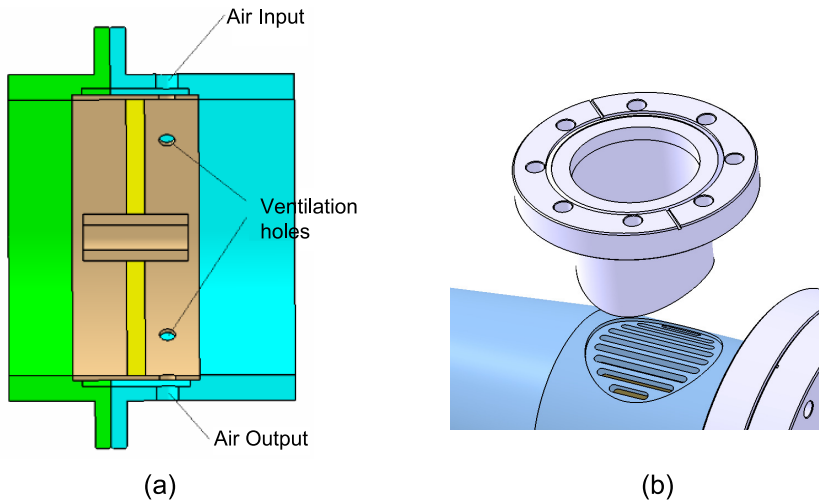


Figure 5.12: (a) Assembly of the window including the cooling chamber. (b) Detail of the vacuum port.

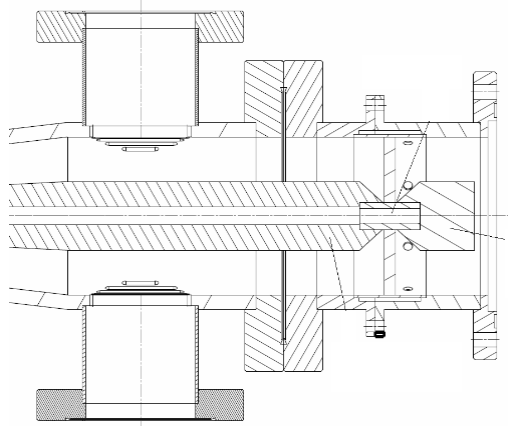


Figure 5.13: Drawing of the ceramic window and vacuum port area for the nose cone coupler.

### Flanges and Input and Output Interfaces

All connecting flanges are standard ConFlat (CF) vacuum flanges, except the input flange which is a standard EIA 4 1/16". The output flange of the coupler can rotate so the loop of the coupler can be properly orientated. The used flanges are the following:

1. Input Port: EIA 4 1/16".
2. Control Flanges: CF 1 1/3".
3. Connecting flanges between the window and the output tube: CF 8" (DN 150).
4. Vacuum Ports: CF 4 1/2".
5. Output Port: Swivel CF 2 3/4" (DN 40).

### Ceramic Window Structure

As shown in Figure 5.11-a, the ceramic window that isolates the vacuum zone is composed of a ceramic crown itself, a metal cylinder which passes through the ceramic and an outer metal ring that supports the assembly. The ceramic crown is 6 mm long and is made of commercial HA-95 alumina whose electrical properties were already defined during the electromagnetic design of the couplers.

The window supporting structure is designed so that the outer metal ring is clamped between two supporting cylinders screwed to each other, as shown in Figure 5.11-b. Thus braze welding can be applied to the whole structure, forming a chamber around the window that we use for cooling. To this end, different holes have been drilled on both the input supporting cylinder and the outer metal ring of the window to cool the air side of the ceramic window. A view of the window assembly including the ventilation holes is shown in Figure 5.12-a. The inner radius of the whole structure remains constant. The ends of the support cylinders are fitted into the corresponding flanges.

A detailed drawing of the ceramic window area of the coupler can be observed in Figure 5.13.

### Vacuum Ports

As depicted in Figure 5.10, two vacuum ports at 180 °C have been included in the mechanical model of the coupler. The ports are formed by a tube of diameter 63.7 mm and thickness 1.7 mm, welded to both a CF 4 1/2" flange and the outer surface of the coupler, as shown in Figure 5.12-b. Moreover, in order to weld both the tube and the longitudinal slots of the vacuum grille, the outer surface of the coupler has been lowered as shown in figure 5.13.

### Control Ports

In order to be able to control unwanted phenomena occurring in the coupler such as, for example, multipacting or arcing, two control ports at 180 °C (Figure 5.10). Each of them consists of a 10 mm diameter and 1 mm thick tube, and a CF 1 1/3" vacuum flange. The joint of the control port with the

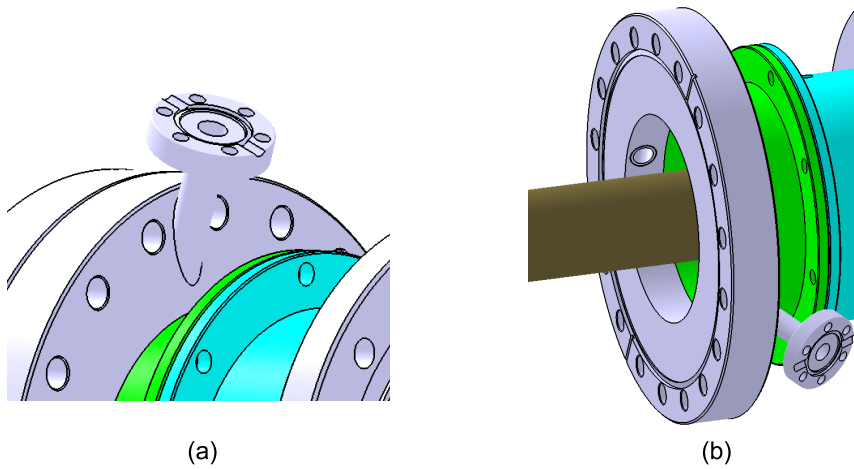


Figure 5.14: Control ports. (a) Outer view; (b) Inner view.

coupler is made through one of the CF 8" connecting flanges. Specifically, the tubes pass through the flange at an angle of  $65^\circ$ , as shown in Figure 5.14. This would not increase the length of the coupler and it would allow the instruments to have a greater sensitivity than if they penetrate at right angles.

### Loop Design

From the electromagnetic model of the loop (Figure 5.15-a), the loop shown in figure 5.15-b has been designed, trying to keep as long as possible the original geometry. To this end, the inner conductor has been extended and the loop is obtained with a single bend of  $90^\circ$ . The loop is attached to the central conductor by a M3 screw, and to the outer tube by the mechanism shown in Figure 5.16-a. Moreover, a cooling system has been considered for the loop, as depicted in figure 5.16-a. The cooling pipe is made of cooper of diameter  $1/8''$ .

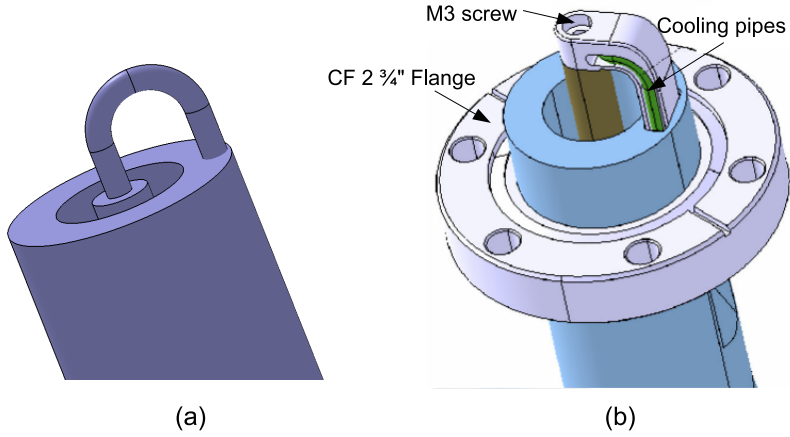


Figure 5.15: Coupler loop. (a) Electromagnetic model; (b) Mechanical model including the cooling pipes.

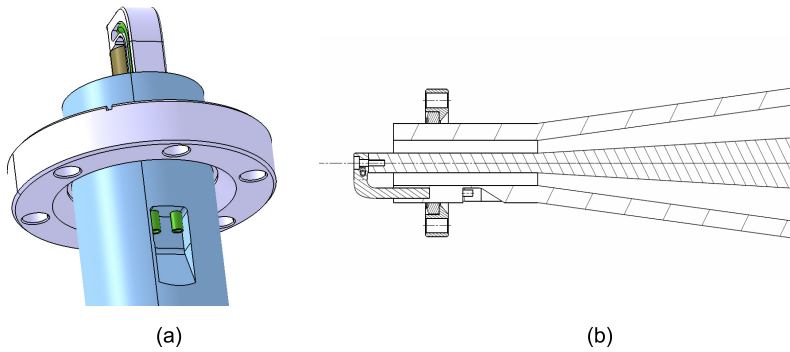


Figure 5.16: Coupler loop. (a) Input and output of the cooling pipes; (b) Drawing of the central section of the loop.

## 5.2 RF Transmitter

The high power RF transmitter is responsible for generating and injecting the RF power into the RFQ. The high power RF transmitter is subjected to space limitations and stringent amplitude and phase requirements.

One dedicated klystron will feed the RFQ, via a Y-junction circulator and a waveguide and coaxial distribution network.

The RFQ transmitter is based on a klystron (a high power vacuum electron tube) featuring a maximum RF peak power up to 2.8 MW, operating at a centre frequency of 352.2 MHz. The klystron will be operated in pulsed mode, fed by a pulsed high voltage modulator (which generate 110 kV, 60 A pulses).

A three-port circulator is used to prevent damage to the klystron arising from reflections at the RFQ ports. A high power water load is connected to the third port of the circulator to absorb the reflected power.

RF power is carried through rectangular waveguides. Waveguide size is EIA standard WR2300, non-pressurised. Both full-height (2:1 aspect ratio) and half-height (4:1 aspect ratio) waveguides will be used, with internal dimensions of  $584.2 \times 292.1$  mm and  $584.2 \times 146.05$  mm, respectively. A waveguide taper transition for converting full- to half-height and several straight (fixed and semi-flexible) sections, as well as H- and E-plane mitered bends, are needed to transport the RF power into the vicinity of the RFQ.

Last line section, interfacing with RFQ power coupler input port (EIA 4-1/16 inch standard), is a coaxial transmission line. A step transition to an EIA 6-1/8 inch coaxial section is also needed, featuring lower attenuation and higher power handling. Length of the coaxial lines must be as short as possible to reduce losses.

Dual directional couplers are used to check both forward and reflected power (i.e., power injected to the RFQ and power returned to circulator/klystron).

Considering the total required RF power to be injected to the RFQ (about 800 to 1000 kW peak estimated) and the coupler's maximum power handling (400 to 450 kW expected), the RF transmitter is to be designed to employ two couplers, with option to be extended to four couplers.

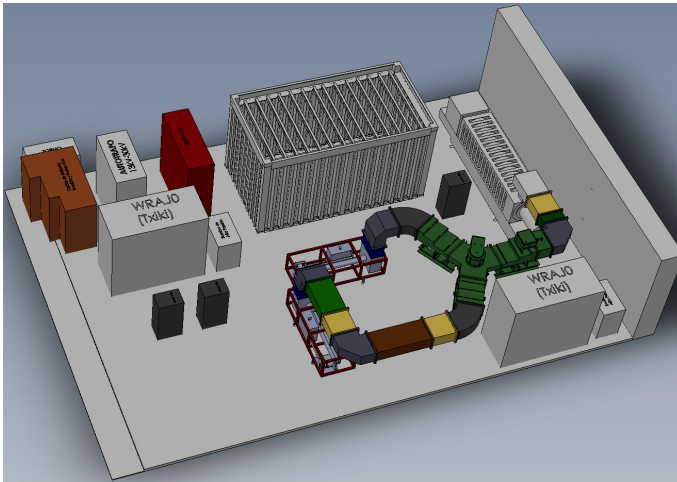


Figure 5.17: RF test stand 3D model.

A custom made half-height waveguide magic-tee power divider splits RF power from the klystron. Power divider output ports include transitions to EIA 6-1/8 inch coaxial lines. In case that 4 couplers are finally needed, two additional coaxial power dividers can be used.

Injection of the RF power into the RFQ shall be located on the third (centre) section of the RFQ. Two opposite RF ports are used to excite the quadrupole mode (diagonally). If an additional pair of couplers are to be included, they shall be located preferably at a different longitudinal position, symmetrically placed around the centre.

Stringent amplitude and phase matching between RF couplings must be accomplished. This imposes tight mechanical tolerances to the waveguide and coaxial lines and components.

In Figure 5.17, a 3D model of the RF test stand is shown. The RF test stand is quite similar to the RF transmitter line for the RFQ, as it includes the same key components.

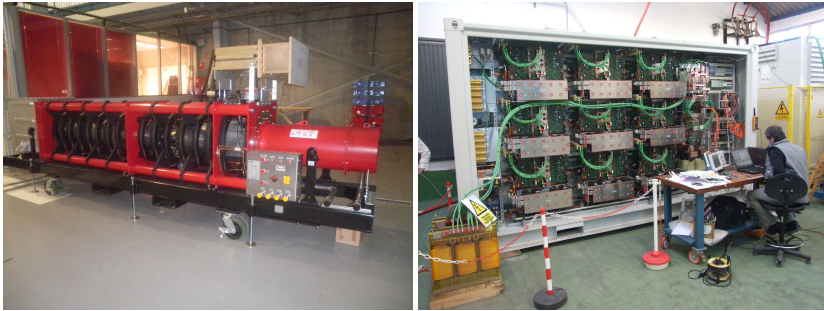


Figure 5.18: **Left:** VKP-8352A klystron. **Right:** HV modulator.

### 5.2.1 Klystron

VKP-8352A power klystron has been developed by Communication and Power Industries (CPI), under ESS-Bilbao specifications, mostly compatible with CERN's LINAC4 requirements. Figure 5.18 (left) shows a picture of the VKP-8352A klystron.

The main specifications of the klystron are:

- Power Supply: 110 kV, 50 A (pulsed)
- Frequency: 352.2 MHz
- Peak Power: 2.8 MW
- Pulse Duration: up to 1.8 ms
- Pulse Repetition Frequency (PRF): up to 50 Hz
- Duty Cycle: up to 9 %
- Average Power: up to 126 kW
- Cooling: liquid (deionized water)

### 5.2.2 Modulator

A high voltage pulsed modulator for the VKP-8352A klystron is under development by JEMA (Lasarte-Oria, Guipuzcoa), according to ESS-Bilbao specifications. Figure 5.18 (right) shows a 3D model of the HV modulator.

The main specifications of the modulator are:

- Output Voltage: up to 120 kV (pulsed)
- Output current: up to 60 A
- Pulse Width: up to 1.81 ms (adjustable)
- Pulse Repetition Frequency (PRF): between 2 and 50 Hz
- Peak Power: up to 7.2 MW
- Average Power: up to 648 kW
- Duty Cycle: up to 9 %
- Input Voltage: 30 kV (50Hz)
- Input Transformer: dry technology
- Efficiency: > 90 %
- Cooling: liquid cooling (demineralized water)

### 5.2.3 Circulator and Water Load

**High Power circulator:** A circulator is a 3-port component which transfers incident RF power from the klystron towards the cavity; while eventual reflected power is sent to a dummy load.

In order to ensure a good performance of the circulators at high power levels (where ferrite permanent magnets could saturate), usually a compensation of the magnetic field is needed. This task can be done by modifying the current flowing through some suitable electromagnets added to the circulators. Different strategies can



Figure 5.19: **Left:** Circulator. **Right:** Water Load

be developed to optimise circulator behaviour, namely by a look-up table stored during calibration and factory tests (as AFT GmbH does), or by sampling forward and reflected powers and minimising power which returns back to the input port (as Ferrite Microwave Technology does).

At ESS-Bilbao, there are available high power circulators from both manufacturers. Suitability of all these circulators will be checked in the high power RF test stand.

**Water Load:** High power RF loads are needed to dissipate the RF power eventually reflected. For very high power levels, usually water cooled loads are employed. After a waveguide-to-coaxial adapter, a certain length of liquid-filled coaxial line is attached. This liquid is a cooling fluid comprised of a 50/50 mix of de-ionised water and Ethylene Glycol, which is pumped in a closed loop system to remove the heat while maintaining a proper RF behaviour.

Figure 5.19 depicts the three-port circulator and the RF water load.

#### 5.2.4 Low Level RF System

A pulsed LLRF system has already been designed, implemented and validated with extensive measurements fulfilling the RAL FETS RFQ specifications (Table 5.1), as well as ESS-Bilbao requirements. The ESS-Bilbao LLRF

Table 5.1: Specifications of the ISIS RFQ system

Nominal frequency	324 MHz
No. of LLRF systems	1
Amplitude stability	1 %
Phase stability	1°
Tuning range	1 MHz
Unloaded Q	9000
RF power (peak)	1000 kW
Synchronous phase	0°
RF pulse width (min)	250 $\mu$ s
RF pulse width (max)	2 ms
Pulse repetition rate	50 Hz

system is based on two parts. The first part is the hardware and FPGA program which regulates the I and Q components of the measured cavity voltage, hence the amplitude and phase of the cavity field and the second part performs cavity frequency tuning to eliminate the reflected power.

The design is based on a fast analog front-end for RF-baseband conversion and a model-based Virtex-4 FPGA unit for signal processing and PI regulation. Complexity of the LLRF timing is significantly reduced in the current design and the LLRF requirements are fulfilled by utilising the RF-baseband conversion method compared to the RF-IF approach. A GUI has also been implemented in MATLAB-Simulink so that the user can set the control parameters and monitor the read-back values while the LLRF system is being tested.

### Amplitude and phase loop

The measured RFQ field are converted to baseband. The I and Q signals are then sampled and fed into the FPGA board for all the processing which is needed to be done on the baseband signals, for example: rotation of the IQ vector (compensation of loop delays), addition of fixed DC values to the I and Q inputs (compensation of DC offsets), PI regulation and addition of feed-forward signals (compensation of predictable errors, also

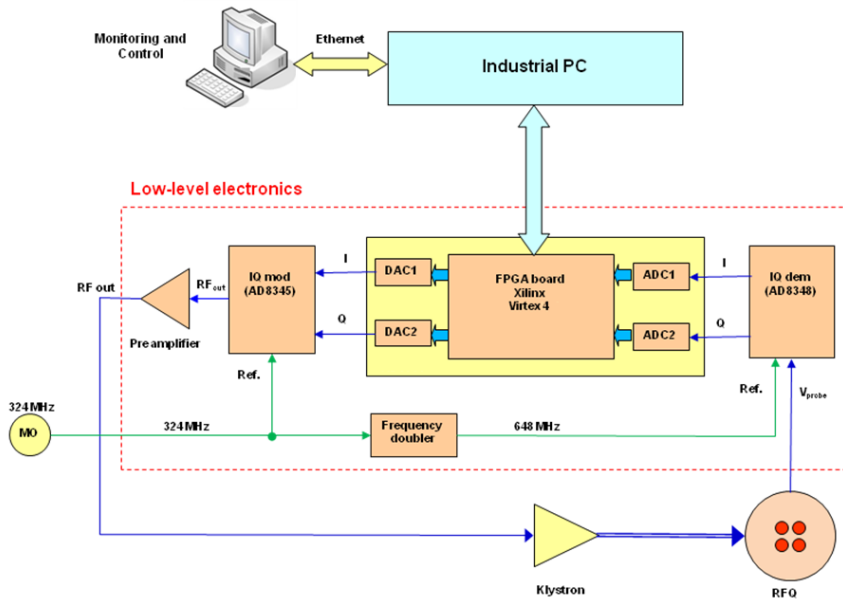


Figure 5.20: Simplified design of the LLRF amplitude and phase loops

for open-loop operation). At the output of the FPGA the I and Q signals are converted to analog by the two DACs and then are fed into the IQ modulator generating the drive for the RF amplifier. The LLRF system can be controlled and monitored by a local computer running under MATLAB-Simulink. This option, however, is mainly intended for test purposes. For the final installation, the LLRF system should be integrated into the global control system of the accelerator facility (EPICS,...).

### Tuning loop

The measured forward and probe voltages are also converted to baseband. These signals are then sampled and fed into the FPGA where CORDIC algorithms are used to calculate the phase difference between the two RF signals (the FPGA and the IQ demodulator for probe voltage measure-

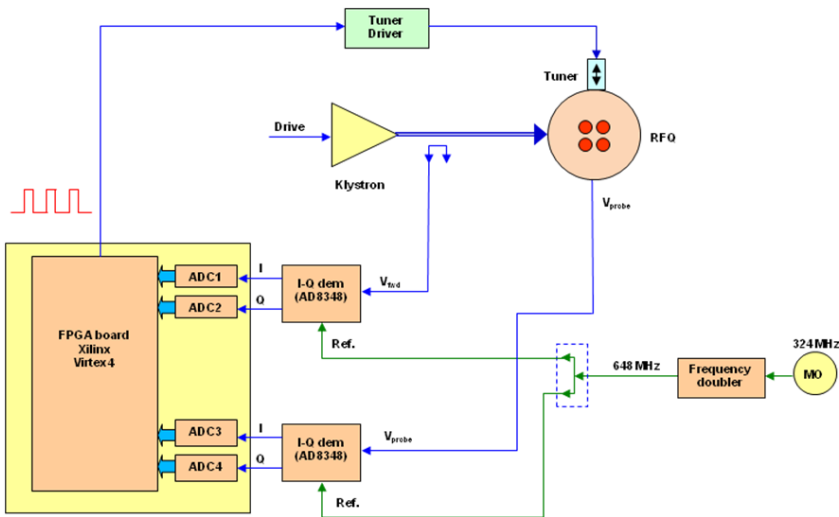


Figure 5.21: Simplified design of the LLRF tuning loop

ment in the tuning loop are physically the same as the ones used for the amplitude and phase loops). RFQ tuning is done by keeping the phase difference as close as possible to its reference where the reference phase is the one giving minimum reflected power from the RFQ in the presence of the beam. This is done by moving the RFQ tuner inward/outward if the phase error (i.e. the difference between the actual phase and the set value) exceeds the upper or the lower thresholds defined.

### Design validation

Firstly, the implemented LLRF was measured using a re-entrant cavity mock-up in the Electricity and Electronics laboratories (Figure 5.22 left) of the University of Basque Country (UPV/EHU). Afterwards the LLRF system was measured and validated with the RAL FETS RFQ cold model in the Imperial College laboratories (Figure 5.22 right). The tests were performed up to 60 W of power.



Figure 5.22: **Left:** LLRF test set-up with a re-entrant cavity mock-up in the UPV/EHU laboratories. **Right:** With the RAL FETS RFQ cold model in Imperial College laboratories.

### 5.3 RF Seals

RF seals must be used along the RFQ, placed between different mechanical parts, in order to improve electrical and RF contact resistance; as well as to avoid radiation and RF leak problems. Berillium-Copper (BeCu) fingerstrips provide a cost-effective and long term performance in terms of electromagnetic shielding effectiveness, without remarkable degradation even in case of repeated opening and closing or sliding of parts. Fingerstrips are available in a variety of shapes, with or without adhesive tape.

In the RFQ, it is mandatory to avoid adhesives and other substances because of vacuum issues. The fingerstrip shape must be selected depending on the joint, taking into account its mechanical spring characteristics to optimise the shielding effectiveness. Then, a careful design of the groove must be carried out.

Specifically, there are three candidate areas which could require RF seals: coupler, probe and tuner ports, transverse joints and longitudinal joints.

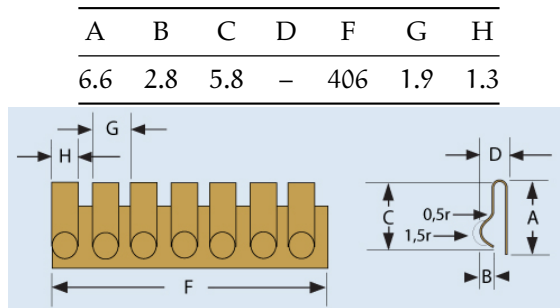


Figure 5.23: Special mounting reverse bend spherical fingerstrip

### 5.3.1 Coupler, pick-up probe and tuner ports

RF ports (coupler and pick-up ports) and the tuner ports (both fixed and mobile) require RF seals. As these joints are circular (with 37.6 mm diameter), a special mounting (see Figure 5.23) reverse bend spherical gasket is needed.

Taking into account the port depth, a  $6.6 \times 2.8$  mm profile (width  $\times$  height) is a suitable choice. Several manufacturers can provide these fingerstrips, such as TBA Electro Conductive Products (P/N: ECP 0694), Holland-Shielding Systems (P/N: 2604-02) or Tech-Etch (P/N: 75RC).

These fingerstrips perform correctly when compressed at least 25 % and up to 50 %. For a 37.5 % nominal compression, groove depth is 1.75 mm, realised on the RFQ port. Groove width is 6.6 mm. Every DN40 port needs less than 30 cm long fingerstrip.

### 5.3.2 Transverse joints

Transverse joints (between RFQ sections) are flat and also require fingerstrip RF seals. Unfortunately, there is no possibility to use the same fingerstrip profile for both flat and circular joints. A snap-on mounting, symmetrical fingerstrip is selected for transverse joints. A narrow profile fingerstrip ( $8.13 \times 2.8$  mm, width  $\times$  height) is a suitable choice, such as TBA Electro Conductive Products ECP 0612, Holland-Shielding Systems 2203-03 or Tech-Etch 187S32.

A	B	C	D	F	G	H
8.1	-	2.8	406	4.8	4.3	

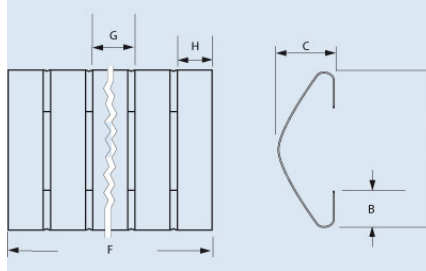


Figure 5.24: Snap-on mounting symmetrical fingerstrip

These fingerstrips perform correctly when compressed at least 25 % and up to 50 %. For a 37.5 % nominal compression, groove depth is 1.75 mm, realized on only one of the interfacing sections. Groove width is fixed to 8.0 mm, thus retaining the fingerstrip in its position during RFQ assembly.

### 5.3.3 Longitudinal joints

Longitudinal joints (between vanes) are also flat. In case of vacuum brazed RFQ vanes, no fingerstrips are needed for these interfaces, but in case of assembly of vanes, the same snap-on mounting fingerstrips can be used on longitudinal and transverse joints.

## 5.4 Cold Model RF Measurements

### 5.4.1 Introduction

The radiofrequency quadrupole cold model (RFQ CM), a mock-up of a segment of the real RFQ has been made of Aluminum, and is currently under test. The model has been built first as a testing ground to control the construction process as much as reasonably achievable and also to develop and test the tuning procedure. All the experimental results will be here

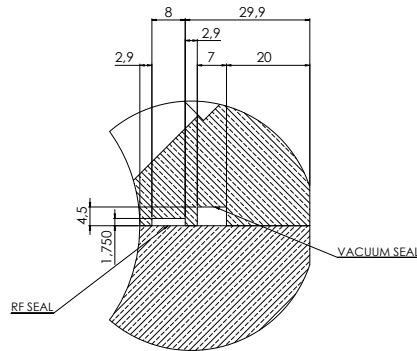


Figure 5.25: Crosssection of the tuner port. Heights are specified in mm.

compared to the simulation results as feedback to analyse and improve the design and manufacturing processes. An Aluminum 1 m cold model which includes a representative modulation of the final structure, has been built as a first step of the construction of the final RFQ (see Figure 5.26). Up to sixteen slug tuners of 34.1 mm diameter symmetrically distributed over the RFQ cold model are used for the field tuning system. Twelve tuners are fixed and left stuck into a chosen position, while four other tuners are movable and are controlled by the LLRF system, to compensate the frequency drifts due to temperature increase during operation. In addition, the cavity also includes eight ports for RF couplers and pick-ups [22]. This section presents the low power experimental tests carried out using such a structure, as well as the ensuing analysis and a final comparison between the simulation and experimental results. This section presents the low power experimental tests carried out using such a structure, as well as the ensuing analysis and a final comparison between the simulation and experimental results.

The measurement set-up consists of a Vector Network Analyser (VNA) to measure the frequency spectrum to identify the different resonant modes, coupling factors, intrinsic quality factor ( $Q_0$ ) and tuning system. The test bench also includes all the instrumentation required for the bead-pull test to characterise the field flatness as well as the effective shunt

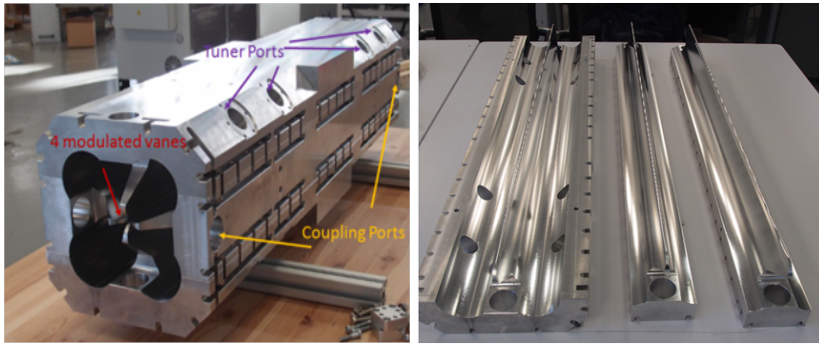


Figure 5.26: **Left:** ESS-Bilbao RFQ cold model **Right:** One major and two minor modulated vanes of the RFQ cold model.

impedance per unit length ( $ZT_2$ ). The bead-pull measurement will determine the correct cavity tuning procedure fulfilling the field flatness specification. The test bench implemented to perform the RFQ CM RF measurements is shown in Figure 5.27 .

On the other hand, the already developed Low Level Radio Frequency (LLRF) system will also be validated with RFQ CM. In order to perform the RF measurements, one coupler or pick-up has been mounted on the RFQ to feed RF power into the cavity, and one pick-up to measure the cavity Scattering (S) parameters in both transmission and reflection modes.

### 5.4.2 Resonant Frequency Modes

The cavity resonant modes are measured with the VNA. The accelerating mode ( $TE_{210}$  quadrupole mode) and the adjacent dipole modes are analysed. The obtained results, with all the aluminium tuners in flush position with the cavity wall, are shown in Table 5.2 and Figure 5.28. Notice the difference in the design frequency with respect to the final operation value of 352.2 MHz which was due to a change in the design just prior to manufacturing. First, the cold model was designed without modulation. Furthermore, with the design closed it was decided including a modulation profile representative of the final structure, which provoked a shift

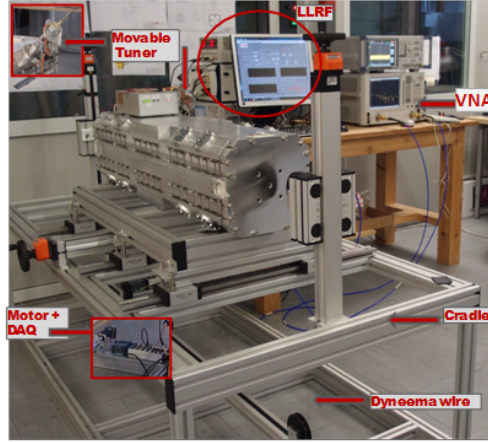


Figure 5.27: Test-bench implemented for the RFQ CM RF measurements in the ESS-Bilbao in Zamudio Facility.

Table 5.2: RFQ Cold Model design specifications and measured values.

RFQ CM Parameter	Simulation	Test
$f_{\text{Quadrupole}} (TE_{210})$	357 MHz	356.5 MHz
$f_{\text{Dipole}} (TM_{110})$	347 MHz	348.9 MHz
Dipolar frequency separation	10 MHz	> 5 MHz

frequency in the quadrupolar mode and in general, in the spectrum modes. Finally, instead of designing again the cold model for the final resonant frequency, the first design including modulation and hence with a different resonant frequency, prevailed with the intention of saving time. Despite the fact of that the cavity resonates at different frequency from the specified, the aim of the mock-up is completely covered.

A minimum frequency spacing between quadrupole and the neighbouring dipole mode is required to ensure the RFQ proper operation. The closest dipolar modes identified are the pair of  $TM_{110}$  modes, which resonate at a lower frequency than the main mode. Instead of a single, de-

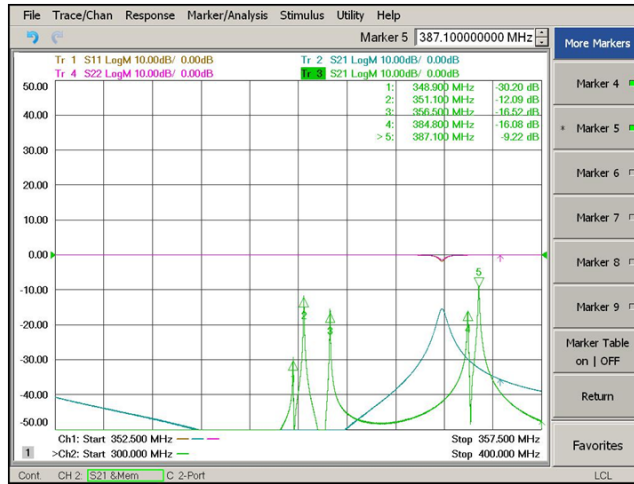


Figure 5.28: RFQ CM resonant frequency modes measured with the VNA.

generate frequency, the measurement shows frequencies at 348.9 MHz and 351.1 MHz, arising from asymmetries brought forward by manufacturing and also by misalignment issues during the cavity assembly. The frequency separation between the quadrupole mode and the nearest neighbouring dipole mode is about 5 MHz. This value is considered separated enough to avoid disruptions in the main mode behaviour. Above the fundamental mode in the spectral frequency, the nearest resonant mode arises very far, specifically at 384.8 MHz.

### 5.4.3 Dipole Stabiliser Rods

Due to the impossibility to perform a 4m long simulation of the RFQ, the possibility of including dipole suppressors must be considered. Since the technique used for EM simulations consists on the *slice by slice* method previously described, it is difficult to foresee the final dipole spectrum. Even when simulations performed from 800 mm building models show enough spanning between quadrupole/dipole modes ( $\approx 8$  MHz). Their spectrum critically depends on the length of the simulated slices. Therefore,

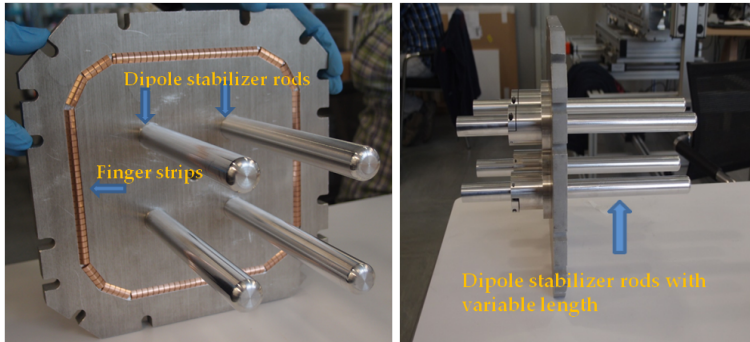


Figure 5.29: Dipole stabilizer rods for the RFQ cold model

their effect in the RFQ cold model is characterised. The rods have been built from Aluminium with a diameter of 20 mm and with a variable protruding length. The rod length is easily tuneable up to a maximum of 220 mm. Rods are assembled in both end wall plates at a distance from the beam axis of  $x = y = 35$  mm. The next pictures show the dipole stabiliser rods implemented in the end wall plates.

Moreover, Figure 5.30 shows the effect of the rods length on the frequency spectrum. We have studied the evolution of the frequency separation between the fundamental and the adjacent dipole modes, below and above the fundamental one, called as Sep\_Dip\_low and Sep\_Dip\_high respectively in the plot.

The experimental tests demonstrate that with a length of 60 mm the effect of dipole suppressor rods is almost negligible. Nevertheless, with a length of 135 mm in the eight rods, the separation between the quadrupole and adjacent dipole mode increases from 5 MHz up 10 MHz. For longer rod lengths, the nearest mode is located above the quadrupole mode frequency. Some discrepancies arise between the simulated and measured dipole mode frequency values. The origin of such disagreements are under study in order to match as much as possible the measurements and the simulation outcomes. Figure 5.31 depicts the effect measured in the spectral frequency of the dipole stabiliser rods for a protruding length of 135 mm.

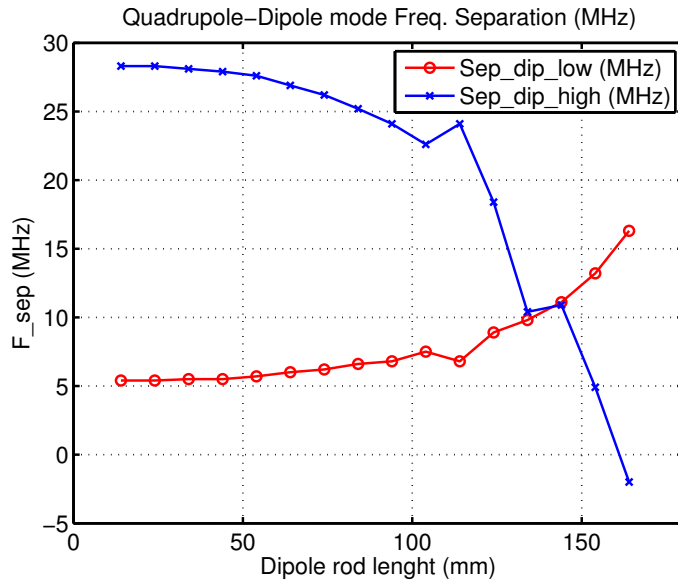


Figure 5.30: Evolution of the frequency spacing between quadrupole and adjacent dipole modes versus the dipole stabiliser rods protruding length.

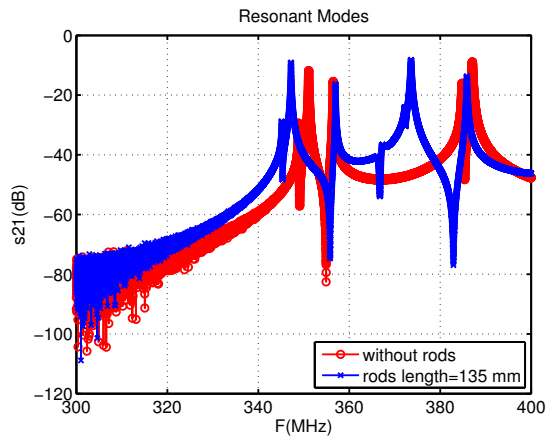


Figure 5.31: Comparison of the spectral frequency of the RFQ CM without dipole stabiliser rods (blue) and with dipole stabiliser rods with a length of 135 mm (red)

#### 5.4.4 Pick-up Coupling Factor

The pick-up is required to perform tests in transmission mode. The design of the pick-up, in this case a weak magnetic loop, has been geared towards a device which behaves weakly enough to provide a negligible perturbation to the cavity performances, but at the same time it is required a minimum coupling value to sample with enough accuracy the field signal. With this requirements the pick-up coupling factor has been established in the range of 0.03–0.08. Figure 5.32 shows the N-type connector pick-up implementation.

#### 5.4.5 Coupling Factor

The RF power is transmitted to the RFQ by means of a loop type magnetic coupler designed with the aim of minimising the reflected power, therefore maximising the RF chain efficiency. The coupling factor specification taking into account the beam loading is established to be within 1.2–1.4 [23]. For this requirement, the effective area needed in the couplers has been analysed considering the effect of different factors in the final configuration such as; coupler position, loop area, loop angle,  $Q_0$  degradation, two couplers setting and pick-ups effect. Figure 5.32 shows the coupler and pick-up implemented in the RFQ CM.

The coupler has been designed with the full-wave 3D electromagnetic design code. A good agreement between simulation and measurement has been obtained. Tests have been performed for a single coupler as well as for two couplers in phase.

#### 5.4.6 Quality Factor

The quality factor is an essential cavity figure of merit since it measures the cavity efficiency. The cavity unloaded quality factor ( $Q_0$ ) depends on the cavity material, surface roughness and the electrical contact between the mechanical parts. The simulated  $Q_0$  of the RFQ cold model result has been obtained from the eigen-mode solver of ANSYS HFSS, a full-wave electromagnetic field simulation tool for 3D structures. There, it has been taken into account the specified manufacturing surface roughness

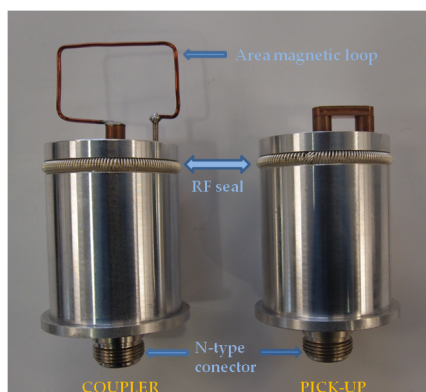


Figure 5.32: Magnetic coupler and pick-up implemented in the RFQ CM measurements. They include N-type connection and RF seal.

$R_a = 1.2 \mu\text{m}$ , which translates into a decrease of the Aluminium effective conductivity to  $2.9 \times 10^7 \text{ S/m}$  from its ideal value of  $3.5 \times 10^7 \text{ S/m}$ . Table 5.3 summarizes the simulation results in both conditions. On the other hand, the  $Q_0$  has been tested with different methods in reflexion and transmission mode using the S parameters data read from the NA [24–30]. The overdetermined method by Kajfez [25] has been identified as the most accurate, as well as with better repeatability (error  $< 0, 1\%$ ), much better than the transmission mode typically used based on the determination on the 3 dB frequency bandwidth. In order to study the effect of the RF seal in the cavity behaviour different types of sealing have been employed. Figure 5.33 shows the RF seal types employed in the RFQ cold model.

Beryllium Copper (BeCu) spring rings have been assembled in all slug tuners, pick-ups, couplers and port caps (see Figure 5.32 and Figure 5.36), while BeCu finger strips have been employed in the end wall plate to improve the electrical contact with the cavity body. Dipole rods also include finger strips. First, the  $Q_0$  was measured without any RF seal. The difference in the  $Q_0$  measured with and without RF seals can be checked from values listed in Table 5.3. It should be noticed that the enhancement due to the RF sealing is not very large, leading to an increase from 4700 to 4820, which represents an improvement of 2.5%. However the use of

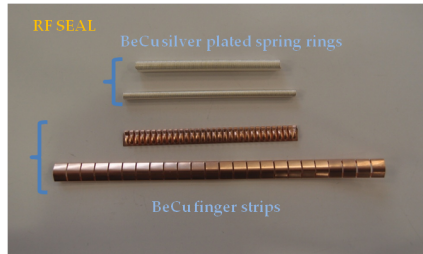


Figure 5.33: RF seal types employed in the RFQ cold model silver plated.

Table 5.3: Simulated and measured RFQ cold model quality factor.

Simulation/Tests	Conditions	$Q_0$
$Q_0$ simulated	ideal Al	8830
$Q_0$ simulated	Al with $R_a = 1.2 \mu\text{m}$	7890
$Q_0$ measured	no RF seal	4700
$Q_0$ measured	RF seal (in all ports and end walls)	4820

RF sealing will guarantee a long term stability behaviour of the quality factor. The final RFQ CM  $Q_0$  measured is 4820, which means a 61 % of the simulated value 7890, a figure which takes into account the material surface roughness. This result is in accordance with the previous experiences of other projects [31, 32].

#### Dipole stabiliser rod effect in the $Q_0$

Dipole stabiliser rods also have an effect on the quality factor, since the cavity dissipation surface increases. Figure 5.34 show the measured  $Q_0$  degradation.

#### 5.4.7 Frequency Tuning System

The RFQ CM manufacturing tolerances are compensated by means of the slug tuners available in the cavity. The tuner diameter is 34.1 mm and

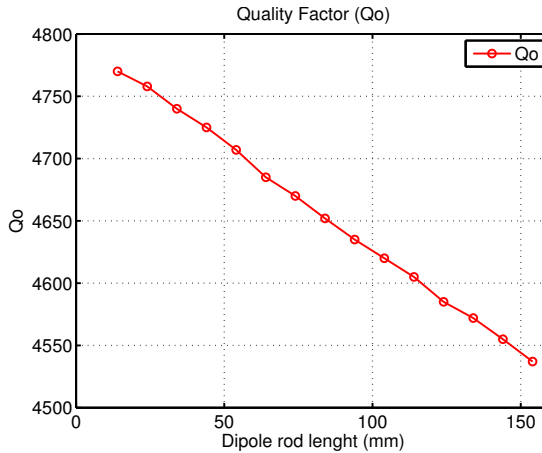


Figure 5.34: Quality factor degradation versus dipole stabiliser rods length

the maximum depth in the cavity is approximately 16 mm. The maximum frequency tuning range is 3.2 MHz. This result is in agreement with the simulation values as well as with results using Slater's perturbation theorem [33].

The RFQ CM dynamic tuning is provided by four movable tuners of a total of sixteen tuners to compensate the frequency deviation during operation due to mechanical stresses and temperature. Each tuner is moved by a stepper motor commanded by the LLRF frequency tuning loop. As a consequence of protruding tuners, the cavity quality factor decreases as shown in Figure 5.37.

The result shows that  $Q_0$  is lowered up a 6% due to such an effect. Furthermore, we have included in the tests the effects of the dipole stabiliser rods with an insertion length of 135 mm (red curve in Figure 5.37). Firstly, we can conclude that the evolution of the  $Q_0$  is similar that in the case of lack of rods, and secondly we check that the final value measured is lower with the dipole rods. Therefore both the dipole rods and the slug tuners decrease the cavity  $Q_0$ , and their effect depends on their volume inside the cavity.

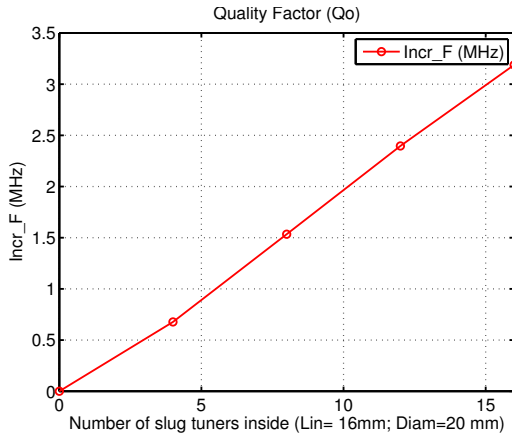


Figure 5.35: Frequency tuning range with different number of slug tuner. The tuners penetration length is 16 mm and the diameter is 34.1 mm

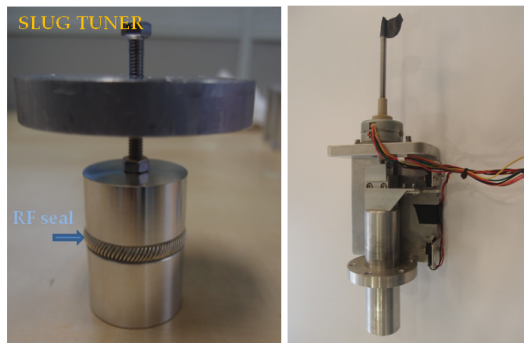


Figure 5.36: **Left:** RFQ cold model slug tuner including the RF seal. **Right:** Movable tuner.

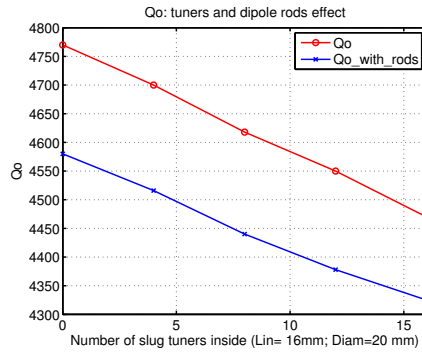


Figure 5.37: RFQ cold model quality factor evolution as function of the number of tuners inside the cavity

#### 5.4.8 Accelerating Field Flatness

The longitudinal field flatness is obtained from the bead-pull test, based on the classical Slater perturbation theory [33]. The setup system consists of a cradle to support the cavity under test, the kevlar wire, an stepper motor with integrated drivers and controllers to pull the bead along the longitudinal axis, and an USB DAQ to accommodate the motor control signals. In order to accurately synchronise the bead position via the motor and data acquisition by the network analyser, a control program has been implemented using LabVIEW to measure the resonant frequency change. The bead-pull test will be devoted to tune the RFQ CM achieving the field flatness specification. The field profile along the bead axis has been obtained from both the resonant frequency shift and the phase change at the unperturbed frequency. The results of both methods are in agreement, although the phase method allows much faster measurements.

Figure 5.38 shows the electric field measured with a dielectric bead. The bead has been located almost touching two electrodes in order obtain a better bead alignment and measurement reproducibility. The first results of the magnetic profile measured in the four quadrants are shown in the Figures 5.39 and 5.40. The magnetic field has been also measured in the four RFQ quadrants at a distance from the beam axis of  $x = y = 35$  mm. The bead used to perform this test is metallic (an Aluminium

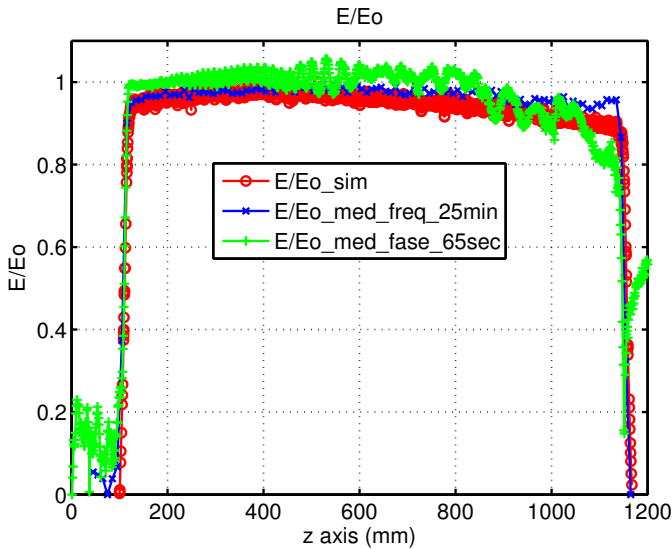


Figure 5.38: Measured and simulated  $E/E_0$  comparison

cylinder). Figure 5.39 show the normalised magnetic field measured in the four quadrants (Q1-Q4) for the quadrupole and adjacent dipole modes. We can notice that the field profile measured in the four quadrants are quite different, which may be a consequence of mechanical errors and misalignment issues. But it also important to remark that some of the quadrants, both profiles (tested and simulated), seem to match pretty well.

More tests are necessary to analyse the results and study the effect of the cavity assembly, manufacturing mechanical errors as well as the configuration test system itself.

#### 5.4.9 Low Level RF System

The LLRF system should control the amplitude and phase of the RFQ field besides the cavity frequency tuning, in order to minimise the reflected power. The ESS-Bilbao LLRF design for the RFQ has amplitude and phase long term stability specifications of 1 % and  $1^\circ$  respectively [34, 35]. The

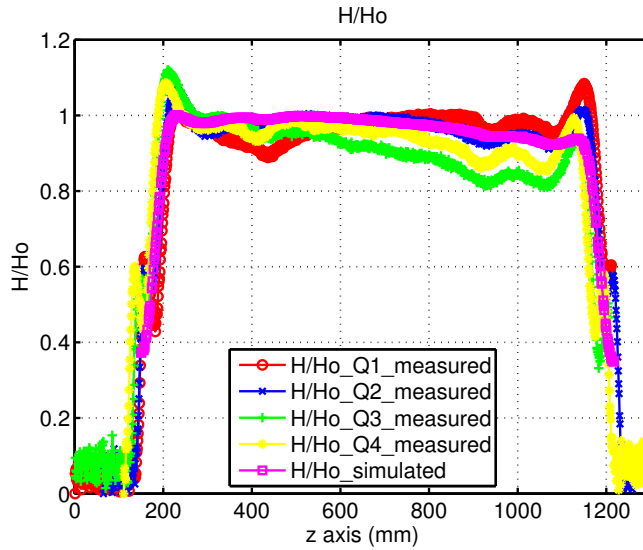


Figure 5.39: Measured and simulated H/Ho comparison

RFQ CM dynamic tuning is provided by four movable tuners of the total sixteen tuners to compensate the frequency deviation during operation due to mechanical stresses and temperature. Each tuner is moved by a stepper motor commanded by the LLRF frequency tuning loop.

Both LLRF control loops have been tested independently with the CM; some enhancements are still under development. The amplitude and phase control were measured satisfactorily obtaining short term amplitude and phase root mean square errors  $< 0.1$  and  $< 0.5^\circ$ , as shown in the LLRF GUI (Figure 5.40). The long term stability will be done in a near future.

The frequency tuning loop has also been validated controlling only a unique movable motor. In the next step, the four movable tuners will be installed and controlled simultaneously by the LLRF.

After the low power tests, the cavity will be fed by the klystron driver which can provide a peak power up to 1000 W [36].

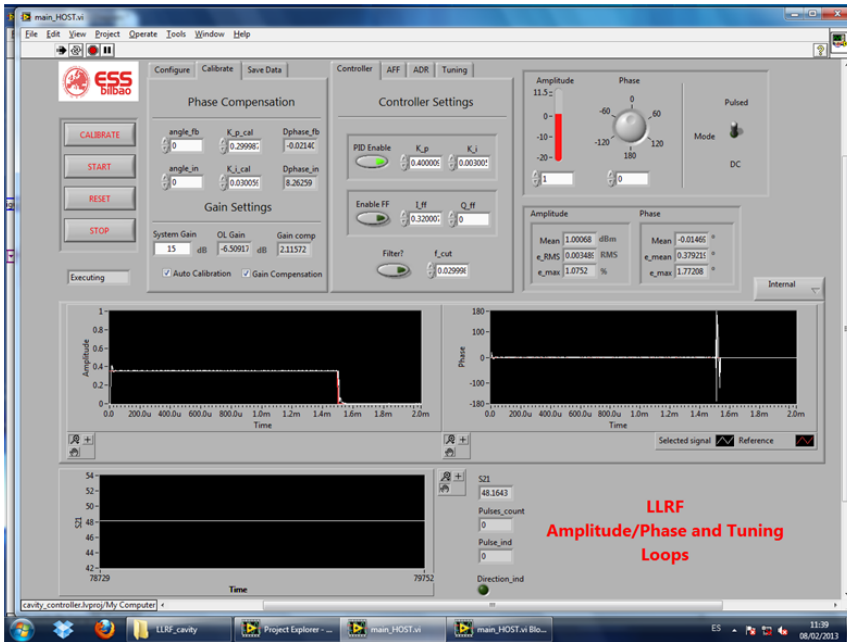


Figure 5.40: ESS-Bilbao LLRF GUI tested with the RFQ CM.



## Chapter 6

# Cooling Requirements & Design

### 6.1 Heat losses

In order to design the cooling system of the RFQ an accurate description of electromagnetic power losses is needed. These losses are computed from the electromagnetic eigenfrequency solution as

$$P = \frac{1}{2} R_s \int_S (\alpha H)^2 dS. \quad (6.1)$$

where  $R_s = 1/\sigma\delta_S$  is the electric surface resistance, that depends on frequency and surface conditions. For copper at 352.2 MHz a value of  $R_s = 0.0052 \Omega$  is used for the calculations. This value is high for OHFC copper and corresponds to a very high surface roughness, as will be discussed on the following sections.  $H$  is the magnetic field at the surface, that must be scaled to the right value using the  $\alpha$  factor. The normalisation criterion used is described below. All calculations are done using COMSOL Multiphysics software, with additional verifications using HFSS.

The surface resistance is calculated as  $R_s = \sqrt{\mu\mu_0\omega/2\sigma_c}$ . The surface roughness is included in the conductivity as  $\sigma_c = \sigma/K_w^2$ , where the factor

$K_w$  is defined as:

$$K_w = 1 + \exp\left(-\left(\frac{s}{2h}\right)^{1.6}\right), \quad (6.2)$$

where  $h$  is the surface roughness ( $R_{rms}$ ) and  $s$  the skin depth penetration. For  $R_c = 0.4 \mu\text{m}$ ,  $R_s = 0.0048 \Omega$ , while for  $R_c = 0.8 \mu\text{m}$ ,  $R_s = 0.00515 \Omega$ . The value of  $R_s = 0.0052 \Omega$  corresponds to a surface roughness of about  $1 \mu\text{m}$ .

The model selected as test-bench for cooling design is a variation of the ESS-Bilbao RFQ aluminium cold model, as the 3D model of the actual 4 m long RFQ was difficult to handle across different computer codes. The modified model includes a set of vacuum grids and has no vane modulation to fasten computer simulations. Radial matchers are included at both ends of the model. In this model, the vane tip from the start to the end does not follow an horizontal line, and vane to vane distance changes along length. This situation creates some anomalies in the electromagnetic characteristics (first dipolar mode D1 is far below D2 and quadrupolar Q modes, which are very close; In the real situation D1 and D2 are very close, and much lower than Q. As a result, the final cooling design should be verified in the final stages with a model closer to real geometry.

The field scaling is based on the comparison of some value with an equivalent electrostatic simulation using an inter-vane voltage of  $V = 85 \text{ kV}$ , for example like the one shown in Figure 6.1. The maximum value of electric field selected is  $E = 3.82 \times 10^7 \text{ V/m}$ . Electromagnetic eigenvalue calculations normalises electric field values to some criterion; for example, total energy stored equal 1 J. To get the field magnitudes that would be obtained in a cavity with power input a power coupler, the electric and magnetic fields obtained for the eigenfrequency solution are then multiplied by a factor  $3.82 \times 10^7 / E_{s, \max}$  to get the right field values.

The obtained solution is shown in Figure 6.2 (surface magnetic field and deposition map). The frequency of the quadrupolar mode is equal to 354.652 MHz.<sup>1</sup> The total power deposited (integration over all surface boundaries) is  $P = 103567 \text{ W}$  (at 100 % duty cycle).

<sup>1</sup> Keep in mind that this frequency corresponds to an artificially modified model used for cooling studies, not to the final RFQ model

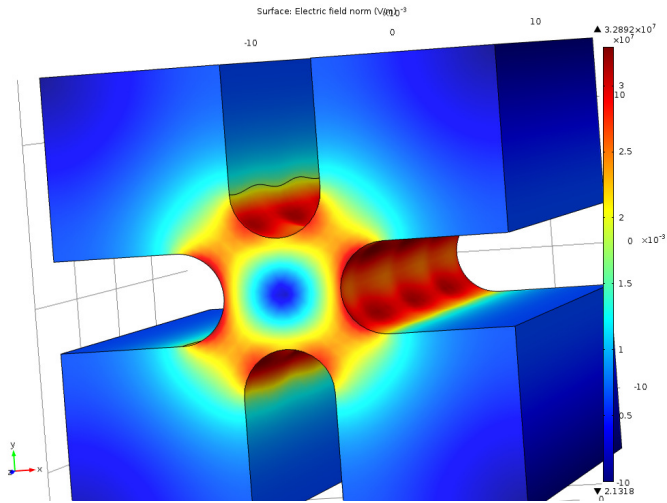


Figure 6.1: Electrostatic solution for vane tips area.

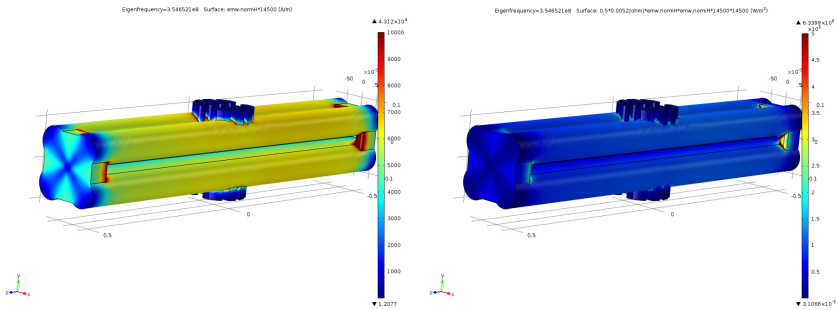


Figure 6.2: **Left:** Surface values of magnetic field (normalised) for the quadrupolar mode of the RFQ model. **Right:** Power loss computed from fields.

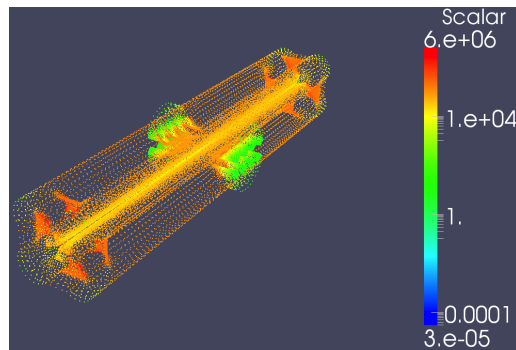


Figure 6.3: Power loss shown from exported data file using Paraview software.

From the electromagnetic software the power loss is exported as a text file that can be used as input for thermo-mechanical and cooling simulations (with a corresponding duty cycle factor of, for example, 0.1). The data contained in this file is shown in Figure 6.3 to check that there is no information loss in the process. Additionally, the volumetric mesh of the vacuum domain where electromagnetic equations are solved is exported to a text file. The thermo-mechanical calculations can act directly on this mesh file applying the deformation of the surface due to thermal stresses. The deformed mesh file is imported back again into COMSOL using an automatic procedure to evaluate the resonant frequency change.

## 6.2 Comparison between baffles and drilled options

### 6.2.1 Introduction

The ESS-Bilbao accelerator includes a 4-meter RFQ. Thermal design is performed in the first of four segments which constitute the RFQ. The total peak power is  $\sim 400$  kW, 100 kW per module. However, the RFQ is not going to be operating at maximum power all the time, but is going to be

operating with a duty cycle of 10%. Hence, nominal conditions are 40 kW on the RFQ and 10 kW on one module.

Following sections will describe the RFQ parameters that have been considered as heat flux fields, duty cycle, etc. and the corresponding thermal outputs (water mass flow rates, temperature, stress and displacements fields and frequency variation effect) in two designs referred as *baffle* and drilled cooling, which are described in what follows.

The following considerations have been taken into account:

- In principle, cooling water will be at room temperature, so it is not necessary to reduce its temperature.
- The RFQ outer walls are adiabatic. Hence, heat exchange occurs exclusively on the channel surfaces.
- All displacements ( $u_x$ ,  $u_y$  and  $u_z$ ) have been forbidden at both ends of the RFQ. This assumption simplifies the mechanical problem, which would be too difficult to deal with if more realistic boundary conditions were applied. However, this procedure produces more conservative results than a more realistic approach, overestimating frequency variation.

### 6.2.2 Calculation Procedure

Several subsequent calculations are necessary to determine how thermal displacements affect the cavity resonance. The analysis starts with a thermal hydraulic study in FLUENT, importing the heat flux map from the electromagnetic case. Then, temperatures are exported to ANSYS (thermo-mechanical calculation), where displacements and stress fields are obtained. Finally, from a simple C program that exports a deformed mesh to COMSOL, it is possible to calculate the deformation effect. Figure 6.4 represents the calculation procedure that has been followed.

A thermal source is applied as a surface heat flux on the cavity surface, considering that only vacuum system ports alter the symmetry. As it was mentioned above, the peak power is around 100 kW in each module (400 kW total peak power for the 4-meter-long RFQ) with a duty cycle of 10%. It is important to perform the thermal design with a safety margin,

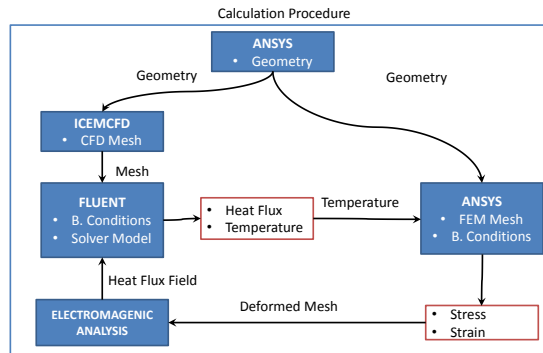


Figure 6.4: Calculation Procedure Scheme

so calculations have been performed with five different power levels on the first segment: nominal conditions (10 kW), 12.5 kW, 15 kW, 17.5 kW and 20 kW. The Figure 6.3 shows the heat flux field in  $W/m^2K$  on the RFQ cavity surface.<sup>2</sup>

### 6.3 Baffle design

The baffle cooling design is based on some baffles where water circulates. These baffles are strategically placed in each vane. The major vane has two cooling baffles placed on each vacuum port side, one cooled vacuum port and eight cooled tuners. The minor vane has three baffles in the axis direction, two of them are placed at the extremes and the last one at the center (see Figure 6.5).

#### Thermal hydraulic design

Major vane thermal hydraulic parameters are listed on Table 6.1. It can be observed that the maximum pressure drop is around 0.07 bar and the maximum velocity is 2.34 m/s. We have performed the thermal hydraulic

<sup>2</sup> Code: RFQ-cm-al-1000-vm2-rfbd2-con-rejilla-sin-agu-mod-2-555K-power-loss. J.L Muñoz

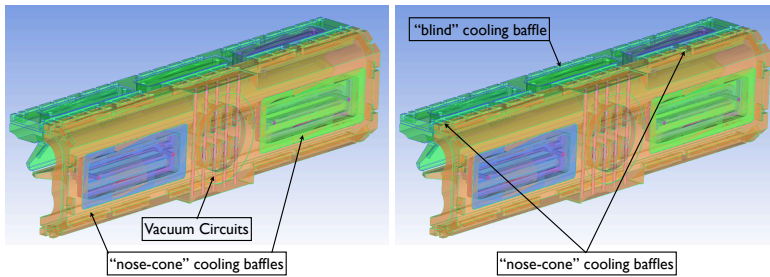


Figure 6.5: **Left:** Major vane cooling design. **Right:** minor vane cooling design.

Table 6.1: Major vane cooling parameters

Parameters	Baffles	Vacuum Port
$T_{\text{inlet}}$ (K)	293	293
Gauge Pressure (bar)	0	0
$\dot{m}$ (kg/s)	$2 \times 0.055$	$5 \times 0.1$
$V_{\text{max}}$ (m/s)	2.34	2.19
$\Delta P$ (bar)	0.07	0.02

calculations taking into account that the maximum value of water velocity into the channels should not be higher than 2.5–3 m/s because of copper corrosion [37].

The primary minor vane cooling parameters are listed on Table 6.2. The highest pressure drop is around 0.06 bar and the maximum velocity in the channels is 2.2 m/s.

For both vanes, these parameters are constant for all the different power levels applied to the RFQ. Because the power increase and thus, the temperature field are linear, only the 10 kW case has been represented (see Figure 6.6 where the temperature field is shown). The other cases present the same pattern. It can be observed that maximum temperature is reached in two zones, vane *noses* considering that is the zone where power is higher and the vacuum port because cooling channels do not reach the vane tip. That maximum temperature is around 25°C.

Table 6.2: Minor vane cooling parameters

Parameters	Baffle 1	Baffle 2	Baffle 3
$T_{\text{inlet}}$ (K)	293	293	293
Gauge Pressure (bar)	0	0	0
$\dot{m}$ (kg/s)	0.05	0.05	0.05
$V_{\text{max}}$ (m/s)	2.2	1.2	2.2
$\Delta P$ (bar)	0.0634	0.0238	0.06125

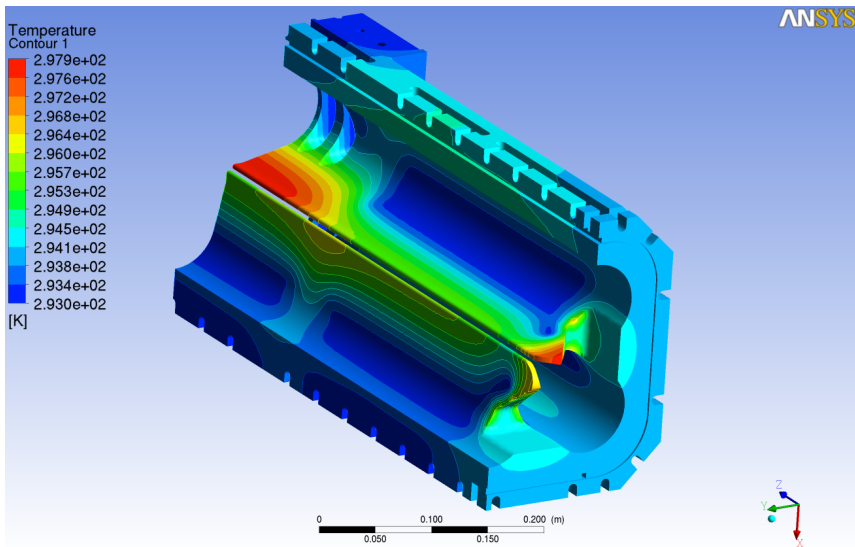


Figure 6.6: Temperature field for 10 kW.

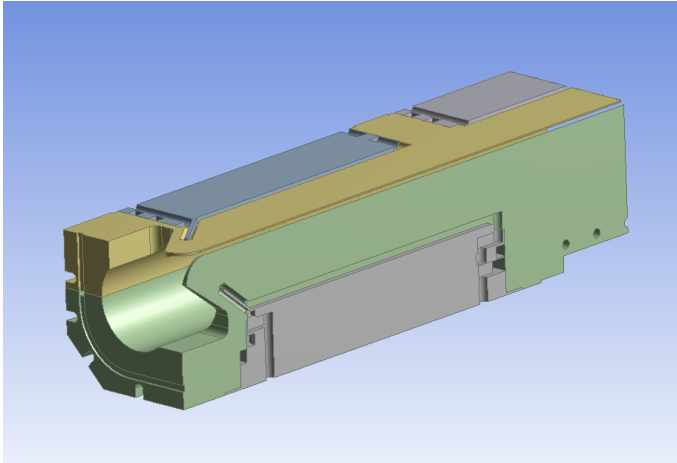


Figure 6.7: Mechanical simplification.

### Thermo Mechanical design

For the thermo-mechanical assessment, an analysis of one eighth of a segment has been performed (see Figure 6.7). The boundary conditions applied are symmetry on the cutting faces and a fixed vane end.

The Figures 6.8 and 6.9 depict the displacements maps in the X, Y and Z axis and the vector sum. In X direction, maximum displacement in the cavity is  $2\ \mu\text{m}$  which is produced in the nose and in the centre of the minor vane, in the Y direction the maximum is around  $7.5\ \mu\text{m}$  in the major vane center and  $2\ \mu\text{m}$  in the nose.

And in the Z axis, maximum displacement is reached both in the nose and in the centre and it is  $3.8\ \mu\text{m}$ .

### Summary

Thermal results obtained from the calculations performed for the different power levels with the baffle configuration are summarised in Table 6.3. A linear pattern can be observed in the table. Maximum displacement, as expected, is reached in the Y direction with a power of 20 kW, in other

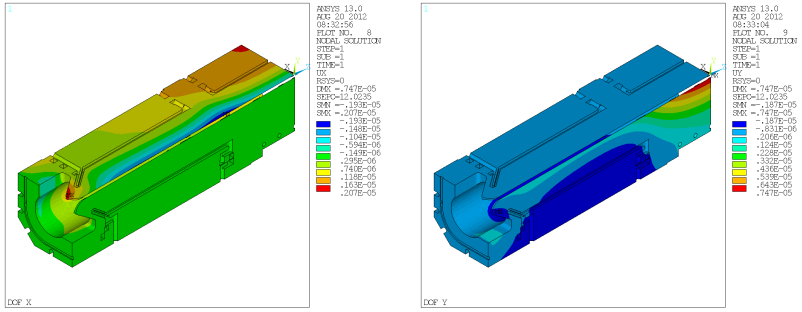


Figure 6.8: X and Y direction displacements field in m.

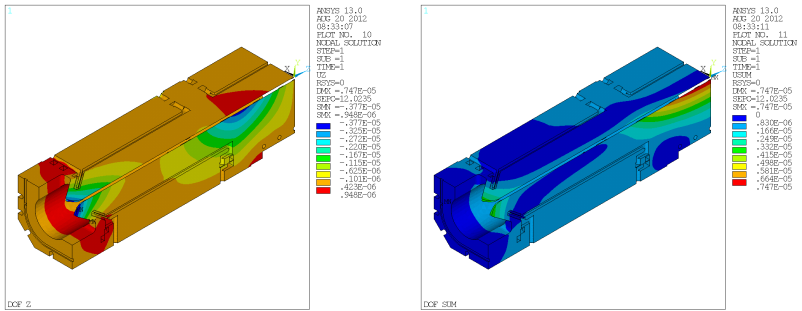


Figure 6.9: Z direction and vector sum displacements field.

Table 6.3: Thermal analysis summarise of TODO configuration.

Power (kW)	$\Delta x$ ( $\mu\text{m}$ )	$\Delta y$ ( $\mu\text{m}$ )	$\Delta z$ ( $\mu\text{m}$ )	$T_{\text{max}}$ ( $^{\circ}\text{C}$ )	$\Delta f$ (kHz)
10.0	2.0	7.5	3.8	25.0	75.2
12.5	2.5	9.6	4.7	26.4	95.4
15.0	3	11.7	5.7	27.5	115.2
17.5	3.5	14.3	6.7	29.7	137.3
20.0	3.85–4.3	16.1	7.5	30.8	155.6

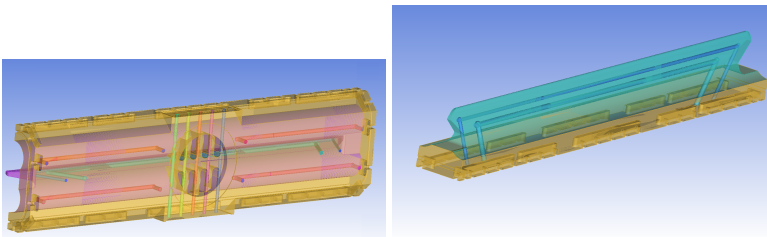


Figure 6.10: CERN major vane (left) and minor vane (right) cooling design.

words, with a safety factor of 2 and its value is around  $16 \mu\text{m}$ . Maximum temperature is  $31^{\circ}\text{C}$ .

Finally, in order to close the calculation procedure, a frequency variation analysis has been performed exporting the deformed mesh to electromagnetic FEM program. Table 6.3 also represents the summary of this study. It can be observed that in nominal conditions (10 kW) the variation is around 75 kHz.

### 6.3.1 Drilled design

Drilled cooling design consists of two main tubes that are manufactured by drilling holes and blocking the extremes by brazing (see Figure 6.10). In order to obtain a homogeneous temperature field in the cavity, water flows in these tubes in counterflow. In the case of the major vane, the vacuum port and four more channels have been included because it is necessary to cool the RFQ bulk and obtain a uniform temperature field.

Table 6.4: Major vane cooling parameters

Parameters	Main Cavity Tubes	Bulk Tubes	Vacuum Port
$T_{\text{inlet}}$ (K)	293	293	293
Gauge P (bar)	0	0	0
$\dot{m}$ (kg/s)	$2 \times 0.05$	$4 \times 0.1$	$5 \times 0.1$
$V_{\text{max}}$ (m/s)	2.31	1.3	2.07
$\Delta P$ (bar)	0.095	0.03	0.02

Table 6.5: Minor vane cooling parameters

Parameters	Outer Tube	Inner Tube
$T_{\text{inlet}}$ (K)	293	293
Gauge Pressure (bar)	0	0
$\dot{m}$ (kg/s)	0.05	0.085
$V_{\text{max}}$ (m/s)	2.38	2.13
$\Delta P$ (bar)	0.09	0.044

### Thermal Hydraulic design

Using the same procedure as the baffle case, tables 6.4 and 6.5 summarise some important parameters in the cooling channels for the major and minor vane respectively. It can be observed that the maximum pressure drop in the major vane is around 0.1 bar and the maximum velocity is around 2.3 m/s.

In the minor vane, the highest pressure drop is around 0.09 bar and the maximum velocity in the channels is near 2.4 m/s.

Regarding the temperature, Figure 6.11 shows the temperature field in the vanes. Maximum temperature is reached in the beam inlet (noses) and it is around 32.4°C. Although temperature is higher than in the Baffle configuration (around 7.5°C), it can be observed that temperature along the beam direction is totally homogeneous and it has an important effect on frequency variation as it will be shown below.

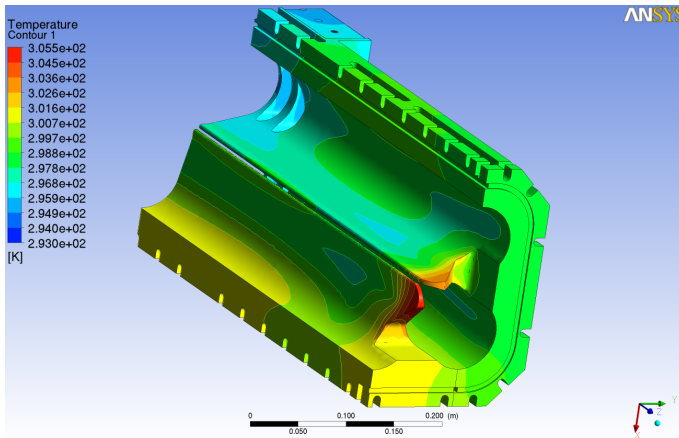


Figure 6.11: Temperature field for the drilled case.

### Thermo-Mechanical design

For the thermo-mechanical assessment, like in the baffle thermal analysis, an eighth of the first module has been considered with the same boundary conditions (symmetry and the vane end fixed). Figures 6.12 and 6.13 show displacements in each axis and the vector sum, respectively. Maximum displacement obtained in the X direction is around  $8.5 \mu\text{m}$  and it is reached in the nose of the minor vane where the temperature is maximum. In the Y direction the maximum is  $5 \mu\text{m}$  also in the major vane nose. Finally, in the Z axis, maximum displacement is around  $12 \mu\text{m}$  in the beam inlet.

### Summary

Like in the baffle option, Table 6.6 summarises the thermal analysis for drilled configuration. It can be observed that in general both the temperature and also displacements are higher than in the pockets channels. For instance, maximum displacement, obtained for 20 kW, is  $24 \mu\text{m}$  in the axis direction, which is three times as much as the baffle case.

Again, in order to close the cycle, it is necessary to obtain frequency variation. So, exporting the deformed mesh this variation can be calculated.

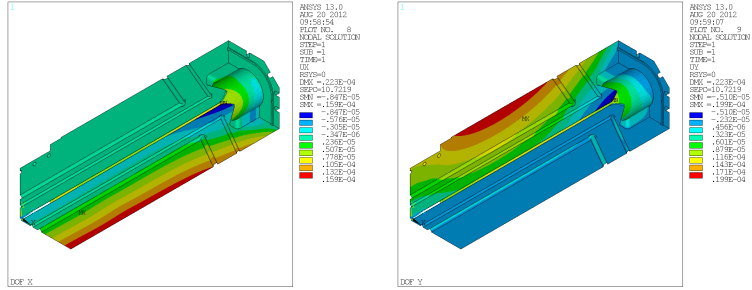


Figure 6.12: X and Y direction displacements field in m.

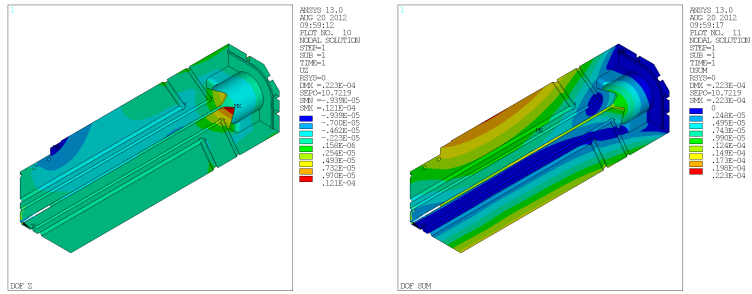


Figure 6.13: Z direction and vector sum displacements field.

Table 6.6: Thermal analysis summarise for drilled desing.

Power (kW)	$\Delta x$ ( $\mu\text{m}$ )	$\Delta y$ ( $\mu\text{m}$ )	$\Delta z$ ( $\mu\text{m}$ )	$T_{\text{max}}$ ( $^{\circ}\text{C}$ )	$\Delta f$ (kHz)
10.0	8.5	5.0	12.0	32.4	28.0
12.5	10.6	6.4	15.0	35.5	34.4
15.0	12.7	7.7	18.1	38.5	43.0
17.5	14.8	9.0	21.1	41.7	48.1
20.0	17.0	10.2	24.1	44.8	54.5

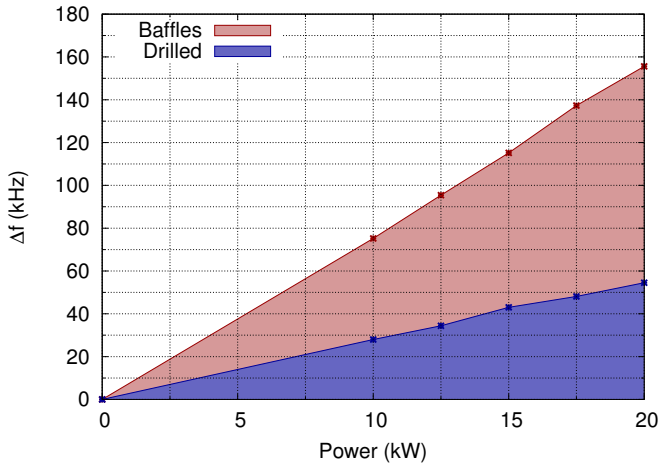


Figure 6.14: Frequency variation comparison.

Table 6.6 also represents the results. Although displacements and temperature in drilled configuration is higher, frequency variation is lower by a factor of three (at nominal conditions it is around 28 kHz). The reason is because temperature field is more homogeneous and also the deformation is uniform, so the RF behaviour is more stable.

### 6.3.2 Conclusions

To conclude this comparison between both configurations, Figure 6.14 shows frequency variation curves which were obtained for each option. It can be observed that they are straight lines and in the case of drilled option, its slope is much smoother. At nominal conditions, which at principle the RFQ is going to be operating, drilled option presents a little bit more RF stability, although in both cooling options the frequency variation is very low and either of them can be chosen.

Table 6.7: Thermal analysis summary for cold water.

	Power (kW)	$\Delta x$ ( $\mu\text{m}$ )	$\Delta y$ ( $\mu\text{m}$ )	$\Delta z$ ( $\mu\text{m}$ )	$T_{\text{max}}$ ( $^{\circ}\text{C}$ )
Baffle	10.0	-10.0	5.0	-7.0/6.6	20.0
	12.5	-9	5.0	-6.7/6.4	21.4
	15.0	4 - 8.5	5.0	-6.5/6.2	22.5
	17.5	-8.3	5.0	-7.4/6.0	24.7
	20.0	-8	5.0	-8.4/5.8	25.8
Drilled	10.0	8.5	5.0	-5.1/4.4	27.6
	12.5	10.6	6.8	-5.6/7.4	30.8
	15.0	12.7	8.1	-6.6/10.5	34.0
	17.5	14.8	9.3	-8.5/13.6	37.1
	20.0	16.9	10.6	-10.8/16.7	40.3

## 6.4 Water temperature sensitivity

One of the thermal hydraulic parameters that could be interesting to assess is the inlet water temperature. So far, room temperature has been considered for water, but it could be reduced if a *chiller* is added to the cooling system. In order to evaluate the impact that water temperature produces mainly in the frequency variation, the same analysis as the previous one has been performed. Only water temperature has been changed, in this case it has been reduced to  $15^{\circ}\text{C}$  ( $5^{\circ}\text{C}$  lower than room temperature).

Table 6.7 summarises the thermal analysis for this study (maximum temperature and displacements). It can be seen that maximum temperature in both cooling channels is  $5^{\circ}\text{C}$  lower than in the previous comparison. According to the displacements there is a curious effect, when water enters at lower temperature it produces a contraction on the RFQ and when the heat power is increasing, this effect is compensated for the dilatation produced due to the thermal load.

Table 6.8 shows the frequency variation in this situation. It can be observed that when there is no heat load, a frequency reduction is produced due to the contraction. In both cases, this variation is around  $-65$  kHz. When the heat load increases, the frequency reduction is compensated for

Table 6.8: Frequency variation summary for cold water.

Power (kW)	$\Delta f$ (kHz)	
	Baffle Conf.	Drilled Conf.
0	-66.1	-64.4
10.0	9.5	-34.6
12.5	28.9	-27.1
15.0	49.4	-19.8
17.5	68.7	-11.5
20.0	89.0	-3.8

the dilatation effect. For the baffle option, at nominal conditions (10 kW) the variation is around 9.5 kHz, which is almost more than eight times lower than the frequency variation produced at room temperature. In the other hand, for drilled design, the lowest value appears at 20 kW and it is around -3.8 kHz. At nominal conditions, in absolute value, the variation is a little bit higher than at room temperature.

Finally, Figure 6.15 represents for each cooling option RF behaviour at different powers when water temperature is colder than room temperature. It can be observed that both curves are straight lines. As it was mentioned above, for baffle design, close to 10 kW the frequency variation is minimal. However, for drilled option, the minimal variation is reached at 20 kW. The reason is because when there is no heat load, frequency variation is around -65 kHz and when the heat power increases, the frequency compensation is different for each option. Namely, as the baffle curve has a higher slope, the compensation is quicker. It is important to say that these curves have the same slope than Figure 6.14, the difference appears at 0 kW.

One of the most important conclusions that can be drawn is that if the inlet water temperature is lower than room temperature, the frequency variation could be close to zero, it depends on the water temperature and the cooling option.

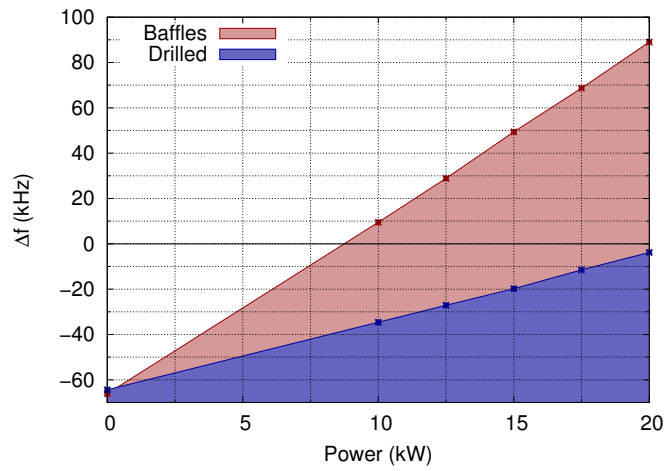


Figure 6.15: Frequency variation for cold water.

**Part III**

**Mechanical Design**



# Chapter 7

## Mechanical & Vacuum Engineering

### 7.1 Supports

The design of the support structure has two main principal aims. First, it has to allow the three linear movements and the three angular movements for the alignment, and second, it has to provide a support bench for the RFQ and all the components with the minimum possible deformation.

The principal weight and pressure to support are the following ones:

- The RFQ own mass, around 365 kg.
- The vacuum pumps weight, 18 kg.
- The pressure produced by the vacuum 1 bar in all the outside faces.

There are still more elements like tuners, couplers and so on, Some of those however, will be built alongside with their own, independent supports. Here, we have considered two different design options to support the RFQ. the first was based on a concept developed at CERN, and is referred to as *jacks* from here on, whereas the second relied on our own design.

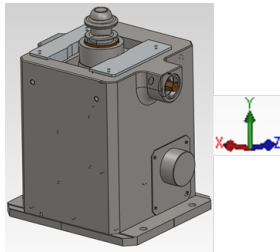


Figure 7.1: CERN's Jack design.

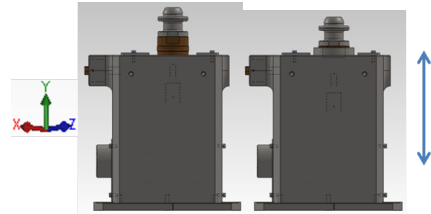


Figure 7.2: Jack's movement.

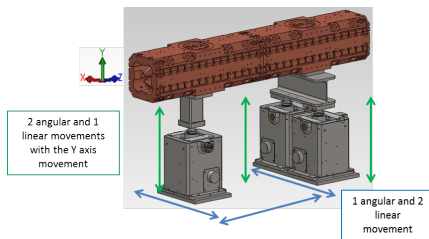


Figure 7.3: Possible movements with 3 Jacks.

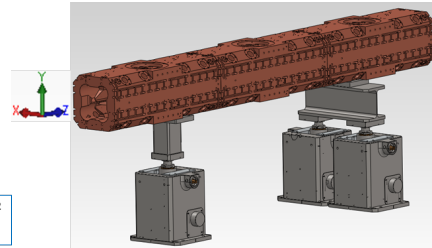


Figure 7.4: 3 Segments mounting.

### 7.1.1 CERN designed Jacks

Figure 7.1 shows the CERN's Jack design. These assemblies are designed to support up to 5 t for each Jack and it allows a 15 mm movement along the Y axis, the vertical axis as Figure 7.2 shows.

With the geometrical arrangement shown in Figure 7.2, an Y axis movement for the RFQ is allowed. If, in addition a set of three Jacks is considered as Figure 7.3 shows, two angular movements are then enabled (X and Z axes angular movements). In fact, the X and Z linear movements and the Y axis angular movements are performed moving the Jacks as shown in Figure 7.3 with the blue arrows.

The minimum distance between the Jacks is limited by their dimension. In the ESS-Bilbao design the length of each segment for the RFQ is of 790 mm so the only way to use Jacks is to put three Jacks for each two

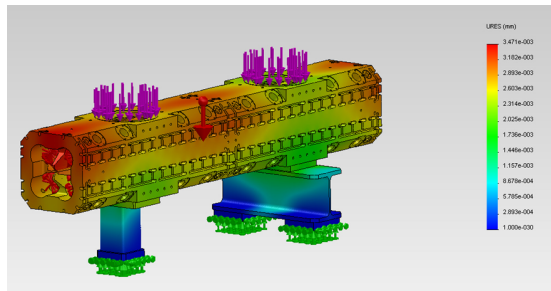


Figure 7.5: Mechanical simulation with the Jacks.

segments. As the RFQ has five segments the only way to align the structure is to have three jacks for every two segments as shown in Figure 7.3 and additional three jacks for the other three segments as the Figure 7.4 shows.

The other issue to consider regards the deformation of the RFQ. Using the Jacks, the distance between them is too large to avoid the deformations. So before entering into the detailed design (how to do the X and Z axes movements) a simulation has been done to check whether the deformation induced to the RFQ is acceptable. Figure 7.5 shows the deformation results which have been calculated with the following boundary conditions:

- Gravity
- Vacuum pump weight
- Pressure generated by the vacuum inside the RFQ

As the simulation shows, the maximum deformation in the RFQ is of 3.5  $\mu\text{m}$ , which is acceptable.

### 7.1.2 Our design for the support

The second support option, is to design our own support. A preliminary design is shown in Figure 7.6, which takes several ideas from implemented at the ISIS FETS.

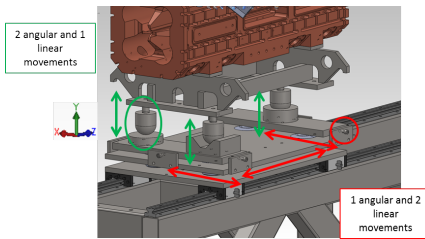


Figure 7.6: Own support design.

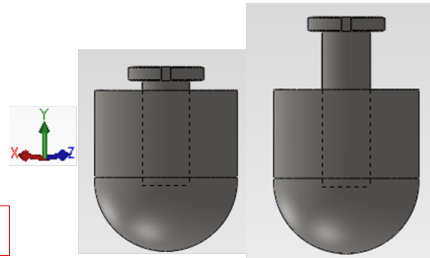


Figure 7.7: Y axis movement.

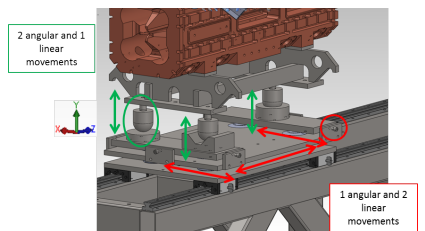


Figure 7.8: Movements possible with the support.

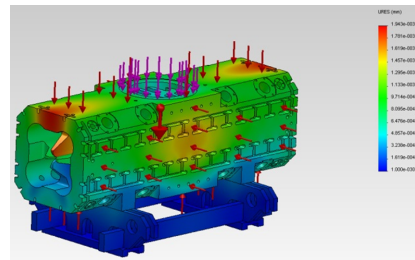


Figure 7.9: Mechanical simulation with the support.

Within this design all the required movements are enabled. The mechanisms shown in Figure 7.7, allow movements along the vertical axis (Y axis).

With a set of three such mechanisms, two angular movements are also allowed (angular movements in Z and X). The red circled mechanisms depicts a screw for the movements in the X and Z axes, allowing the last angular movement (angular movement in Y) as shown in Figure 7.8.

The screws used to move the RFQ along the X and Z axes, are DIN 912 12.9 M8x 35 fine thread screws. The main characteristics of these screws are:

- $R_m = 1200 \text{ N/mm}^2$
- $R_e = 1080 \text{ N/mm}^2$
- Thread = 1 mm

So turning the screw  $360^\circ$ , the RFQ will move 1 mm. The next requirement is the deformation of the RFQ with the gravity, vacuum pump weight and the vacuum inside the RFQ. A simulation has been done under these conditions and the result is shown in Figure 7.9.

As the simulation shows, the maximum deformation in the RFQ is of  $1.95\ \mu\text{m}$ , which is even less than the previous simulation, and therefore fully acceptable also.

### 7.1.3 Girder

A girder is commonly used in all accelerators due to its strength and ease way to align. This type of support, gives the possibility of placing *fiducials* in each corner to facilitate the realignment between components, even if it is not something necessary.

A girder should be considered as support to use in all components. In our case, the presence of a number of vacuum devices and connections make mandatory to drill the girder from below to allow vacuum pumps to be located underneath the component. underneath the component). However, the main problem a girder has concerns its length. A girder not larger than two meters could be built if its features like strength, plain and stability are to be kept. Being ESS-Bilbao RFQ more than three meters long divided in five sections, the only practicable option would be to use more than just a single girder. This option would however complicate the joining between them.

### 7.1.4 Conclusions of the support design

Here we summarise the main results derived from the simulations.

- Advantages of the Jacks
  - The most important advantage of using Jacks is that the design is done and tested and some pre series are already manufactured. So the manufacturing which guarantees the tolerances required is already defined.
- Disadvantages of the Jacks

- Two or three segments should be aligned and fixed before mounting them with the Jacks. This alignment has to be done with a tridimensional machine. So, almost three meters long tridimensional machine is needed, which is not the most common machine.
- Advantages of the own, ISIS-FETS based, support
  - It results in a smaller deformation than the previous option.
  - Is not necessary to fix the segments before mounting in the Jacks.
  - Manufacturing of such structure will be cheaper than that considered above.
- Advantages of the Girder
  - The girder has comparatively more strength than the previous options.
- Disadvantages of the Girder
  - There seems to be some difficulty to manufacture a three meters long girder with the required tolerances.

From the comparison list shown above, we have chosen our own design as the most adequate support for the RFQ. Figure 7.10 shows a preliminary design of such a support, also showing some auxiliary components.

This latter design however is not yet frozen since there remain some points to be clarified before reaching a final version and concern,

- The number and position of the couplers in the final RFQ. As the coupler is so large each coupler will have its own support.
- The number and position of the tuners and pick-ups.
- The final design details for the cooling circuits, which have an impact onto the RFQ geometrical details. support the RFQ. Depending of the refrigeration the support will be different.

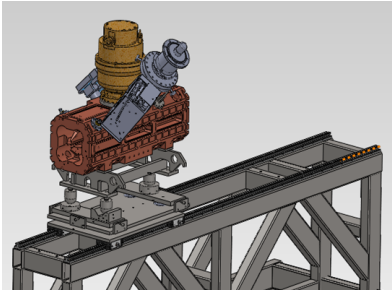


Figure 7.10: Designed support with auxiliary components.

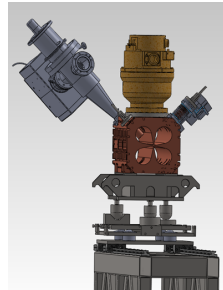


Figure 7.11: Detail of the couplers' support.

## 7.2 Ancillaries

Also, the number of tuners, either fixed or mobile and the number of couplers (two of four) to be used, need to be decided before freezing the design. As a matter of fact, as Figure 7.11 shows, the couplers are heavy and bulky, so they will need their own support. This support will be designed once the number and position of tuners and so on are finally set.

## 7.3 Vane assembly

Once the four vanes are manufactured the next step is to assembly them. In the mounting operation there are two main design issues concerning the vane to vane alignment and the chosen method to fix them. On the latter issue, we found three main options carry out the vane to vane fixation, namely a bolted option, the use of braze welding and finally recourse to electron beam welding. To carry out some tests concerning in the brazing and electron beam welding procedures, we have built several prototypes comprising models for four major vanes and another four minor vanes.

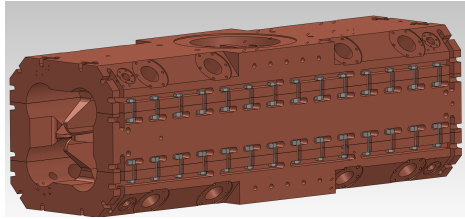


Figure 7.12: Bolted fixation of the RFQ.

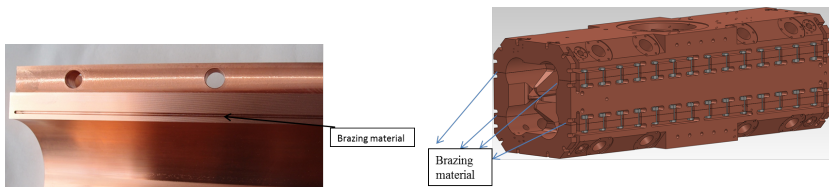


Figure 7.13: **Left:** Brazing alloy position. **Right:** Brazing welding fixation of the RFQ.

### Bolted fixation

The first option, which relies on the use of a bolted joint, is in principle the simplest option since the four vanes are assumed to be perfectly aligned, and also seems the best option of the vane to vane alignment options. Figure 7.12 shows how bolts are distributed along the RFQ.

### Braze welding fixation

The vanes manufactured to carry out the braze welding test had a small milling zone where to put there the brazing alloy. The dimension of this milled zone will depend on the dimensions and thickness of the braze material. Figure 7.13 (left) shows the milled zone.

In the Braze welding fixation method, once the four vanes are aligned, the assembly has to be bolted previously to the deposition of the braze material. Once the brazing alloy is filled, the assembly will be inserted in the brazing furnace. Figure 7.13 (right) shows where the brazing material will be inserted along the 790 mm of the RFQ.

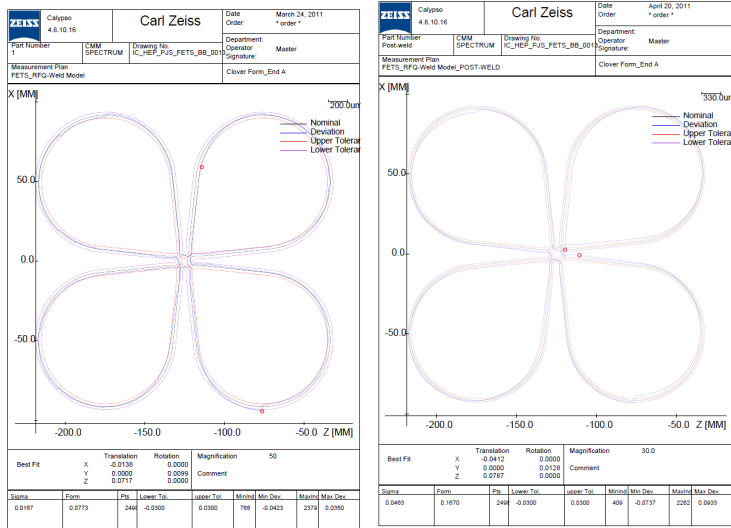


Figure 7.14: **Left:** Metrology report before the welding. **Right:** Metrology report after (right) the welding.

According to some tests performed by our colleagues at the *Rutherford Appleton Lab.* using a closely related design for the the RFQ, welding results in a significant loss of mechanical properties. In fact, if we consider that the required tolerance comes to be about  $\pm 0.03$  mm, nearly achieved before welding (maximum deviation deviation 0.0350), and that such a value rose up to 0.1670 after brazing (see Figure 7.14), we find that something needs to be done to control such a large, heat-induced deformation. To such an avail, we plan to do a thermal treatment before braze welding the four vanes, in order to minimise such deformations. In this respect a test will be carried out at the ESS-Bilbao installations in Jundiz, Vitoria-Gasteiz. The optimum thermal treatment is still being discussed.

### Electron beam welding

The electron beam welding will be done in two steps. First, the four aligned vanes will be bolted, using however less screws than for the other two

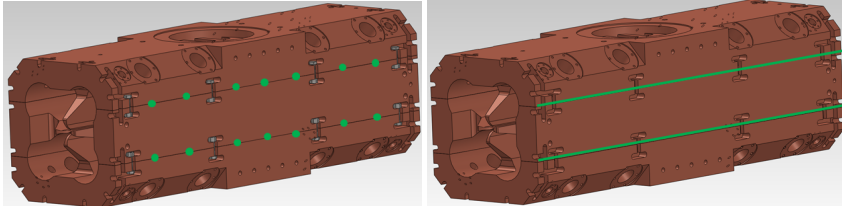


Figure 7.15: **Left:** RFQ with the welding points. **Right:** Electron beam welding fixation of the RFQ.

fixation options. Once the vanes are fixed some welding points will be weld as shown in Figure 7.15 (lef).

With the welding points the four vanes are positioned. The next step is to remove the screws and weld the vanes along the RFQ as Figure 7.15 (right) shows.

This electron beam weld method will be tested in the ESS-Bilbao installations in Jundiz, Vitoria-Gasteiz. Four vanes have been manufactured previously and some test will be done to clarify:

- How much is going to be the penetration of the welding, to avoid damaging the RFQ and not to produce any perturbation in the RF.
- To measure the deformations generated by the temperature reached in the electron beam welding.

### Advantages and disadvantages

The main advantage of the first method is the possibility to disassemble the RFQ whenever it is necessary, a possibility ruled out in the other two options. In addition in the assembly operation, with both welding methods, if welding is not adequate, leading to a gross misalignment, the four vanes would have to be fabricated again. In contrast, the bolt option offers the possibility to de-assemble disassemble and try to align it again, using the same vanes.

## 7.4 Alignment

The alignment of RFQ comprises three different operations, namely

- Vane to vane alignment; based on mechanical designs, no alignment with any external device is performed. It will not be discussed in this document. Such alignment will be performed by the company responsible of manufacturing the structure,
- RFQ alignment with respect to the beam axis
- Segment to segment alignment

The designing of the support, key issue for the alignment, was already discussed above. Here, we describe how we intend to align the RFQ by using different techniques and devices such as Laser Tracker and a Telescope.

### 7.4.1 RFQ alignment with respect to the beam axis

The manner to align RFQ with respect to the beam axis is first comprises, the section by section alignment. Before any alignment of the components is performed, the whole device (RFQ and its support) will be placed on a metallic surface in order to be as flat as possible. All components of the accelerator will be aligned with respect to the beam line. In this way, the height from the flat surface to the beam line is known as, it is also known the distance from the beam line to the fiducial points as derived from the drawings. By placing the Spherical Mirror Reflector (SMR) in each fiducial point (see blue dots in Figure 7.16 left) and using a laser tracker, the height of those fiducial points will be identified. To raise or lower those points, some mechanisms are used (see above), analogue to those employed for other components of the accelerator (ie, LEBT, already constructed).

Once a section of the RFQ is aligned using the laser tracker, a target is placed at the rear end of the component, at the height where the beam travels. The target that is usually used is a Taylor Hobson Sphere (THS). Looking right through the telescope along the beam line (see blue arrow in Figure 7.16 right), the first segment of the RFQ will be accurately aligned as soon as the target is seen from the telescope.

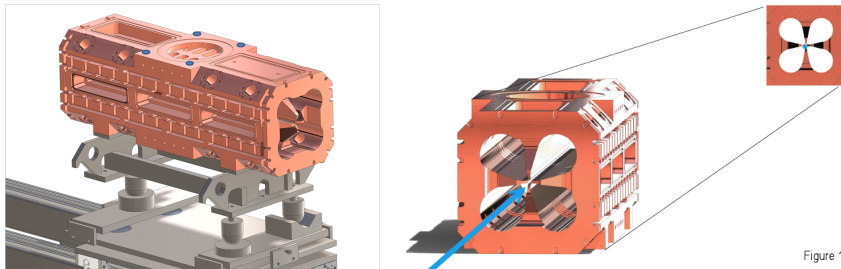


Figure 1

Figure 7.16: **Left:** The fiducial points painted in blue. **Right:** Beam line passing through the RFQ to the target (THS).

## 7.4.2 Segment to segment alignment

The ESS-Bilbao RFQ is divided into five segments. The alignment between the sections is the last process of all. Once the first RFQ is aligned with respect to the beam line (see section above), the next segment is aligned with respect to the previous one already aligned. Therefore, for a rough alignment of the second section of the RFQ, and analogously to the alignment of a single segment, a laser tracker is used.

The second section is assembled to the one aligned already (first section) by a mechanical piece, leaving  $200\ \mu\text{m}$  separation between them due to possible dilatation. By using the laser tracker, a first rough alignment is made by placing the SMR onto the fiducial points (see Figure 7.16 left) as it was made for the first section.

Once this rough alignment is performed, a telescope is used for an accurate alignment. Pointing the telescope to the rear end through the RFQ sections (see blue arrow in Figure 7.16 right) to a target and, once the target is seen from the front end (from the telescope), the section is aligned. In this way, all RFQ sections will be aligned between themselves when the target placed at the rear end of the last RFQ can be seen from the front end of the last RFQ section. For the alignment of a single section, mechanical structures have a strong importance as the RFQ vanes must fit perfectly. This fact is already considered in this document as the manufacturer will deliver the component aligned within the tolerances given by ESS-Bilbao.



Figure 7.17: **Left:** mechanisation process of the WTM. **Right:** Assembly of one of the WTM, in the Imperial College of London. Different vacuum tests have been performed to this model.

## 7.5 Prototypes

As referred above, this resonant structure must be made of the highest quality metal which needs to be machined to high accuracy in order to keep RF losses to a minimum and also to avoid the formation of sparks. In turn, large losses, may translate into overheating the metal structure beyond the cooling capacity which will result in significant mechanical deformations leading to a poor performance. All such issues are duly addressed in the following chapters. At any rate, the most critical decisions taken in the design process need to be supported from prototyping work carried out on prototypes or *cold models* where the effects of the action of different fields (RF, heat etc.), can be quantified in detail.

As a part of the development of the ESS-Bilbao Accelerator in Spain, two different sets of radio frequency quadrupole (RFQ) models have been developed. On one hand, a set of four oxygen free high conductivity copper *Weld Test Models* (WTM) has been designed and manufactured, in order to test different welding methods (electron beam, laser and vacuum brazed welding) as well as other mechanical aspects involved in the fabrication of the RFQ (see Figure 7.17).

For detailed studies on the field distribution, a 352.2 MHz four vane RFQ cold model, with a length of 1 meter, has been designed and built of

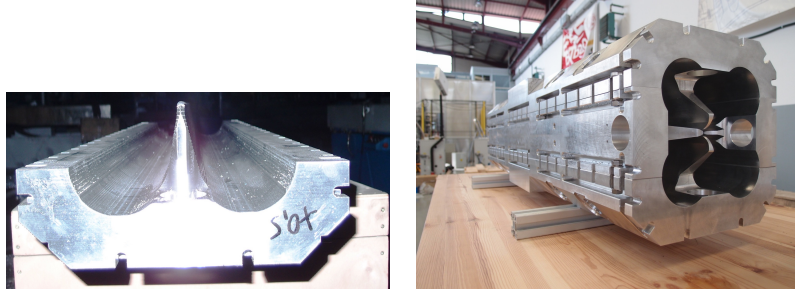


Figure 7.18: Major vane during machining phase, after first rough machining at *Mecanizados Mandrinados Mancisidor* and assembled version at Zamudio R&D centre.

Aluminium, see Figs. 7.18. It serves as a test bench to investigate the validity of different finite element analysis (FEA) software packages. This is a critical part, since the design of the final RFQ will be based on such simulations. The cold model also includes 16 slug tuners and 8 couplers/pick-up ports, which will allow to use the bead-pull perturbation method, by measuring the electric field profile, Q-value and resonant modes. In order to investigate fabrication tolerances, the cold model also comprises a longitudinal test modulation in the vanes, which is similar to the one designed for the final RFQ. In addition, it represents a useful tool to explore the influence of the modulations in the electromagnetic design.

### 7.5.1 Al Cold Model

The manufacturing process is one of the most critical parts in the RFQ fabrication. The tolerances required<sup>1</sup> are so exigent, so is necessary to find the optimum manufacturing process to achieve the required tolerances.

After discussing with the facilities, the fabrication followed for the cold model has been the combination of two different machines, 3 axis milling machine and a bore drilling machine. The latter machine has been used

<sup>1</sup> The Cold model is 20 cm longer than the one the final segments designed for the final RFQ, so the final error achieved with this test is expected to be higher than the final error with the real length.



Figure 7.19: DIXI 5S boring machine



Figure 7.20: 3 axis milling machine

to obtain the planar lean faces and the 3 axis milling machine to machine the modulation. The bore drilling machine used to the manufacturing is a DIXI 5S, with additional control systems, shown in the Figure 7.19. The most relevant characteristics of this machine are:

**Machining strokes**  $X = 2000 \text{ mm}$ ;  $Y = 2000 \text{ mm}$ ;  $Z(H) = 1000 \text{ mm}$

**Accuracy** Flatness of  $2/3 \mu\text{m}$  in 2 m. Position accuracy between holes centres  $0.001 \text{ mm}$ . Turn error of  $0.0002^\circ$  in a  $360^\circ$  turn.

The 3 axis milling machine used is a HM-2010 Kondia shown in Figure 7.20. The most relevant characteristics of this machine are:

**Machining strokes**  $X = 2000 \text{ mm}$ ;  $Y = 1000 \text{ mm}$ ;  $Z(H) = 510 \text{ mm}$

**Accuracy (ISO 203-2)** Position accuracy (scales) =  $0.01 \text{ mm}$ . Repeatability  $0.006$ . Resolution  $0.001 \text{ mm}$ .

The four most important parts of the process are:

**Rough milling** The rough milling operation has been done with a 3 axis milling machine. In this operation 5–6 mm have to be left for each coat. The most important parameters are to control the milling zone temperature and the clamping operation, in order to avoid linear or torsional deformations generated by temperature gradients or by the



Figure 7.21: Rough milling of a minor vane



Figure 7.22: Major vane once the rough milling process is finished

clamps. Figure 7.21 shows a minor vane in the rough milling process with a high quantity of lubricant to avoid the thermal deformations. The lubricant used during the machining has to be special to work with OFE copper, not to contaminate it. This lubricant has to be free of silicones and halogens.

Figure 7.22 shows the major vane once the rough milling process is finished.

**Annealing** Annealing is a stress relief heat treatment. A heat treatment to relieve stress generated during the rough mill operation is applied to each vane after the rough machining.

The heat treatment conditions are:

- Treatment in inert atmosphere, holding temperature between  $300^{\circ}\text{C}$  –  $345^{\circ}\text{C}$  over 3 hours, not surpassing  $345^{\circ}\text{C}$  in any case (e.g.  $320^{\circ}\text{C}$  is correct).
- Slow heating, slow cooling ( $< 50\text{K/h}$ ) down to  $< 150^{\circ}\text{C}$ .

**Pre finish operation** Finish the less important parts of the piece and prepare the important faces to finish.

**Finish operation** Finish with high precision all the functional faces (the modulation and the lean faces). In the two last steps the most important parameters are the control of the room temperature and



Figure 7.23: Major vane measuring with CMM

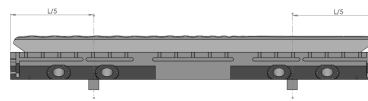


Figure 7.24: Major vane positioning

especially the clamping operation. It is really important not to generate deformations while the clamping operation and avoid thermal deformations in order to obtain a high precision piece.

### 7.5.2 Metrology

Once the machining is finished, the next step is to verify the dimensional and geometrical tolerances with a CMM (Coordinate Measuring Machine). It has been measured by Carl Zeiss S.A. in Elgoibar, Gipuzkoa (Spain). Figure 7.23 shows how the major vane is positioned.

To obtain the best results, the temperature of the room has to be controlled with  $\pm 1^\circ\text{C}$  precision, not to create deformation due to thermal conditions. The other important point is where the part is supported, as Figure 7.24 shows it has to be supported in a  $L/5$  distance from the both corners.

Once the positioning is correct and the temperature of the room is controlled and it is stable the part is ready to be measured.

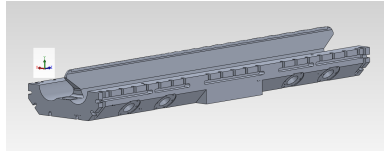


Figure 7.25: Axes definition

	01_Planitud_A	0.0339	0.0000	0.1000	-	0.0339
	02_Perpendicularidad_B1-A	0.0049	0.0000	0.1000	-	0.0049
	03_Perpendicularidad_B2-A	0.0085	0.0000	0.1000	-	0.0085
	04_Paralelismo_B1-B2	0.0144	0.0000	0.1000	-	0.0144
	05_Paralelismo_Cresta-B	0.0046	0.0000	0.1000	-	0.0046

Figure 7.26: Metrology report

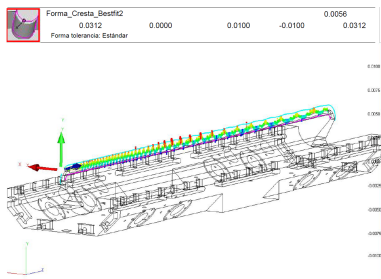


Figure 7.27: Modulation form error

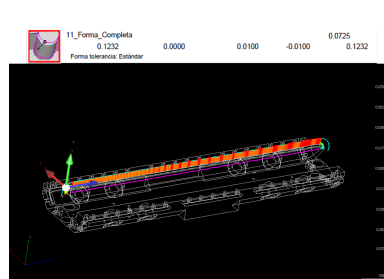


Figure 7.28: Modulation form and position in Y error

## Metrology results

Figure 7.25 shows the X, Y and Z axis to understand the metrology results. Just the more critical tolerances have been measured: The flatness of the important faces, the modulation form and the modulation position in the 3 axes.

**The flatness of the important faces.** The next small metrology report of Figure 7.26 summarises the flatness, perpendicularities and parallelism results of the faces.

**The modulation form.** Figure 7.27 shows just the form of the modulation, not the position of the modulation in the Y axis. The worst point measured is 15.6  $\mu\text{m}$  away from the ideal spline, 5.6  $\mu\text{m}$  out of tolerance.

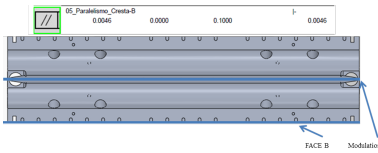


Figure 7.29: Parallelism between the modulation and the face B

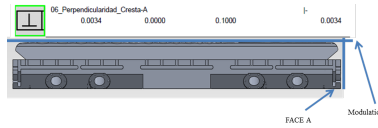


Figure 7.30: Perpendicularity between the modulation and the face A.

**The modulation position in Y axis.** Figure 7.28 shows the form of the modulation, and the position of the modulation in the Y axis. All the modulation is more or less 60 microns higher than the ideal position. In conclusion, adding the form deviation, the worst point is  $72.5\mu\text{m}$  away from the ideal spline.

**The modulation position in Z with the functional face.** Figure 7.29 shows the parallelism between the modulation and the face B, is in  $4.6\mu\text{m}$ . This excellent result ensured when the face B is correctly aligned, the modulation is well aligned too.

**The modulation position in X axis with the functional face.** Figure 7.30 shows the result of the perpendicularity with Face A and is also an excellent result. The perpendicularity between the modulation and the face A, is in  $3.4\mu\text{m}$ . This excellent result ensured when the face A is correctly aligned, the modulation is well aligned too in this direction.

### Conclusions of the manufacturing process

The main conclusions obtained of the manufacturing process are:

1. The error of the modulation form is acceptable.
2. The position of the modulation is too high in the Y axis. Nevertheless the position in the two other axes is excellent. This deviation could be corrected with another milling operation but for this test it has been considered a good result, if it happens in the final vane it would be remachined to achieve the correct height.

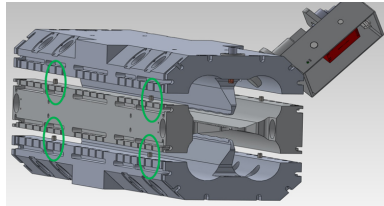


Figure 7.31: Insertion of the prism

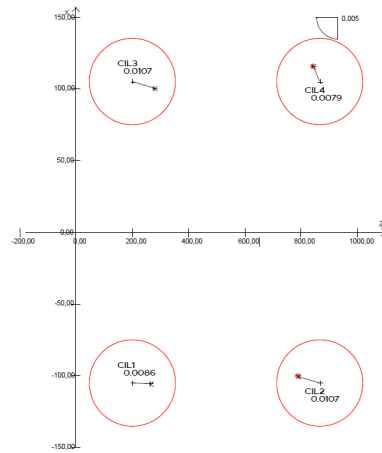


Figure 7.32: Metrology report. Alignment holes

3. Due to the deviation in Y axis, one possible conclusion could be the tool wear. In the next machining process some controls will be done to verify the tool wear during the manufacturing process.

### Cold model Alignment: Vane to vane alignment

For the vane to vane alignment two different options have been developed, alignment centred by pins and alignment in a tridimensional machine. The alignment centred by pins has been used in the cold model. 8 pins are used, to align the four vanes. The pins used to align the 4 vanes are 8 pins of  $\varnothing 8\text{m}6 \times 20\text{ mm}$  and the holes dimensions are  $\varnothing 8\text{ H}7$ . Figure 7.31 shows how the pins are inserted and fixing the vanes in the correct position.

The metrology measurement done to the first major vane, shows that it is possible to achieve this tolerances in the holes. Figure 7.32 shows the metrology results.

The value within the circles means the deviation of each hole. As the figure shows the worst deviation is of 0.0107 mm, just 0.7  $\mu\text{m}$  out of tolerance which is acceptable.



Figure 7.33: OFE machined vanes

Once the vane to vane alignment is done, this assembly is going to be measured in a tridimensional machine to verify the alignment capacity of this method.

### 7.5.3 OHFC Weld test Models

250 mm long 2 mayor vanes and 2 minor vanes have been already manufactured in the above mentioned machine for the Weld test models. Figure 7.33 shows the manufactured parts.

A metrology test has been done to one of the manufactured mayor vanes, to verify the precision capacity of the used machine. Figure 7.34, shows the measured values.

The metrology report shows good results. There are just 6 heights out of tolerances:

- COTA 1 PLN A = 4  $\mu\text{m}$  out of tolerance

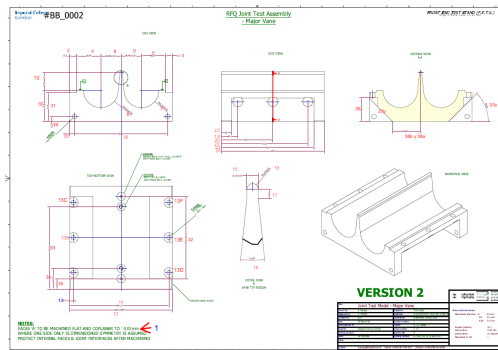


Figure 7.34: Major vane drawing

- COTA 9 CIR8 A CIR 9 (EJEX) = 4  $\mu\text{m}$  out of tolerance
- COTA 15 CIR 9 = 8  $\mu\text{m}$  out of tolerance
- COTA 15 CIR 9 = 4  $\mu\text{m}$  out of tolerance
- COTA 100 PLN TRASERO = 3  $\mu\text{m}$  out of tolerance
- COTA 32 CIR1 A CIR 4 (EJEZ) = 84  $\mu\text{m}$  out of tolerance

Just the last tolerance is out of tolerance, but it is not a critical cote. In conclusion, the major vane is an acceptable part.

As Figure 7.34 shows, in this case the major vane has not any modulation. To verify the manufacturing precision even in the modulation, a re-machining process will be done. A modulation, an input radial matcher and ecliptics radius in the final face will be manufactured in the existing major vane to verify the capacity of the machine in this machining processes. Figure 7.35 shows the last major vane.

The machined input radial matcher has the dimensions used for the cold model and the modulation corresponds to the first part of the cold model. In the finish face of the mayor vane an elliptical radius will be manufactured. This radius is to avoid any perturbations in the vane to vane gap leaved in the final mounting (see Chapter 4).

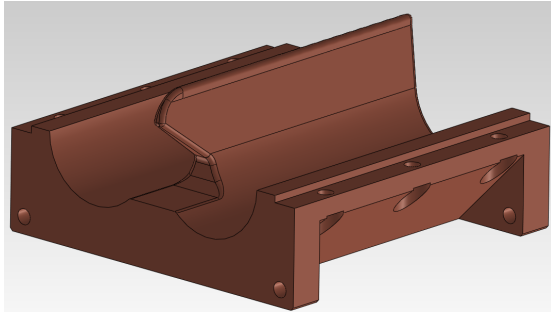


Figure 7.35: Weld test major vane with modulation

### Vane tip modulation

One of the Weld Test Major Vane has been re-machined to see the machines capacity adding the following changes:

- A vane tip profile (see Chapter 2)
- An input radial matcher (see Chapter 4).
- An elliptical shape gap section (see Chapter 3).

**Results.** The results obtained after doing the metrology can be summarised by means of two figures: Figure 7.36 shows the real position of the vane tip compared to the 3D model. The conclusion is that the average vane tip position is below the expected position (CAD model as reference). The worst point is 0.07 mm far away from the theory one.

Figure 7.37 shows just the shape of the vane tip, considering we are offsetting the reference position of the vane conveniently: i.e. If we move the references A and C the following values:

**Reference A** TransY  $-0.02658$  mm

**Reference C** TransZ  $-0.00944$  mm

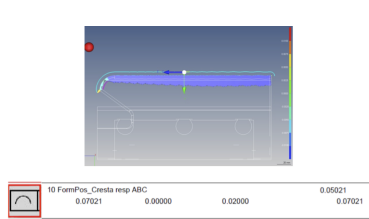


Figure 7.36: Form and position of the vane tip

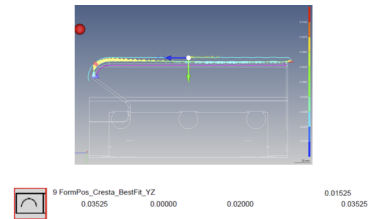


Figure 7.37: Form of the vane tip considering the best fit solution.

In this scenario, the achieved tolerances are better than expected; The vane tip is within the  $\pm 7.5 \mu\text{m}$  range. Nevertheless, there is some deterioration in the input radial matcher region. In this area the worst point is  $35 \mu\text{m}$  away from the theoretical one.

### Comparison between the metrology report before and after the re-machining.

The more unexpected displacement we observed is related to the flatness tolerance of face A. This flatness has worsened from  $10 \mu\text{m}$  to  $20 \mu\text{m}$ . Please note that such face has not been machined at this stage.

This worsening is due to the following reason: As part of the input radial matcher machining, internal stresses are generated in the piece, because it is clamped. When roughing this part of the piece although very small depths of cut are performed, internal stresses are generated in the material, as this is subjected to forces of a 18000 rpm rotating tool.

## 7.6 Vacuum requirements & design

### 7.6.1 Introduction

The pressure level in the RFQ is a critical issue to ensure that there will not be arcing between the poles, and to avoid beam losses due to Bremsstrahlung resulting from the collision of the beam with the residual gas on the accelerator [38]. To illustrate this, Figure 7.38 taken from Lisovski et

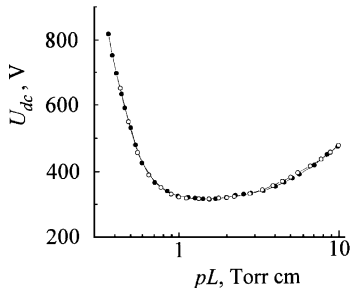


Figure 7.38: Electric breakdown potential as a function of pressure and electrode distance from [39].

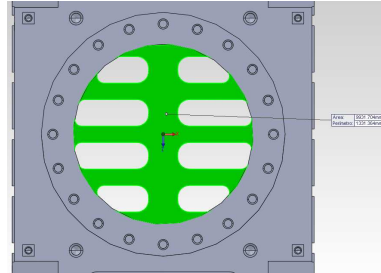


Figure 7.39: Pumping port for the RFQ, based on the ISIS/ FETS RFQ.

al [39] shows an example of how the minimum distance required to avoid high voltage arcing is related to the ambient pressure. The calculation of the minimum tolerable distance or the maximum electric field do not fall within the scope of this chapter, the figure is only presented as an example, and has to be noted that it is not applicable to the problem of an RFQ, for several reasons, amongst them the fact that the graph is only valid for DC fields, and for flat parallel plates. Both curved surfaces and alternating fields reduce the minimum field required for arcing for a fixed distance. All the calculations presented in this chapter are based on a maximum pressure of  $10^{-7}$  mbar within the cavity.

From the vacuum point of view, the supply of power in the form of radio frequency waves presents a problem, since the vacuum ports have to be partially obstructed to keep the energy within the cavity. However, these restrictions reduce the capacity of the pumping equipment to generate vacuum within the chamber. Given the complex geometry of the cavity, the vacuum conductance and the relative pressure profile of the cavity have to be calculated using a Monte Carlo based simulation tool, in this case all calculations were done using Molflow+ [40]. The procedure used to obtain the vacuum conductance of the structure from the simulation results, is the one proposed by R. Kresevan [41].

### 7.6.2 Calculations

The pressure of a chamber is related to the gas load  $Q$  and the effective pumping capacity of a system by

$$P = \frac{Q}{S_{\text{eff}}}. \quad (7.1)$$

By setting the total gas load to  $Q = 1$  and evenly distributing the gas source among the inlet facets of the simulation model, the previous equation is simplified and becomes

$$S_{\text{eff}} = \frac{1}{P}. \quad (7.2)$$

Since the installed pumping capacity is known, the conductance  $C$  can be calculated as

$$C = \frac{S_{\text{eff}} \times S_{\text{inst}}}{S_{\text{eff}} + S_{\text{inst}}}. \quad (7.3)$$

#### Simulation results

The shape of the RF grid at the pumping ports is shown in Figure 7.39. In this port configuration the open area of the port corresponds to approximately 52 % of the total area of a port of the same nominal diameter.

The results of the Molflow+ simulation is shown in Figure 7.40. For the simulation the temperature was set to 300 K, and the mass of the gas in the simulation was set to 2 amu. The software can only simulate a single gas at a time, but it is quite fair to assume that Hydrogen will be the most prevalent gas in the system at this point. The pressure is only calculated along the beam axis, because that is the most relevant point in the cavity. To be consistent, the pump capacity was set to 550 l/s, this is the quoted pump capacity for Pfeiffer's HiPace 700 turbo-molecular pumps, which will be used in the accelerator.

The normalised pressure profile can be extracted from the program, and a plot of the pressure along the beam axis is shown in Figure 7.41.

Using the equation presented in the previous section and the results from the simulation, the effective pumping capacity of a single segment is approximately 416 l/s, and therefore the conductance of the RFQ segment is approximately 264 l/s.

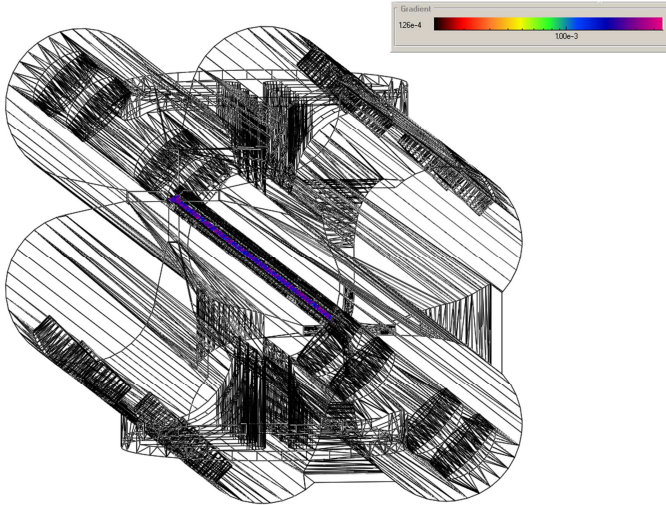


Figure 7.40: Results of the simulation of a segment of the RFQ.

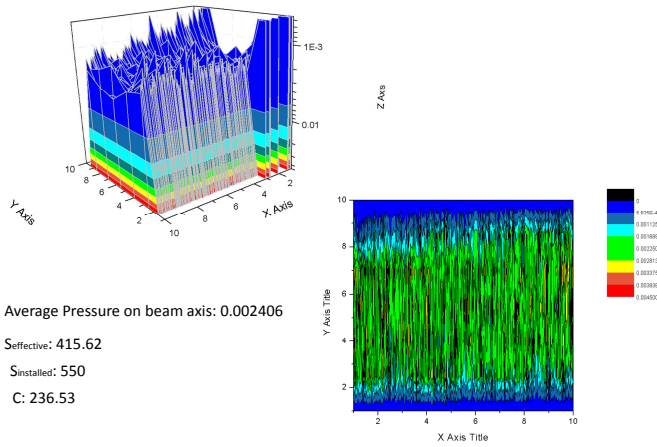


Figure 7.41: Normalised pressure profile along the beam axis.

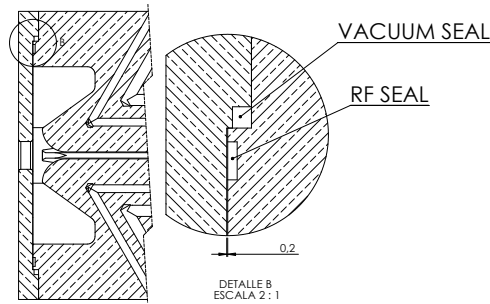


Figure 7.42: RFQ cross-section indicating the location for the vacuum and RF seals with both end plates.

### Pressure calculation

Rather than brazing the four sections that make up each segment of the RFQ, it was decided that the sections would be bolted together, and polymeric gaskets would be used between the sections. This strictly from the point of view of the vacuum, is a poor choice. The total leak rate of the RFQ will be much higher, than for a fully brazed structure. An approximate value for the leak rate can be calculated using the empirical formulas proposed by the National Air and Space Administration of the United States (NASA) for large volume vacuum chamber seal design guidelines [42], the surface desorption of OFHC copper without baking out is comparatively quite low.

Even with a very pessimistic leak rate, with the current design the pressure at the pump inlet will be of the order of low  $10^{-9}$  mbar, and the pressure on the beam axis at the inlet of the RFQ will be in the  $10^{-8}$  mbar range, which is the highest vacuum level achievable in structures with large polymeric gaskets according to NASA.

### 7.6.3 Conclusions

The current configuration of the RF grids on the vacuum ports and the pumping capacity of the pumps that can be installed on the RFQ are

sufficient to achieve the vacuum levels required. Any changes in the configuration of the vacuum grids that do not reduce the open area percentage will only result in an improvement of the conductance, and therefore a better vacuum in the RFQ.



**Part IV**

**Diagnostics**



# Chapter 8

## Mobile Test Stand

Injection of the proton beam exiting the RFQ into the Drift-Tube-Linac (DTL) requires some fine-tuning operations to optimise the beam transport performance of the accelerating chain. To such an avail, characterisation of the beam parameters at the exit of the RFQ is mandatory. Here, we describe the test stand MOTS (MOBile Test Stand) which has been designed to meet such requirements.<sup>1</sup>

Our design banks on previous experience gained from other accelerator laboratories (CERN, CEA-Saclay etc.) which have shown that it is possible to build a device equipped with a set of diagnostic tools to fully characterise the beam.

This chapter thus describes the beam properties that will be measured and presents a general layout of MOTS.

### 8.1 Beam parameters

The main goal of the RFQ is to accelerate a given beam current to 3 MeV. The DTL is designed to further accelerate an input beam entering the structure with this specific energy, and its efficiency will be dependent

---

<sup>1</sup> MOTS is designed to measure beams up to 12 MeV and will be used after the MEFT and first tank of the DTL; hence the stand is mobile.

upon the average energy and energy spread of the particle beams leaving the RFQ. In fact, the acceptance of the DTL is around  $\pm 0.2$  MeV around the nominal energy (See Figure 11 in [43]). The Time of Flight (TOF) method [44] will be implemented for the ion beam energy measurement.

The measurement of the beam current at the input and output ends of the RFQ will define its transmission. Sought values for this quantity for present-day RFQs are of 95 % or better. The three beam properties, current, energy and energy spread are the basic parameters of such a beam and ought to be measured accurately.

The next group of parameters are related to the *beam quality*. First, let's consider the emittances, which are proportional to the size of the beam in phase space. Its transverse components gives an idea on the beam size as well as its divergence in each direction perpendicular to the beam propagation. Large values for transverse emittance translate into more chances to lose particles by impact with the surrounding elements, thus reducing the transmission. For the beam energy range under consideration we envisage to measure the transverse emittance using a slit-grid system, and scanning the beam which goes through it [45]. In this scheme, the transverse emittance for both horizontal and vertical planes are done separately with one scan per single pulse. These set of measurements should be made as close as possible to the RFQ exit to avoid effects of space charge.

An slit will be the first device at the input of MOTS to reduce space charge effects and the beam divergence. Placing the slit in horizontal and vertical planes would sample a small slice of phase space. By using the profile monitor, a Secondary Electron EMision grid (SEM grid), at the end of the line, one can reconstruct the beam phase space and its transverse emittance. The slit should be able to scan through the whole beam width. The slit must stand considerable heat loads during the beam pulse.

The direct measurement of the longitudinal emittance is less common than that related to its transverse counterpart. In contrast, one can gain access into this quantity by measuring the bunch shape and the beam phase, which are easier to perform. It is also worth remarking that the value for the longitudinal emittance is related to the beam energy spread and the phasing of the particle with the RF signal. The acceleration of the particles is sensitive to this two parameters.

The energy spread measurement will be carried out in the spectrometer line with a system composed by a dipole plus a SEM grid. The grid is located at a certain distance from the centre of the magnet. The energy spread will be calculated from measurements of the beam sizes at the grid from knowledge of the local dispersion values.

The slit which is positioned at the entrance of MOTS can modify its aperture in order to cut out a small slice of phase space. At the SEM grid position the beam size is due to:

- The energy spread and divergence of the beam.
- The size of the opening at the slit and space charge effects after it.

Two Beam Position Monitors (BPM) made from sets of pick-up buttons or from stripline detectors are planned to be installed after the RFQ in order to accurately measure the position of the beam. Beam position and phase monitors will be essential instruments at the time of commissioning to measure:

- The absolute beam position and beam phase.
- The relative beam intensity between pick-ups.

The monitors should be located at positions along the test bench where the beam is not yet completely debunched.

## 8.2 Diagnostic instruments and layout

Table 8.1 lists the relevant beam parameters and their associated diagnostic instruments. Figure 8.1 shows a schematic view of the preliminary layout. The basic idea for such a layout is taken from Linac4's 3 MeV Test Stand [46]. The following remarks are of interest:

- Most of the diagnostic instruments are to be located as close as possible from the RFQ exit.
- The current is measured with an AC current transformer (ACCT). A second ACCT will allow us to measure any beam loss within MOTS.

Table 8.1: List of relevant beam parameters and associated diagnostic instruments.

Parameter	Instrument
Transverse plane	
Transverse position	Beam Position Monitors
Beam emittances	Slit-SEM Grid
Longitudinal plane	
Beam current	ACCTs and Faraday cup
Beam energy	FCTs and spectrometer dipole
Energy spread	Dipole – SEM Grid
Beam phase	Beam Position Monitor
Bunch shape	Bunch Shape Monitor

- To measure accurately the time at different positions for the TOF measurement, two Fast Current Transformers (FCT) are located with a separation of 1.0 m to 1.5 m.
- The energy measurement is cross-checked with the value from the spectrometer (dipole) measurement.
- The spectrometer is also used to measure the energy spread, because it converts a difference in energy into a difference in beam position at the SEM Grid. In this setup, quadrupoles are used to focus the beam on the SEM Grid.
- The transverse emittances are calculated varying the focusing of the quadrupoles and measuring the beam size in the SEM Grid located in the straight section.

The beam current and intensity, current pulse width, energy, profile and emittance are the main parameters of the beam which shall be measured and monitored in MOTS. The different diagnostics devices will be explained in the next subsections.

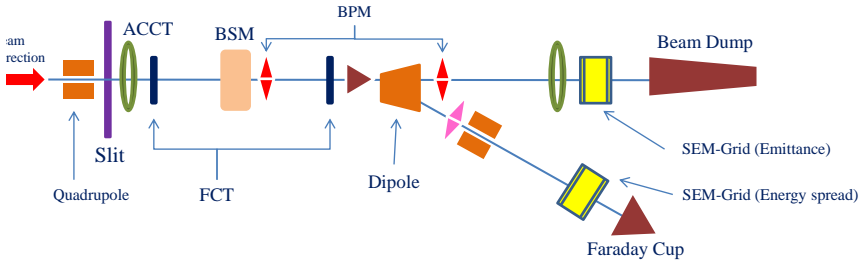


Figure 8.1: Schematic view of the MOTS layout (Image thanks to Seadat Varnasseri).

### 8.2.1 Position Monitors

A versatile and configurable electronics system [47] has been developed, in collaboration with the Electronics and Electricity department of the UPV/EHU, in order to miniaturise the beam position monitors and to meet all the requirements of the future Linac of ESS-Bilbao. At the same time, the design has been conceived to be open and configurable so that it could eventually be used in different kind of accelerators; independently of the charged particle with minimal change. The design of the Beam Position Monitors (BPMs) system includes a test bench for both pick-ups (PU) and striplines (SL), the Electronic Units and the control system (see Figure 8.2).

The Electronic Units consist of two main parts; an Analog Front-End (AFE) unit where the RF signals are filtered, conditioned and converted to base-band; and a Digital Front-End (DFE) unit based in an FPGA board where the base-band signals are sampled, with a high sample frequency of 105 MHz, in order to calculate the beam position, the amplitude and the phase. The AFE unit includes two in-house boards, a logarithmic amplifier for measuring the position of the beam and an IQ demodulator for measuring the amplitude and the phase. To manage the FPGA a Java interface has been also developed including the EPICS integration by means of JavaIOC and Archiver Instance.

To characterise the BPM system different beam conditions have been measured. Several tests have been performed at 175 MHz and 352.2 MHz. The results have been satisfactory, leading to resolution and accuracy

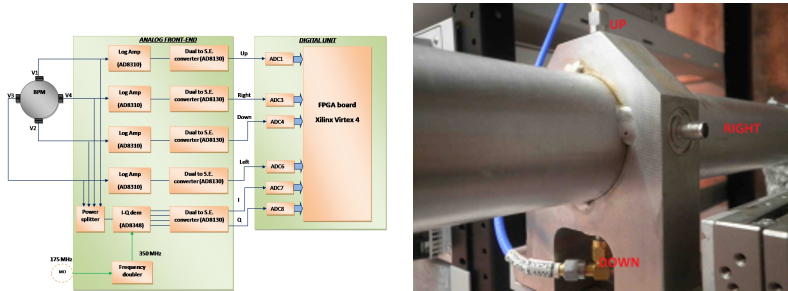


Figure 8.2: Schematic of the BPM electronics system (left) and test stand of the buttons BPMs of ESS-Bilbao (right).

values fulfilling the ESS-Bilbao requirements. The beam positioning system measurements depicts an stability of less than  $40\ \mu\text{m}$  for both continuous and pulsed wave mode. The position resolution is less than  $6\ \mu\text{m}$  for both modes, and the phase resolution is less than  $0.2^\circ$ .

## 8.2.2 Current Monitors

There are a variety of devices for beam current and charge measurement in accelerators. Current transformers (FCT, DCCT, ACCT, BCM,...) and Faraday Cups are the most common devices. Depending on the beam current, pulse width, rising and falling time, the appropriate device can be identified for the measurement system. In MOTS, two devices that meet the beam parameters, will be used: ACCT-HR and Faraday Cup. FCTs will be used for ion beam energy measurements through the TOF method.

### AC Current Transformers

ACCTs shall be installed permanently in the entry of the MOTS and can measure the beam current in the nominal values. Two ACCTs should be installed on the diagnostics test bench: one upstream of the dipole in the inline part and a second one in the spectrometer line. The devices need a magnetic shielding to avoid electromagnetic coupling with the pulsed magnets that may be close to the detectors.

A test bench for the ACCT (HR-Bergoz) [48] has been installed in the Control and Diagnostics laboratory (Figure 8.3 left). The results show that it can measure the beam current down to 0.1 mA and pulse width from 10  $\mu$ s to 2 ms without any drop [49]. However, larger pulse widths can be measured with a drop in the flat top of the pulse. The nominal bandwidth of the ACCT is 3 Hz and 300 kHz at the lower and higher cut-off frequencies. It is not possible to use FCTs alone to measure current pulse at MOTS. It is due to the low cut-off frequency of all the available FCTs. The lower cut-off frequency of the FCTs are so high, that makes them useless for accurate pulse width measurement of an ion source.

### Faraday Cup (FC)

For very low currents particularly during the conditioning of the accelerator, ACCTs can not measure the current amplitude. In this case a retractable Faraday Cup at the beam exit will give the information of the beam current and pulse. After amplification with a transimpedance current amplifier, a FC can measure currents of less than 1  $\mu$ A.

Apart from the beam current measurement, a FC could be used as a beam stop during conditioning of the beam for the protection of devices which are installed downstream of the vacuum chamber. The maximum energy of 3 MeV protons can be stopped by the FC; however due to high beam power and high temperature on the copper surface, it can not be used as a permanent beam stop. The beam average power up to 600 W and 10 kW pulse are the working ranges of the FC-100 [50] model from NTG. This model of FC is already in use at ISHN. A separate beam stop has been designed and will be installed for 3 MeV and higher energies.

### Fast Current Transformers

For the TOF technique two FCTs [51] from Bergoz with high bandwidth (up to 1.5 GHz) will be used. The high bandwidth of the FCT gives the possibility to have very short rise time and jitter, that is, of the order of nanoseconds. For MOTS, an in-flange type FCT is chosen; where the FCT is inserted between two standard flanges of the vacuum chamber (probably DN63), and does not require any extra shielding or ceramic insulation.

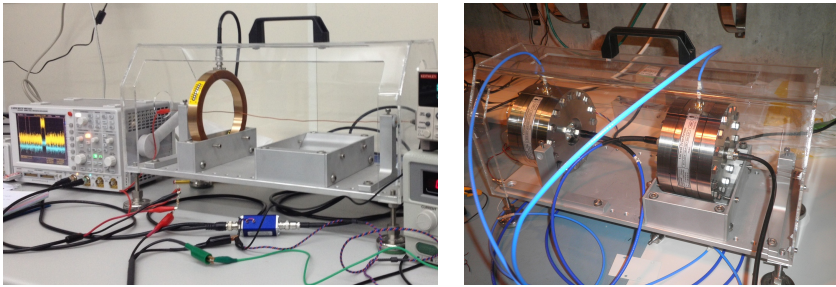


Figure 8.3: ACCT test (left) and FCTs assembled (right) in the test stand for current transformers.

In order to investigate and check the TOF method with FCTs prior the installation on the MOTS, one specific test bench has been installed at the Control and Diagnostics lab (Figure 8.3 right). The idea is to precisely measure the delay of signals coming out of the two FCTs sensors with sub-nanoseconds resolution and from this delay, calculate the velocity of particles and hence determine the energy of the beam. One coaxial cable with low attenuation is used to mimic the delay between two FCTs which is representing the time of flight of the beam between two FCTs. The overall length of the cable leads to a delay of 15 ns. Measuring the jitter and the accuracy of the signals will give us the resolution. The jitter values for the bunched beam are less than 50 ps. Specifically for a 352 MHz beam current of 40 mA, the rms value of the jitter is 11 ps. The accuracy of delay mean value for many consecutive pulses is measured to be 17 ps. The accuracy of delay mean value for a single pulse is 100 ps [52].

These values show that the TOF scheme with corresponding FCT specs could be implemented for the energy measurement with the required resolution. The whole setup for precise TOF measurements will be installed after the RFQ section, within which the beam is already bunched.

### 8.2.3 SEM Grid

There are variety of methods for the transverse profile measurement. Not all of them are suitable for ion linac beam profile measurement. The

scintillator monitor, SEM grid and the wire scanner are the most common systems. Scintillator monitors with TV camera and SEM grids are good candidates for MOTS profile measurement. Since the scintillator monitor is a destructive device which kills the beam during measurement, a SEM grid is proposed for the profile monitor of MOTS. Since the ion beam in MOTS has a maximum radius of 5 mm, then a SEM grid coverage of  $16 \text{ cm}^2$  with wire distances of 0.5 mm could be used. The diameter of the wires can be about  $100 \mu\text{m}$  in order not to deteriorate the beam emittance. Depending on the number of wires, the required number of I/Us and Mux channels will be selected.

In the framework of the ESS-Bilbao accelerator, with the collaboration of the Electronics and Electricity department of the UPV/EHU, a test stand for the development of SEM grids has been designed and manufactured as a part of the diagnostics system for beam profile measurements [53] (see Figure 8.4). This test stand is a vacuum system based on an EQ 22/35 electron source from SPECS used as a beam injector. This electron source has an energy range from 0 keV to 5 keV and a maximum beam current up to  $200 \mu\text{A}$ . Two prototypes of 16 Titanium wires (8 wires in each X and Y direction) of  $250 \mu\text{m}$  diameter and spaced 1 mm and 2 mm, respectively, have been built in order to develop an electronics readout system. The secondary emission current from each wire will be integrated and amplified to provide a significant voltage signal that can be measured by our acquisition system.

#### 8.2.4 Beam Shape Monitor

The Beam Shape Monitor (BSM) has been developed by Feshenko [54], and consists of a wire which can be inserted into the beam. Secondary electrons created through the interaction of the beam with the wire are accelerated by HV applied to the wire. The electrons pass through an input collimator and are deflected by an RF deflector whose RF pulse is synchronous with the accelerating RF. The deflected electrons pass through an output collimator and are detected by an electron detector. The phase of the deflecting field can be shifted to scan the longitudinal intensity distribution of the incoming beam. The BSM will be able to monitor the full 1.5 ms pulse and the maximum peak current (75 mA after the RFQ).

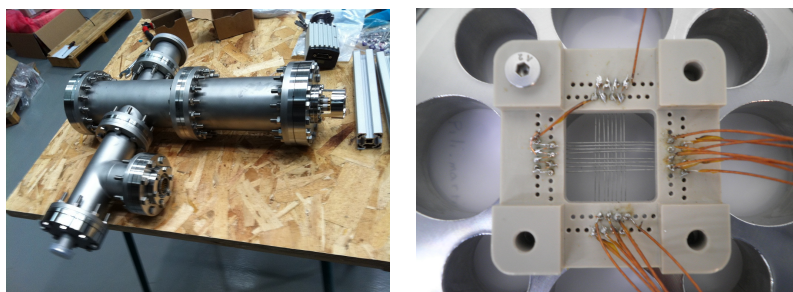


Figure 8.4: Vacuum test stand for SEM grid (left) and first prototype of SEM grid of ESS-Bilbao (right).

### 8.3 Diagnostics Control system

ESS-Bilbao Control group has proposed an ITER CODAC like control system. This type of Control supposes four independent control networks: Control (CN), Interlocks (IN), Timing (TS) and Human Safety (HS).

The goal of this methodology of control is to maintain independence between the Control itself, the interlocks to protect the machine, the timing and synchronisation processes and the safety of the personnel.

The Figure 8.5 presents the General Control scheme. Three layers, Local, Middle and Control Room, can be distinguished.

The Local layer contains all the accelerator structures and the auxiliary systems (vacuum, refrigeration, electrical power,...). Each local system is divided into the control networks mentioned above and connected to them.

The Middle layer is in charge of:

1. Control and monitor each network independently.
2. Relate the networks if necessary.
3. Format the data to be accessible for the next layer.

Finally, the Control room layer deals with the relation between operators and machine and with the data logging.

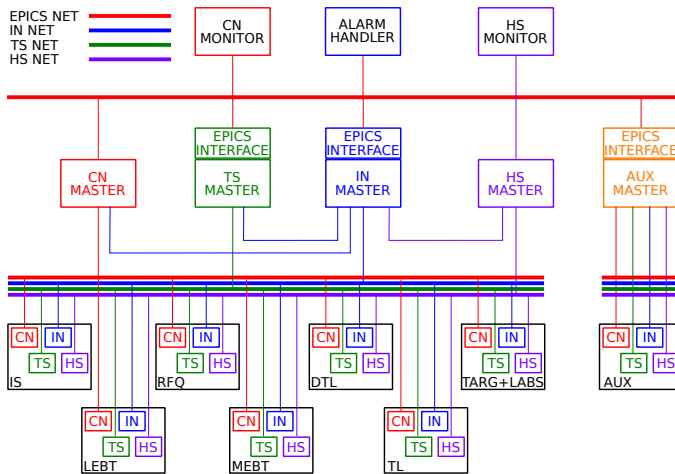


Figure 8.5: General control scheme.

Since the scope of this chapter refers to MOTS, only the local layer is described. Besides, this document is focused on the diagnostics to be installed.

### 8.3.1 Position Monitors

Position monitors have their own control made with a multipurpose controller (MC). This controller has the capacity to integrate this diagnostic into the EPICS network. Therefore, this MC is going to be in charge of the control.

### 8.3.2 Current Monitors

As it has been done both at laboratory tests and at ISHN and ISHP, the currents which come from the ACCTs are planned to be measured with a FPGA card installed into a PXI chassis. The same method will be used to capture the current from the transimpedance amplifier of the FC.

The case of the FCTs is different because they are used to measure the beam energy. Hence, a high time resolution (about 1 ns) is needed. It is

important to note that the time measurement is relative and not absolute. This implies that it is not necessary to associate a timestamp to each measurement. In this way, an oscilloscope can be installed in order to perform the measurement. Then, this device has to be integrated into the EPICS network. Such a process could be done controlling the oscilloscope with LabVIEW and publishing the required variables through an EPICS server.

### **8.3.3 Slit**

At the moment, the slit is not fully specified and, therefore, no control device has been designed. Probably, the device's hardware will be enough to be integrated in the PXI. If it is not the case, the hardware will be enhanced with other cards to fulfil the requirements.

### **8.3.4 SEM Grid**

The controller for the SEM Grid is already in the laboratory and consists on a PXIe with very precise acquisition cards and synchronisation features.

### **8.3.5 Beam Shape Monitor**

From the control point of view, the case of the Beam Shape Monitor is the same as of the slit. It will have its own electronics and control. Therefore, the control effort should be small and the integration into the PXI easy.

**Part V**

**Design Update 2015**



## Chapter 9

# Introduction and scope of the design update

On July 2013 the design of the ESS-Bilbao RFQ was presented to a Technical Advisory Committee (TAC) of international experts on RFQ design and operation. The subsequent review of the design options and the comments and recommendations issued by the TAC have been duly analysed and have fructified in a new design of the RFQ (RFQ-2014). Although some design options have been kept from the RFQ-2013 design (notably the round shaped cross section and the bolted assembly process), these options have been discussed and the decision to choose them more documented.

In this document the main points raised out by the TAC in the 2013 review document are discussed. The work done during 2014 by the ESS-Bilbao RFQ team on the critical points is described in details. For this reason, this document should not be taken then as a complete RFQ Technical Design Report, but on the contrary have to be taken as complementary to the previous report and the reviewers comments.

The report represents an important milestone in our way to understand and control a structure as complex as an RFQ. The pertinent comments and suggestions issued by the Technical Committee have contributed very strongly to direct our efforts in the right directions and to improve our

knowledge on RFQs and our confidence on the design and operation of the device. So this document is not a presentation of a final and closed design. Still much work must be done in certain areas to reach the final target of a successful RFQ operation.

The structure of this report is then to provide adequate answer to the main concerns and question raised by the TAC members. Each section has tried to summarise our efforts in this direction.

## 9.1 Summary of the technical aspects recommended by the Technical Advisory Committee

The main points and recommendations are summarised in the following list:

- **Reduce the injection energy.** The input energy of the RFQ has been reduced from 75 keV to 45 keV (section 10).
- **Shorten the RFQ by 20 %.** The new modulation has a length of 3.09 m, much shorter than the 3.90 m of the 2013 design (see section 10)
- **Use the 2-term potential function to define the modulation.** The new modulation uses the 2-term potential function. A deep analysis of the 2-term vs sinusoidal modulations have been done (see section 10).
- **Independently prove the viability of the proposed vacuum and RF gaskets design.** An aluminium model has been built to test the vacuum gasket design. Preliminary results are successful (section 14). Work on the RF seals will proceed during following months.
- **Review the dynamic control options.** The mechanical tuners option for dynamic control has been substituted by a combination of static plunger tuners and a dynamic control provided by the water cooling.

A subsequent analysis of the 3D RF design and behaviour has also been done (see sections 11 and 13).

- **Develop a mathematical model of the cavity to better understand the effects of perturbations.** This model has been developed and has been used in the tuning strategy design. Detailed FEM simulations have also been done on this subject (section 11).
- **Extend the cold-model to at least 2 segments.** This recommendation has not been implemented, as there is no time in our schedule to perform it. Nevertheless, the model built to test vacuum gaskets is planned to be attached to the aluminium cold model to test vacuum performance with a cavity to cavity connection.
- **Pursue a single power coupler prototype.** Only one of the prototypes described in the previous document is going to be considered for the RFQ.
- **Generate a commissioning plan from which you can derive the required diagnostics.** This plan has been done and is described in section 15.



## Chapter 10

# Modulation design and beam dynamics

This section deals with the modulation design and beam dynamics results of the ESS-Bilbao RFQ. In the 2013 TDR we presented a modulation which the Committee of experts found to have margin for improvement in some areas. As a consequence of these recommendations, we have changed some aspects of the design, thus reaching our current working modulation. This new design has been extensively studied, both in terms of beam dynamics performance and robustness to non ideal operating conditions, and fulfils all the goals set by the Committee. The modulation redesign process is described in detail in the following sections.

### 10.1 Characteristics of the previous design

The modulation presented in the 2013 TDR, coded 11.4, was created using Alan Letchford's RFQSIM. Table 10.1 summarises its main characteristics.

Modulation 11.4 was designed for a beam input energy of 75 keV (which at the time was the intended energy for our ion source) and 60 mA of peak current, with a transverse rms emittance of  $0.25 \pi$  mm mrad (which

Table 10.1: Main characteristics of modulation 11.4, presented in the 2013 TDR.

Parameter	Value
Particle	Proton
Input energy	75 keV
Voltage (constant)	85 kV
Beam current	60 mA
Input transverse emittance	$0.25 \pi$ mm mrad
Modulation shape	Sinusoidal
Length	3.9 m ( $4.58\lambda$ )
Number of segments	5
Transmission (4 different codes)	91–95 %
Kilpatrick factor	1.77

would account for a  $\sim 0.05 \pi$  mm mrad growth along the LEBT, starting with a predicted  $\sim 0.20 \pi$  mm mrad in the ion source).

The modulation presented a total length of 3.9 m ( $4.58\lambda$  at an RF frequency of 352.2 MHz). It was composed of 280 regular cells of sinusoidal shape, plus a transition cell and circular matching section at each end.

The beam dynamics simulations were performed with four different codes (RFQSIM, GPT + Multipoles, TOUTATIS, and GPT + Comsol), achieving 3 MeV transmissions in the range of 91 – 95 %, with acceptable transverse and longitudinal emittances. The maximum surface field, obtained by means of cell-by-cell finite element simulation with Comsol, was found to be 32.6 MV/m (1.77 times the Kilpatrick limit), located at the end of the Shaper section.

## 10.2 Recommendations of the review Committee and changes implemented

In their review report, the Committee made the following main recommendations concerning the design of the modulation:

- **Lower injection energy:** The Committee found the input energy to be unnecessarily high, and therefore recommended lowering it to

45 keV, in consonance with other recent RFQ designs with similar overall characteristics. Although this is not strictly an RFQ design decision, but rather a requirement to be met, it demands the design of a new modulation.

- **Shorter modulation:** In the Committee's experience, an RFQ with a length over  $4\lambda$  is harder to tune. Therefore, they recommended shortening the modulation by  $\sim 20\%$ , which carries the additional benefit of a reduced cost. The above recommendation of lowering the input energy should have a clear positive impact on the length reduction.
- **Modulation shape based on 2-term potential:** The Committee recommends changing the longitudinal shape of the cells to follow the 2-term potential function. Although the reason is not fully understood why, it seems that the sinusoidal shape produces a higher variation of the quadrupolar mode resonance frequency along the vanes, which in turn results in a harder to tune RFQ.

The following sections describe the changes that we implemented in the modulation design procedure, in order to meet the recommendations presented above.

### 10.2.1 Injection energy

The new modulation search has been carried out for an input energy of 45 keV. However, contrary to the Committee's prediction, we found that it did not contribute to shorten the modulation, provided the goal performance (transmission, surface field, etc.) was kept the same.

The widely stated principle is that some length is saved due to a lower value for  $\beta\lambda/2$  in the early bunching cells (Shaper and beginning of the Gentle Buncher). However, the cell length difference between 45 and 75 keV is just 1.2 mm. Even if this gain was roughly the same over the first 100 cells, it would only account for a total save of 12 cm. On the other hand, one still needs some length to account for the energy gain between 45 and 75 keV, which will typically take a few centimetres too. In the end, these effects nearly cancel each other out, so the total length, which depends

much more strongly on other design strategies, turns out to be very similar. In a recent conversation with Lloyd Young, he agreed with these findings, and confirmed to have observed the same cancelling effect over his many years of experience in designing RFQs.

### 10.2.2 Modulation length

The high accuracy CNC workshop where ESS-Bilbao RFQ vanes are expected to be machined can fit pieces up to 80 cm. Therefore, a total length shorter than 3.20 m would be very convenient, allowing us to make the RFQ with only 4 segments. We have finally assumed a maximum length of 3.10 m as a design goal, leaving some space for possible modifications of the high energy end.

Having found no significant length decrease by lowering the input energy, the job of achieving the goal length relied on two combined strategies:

- Selection of some design parameters mostly oriented towards decreasing the modulation length, with preference over other goals, such as maximising the transmission or maintaining a conservative Kilpatrick factor. As an example, compared to the design presented in the 2013 TDR, we concentrated the parameter space search on areas with lower clear aperture  $a_{gb}$  and energy  $W_{gb}$ , and less negative synchronous phase  $\phi_{gb}$  (all referred to the end of the Gentle Buncher). Particle tracking results obtained with RFQSIM presented worrying transmissions below 90 % for modulations found in this region of the parameter space. However, later simulations with other codes presented much better results (see section 10.4). This strategy also produced higher surface fields, with a peak at the end of the Shaper typically above 1.8 times the Kilpatrick limit.
- Progressive reduction of the aperture in the Acceleration section. RFQSIM originally built the 2-term based Acceleration section using a constant aperture and modulation factor, following the rules proposed by Kapchinskiy-Tepliakov. This produces slowly decaying fields along  $z$ , due to the increased cell length. We modified the part of RFQSIM that creates the 2-term modulation to incorporate custom aperture reduction strategies in the Acceleration section, as well as

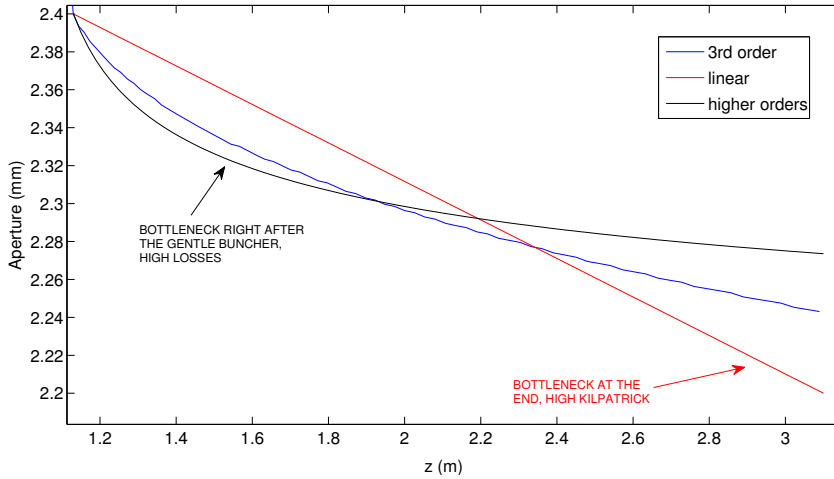


Figure 10.1: Three different shapes of the aperture  $a$  along the Accelerator section, with a certain total length ( $\sim 3.1$  m in this example) set as a constraint.)

the ability to set a goal total length for the modulation. Figure 10.1 illustrates the effect of different aperture reduction strategies on the transmission and surface field. Basically, if the aperture is reduced linearly (red curve), the goal length can only be achieved with a steep slope, which creates a very undesired bottleneck at the high energy end, resulting in an increase of the particle losses and the surface field. The opposite strategy would be to decrease the aperture very fast at the start of the Acceleration section and more slowly onwards (black curve), but the bottleneck is now created right after the Gentle Buncher, where most of the transverse losses typically take place. After exploring many strategies, we found a good compromise with a function for the modulation factor in the form of:

$$m_i = m_{i-1} + K/m_{i-1}^3, \tag{10.1}$$

where the index  $i$  denotes the cell number, and  $K$  is a constant that must be solved numerically to meet the total length constraint. This function is represented by the blue curve, which can be seen to

avoid narrow bottlenecks at both ends of the Acceleration section, thus minimising the transverse losses. The aperture at the end of the modulation is such that it will typically create a second local maximum in the surface field. One of the design constraints is to produce a modulation in which this second maximum is as close as possible to the peak at the end of the Shaper, in order to optimise the length reduction without increasing the surface field set by the first peak. Figure 10.4 (in section 10.3) depicts this new shape of the surface field curve.

### 10.2.3 Modulation shape

We have investigated the effect of the modulation shape on the frequency flatness. The sinusoidal modulation of the 2013 TDR produced a quadrupolar resonance frequency variation along the RFQ of  $\sim 1.5$  MHz. After some conversations with Ken Crandall and Lloyd Young, we have come to the conclusion that the conditions to achieve a flat resonance are 1: longitudinal profile of the modulation following the 2-term function, and 2: constant  $\rho/R_0$  along the whole length.<sup>1</sup> This is due to the fact that the stated conditions produce a flat capacitance per unit length, which is not ensured otherwise [55].

The correspondence between the resonance frequency of the quadrupolar mode and  $\rho/R_0$  can be observed in Figure 10.2, obtained from a 2-term based modulation with constant  $\rho$  and varying  $R_0$  (deliberately enlarged to magnificate the effect). The similarity between the  $R_0(z)$  and  $\text{freq}(z)$  curves is notable.

As a consequence of these findings, we have followed the recommendation of the Committee and aimed for a 2-term modulation with constant  $R_0$  and  $\rho$  in our new modulation search. This demanded providing RFQSIM with the ability to deal with 2-term modulations, as it was originally written for sine-like cell shapes. We had to modify the code that creates the preliminary 2-term modulation, as well as the multipole expansion calculation and the further geometry modification to account for the higher

---

<sup>1</sup> Of course, any other arbitrary shape for the modulation can in principle have its frequency flatness corrected by carefully tuning the cavity parameters for each cell. However, with the 2-term potential, constant  $R_0$  and  $\rho$  result in a flat frequency profile straightforwardly.

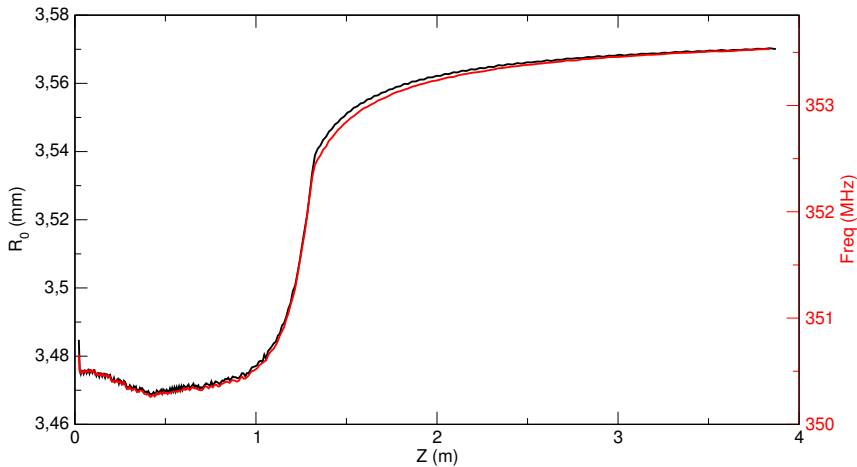


Figure 10.2: Mean aperture  $R_0(z)$  (left axis) and resonance frequency of the quad-polar more (right axis), plotted along the longitudinal direction. With a careful selection of the scale, both curves are almost identical in shape.

order pole terms. The cell shape is now solved numerically, since  $x(z)$  and  $y(z)$  cannot be deduced analytically from the 2-term potential expression. The new features added to the code seem to work fine, and we have successfully used RFQSIM to create the new ESS-Bilbao modulation, which is presented in the next section.

### 10.3 New design: modulation 15.7.3.19

We have performed a search of the parameter space with RFQSIM, applying the procedures and constraints explained in the previous section. Since we have added the possibility of specifying a maximum modulation length to the code, all the studied versions met the requirement of  $L < 3.10$  m. Therefore, the preliminary evaluation of the candidates was based on beam dynamics simulations performed with RFQSIM itself, and surface field values of both peaks (end of the Shaper and last cell), obtained from finite element calculations carried out in COMSOL.

Table 10.2: Main characteristics of modulation 15.7.3.19.

Parameter	Value
Particle	Proton
Input energy	45 keV
Voltage (constant)	85 kV
Beam current	60 mA
Input transverse emittance	$0.25 \pi \text{ mm mrad}$
Modulation shape	2-term
$R_0$ (constant)	3.44 mm
$\rho/R_0$	0.85
Number of cells	273
Length (without high energy end)	3.09 m ( $3.63\lambda$ )
Number of segments	4
Transmission (4 different codes)	87–94 %
Kilpatrick factor	1.85

The main characteristics and design parameters of the selected new modulation, coded 15.7.3.19, is presented in Table 10.2. The total length (without the high energy end, that is, final transition cell + output matcher) is 3.094 m ( $3.63\lambda$ ), 80 cm shorter than the modulation presented in the 2013 TDR. The 3 MeV transmission, calculated with 4 different codes, is in the range of 87–94 %, although the results are very unevenly distributed along that range: while RFQSIM gives a result of 87 %, the other three codes (TOUTATIS, GPT+COMSOL and PARMTEQ/RFQGen) present transmissions very close to 94 %. This will be discussed in more depth in section 10.4.

Figure 10.3 presents the evolution of some parameters along the vanes. The end of the Gentle Buncher and start of the Accelerator can be clearly identified at cell number 193. Compared to the 2013 modulation, this design presents a mean cell radius  $R_0$  about 0.5 mm larger, a narrower clear aperture  $a$ , a notably higher acceleration efficiency  $A$ , and a slightly higher (and more constant) focusing factor  $B$ .

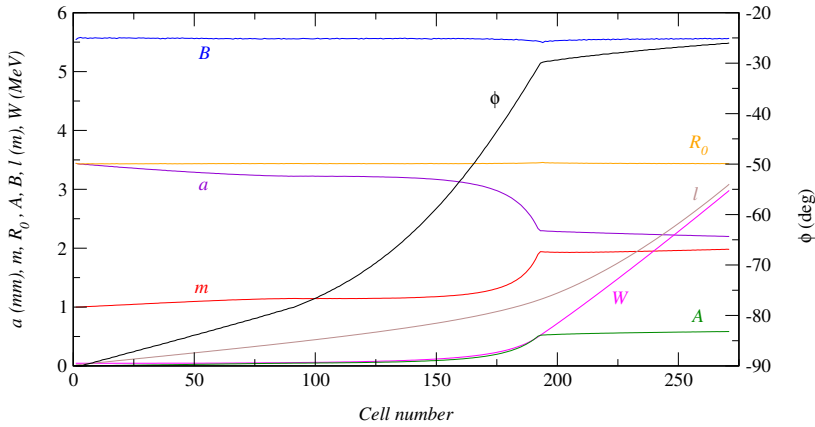


Figure 10.3: Evolution of several modulation parameters as a function of the cell number.

The present curve only covers the Input Matcher and all the regular cells (i.e. with a length of  $\beta\lambda/2$ ), as created by RFQSIM's modulation generator. The high energy end will be composed by two custom shaped additional cells: a transition cell of 17 mm that brings the modulation from either  $a$  or  $ma$  to  $R_0$ , and a circular Output Matcher with a radius of 14 mm (identical to the Input Matcher), bringing the length to a total of 3.12 m. The combination of these two cells creates a nearly circular beam at the output of the RFQ, with similar betas and very small alphas ( $\alpha_x$  being slightly over 0 and  $\alpha_y$  slightly below 0). This beam produces an optimal matching into the current MEFT design, resulting in a 100 % transmission through the DTL, according to the simulations [56].

Figure 10.4 depicts the evolution of the maximum surface field per cell (left axis) and local frequency of the quadrupolar mode (right axis). The surface field curve presents, as explained before, two local maxima taking place at the end of the Shaper and at the last cell. Both values are very close to 34.1 MV/m, which equals a Kilpatrick factor slightly below 1.85 at our working frequency. Although this is above the design value of 1.8 typically used as reference, several RFQs have been recently designed with similar values, such as CERN's LINAC<sub>4</sub> with 1.84 [57] and Los Alamos' LEDA,

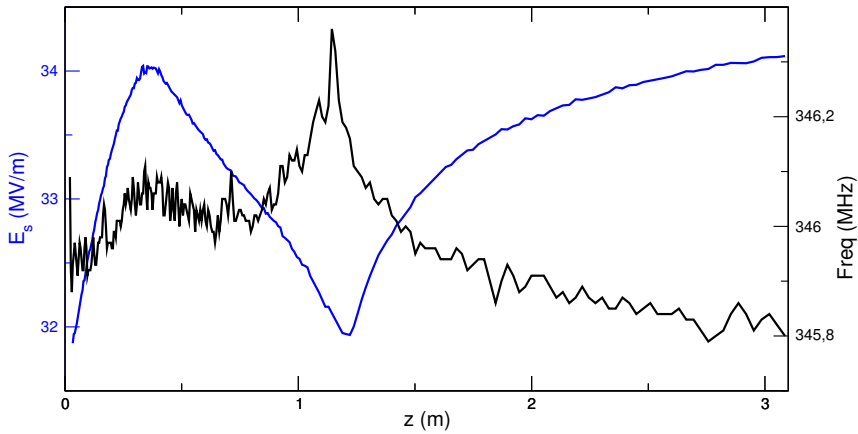


Figure 10.4: Evolution of the maximum surface field (blue curve, left axis) and the resonance frequency of the quadrupolar mode (black curve, right axis), along the modulation.

which was designed for 1.8 but successfully operated at 2.0 [58]. Besides, if sparking issues were to be found at nominal conditions, the power could be lowered to safer values with very little impact on the particle transmission, as the results presented in in section 10.5 will demonstrate.

The resonance frequency presents a maximum variation of about 500 kHz along the vane, which is three times smaller than the 1.5 MHz variation presented in the 2013 TDR. However, most of the cells lie in an interval of  $\sim 300$  kHz, with a narrow region at the end of the Gentle Buncher presenting a slightly higher resonance frequency. This is due to the  $R_0$  curve having the exact same shape as the resonance frequency (as demonstrated in Figure 10.2), having lost its perfect flatness in the geometry adjustment performed by RFQSIM after the multipole expansion. Since  $\rho$  is designed to be constant to simplify the machining process, the small variation in  $R_0$  is reflected in  $\rho/R_0$ . In any case, if this deviation was to be corrected by adjusting  $\rho(z)$  accordingly, it would require a maximum correction of 16 microns from the current value, which is well below the machining tolerance.

## 10.4 Beam dynamics results

We have subjected our current modulation design to the same degree of testing implemented for the previous one, which involves performing beam dynamics simulations with a wide range of codes. These simulations have been performed under the same basic conditions (45 kV beam, 60 mA of current,  $0.25 \pi$  mm mrad of transverse emittance). The C-S parameters of the input beam varied slightly from code to code, depending on the optimal match calculated in each case, with alphas typically a little above 1, and betas about 0.03 m/rad.

We have performed beam tracking simulations with four different codes. Three of them (RFQSIM, TOUTATIS, GPT + COMSOL) were also used in the 2013 design (chapter 2), and a description of each method can be found in the corresponding report [59]. We have included an additional code, RFQGen, an improved fork of PARMTEQ written by Lloyd Young. However, the implementation of our design in RFQGen is not completely accurate, since this code does not include an option to import a cell-by-cell description of the modulation.<sup>2</sup> Therefore, our approach has been to let RFQGen create a modulation starting from the same input parameters and constraints used in the original design performed with RFQSIM. The resulting modulation, although very similar, is not identical to our working design. In consequence, the current RFQGen results must be considered as orientative.

Table 10.3 presents the main results of the particle tracking simulations. The accelerated ( $\sim 3$  MeV) beam transmissions of TOUTATIS, GPT + COMSOL and RFQGen are almost identical ( $\sim 94\%$ ), and comparable to the results achieved with the previous 2013 modulation (91–95%, depending on the code used). The emittance results are very positive, with virtually null increase of the transverse emittance, and a value of 0.12–0.13 deg MeV for the longitudinal emittance (similar to that of much longer designs, focused on achieving a low longitudinal emittance [60]). The surface fields, while not identical (they are calculated by different approaches), lie within 1.81–1.85 times the Kilpatrick limit.

---

<sup>2</sup> Lloyd Young is currently working on implementing that feature, so we expect to be able to build and simulate our exact modulation with RFQGen soon.

Table 10.3: Simulation results at the output of the RFQ for the four methods used. The figures of merit are: full transmission (%), accelerated transmission (%), transverse normalised rms emittance ( $\pi$  mm mrad) calculated as the average between the horizontal and the vertical values, longitudinal rms emittance ( $\pi$  deg MeV) and maximum surface electric field (MV/m).

Simulation method	$T_{\text{all}}$	$T_{\text{good}}$	$\epsilon_t$	$\epsilon_z$	$E_s$
RFQSIM	90.7	86.8	0.243	0.120	30.4
TOUTATIS	94.6	93.6	0.266	0.131	33.4
GPT + COMSOL	95.2	94.1	0.264	—	34.1
PARMTEQ/RFQGen	96.2	94.1	0.241	0.125	33.7

RFQSIM, however, gives a poorer transmission than the other three codes, which is mainly due to a predicted transverse loss of almost 10% of the beam. We have investigated this effect, but no definitive conclusions have been drawn. In any case, we are confident that the other three codes represent the actual transmission of the RFQ more accurately, given that:

- TOUTATIS and RFQGen (PARMTEQ) are the most widely used codes in the field of RFQ beam dynamics.
- The field map provided by COMSOL comes from a very accurate finite element simulation, performed on the *actual* 3D vane model that will be machined. The tracking is then performed with GPT, a code extensively used in beam dynamics simulations of other accelerator elements.

Since, as explained above, the RFQGen simulation was not carried out with our exact working modulation, all the results presented from now on will be restricted to TOUTATIS and GPT + COMSOL.

Figure 10.5 shows the transverse losses (due to particles impacting with the vanes) along the RFQ, by depicting the beam power lost per centimetre of length. The curves are very similar in the Shaper and Gentle Buncher regions (first 1.2 m), with slightly higher power loss predicted by GPT + COMSOL in the Acceleration section. The total power lost (integral

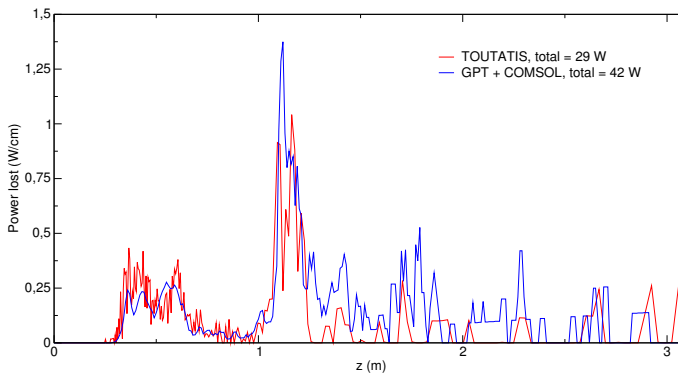


Figure 10.5: Beam power loss per centimetre of RFQ length, simulated with two different methods.

of the curves) remains within reasonable values in both cases, since most of the lost particles impact the vanes with energies in the hundreds of keV.

In summary, the results presented above prove the validity of the proposed vane modulation in terms of beam dynamics, as tested with different particle tracking and field map calculating methods. Although some of the new design constraints (especially the  $\sim 20\%$  length reduction) were initially expected to reflect negatively on the beam transport performance, this is only apparent in the RFQSIM results, with the other three codes presenting transmissions of  $\sim 94\%$ . Moreover, the emittance results (both transverse and longitudinal) are much better than those of the 2013 modulation.

## 10.5 Beam dynamics under non ideal conditions

We have examined the effects of varying certain simulation parameters, which allows us to predict the behaviour of the RFQ when operating under non ideal conditions. As argued in the previous section, we have done this study with TOUTATIS and GPT + COMSOL.

Figure 10.6 (a) presents the 3 MeV transmission as a function of the input peak current. The results for both codes are very similar along the

whole current range. The captured transmissions remain close to 100 % at low current conditions, and only drop below 90 % above 75 mA.

In order to understand how the RFQ transmission depends on the input beam geometry, we conducted a study in which the Courant-Snyder parameters  $\alpha_x$ ,  $\alpha_y$ ,  $\beta_x$  and  $\beta_y$  were scanned along a wide range of values. We used the beams thus created as inputs to particle tracking simulations performed with TOUTATIS (chosen over the other codes due to shorter computation times). In particular, we were interested in the transmission dependence on the input beam angle, due to some concerns expressed by the panel of experts during the 2013 TDR. In figure 10.6 (b) we plot the best 3 MeV transmission obtained for each value of  $\alpha_x$ . Although the other Courant-Snyder parameters for each beam are not plotted, they all fulfil  $\alpha_y \simeq \alpha_x$  and  $\beta_x \simeq \beta_y \sim 0.3$  m/rad.

The curve shows a maximum transmission for  $\alpha_x \sim 1.4$ , which in our conditions corresponds to an input beam rms angle of  $\sim 50$  mrad. However, the results for much lower values of  $\alpha_x$  are still acceptable, with transmissions over 90 % for  $\alpha_x \geq 0.75$  ( $\simeq 35$  mrad). Although we are confident that our LEBT should be able to provide the desired values for  $\alpha_{x,y}$ , this study predicts a small beam loss in case of having to moderate the input beam angles. Besides, the other three codes achieve their best transmissions for  $\alpha_x$  values much lower than the 1.4 preferred by TOUTATIS ( $\sim 1.1$  for RFQSIM,  $\sim 1.12$  for PARMTEQ/RFQGen,  $\sim 1.15$  for GPT + COMSOL).

Figure 10.7 (a) presents the 3 MeV transmission as a function of the vane-to-vane voltage. Although the voltage cannot be directly controlled or measured in operation, the interest of this study lies in the fact that it serves as a multiplier to the electric field, with obvious implications in the transport and focusing abilities, as well as the appearance of sparking problems. Starting from 90 kV, the transmission decreases quite slowly until  $\sim 80$  kV, after which it drops dramatically. Dropping the voltage from 85 to 82 kV would allow us to decrease the Kilpatrick factor from 1.85 to 1.78 (using COMSOL's estimation for our maximum surface field), while keeping the transmission above 90 %.

Figure 10.7 (b) depicts the 3 MeV transmission as a function of the input beam energy. Both present very similar results above the nominal value of 45 keV, but GPT + COMSOL predicts poorer transmissions for lower input energies. The 90 % reference value is achieved in the range of 43.5–47 keV,

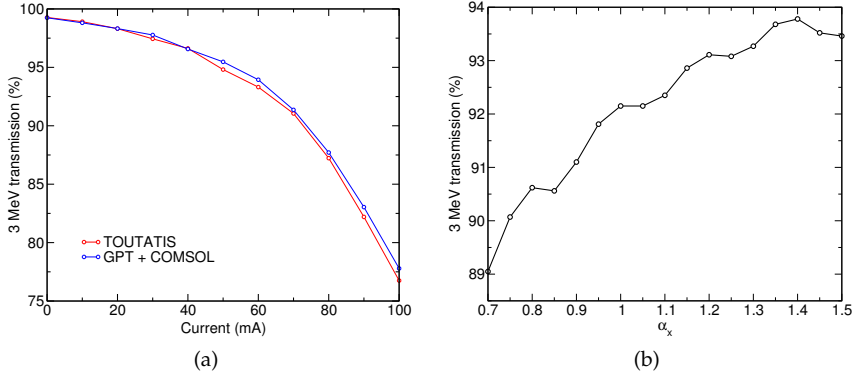


Figure 10.6: Transmission as a function of the input beam current (a) and  $\alpha_x$  (b).

much wider than the expected ion source dispersion of about 100 eV.

Finally, we have performed two transverse emittance related studies. In the first one, presented in figure 10.8 (a), we plot the transmission as a function of the input beam rms emittance. The transmission remains above 90% for input emittances below  $0.35\pi$  mm mrad, which leaves a wide margin for emittance growths in the LEBT.

In the second transverse emittance related study, we have investigated the zero current acceptance of the RFQ with GPT + COMSOL. This is the maximum size of the input beam that gets successfully transmitted when the particle-to-particle interactions are neglected. In order to do this, a very high emittance beam is used as input, only part of which will be transmitted. The emittance of those transmitted particles, calculated at the input of the RFQ, is defined as the zero-current acceptance. Figure 10.8 (b) shows both the full input beam (red) and the part that gets transmitted (blue), plotted in the horizontal phase space. The figure for the vertical phase space, not shown, looks very similar. The acceptances (rms emittances of the blue beam) are  $1.01$  and  $1.06\pi$  mm mrad for the horizontal and the vertical phase spaces, respectively. In principle, any beam contained in the blue region should be transmitted, provided the current is very low. At non-negligible currents, space charge effects create transverse forces that

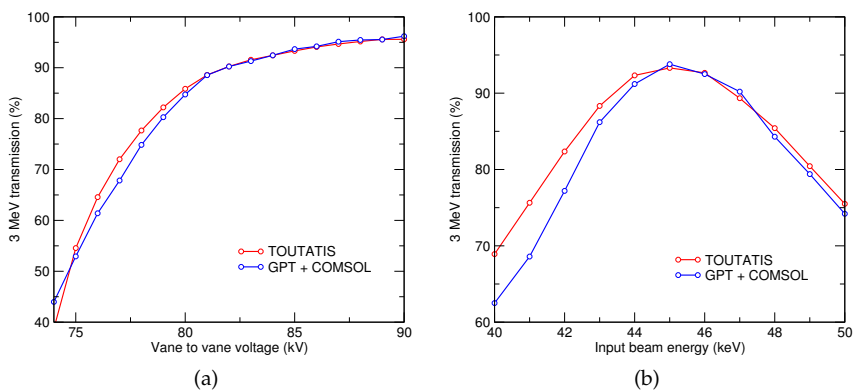


Figure 10.7: Transmission as a function of the vane to vane voltage (a) and input beam energy (b).

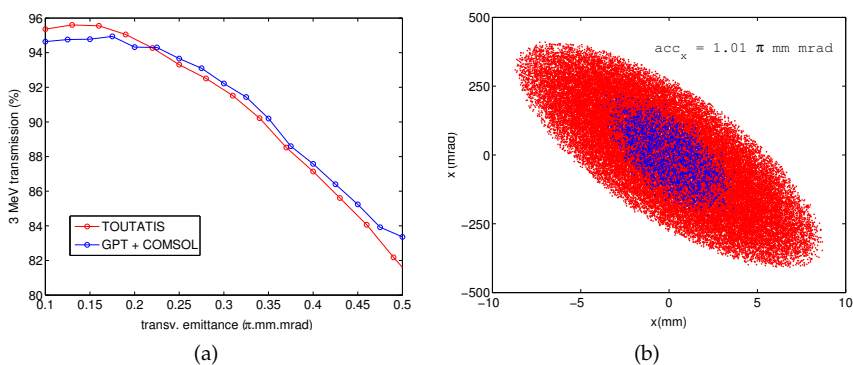


Figure 10.8: Emittance study: transmission as a function of the transverse emittance of the input beam (a) and zero current acceptance of the horizontal plane (b).

result in an increased particle loss.

## 10.6 Conclusions

We have updated the RFQ modulation design to comply with the recommendations made by the Committee after the 2013 review:

- The input energy has been lowered to 45 keV.
- We have designed a modulation with a 2-term function profile, which required adapting several parts of RFQSIM, initially written for sinusoidal cell shapes.
- We propose a new strategy to build the Acceleration section, in which the modulation factor is varied following a specific rule, which minimises particle losses and avoids too high surface fields.

The new proposed design, although being 3.12 m long (~20% shorter than the 2013 one), presents very good results in terms of transmission (in three of the four codes used) and emittance, with reasonable values for the surface field and a narrow resonance frequency range. We believe the new ESS-Bilbao RFQ modulation meets the design goals proposed by the Committee in the 2013 review.



# Chapter 11

## Cavity design

### 11.1 Electromagnetic design, 2D cross section

For RFQ 2013 design a rounded (so-called *Montgolfier*) cross section was chosen (chapter 4) based on different arguments, including technical and strategical ones. The TAC reviewed the design and proposed modifications in the design. The comments and recommendations are discussed in this section, together with ESS-Bilbao designs decisions and their reasons. Finally, the chosen design is presented.

**Round-shaped quadrants** The TAC recommended to change the rounded-quadrant to a more conventional flat-quadrant design. The supposed benefit of having a better Q-value for the rounded-quadrant cavity was superseded by the following items:

- The increased difficulty on quadrant machining
- Flat-quadrant would allow for a variable vane tip radius modulation design by allowing quadrant area variation
- Plunger tuner insertion has a simpler effect on the flat-quadrant design
- The expected lower cross-section size would allow to provide a proper braze joint between segments

After carefully reviewing the experts recommendations, an internal discussion process was initiated in this matter. As a result of this discussion it was decided by the former management to keep the round-shaped quadrant design, but modifying the vane profile to a straight shape. The main argument behind this decision was to rely on the strategical decision taken: the changing of the cross section would also have meant to modify the strategies for cooling the RFQ and the assembly and vacuum design.

Nevertheless, the items pointed out by the committee were considered very seriously and countermeasures for the expected problems were taken. In summary:

- The machining of the rounded shape has been proven successful by fabricating different models, like the 1-meter long aluminium cold model, the short models in copper used for welding tests and for testing the machining of the input section and the modulation. As a conclusion, we are confident that with the adequate fabrication strategy the workshops that would be involved in the fabrication will reach the quality requirements.
- The 2-term modulation that has been designed (section 10) fulfils all the requirements (80 cm shorter than the previous one, constant frequency profile along z axis, good figures for transmission and Kilpatrick factor) while keeping a constant vane tip radius. For this reason the quadrant cross section will also be kept constant.
- Plunger tuners effect on the rounded cross section has been thoroughly studied by the ESS-Bilbao team. The cold-model and all the numerical simulations performed had used this approach so we believe to have enough experience with it. The increased difficulty to model analytically the insertion effect will be discussed in following sections.
- The chosen vacuum and assembly strategy will use bolted segments (see discussion and experiments on section 14), and the tests and considerations already made have always considered the rounded-section, so it was chosen to keep this design option.

**Resonant frequency** The RFQ-2013 design had a design frequency for the 2D cross section of 351 MHz, quite close to the operating frequency. This means that in the real cavity the operational frequency would be reached with the tuners near flush position. The reason behind this decision was connected to the cooling of the movable plunger tuners: it was calculated that with the penetrations needed to compensate the frequency the cooling requirements of the tuners were much simpler. The main drawback of this approach was that the design frequency needs to be close to the operational.

This design option was not practical and this fact was pointed out by the TAC. The best option is that the 3D cavity will reach its operating frequency with the plunger tuners at about the mid excursion of their movement, so the 2D cross section must be designed at a slightly lower frequency. According to the previously obtained tuning range studies, it was decided to use a frequency design of 346.0 MHz. As it is described in section 12, the tuning range of the plungers allows to tune the achieve this frequency without problems. Apart from the value of the resonant frequency of the cavity, the action of the tuners will also perturbate the electric field in the axis. This perturbation can be computed by using finite element or mathematical models, and the resulting field maps will be used to feed particle tracking codes to quantify the effect on the quality of the transmitted beam. As a result of these studies, the 2D frequency of the cavity can be raised to 348.0 MHz by changing the quadrant radius. Final frequency has been chosen to be 348.61 MHz, corresponding to a quadrant radius of 39.4 mm. The dependence of the frequency on the quadrant radius ( $r_{circ}$ ) is shown on Figure 11.1. Dependence on vane tip radius is also shown in this figure for completion, although this parameter is fixed by beam dynamics and the modulation design.

**Mechanical restrictions** The mechanical restrictions on the shape and size of the RFQ cross-section are the same than for the RFQ-2013 design. This means that a maximum width of minor-vanes of 110 mm still applies, and also fixes the minimum width for the vanes due to the cooling channels (see Figure 11.2).

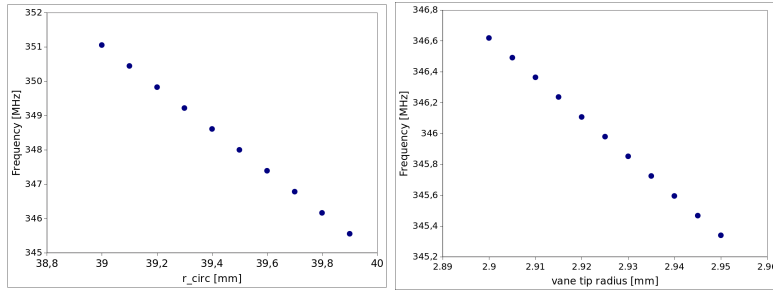


Figure 11.1: Dependence of 2D quadrupolar mode frequency on the quadrant radius (left) and vane tip radius (right).

### 11.1.1 RFQ-2014 design

With the above described considerations a cross-section design was chosen following the same optimisation procedure as for the former design. The main characteristics and figures of merit and their comparison to the RFQ-2013 model are shown in Table 11.1.

The geometry of the 2D cross section of the updated design is shown in Figure 11.2.

## 11.2 Electromagnetic design, 3D design

Once the cross section is defined the 3D cavity body is built by extrusion of the 2D shape, adding later the vane modulation. This can be done directly by the constructing the surface from its geometric description in the FEM solver, or building it in the CAD software and exporting it to solver afterwards. The process of obtaining a model suitable for electromagnetic computations from the CAD description has improved much since the original TDR was written. This has allowed for quick prototyping and designing.

The overall 3D design is quite similar to the rfq-2013 design and no further description is provided here.

Table 11.1: Comparison of main parameters of figures of merit for the 2D cross section designs RFQ-2013 and RFQ-2014.

Parameter	Old RFQ-2013	New RFQ-2014
$r_{\text{vane}}$ [mm]	2.95	2.922
$y_p$ [mm]	16	16
$x_{\text{circ}}$ [mm]	55	50
$y_{\text{circ}}$ [mm]	55	50
$r_{\text{circ}}$ [mm]	37.160	39.40
$(x_b, y_b)$ [mm]	—	(10.0, 30.0)
$l_{rb}$ [mm]	—	20.0
Modulation code name	11.4	15.7.3.19
Average radius [mm]	3.485	3.438
Frequency, quadrupolar mode [MHz]	351.0	348.61
Frequency, two dipolar modes [MHz]	342.1	337.94
Cross-section area [m <sup>2</sup> ]	0.02195	0.02202
$Q_0$	10786	11103

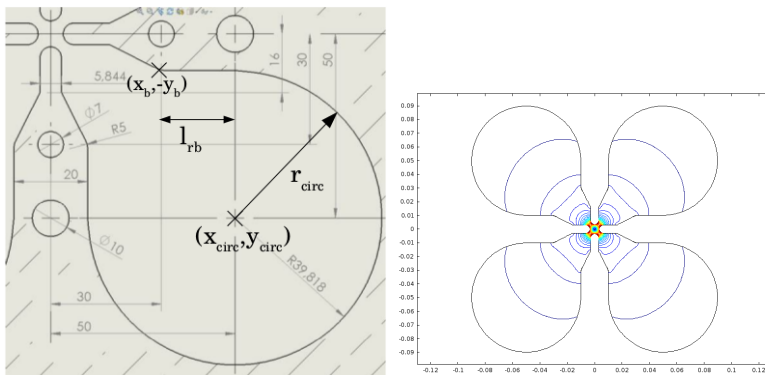


Figure 11.2: Cross section schematics showing the main parameters and dimensions (left) and field lines in the quadrupolar mode (right). Please refer to Table 11.1 for the actual values.

Table 11.2: Comparison of input section parameters between designs RFQ-2013 and RFQ-2014.

Parameter	RFQ-2013	RFQ-2014
$R_{\text{matcher}}$ [mm]	21.527	16.674 (input) / 14.0 (output)
$z_{\text{cover}}$ [mm]	16	7.5
$x_{\text{ymatcher}}$ [mm]	90	88
$r_{\text{lobe}}$ [mm]	20	25
$z_{\text{matcher lobe}}$ [mm]	48.9	22.60 (input) / 20.2 (output)

### 11.2.1 Input and output sections

The design of the input sections has followed the same ideas and procedures than for the rfq-2013 model. The angled portion assures that cooling channels reach the RFQ tip adequately. The parameters are described in Figure 11.3 and summarised in Table 11.2. The distance from the tip of the vanes to the RFQ cover has been defined at 7.5 mm, half of that of the previous model, due to beam dynamics considerations.

The input section has been optimised running parametric simulations in a portion of RFQ. In the optimisation runs, the  $z_{\text{matcher}}$  parameter was let free in order to provide the desired resonant frequency as a constrain for a given set of the other parameters. That is, for a given set of parameters  $\{r_{\text{lobe}}, x_{\text{ymatcher}}, z_{\text{cover}}\}$  the parameter  $z_{\text{matcher}}$  is then modified so the section resonates at the required frequency.

The target frequency chosen was 348.61 MHz, the same value than for the 2D cross section. The whole cavity will have a uniform frequency of 348.61 MHz along  $z$  coordinate with the tuners at flush position. The static tuners will then operate on all its length achieving then an uniform field distribution. This has been verified using a model of the whole first segment and also with models of the whole length of the RFQ, but computing only one quarter. In figure 11.4 some curves of this optimization procedure are shown. In figures 11.5 and 11.6 different field profiles are plotted for the first segment of the RFQ in the case of designing the RFQ head at 346 MHz or at 352.2 MHz.

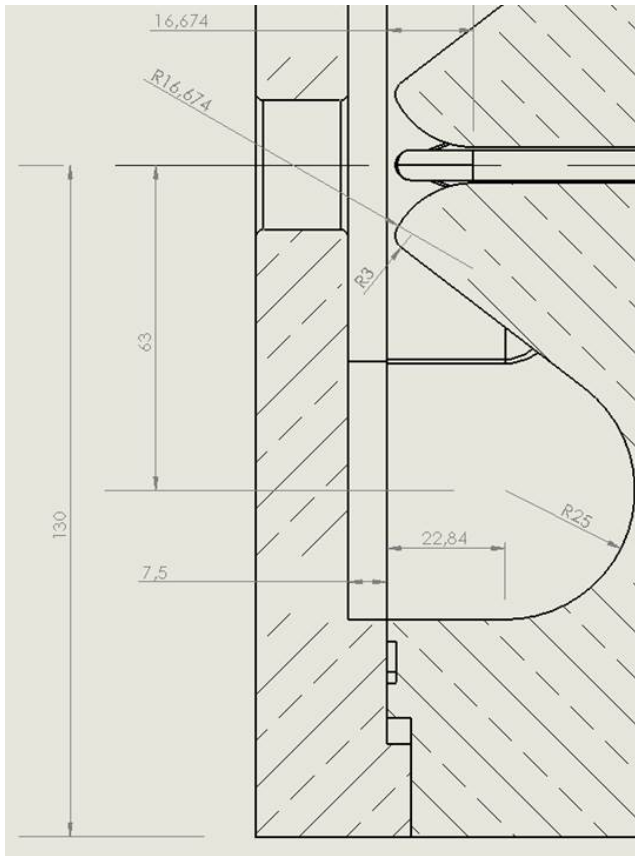


Figure 11.3: Schematics of the input matcher section parameters.

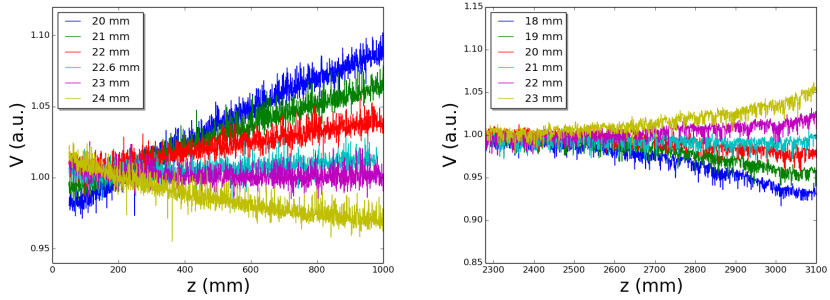


Figure 11.4: Voltage profiles for the input (left) and output (right) sections of the RFQ with different values of the input (output) matcher parameters.

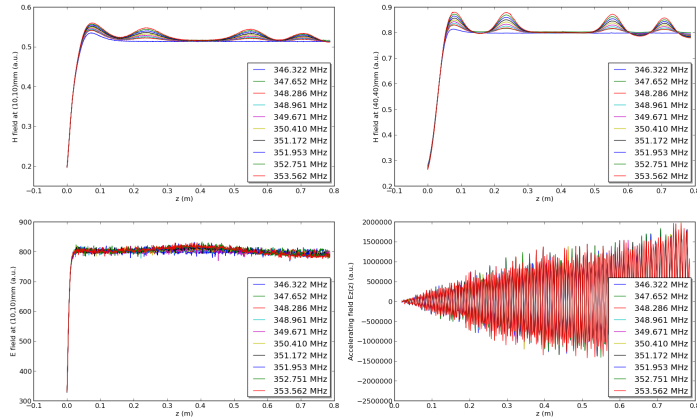


Figure 11.5: Longitudinal fields distribution (for the first segment of the RFQ) with the input section designed to resonate at 346 MHz. Upper graphics represent magnetic field long lines at  $[x y] = [10 \text{ mm}, 10 \text{ mm}]$  and  $[40 \text{ mm}, 40 \text{ mm}]$ . Lower left is the electric field along  $[10 \text{ mm}, 10 \text{ mm}]$  line, while lower right is the accelerating field at axis. Different curves correspond to different tuner penetrations from flush position, pointing out the resonant frequency of the whole model. Field flat profile is clearly achieved.

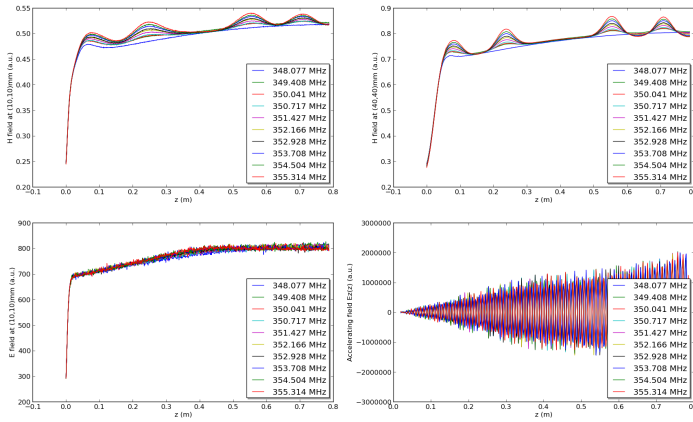


Figure 11.6: Longitudinal fields distribution (for the first segment of the RFQ) with the input section designed to resonate at 352 MHz. Upper graphics represent magnetic field long lines at  $[x, y] = [10, 10]$  mm and  $[40, 40]$  mm. Lower left is the electric field along  $[10, 10]$  mm line, while lower right is the accelerating field at axis. Different curves correspond to different tuner penetrations from flush position, pointing out the resonant frequency of the whole model. The fields profile is not flat but corresponds to one with the start section detuned.

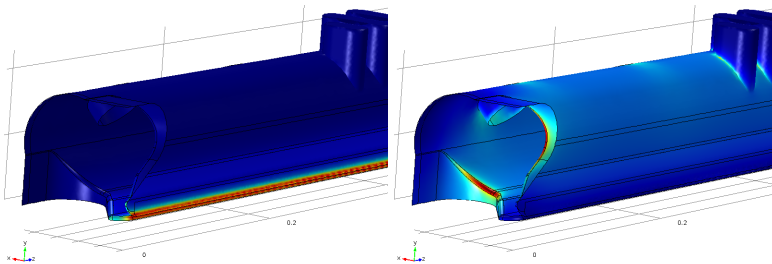


Figure 11.7: Electric (left) and magnetic (right) surface fields for the input matcher section of the RFQ.

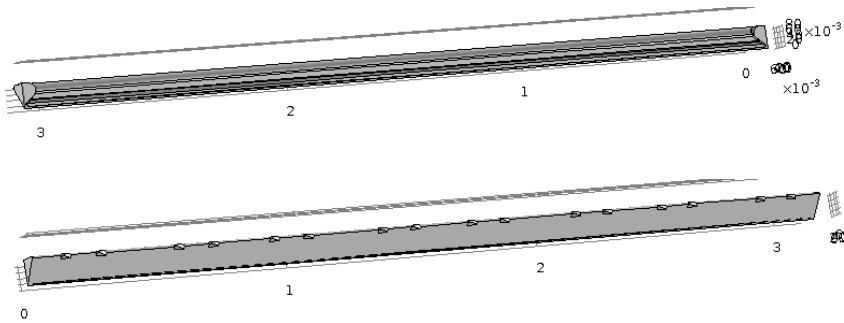


Figure 11.8: Geometry models of RFQ with correct input and output sections and length, but without modulations. These models allow to study voltage profile effects of input/output sections and tuners.

In Figure 11.7 the surface fields are shown for the optimised input section. As a final step of design refining, the input section rounding of edges and other aspects could be optimised to further reduce power loss in the area.

### 11.2.2 Full length simulations

Models with the whole length of the RFQ, including input and output sections with the adequate parameters in radial matcher have being built. These models have no modulation, so results concerning the tuning of the end regions and the tuners perturbation can be easily calculated. This takes advantage of the very flat RC<sub>3</sub> modulation frequency profile. Models without and with tuners are shown in Figure 11.8. Results for voltage profiles can be seen in figures 11.9.

### 11.2.3 Vacuum grid detuning compensation

The vacuum grids opened in the RFQ body to provide the required pumping modify slightly the resonant frequency of the cavity. In the previous design (RFQ-2013) this perturbation was planned to be corrected by making use of the slug tuners. It was pointed out by the TAC that it is a better

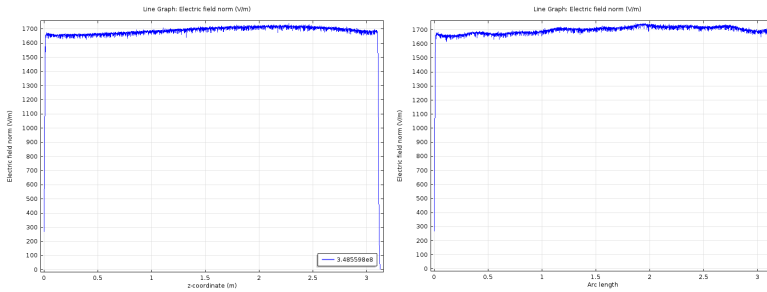


Figure 11.9: Voltage profiles obtained for full length RFQ models (one quadrant) without and with tuners providing the right operational frequency.

idea to compensate directly the grid detuning using ridges that penetrate the cavity, so in this way tuners can be better used for the main tuning tasks. This idea has been implemented in the design, and the optimum penetration value has been defined. In Figure 11.10 the solid models of the cavity with the vacuum port and the tuning ridges. The cavity with the vacuum port open without compensation is reduced from 346 MHz to about 345.2 MHz. The frequency change with the penetration of the ridges is shown in Figure 11.11. Final values for the ridge penetration will be presented in the tuning section in joint operation with the static tuners.

### Effect of vacuum port detuning compensation on field flatness

The field profile has been also computed for different values of the vacuum port ridge length. No significant effect on field flatness has been computed (see Figure 11.12).

## 11.3 Cavity modes spectrum

The modes dispersion curve follow the classic hyperbolic shape expected for a uniform structure. For the modes computed for a model of the first segment of the RFQ, with a magnetic wall at the end of the segment and

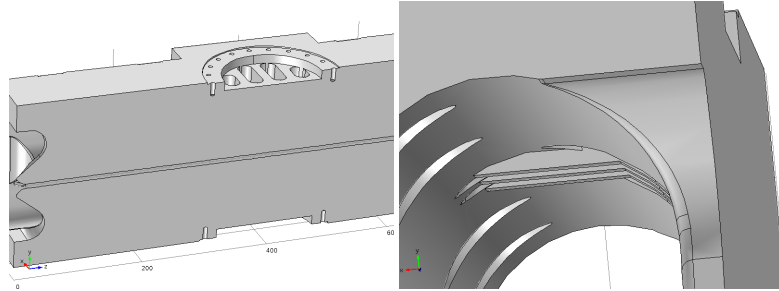


Figure 11.10: Solid models of the first segment of the RFQ showing the vacuum grid (left) and the penetration of the vacuum grid ridges in the cavity to compensate the frequency shift.

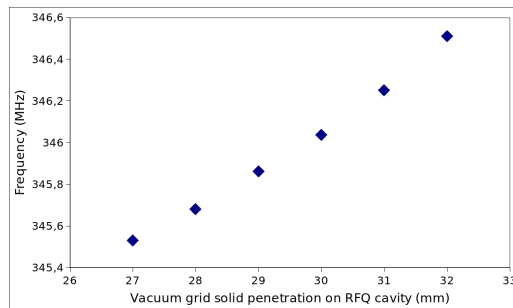


Figure 11.11: Compensation of the frequency shift caused by the open vacuum ports by means of grid ridges of different lengths penetrating the cavity. Optimum value is selected for a frequency of 346 MHz (cavity design frequency with tuners at flush position). The ridge length is measured from the top of the port, penetration in cavity vacuum is much smaller.

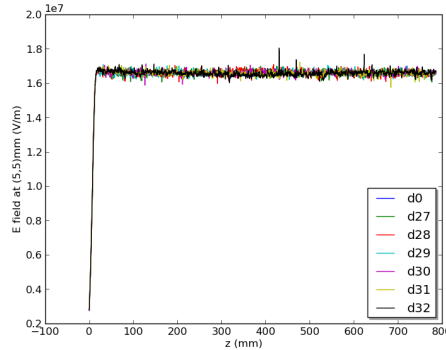


Figure 11.12: Electric field profile (field value along a line at coordinates (5mm,5mm)) for different values of the vacuum port gaps. No important variation is detected.

the designed input section correctly tuned up, the modes frequencies fit well with the expression

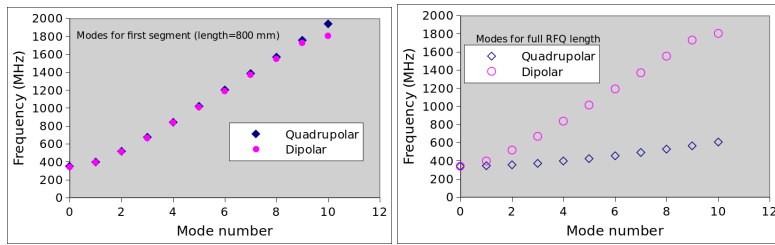
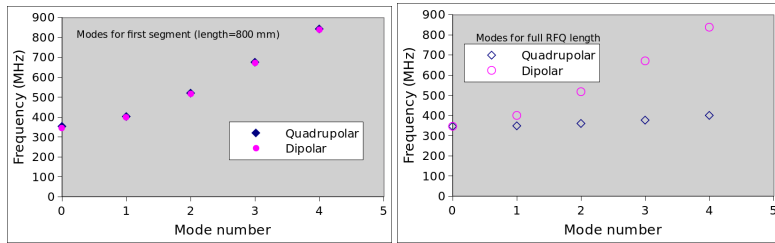
$$f_n^2 = f_0^2 + \left( \frac{nk}{l_V} \right)^2, \quad (11.1)$$

where  $f_n$  is the frequency of the  $n$ -th mode,  $f_0$  is the fundamental,  $k$  is a constant and  $l_V$  an effective vane length. The computed modes are shown in figures 11.13 and 11.14 for models without and with static tuners in operation, respectively. Modes are computed for the first segment only. Values for the full RFQ length are extrapolated using expression 11.1 changing the effective length to  $l'_V = 4l_V$ . For the dipolar dispersion curve only one of the degenerated pair of dipolar modes is shown. The frequency values are shown in Table 11.3.

It is clear that the dipolar modes dispersion curve overlaps the quadrupolar curve. The separation in frequency for the second and third dipolar modes from the fundamental quadrupolar are of about 4 and 7 MHz, that seems far enough to avoid degeneracies.

Table 11.3: Frequencies (MHz) for the mode spectrum of the first segment and the full length of the RFQ.

<b>n</b>	<b>Q</b>	<b>D1</b>	<b>D2</b>	<b>Q (3 m)</b>	<b>D1 (3 m)</b>	<b>D2 (3 m)</b>
0	352.21	345.01	345.05	352.21	345.01	345.05
1	401.53	399.55	399.60	353.48	346.31	346.35
2	519.95	517.53	517.59	357.26	350.16	350.20
3	677.30	673.56	673.64	363.47	356.50	356.53
4	847.32	842.24	842.34	371.98	365.18	365.21

Figure 11.13: Frequency spectra simulated for the first segment of the RFQ (left) and extrapolated to total RFQ length using expression 11.1 (right). The tuners in the computation are in flush position, so fundamental quadrupolar frequency is  $f_0 = 346$  MHz.Figure 11.14: Frequency spectra simulated for the first segment of the RFQ (left) and extrapolated to total RFQ length using 11.1 (right). All available tuners are used in the simulation. The fundamental quadrupolar frequency is  $f_0 = 352$  MHz.

# Chapter 12

## Cavity static tuning

The static tuning of the RFQ cavity will be done by inserting fixed slug tuners, with defined penetration, at certain longitudinal positions. Once the cavity is tuned, these plunger tuners will remain fixed and the dynamic control will be carried out by the effect of the cooling water temperature (thermal tuning). The characteristics of the static tuning will be described in this section.

### 12.1 Number and position of tuners

These values are the same than for the RFQ-2013 design, and are included here for completion. As before, tuners are taken for simulation purposes as cylinders of diameter 37.6 mm. Tuner ports position can be seen in Figure 12.1. There are four sets of four tuners per segment, all placed at the same longitudinal position at coordinates  $z_{t1} = 136$  mm,  $z_{t2} = 256$  mm,  $z_{t3} = 526$  mm,  $z_{t4} = 646$  mm from the start of the segment (see Table 12.1). This gives us a total of about 60 slug tuners for tuning the cavity ( $16 \times 4$  segments, leaving two ports for power couplers and two for other tasks).

Table 12.1: Longitudinal position of slug tuners ports for an RFQ segment. Coordinates are the same for the four segments.

Position in segment	Coordinate
1	135.865 mm
2	255.865 mm
3	526.865 mm
4	646.865 mm
Tuner port diameter	37.6 mm

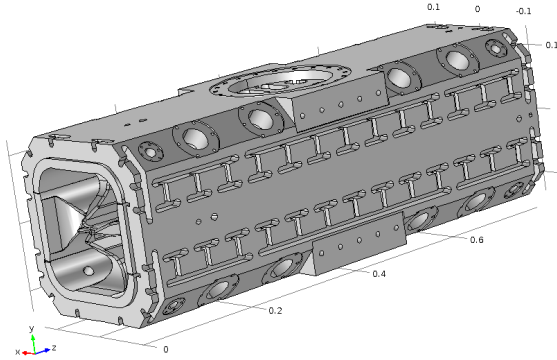


Figure 12.1: Geometry of the first segment of the RFQ showing the openings for the tuner ports. These ports are standard and can be used also for pick-ups or for the power coupler in the central segment of the RFQ. Vacuum ports are not shown in this CAD image.

## 12.2 Frequency profile along RFQ length

As described in section 10, the RFQ-2013 model included a sinusoidal type modulation that resulted in a 'step-function' like frequency profile along the RFQ length. This profile is obtained calculating the resonant frequency for each cell of the RFQ and plotting the frequency obtained as a function of the initial coordinate of the cell. This frequency variation was planned to be compensated by the operation of the plunger tuners. The solution proposed by ISIS-RAL to overcome the same issue was also considered and proposed for the RFQ-2013 design. The ISIS solution consisted on modifying the lobe geometry incorporating some machined grooves to locally change inductance and compensate the frequency variation.

In the design review, it was pointed out by the TAC that a more practical approach would be to use a 2-term modulation type instead of the sine-wave like, so a more constant frequency profile would be obtained. The work done on this subject and described in section 10 fructified in a modulation that resulted in a frequency profile shown in Figure 12.2. Both curves are plotted with the same approach, computing the frequency of 3D slices of the RFQ enclosing one modulation cell, without including any port opening. When the modulation variation is small for the initial cells of the RFQ, the frequency is practically that of the 2D design models for both models. When the modulation variation is bigger for the accelerating section of the RFQ, a strong change in frequency profile is observed for the RFQ-2013 sine-like design. On the contrary, the RFQ-2014 2-term design frequency variation is kept quite constant along its length, except for a small peak at the end of the gentle buncher section.

## 12.3 Frequency tuning effect of plunger tuners

The penetration of the plunger tuners in the cavity results in an increase of the resonant frequency of the cavity. Considering only the first segment of the RFQ as a single cavity, the frequency variation that can be achieved with different sets of tuners in operation is described in Figure 12.3. The desired target frequency is within range of the plunger tuners for all configurations. With lower number of tuners the penetration needed is higher.

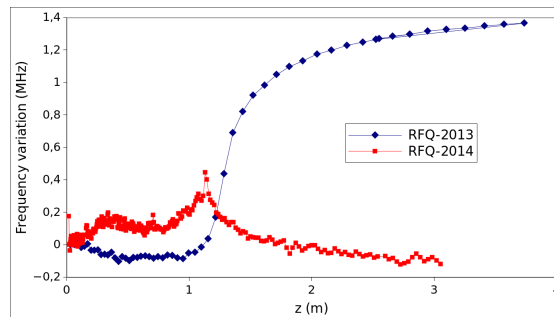


Figure 12.2: Comparison of the frequency profile along the RFQ length for the RFQ-2013 and RFQ-2014 designs.

This would increase the power losses in the tuners and consequently the cooling requirements. Also, the perturbation on the field profile would also be more important for the tuners with deeper penetration.

## 12.4 Field profile effect of static tuners

The penetration of the tuners in cavity volume will modify the local frequency that translates in a field or voltage profile along the RFQ. Once the field profiled has been optimised to a flat profile using the input matcher section as a coupled resonator (see Figures 11.12) the tuners will rise the frequency to the operating one, but in this process additional perturbation will be created.

### 12.4.1 Finite element model

In Figure 12.4 different electric field profiles along first segment of the RFQ are shown. Each curve corresponds to a different tuners configuration, all of them resulting in the same overall frequency of the cavity. The less perturbing situation correspond to that with the highest number of tuners in operation, while the most perturbing configuration uses three out of the four tuners (per quadrant) for the RFQ segment. The configurations using two tuners are in between.

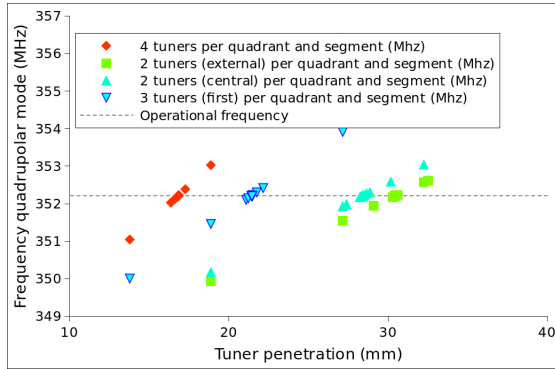


Figure 12.3: Frequency variation of the first segment of the RFQ as a function of the penetration of different sets of plunger tuners.

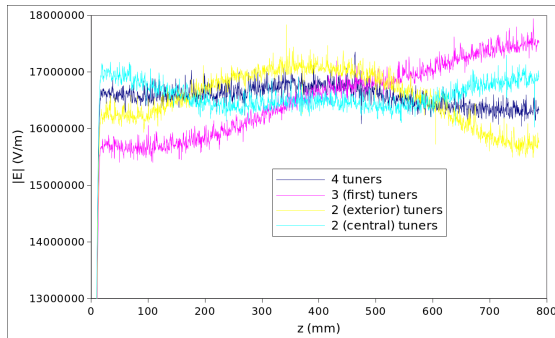


Figure 12.4: Electric field profile along a line at coordinates (5 mm, 5 mm) for different tuners configurations. Results correspond to the first segment of the RFQ. In all situations the resonant frequency of the cavity is the same.

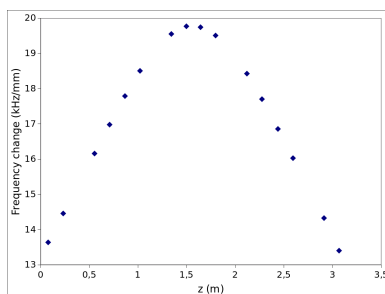


Figure 12.5: Change in frequency caused by individual slug tuners, placed at their corresponding longitudinal position  $z$  in the whole length of the RFQ. It is clear that the tuners in the mid-section of the RFQ would have stronger effect.

Taking advantage of the rather flat frequency profile in the RFQ-2014 design, a finite element model of the whole length of the RFQ can be built without considering vane modulation. This model will have an uniform cross section (and frequency profile) and the effect of individual or groups of tuners can be studied and compared to the results of the mathematical model. The change in frequency for each of the tuners in a quadrant depends on its longitudinal position, as shown in Figure 12.5

As described in the cavity design section, a finite element model of the whole length of the RFQ has been built, with and without modulation, to verify the tuners effect in frequency and in voltage perturbation. These models have the correct input and output sections. A model is shown in Figure 12.6. Results with this model without and with modulation are shown in figures 12.7 and 12.8. These results show that the RFQ can be tuned with the plunger tuners to provide the right frequency. Voltage perturbations are evaluated by extracting the fields and running beam dynamics simulations.

### 12.4.2 Transmission line perturbation model

Results described in the previous section can be used to validate a transmission line perturbation model as the one presented by Young [61] and described by Wangler [62]. An implementation of this model considering

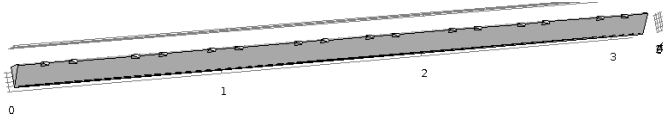


Figure 12.6: Geometry model of RFQ with correct input and output sections and length. Frequency change and voltage perturbation are obtained from simulation from this model.

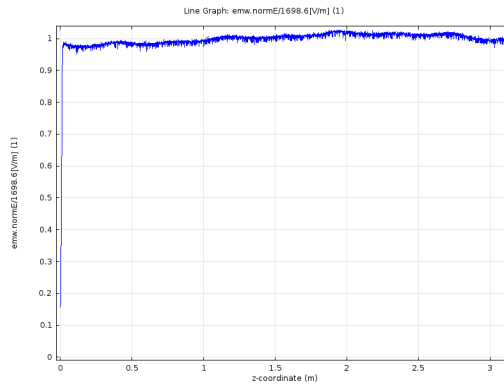


Figure 12.7: Electric field (norm) profile along the line [5,5,z] (mm) for the model without modulation. Tuners are penetrating the cavity uniformly to provide the right operating frequency of 352.2 MHz.

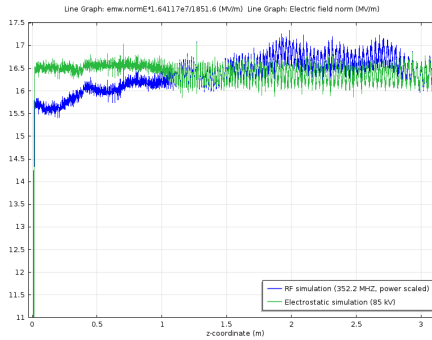


Figure 12.8: Electric field (norm) profile along the line [5,5,z] (mm) for the model with modulation. Tuners are penetrating the cavity uniformly to provide the right operating frequency of 352.2 MHz. Field from a scaled electromagnetic simulation is compared to a electrostatic simulation. Tuner configuration is not optimized to provide a flat field (tuners penetrate uniformly).

the tuner perturbations as delta functions has been coded in a python script. Results for the first segment of the RFQ are shown in Figure 12.9.

If instead of only the first segment the total length of the RFQ is used, and all the plunger tuners are incorporated in the model in their particular  $z$  position, it is possible to use the model to obtain the voltage profile for the whole RFQ. Several examples of this, with different tuner penetration patterns, can be seen in Figure 12.10.

### 12.4.3 Application of perturbation model to RFQ tuning

The model used for creating Figures 12.9 and 12.10 can be used as a tool to assist in the tuning of the RFQ. This was one of the recommendations issued by the TAC. In order to perform the tuning procedure, the unperturbed base line (that in the previous analysis was taken as perfectly flat) should reflect the voltage profile derived from the local frequency profile induced by the modulation (see Figure 12.2). The effect of the tuners penetration can then be incorporated and the total profile being computed. An optimisation or an algebraic algorithm can then be used to obtain the best tuner configuration for the whole RFQ.

The experimental tuning of the RFQ cavity would require the measurement of the unperturbed voltage profile by means of the bead-pull setup and take it as the base line for the perturbations. The perturbation induced by each tuner is included in the model as a local variation in resonant frequency  $\Delta\omega/\omega$ . This variation can be calibrated by measuring the effect of inserting the tuners in the bead pull profiles. Once the frequency effect of the tuners are calibrated, the algorithm described above can be used to get the optimum tuner configuration. Using the tuner field profile once again as a base line, the procedure can be repeated iteratively until an optimum stable configuration is achieved.

## 12.5 Proposed static RFQ tuning strategy

The proposed tuning strategy to achieve a flat field profile, once the tuner effect has been properly calibrated using experimental results, will follow these steps:

- Set all tuners to provide an uniform perturbation in frequency that results in the right operational frequency. For this purpose the penetration of the tuners must be different, according to each individual effect. Call the tuners configuration  $\{T_{0j}\}$  for each tuner  $j$ .
- With this configuration, measure the field profile  $V(z) = V_{0i}$  by means of the bead pull method.
- Naming  $V_i = V(z_i)$  the desired field profile (flat profile), make use of linear relationship:

$$V_i - V_{0i} = \sum_{j=1}^N \frac{\partial V_i}{\partial T_j} (T_j - T_{0j}) \quad (12.1)$$

to obtain the new tuner configuration  $T_j$ . This can be done solving the linear equations system using a numerical algebra package.

- As the reality will be non-linear and with errors, the process can be repeated several times until convergence and stability are achieved.

The process will be validated with simulation models of the RFQ and using the aluminium cold model as a test-bench.

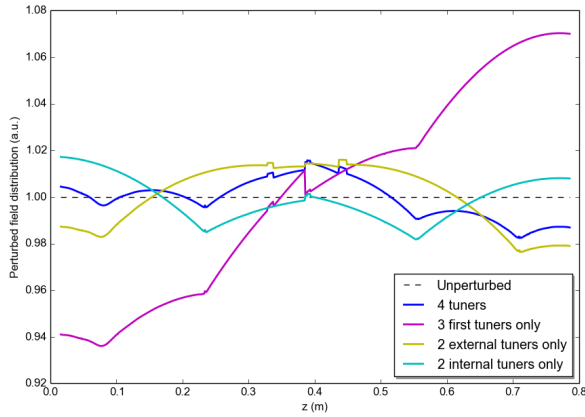


Figure 12.9: Electric voltage along the length of the first segment of the RFQ computed using a transmission line perturbation model. The tuner configurations are the same than for Figure 12.4. The simple model reproduces quite well the behaviour obtained by FEM models.

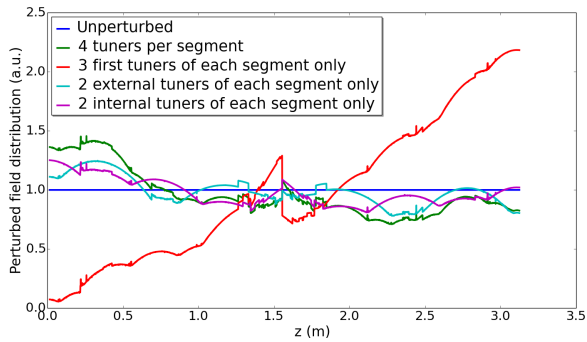


Figure 12.10: Electric voltage along the length of the RFQ computed using the transmission line perturbation model. The tuner configurations for each segment are the same than for figures 12.4 and 12.9.

## Chapter 13

# Cavity thermo-mechanical design and thermal tuning

The design and the calculation work on thermo-mechanical aspects of the RFQ have been revised following the TAC recommendations on the previous review. Although much work has been done in this issue, only the aspects relevant to the cavity design and the progress on the reviewers comments are described in this document.

The main points discussed here are relative to the cooling scheme itself (channels, water flow rate and temperature, etc.). Also, the effects of the cavity cooling on electromagnetic characteristics (frequency, voltage law, ...) are discussed, including the use of the water cooling as a dynamic tuning system for the RFQ.

### 13.1 Power loss

Power loss in the cavity walls is calculated from the electromagnetic model of the first segment, with all static tuners to provide a frequency of 352.2 MHz. The magnitudes of the fields obtained by the electromagnetic eigenvalue solver are not scaled to the right values, as there is no power

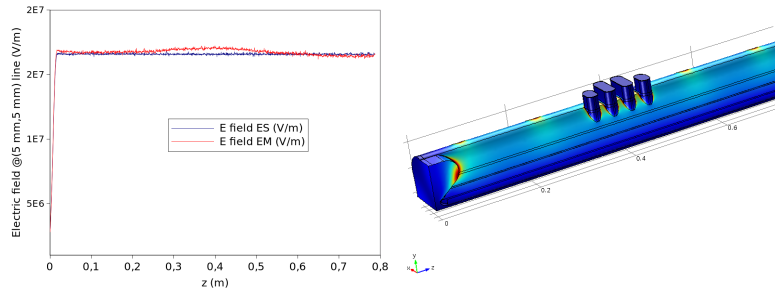


Figure 13.1: Left: Electric field in the intervane region along a line at transverse coordinates (5, 5) mm. Field computed from an electrostatic model (used for scaling) is compared with the scaled electromagnetic model. The scaled fields are then used to compute power losses in the model (right). The non-flat profile of the field has already been discussed in the tuning section.

input in the model. To obtain the right values, a scale factor is included multiplying field values (and consequently scaling also power losses).

This factor is obtained by comparison of the eigenvalue model solution to an electrostatics model where the correct design vane voltage of 85 kV is imposed. In Figure 13.1 the power losses colour map and the scaled electric field is shown.

The power loss integrated for all the metallic surfaces of the first segment amounts to about 105 kW (at 100 % duty cycle). The total power loss (at 100 % duty) for the whole length of the RFQ (4 segments in total) is expected then to be about 400 kW. This value is higher than the one presented for the 2013 model, but this one considers also the power losses at the slug tuners and the ridges for vacuum port detuning compensation.

It is worth to mention that the RFQ-2013 design was planned to be used at a higher power than current design. The previous design operational value was of 10 % duty cycle, while now as the RFQ use will change from neutron production to testing of MEBT components required powers are much lower (about 3–4 % duty cycle at maximum). This relaxes cooling designs specifications.

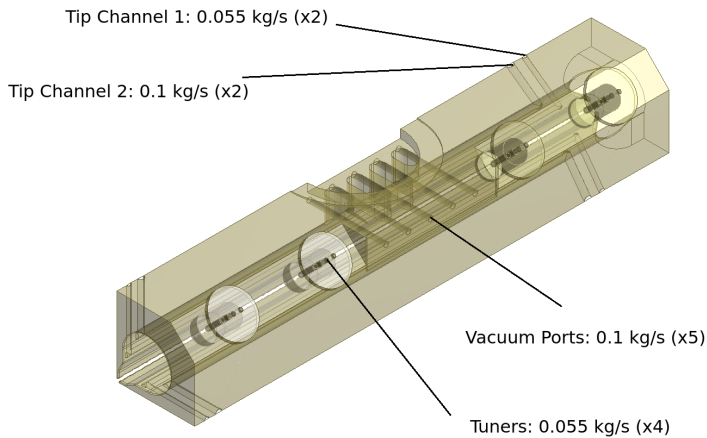


Figure 13.2: Input mass flow rates for all the channels.

## 13.2 General cooling strategy

In the previous report two different cooling strategies were presented, one based on ISIS design (using baffles) and another (we called it CERN-LINAC<sub>4</sub> type) using deep-drilled channels along the vanes. Results on simulations and studies with this two strategies were presented in parallel. Based on mechanical arguments and on the results of cooling performance, a final cooling strategy was chosen: the drilled channels scheme.

The chosen water circuits are shown in Figure 13.2. For each of the segments, there are two channels running along the vane at different heights. A second water circuit will cool down the area close to the vacuum port. Additional circuits for each of the slug tuners are also considered. In this cooling design update, water velocity has been increased and now the maximum is around 5.3 m/s, which is the double than for the 2013 model. A colour map of the water velocity is shown in Figure 13.3.

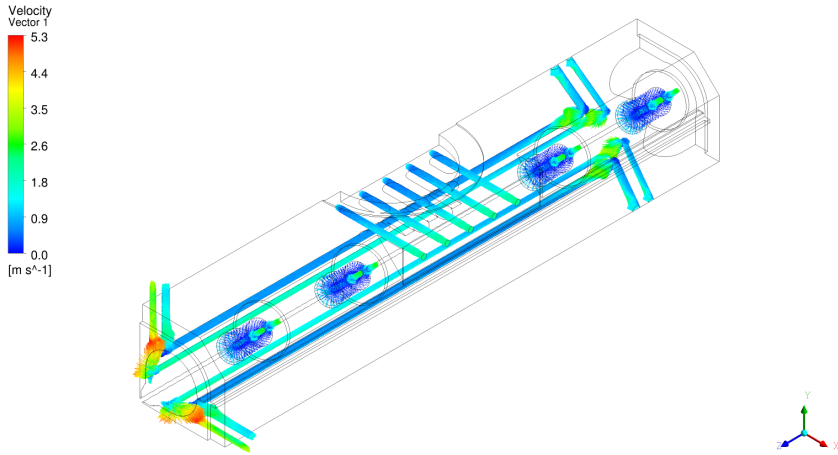


Figure 13.3: Water velocity within all the cooling channels.

### 13.2.1 Water temperature

The cooling water temperature considered for the updated design is higher ( $26\text{--}27^\circ\text{C}$ ) than for the previous design. This is done to avoid water condensation as suggested by the TAC.

## 13.3 General results

In figures 13.4 and 13.5 the results for a water cooling temperature of  $27^\circ\text{C}$  are shown. The frequency of the model changes from  $352.69\text{ MHz}$  in the starting model (original mesh without thermo-mechanical or power deformations) to  $352.36\text{ MHz}$  in the steady state when the water is running in the vane channels and in the vacuum port with an input temperature of  $27^\circ\text{C}$  and no power. The same situation but with RF power at a duty cycle of 10% reduces further the frequency to  $352.19\text{ MHz}$ . Frequency change is mainly due to deformation of the vanes.

The deformation in the vane area without RF power (see Figure 13.5 on the left side) is about 21  $\mu\text{m}$  in the central section of the segment. The elongation of the vane tip in the longitudinal direction is bigger when there is RF power in the cavity, around 40  $\mu\text{m}$  (see Figure 13.5 on the right side). These values are for a duty cycle of 10 %, much higher than the expected operational values for the RFQ.

The effect of the duty cycle can be seen on Figure 13.6. The displacement of the vane is not uniform even in the absence of power due to the cooling. As power increases the deformation also increases.

### 13.3.1 Deformation of fields

As suggested by the TAC, the vane deformation due to heating and cooling can change the shape of the field distribution. The accelerating field  $E_z(z)$  is shown in Figure 13.7 for different conditions: Electrostatics model, pure RF model, RF with cooling water and no RF power input, and RF with cooling and a RF power corresponding to a duty cycle of 10 %. The effect on the field does not seem very important, but fine field maps will be produced and particle tracking simulation carried out to rule out any harmful effect.

Apart from the accelerating field, the elongation of the vane tip can change the resonant frequency of the input section causing a slight detuning. This effect is also expected to be small.

## 13.4 Tuning of cavity frequency with water temperature

The cooling circuits and strategy for the RFQ-2013 model were not designed for the specific use of dynamic tuning of the RFQ. As due to other considerations (mechanical design, initial strategy, ...) the cooling design for the RFQ-2014 model is very similar to the RFQ-2013 design. It is then necessary to prove the thermal tuning capabilities of the design. This has been done making use of finite elements models combining RF, thermo-mechanical and CFD calculations, in 3D models of the first segment of the RFQ.

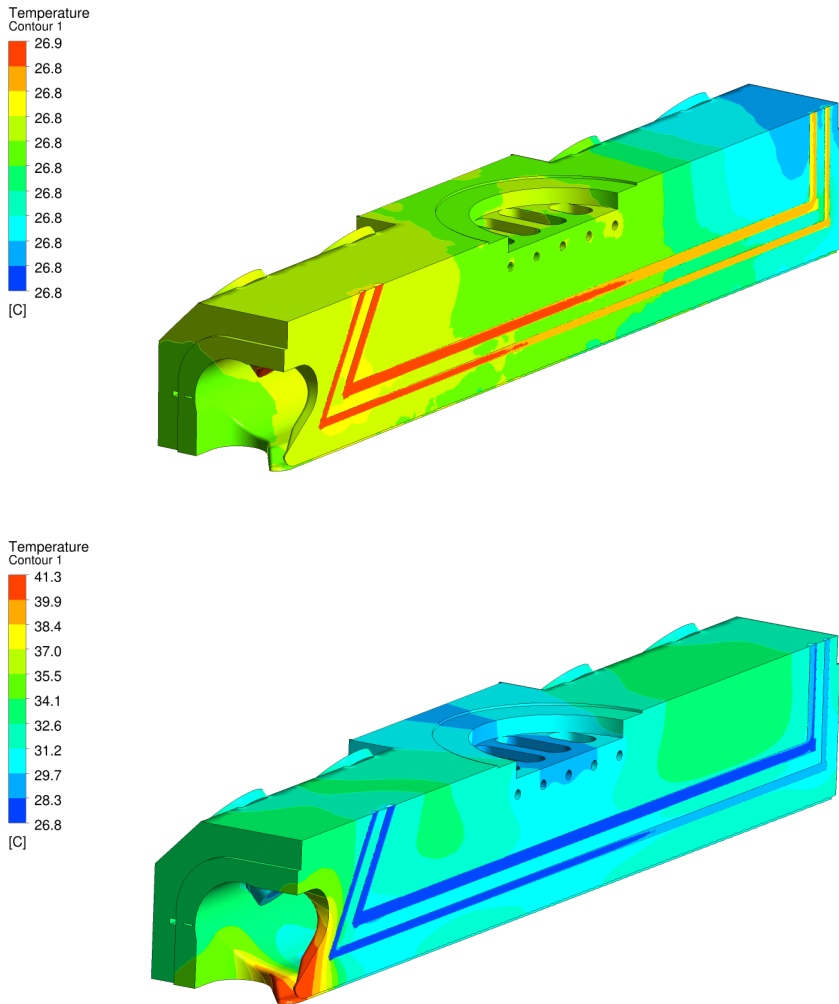


Figure 13.4: Temperature map in the solid (input water temperature 27°C in all circuits) without power (top) and with power with a duty cycle of 10% (bottom).

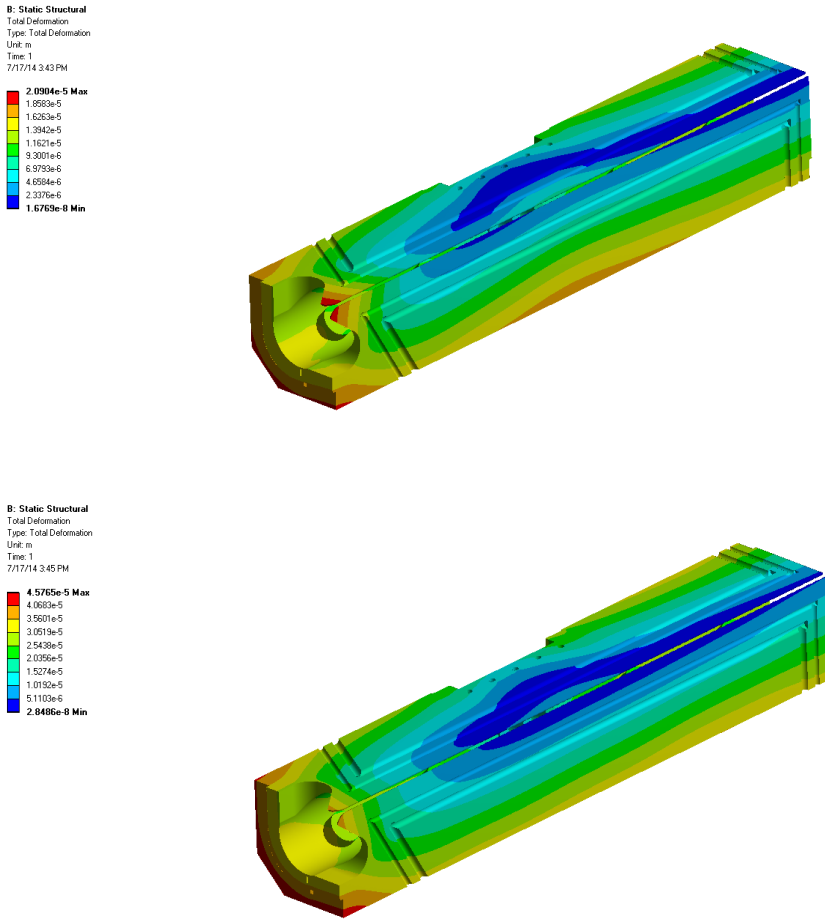


Figure 13.5: Deformation (total displacement) map in the solid (input water temperature 27 °C in all circuits) without power (top) and with power with a duty cycle of 10 % (bottom).

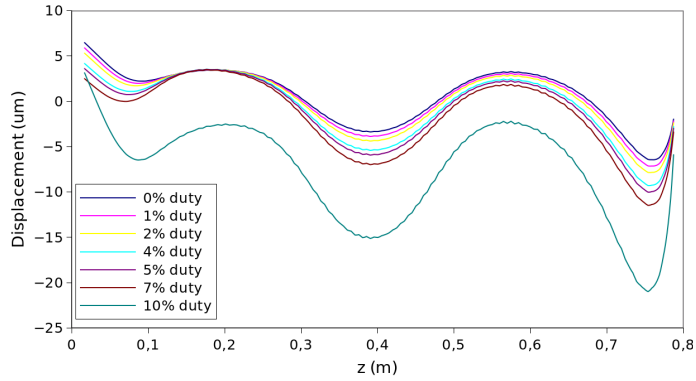


Figure 13.6: Displacement of the vane (positive displacement is movement away from beam axis) along the vane tip for the first segment of the RFQ. For each curve cooling water conditions are the same, but duty cycle is increased from 0 % to 10 %.

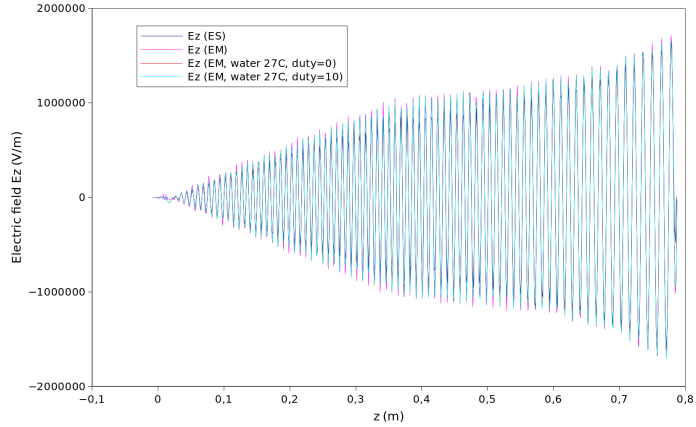


Figure 13.7: Comparison of on-axis accelerating field for four models: electrostatic, RF, RF with cooling and no power and RF with cooling water and 10 % duty cycle.

### 13.4.1 Effect of vane cooling water temperature on cavity frequency

In order to use the temperature of the cooling water as a control parameter for the frequency of the cavity during operation, we need to know how the cavity frequency changes with the water temperature,  $\omega_{\text{resonance}} = f(T_{\text{water}})$ . This dependence should also be as simple as possible to simplify control algorithms. Although this dependence will be experimentally determined using low power RF measurements when the first segment of the RFQ is fabricated, computer simulations have to be used at design stage to validate the planned strategy and to estimate the expected behaviour.

To study this effect, a set of coupled simulations has been run. In these simulations, the slug tuners temperature is kept constant, and the same is done with the vacuum grid cooling water. The cavity then deforms under the combined action of the RF power loss and the cooling circuits. Different water temperatures for vane circuits are considered. The deformation of the solid cavity body is directly translated into a deformation of the mesh of the vacuum region, so the resulting resonant frequency can be computed and compared to the original non-deformed one.

In the study shown here, the cooling water temperature of the two vane channels is changed simultaneously and a steady state solution is computed. Results are shown in Figure 13.8. It is clear that dependence is quite linear, as expected. A change of frequency of about 16 kHz per degree of vane water temperature is obtained.

### 13.4.2 Effect of duty cycle on cavity frequency

In a similar way than in the previous section, the effect of changing RF power duty cycle on cavity frequency is also studied. It is also expected that this dependence is also linear. Increasing duty cycle from 0 % to 10 % while keeping cooling parameters constant, and running a set of simulations similar to ones in the previous section, the results shown in Figure 13.9 are obtained. Again, a clear linear dependence is obtained.

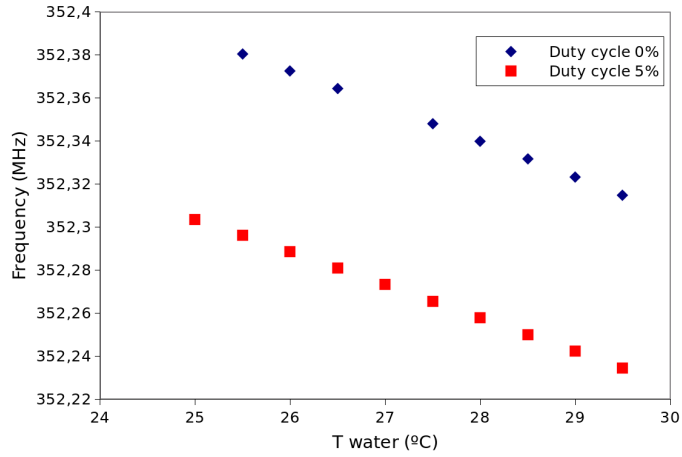


Figure 13.8: Resonant frequency dependence on the vane cooling water for the first segment of the RFQ, for two different power conditions (without power and with RF power at a duty cycle of 5%).

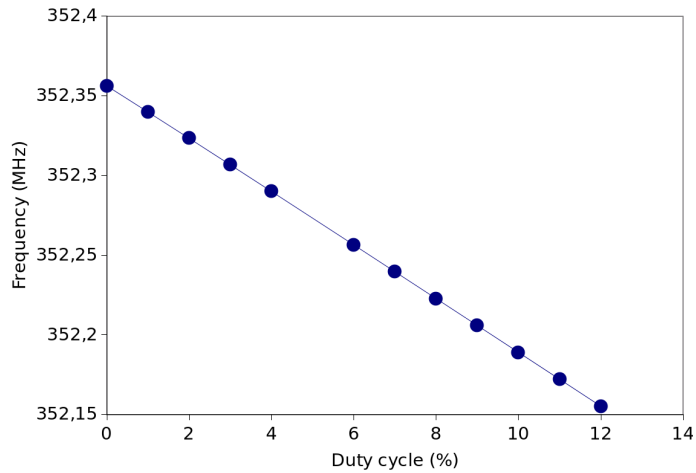


Figure 13.9: Resonant frequency dependence on the duty cycle for the first segment of the RFQ, with the same water cooling conditions.

### 13.4.3 Application to cavity dynamic tuning

The behaviour described in the preceding sections can be used to plan the RFQ operation. Starting with a cavity without RF power, a value of water temperature that results in the operational resonant frequency must be set. As input power is increased from 0 to the operational value, the frequency of the cavity will change following a dependence like the one shown in Figure 13.9. Water temperature have to be changed at the same time (decreasing temperature) in order to keep the cavity frequency equal to the operational value. This transitory proceeds until the RF power set-point is reached and the water then stabilizes. The process should be slow enough to compensate the thermal inertia of the solid cavity body.

This complex operation will be further studied using computer models steady and time dependent, in combination with control algorithms, during following months. An example of the ongoing work is shown in Figure 13.10. Transient simulations are done in the first segment of the RFQ (without the tuners inserted, thus the value of frequency below the operational). In the first situation (blue curve), at time  $t = 0$  cooling water is turned on and RF power is set at 5%; power is then turn to zero at a certain time. Transient coupled thermo-mechanical and electromagnetic simulations are run to compute the evolution of the resonant frequency. In the red curve the opposite situation is considered (RF power is established at a certain time).

These finite element studies are the input for a dynamic mathematical model of the thermal effects on RFQ frequency that will be used for the cavity tuning.

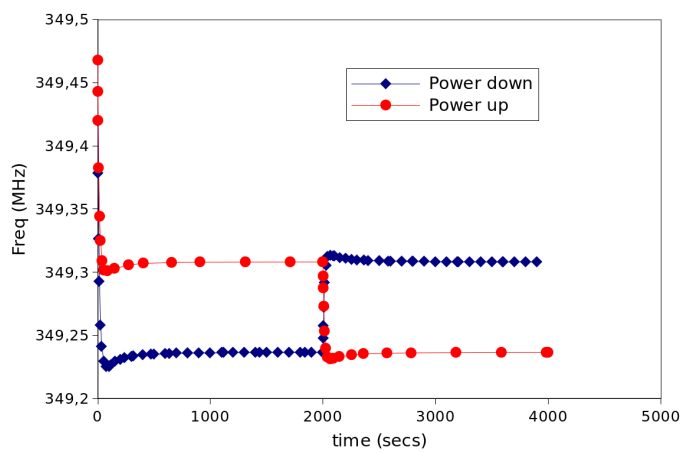


Figure 13.10: Transient simulations of the resonant frequency of the first segment of the RFQ as a function of time. Two situations are simulated a step down in RF power and an step up in power.

## Chapter 14

# Cavity assembly, support and vacuum strategy

One of the points raised out by the TAC was the cavity assembly and the influence it may have on the vacuum performance of the cavity. After the design review meeting it was decided by the project team to keep the bolted cavity approach instead of pursuing a welding strategy. This has the main advantage of allowing the opening of the cavity for re-alignment, mechanical modifications, etc.; but has also the drawback of possible lack of the required vacuum tightness. In order to improve our knowledge of the assembly technique and to validate the results that can be achieved, a model cavity has been built in aluminium and has been assembled using the same procedure intended for the RFQ cavity. Vacuum tests have then been done using this model.

Although work on these issues will proceed during the next months in this section we present a description of the assembly process and the results obtained with the aluminium model.

## 14.1 Support

The support configuration has been reviewed and, from the options presented in the 2013 design report (chapter 14), the solution that makes use of CERN-type jack supports has been chosen. The design of the support structure has two main principal aims. First, it has to be able to allow the three linear movements and the three angular movements for the alignment and in the other hand it has to be able to provide a support bench for the RFQ and all the components with the minimum possible deformation.

The principal weight and pressure inputs for the support are:

- The RFQ own mass, around 1460 kg.
- The vacuum pumps weight, 4 pumps of 18 kg, 72 kg.
- The pressure produced by the vacuum 1 bar in all the outside faces.

There are still more elements like tuners, couplers and so on, some of those however, are built alongside with their own independent supports. The most suitable support which embraces such features is CERN type support. Figure 14.1 shows CERN's Jack design. These assemblies are designed to support up to 5 t for each jack. Using 3 jacks, all the linear and angular movements for the alignment are allowed as is shown in Figure 14.2.

The other issue to consider regards the deformation of the RFQ. A simulation has been done to check whether the deformation induced to the RFQ is acceptable. Figure 14.3 shows the deformation results which have been calculated considering gravity and vacuum pump weight as boundary conditions. As the simulation shows, the maximum deformation in the RFQ is less than 10  $\mu\text{m}$ , which is acceptable.

The most important advantage of using jacks is that the design is done and tested. Also, some series are already manufactured by ESS-Bilbao in collaboration with two local partners, so the manufacturing process which guarantees the tolerances required is already defined.



Figure 14.1: CERN-type jack design built by ESS-Bilbao.

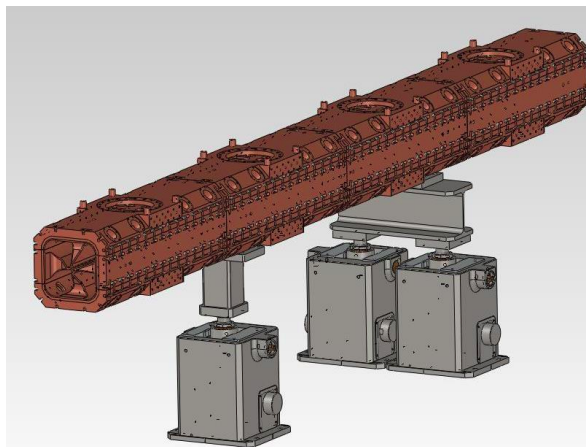


Figure 14.2: CAD image of the RFQ assembled upon the jacks.

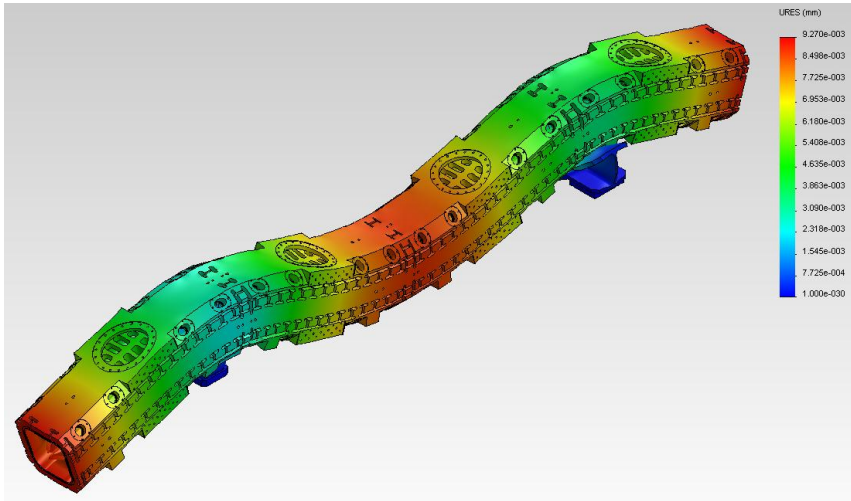


Figure 14.3: RFQ deformation under its own weight and vacuum pumps.

## 14.2 Vanes assembly

Once the four vanes are manufactured, the next step is to assemble them. In the assembly operation there are two main design issues concerning the vane to vane alignment and the chosen method to tie them up. On the latter issue, we found the bolted option based on ISIS. Figure 14.4 shows how bolts are distributed along the RFQ.

In order to achieve the vacuum level required along the RFQ, a polymeric gasket is used. This polymeric gasket geometry is shown in Figure 14.5. This gasket is built by 4  $\phi 6$  o-ring along the RFQ which are glued by Loctite 406 with two planar gaskets. The o-rings ensure the vacuum between the vanes and the planar gasket between segments. To carry out some tests to verify the vacuum level achieved with the polymeric gasket, an aluminium vacuum test prototype has been built (model and experiments are described in section 14.4).

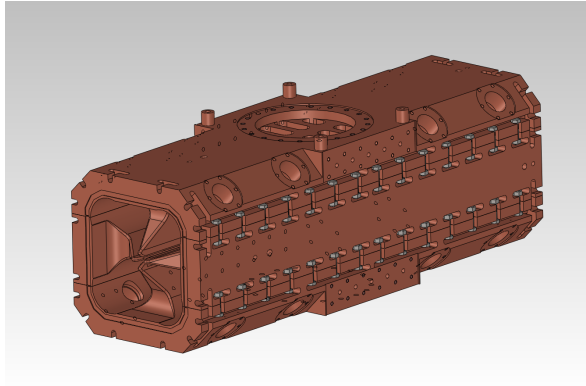


Figure 14.4: RFQ bolted assembly.

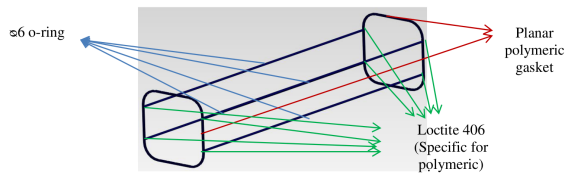


Figure 14.5: Polymeric gasket to be used in the assembly.

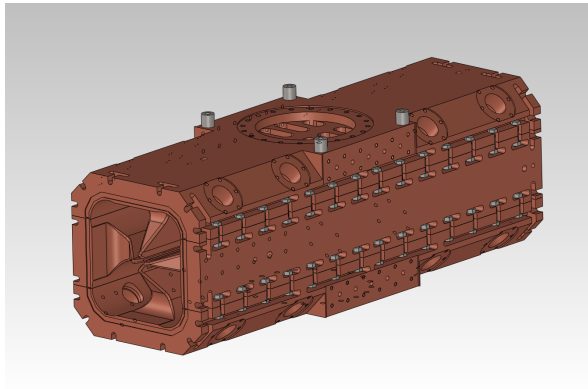


Figure 14.6: RFQ Fiducial points.

### 14.3 Alignment

The alignment of RFQ comprises three different operations:

- Vane assembly and alignment; based on mechanical designs.
- Segment to segment alignment
- RFQ alignment with respect to the beam axis

The design of the support that is a key issue for the alignment has already been discussed in the above section. Now a brief description of the alignment process is shown. The tools to help in the alignment will be the a Laser Tracker and a 3D coordinate measuring machine.

As for the rest of the accelerator components, RFQ will be also aligned with respect to the beam line. Again, RFQ has its own fiducial points (see Figure 14.6). These fiducial points are referenced to the front and rear end of the RFQ beam line by Cartesian coordinates.

In another hand, a lid is manufactured with a hole right in the middle of it to reference the fiducial points with respect to the RFQ beam line which obviously coincides with the centre of the hole. Once the vanes are aligned,

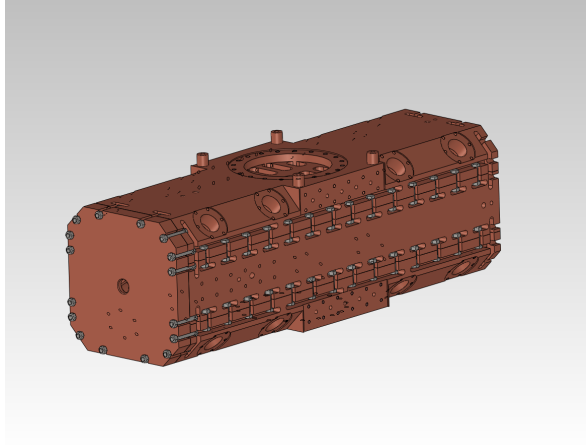


Figure 14.7: Lid with a centre hole.



Figure 14.8: 1.5' SMR with its rod-support.

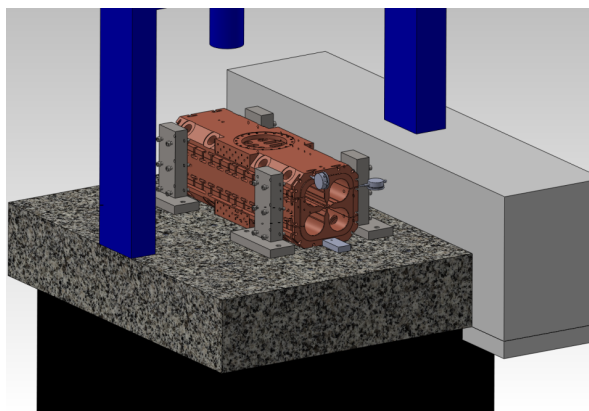


Figure 14.9: RFQ on the CMM for alignment.

it fits perfectly with centre of RFQ vanes as Figure 14.7 shows. This can be proven by using the Coordinate Measurement Machine (CMM).

Using a 1.5' SMR (spherical reflector) with its rod-support (see Figure 14.8) in a continuous measurement with the laser tracker, the circumference of the hole is calculated and consequently its centre. By making this point as a coordinate origin and placing the SMR in each fiducial point, the centre of lid, and so, the centre of the RFQ vanes, will be referenced by those fiducial points. The Cartesian coordinate axes are easy to deduce using those fiducial points. The straight line between them gives two axes, thus, longitudinal and transverse vectors. The plane which is compound by those points has a perpendicular vector which is basically the third axis.

### 14.3.1 Vane assembly and alignment

It is probably the trickiest step and a key issue for the whole alignment. All four vanes are assembled in a CMM machine. Once all vanes are mounted, the CMM machine is used to check the misalignment between the vanes inside the structure. When the misalignment is known it can be corrected using the structure shown in the Figure 14.9 which allows the relative movements between different vanes.

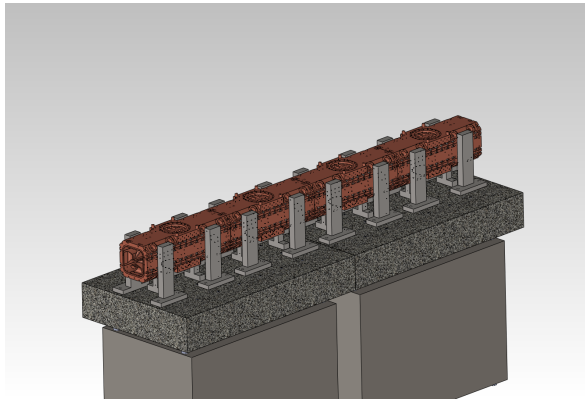


Figure 14.10: Segment to segment alignment. Positioning of the segments on the assembly bench.

To move the vanes, dial indicators are used with a precision of 0.001 mm. This process should be repeated until the tolerance required is achieved.

### 14.3.2 Segment to segment alignment

ESS-Bilbao RFQ is divided in four segments. Before placing and aligning them with respect to the beam line, an alignment between each section is done as it was indicated above in this document. To carry out this alignment, firstly segments are placed on a specific tool (see Figure 14.10) designed with all direction movement and turn. Once those segments are relatively aligned, the laser tracker is used for the accurate alignment, by placing the SMR on each segment's fiducial point. In an analogue way, once the first two segments are aligned, the third segment is aligned and so the fourth. Once all the structure is aligned, the RFQ is tied with the screws. For shifting the whole structure onto the jacks, avoiding deformation or misalignments, handles were created (see Figure 14.11).

When the RFQ is finally situated on the jacks (see Figure 14.2), the alignment with respect to the beam line and therefore with respect to the previous accelerator component (LEBT) is performed, as described in the next section.

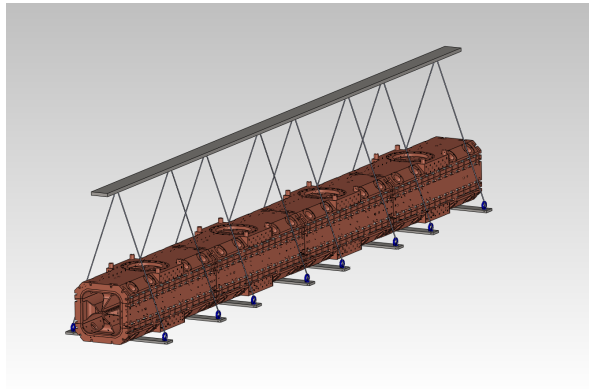


Figure 14.11: Segment to segment alignment. Handles to shift structure on the jacks.

### 14.3.3 RFQ alignment with respect to the beam axis

Once all segments are aligned between them, the whole structure is aligned with respect to the beam line. Again, by knowing the position of centre of the front and rear end of the whole RFQ structure referenced to the fiducial points it is easy to align it to the previous accelerator component, the LEBT. To raise or lower the RFQ, the support itself (jacks) is used as it got three linear axes movement as it was said before.

## 14.4 Aluminium model for vacuum tests

In order to validate the vane assembly method chosen (bolted option), a small aluminium prototype has been manufactured (Figure 14.12). The dimensions of this model are  $260\text{ mm} \times 260\text{ mm}$  (the same external dimension of the final RFQ) and 400 mm long (half of an RFQ segment).

The major risk of this assembly method is to achieve the required vacuum levels. For that a polymeric gasket has been designed. This gasket is built by 4  $\varnothing 6\text{ mm}$  o-rings and specially designed 5 mm depth planar gaskets. All the components are glued by LOCTITE 406 in 8 points (see Figure 14.5). Once the model is assembled, the alignment of the

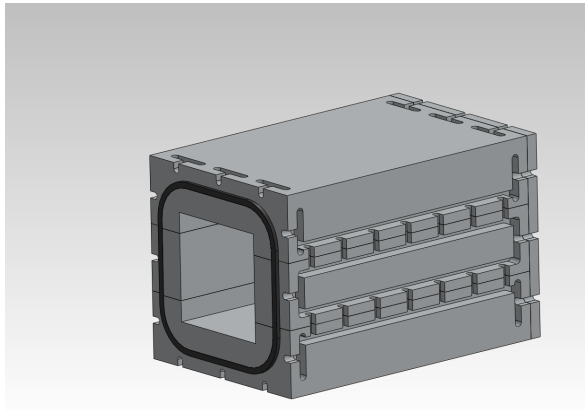


Figure 14.12: RFQ model for vacuum tests design.

model has to be done. For that a CMM is used. When the prototype is perfectly aligned, the assembly is bolted and the 2 lids are also attached (Figure 14.13).

One of the two lids has a DN60 hole in the middle, to be used as a vacuum port. The final model is shown in Figure 14.14. The pump used is a HiPAce 700 model, the same that will be used for the final RFQ. With the assembly shown above, the vacuum level achieved is of  $3.4 \times 10^{-7}$  mbar, in about 5 hours (Figure 14.15).

This good value obtained with a preliminary test give us confidence in the assembly method chosen, but of course the results are not conclusive, and further tests are going to be carried out during following months. These test involve the following aspects:

- Further tests with the same model and different configurations of gaskets, adhesive, etc.
- Modifications in the aluminium cold model that will allow for vacuum tests. This would allow to tests the RF seals also with measurements in vacuum and low power RF.
- Connection of the vacuum test cavity to the aluminium cold model.

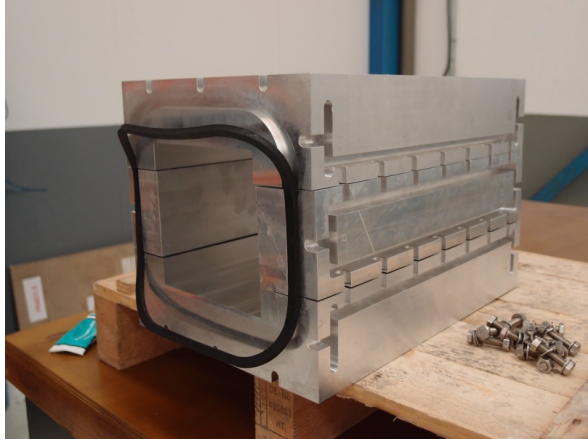


Figure 14.13: Assembly of the RFQ vacuum test model.



Figure 14.14: Model in the vacuum test platform.



Figure 14.15: Pressure level achieved with the vacuum model.

This will allow to test the conditions of the segment to segment connection.

As mentioned above, the experimental work on this subject will continue during following months, and other specific models and tests can be devised to minimise the risk and increase our experience and confidence on the assembly method, but the final (and definite) proof of principle will only be attained when the tests with the first segment of the final RFQ are performed.



## Chapter 15

# Commissioning plan

The main objective of the beam commissioning campaign is to find an operational set-point with the best transmission for the 3 MeV goal energy and the best beam quality in terms of profile and emittance. To reach this goal, it is essential that to precede the RFQ commissioning by an exhaustive commissioning of the Low Energy Beam Transport (LEBT).

The goal of this work is to present a coherent strategy to beam commission the RFQ. It presents the main beam parameters to be measured and the techniques to measure them.

The characterisation of the LEBT, as explained in section 15.5, will give us an configuration for the solenoids and steerer to inject the beam in the RFQ. This configuration is the starting point of the RFQ commissioning. The RFQ commissioning is composed by a mandatory fundamental characterisation (section 15.2) and an optional, but highly desirable, additional characterisation (section 15.3). Not all the measurements required by the commissioning can be (or should be) performed with the nominal beam. Section 15.1 explains which are the beam modes to be used for the commissioning.

Table 15.1: Beam modes.

Mode	Peak current (mA)	Pulse length (ms)	Duty (%)
Tuning	$\geq 2$	$< 0.05$	$\leq 0.05$
Diagnostic	$\geq 45$	$< 0.1$	$\leq 0.05$
Nominal	$\geq 45$	1.5–2.86	$\leq 5$

## 15.1 Beam Operation Modes

Three different modes of operation considered are expressed in Table 15.1. Tuning conditions are defined by a very low current, pulse length and duty. This mode is necessary to tune RF cavities; the RFQ itself and RF cavities installed later downstream.

Diagnostic mode is necessary to adjust all focusing devices, when nominal current is reached. A lower duty cycle is imposed to reduce power deposition in interceptive diagnostics to avoid damage.

Nominal conditions should be reached once machine optimum operational set-point is achieved.

## 15.2 RFQ fundamental characterisation

In order to consider that the RFQ is ready for the commissioning, the following services must be provided:

**Mechanically ready** The RFQ has to be mounted and mechanically aligned.

**Utilities ready** Cooling must be provided and vacuum tight.

**RF ready** Power must be provided and it has to be tuned to the right frequency.

To optimise the working conditions of the RFQ, at least, three beam parameters should be measured: The transmission of the particles with the correct energy; which implies to measure the energy spectra, and the transverse emittance. We foreseen the following steps in the commissioning stage:

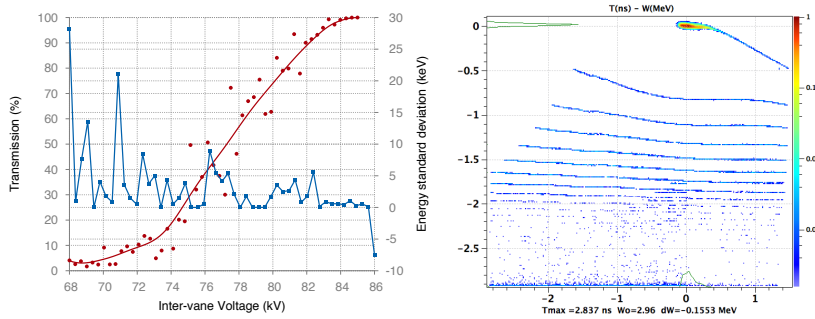


Figure 15.1: **Right:** Transmission excluding the unaccelerated particles in the RFQ, (in red) and mean energy deviation (in blue) value for the accelerated particles bunch. **Left:** Output distribution of particles at the end of the RFQ, when vanes do not reach nominal value, in this particular case  $\Delta V = 80$  kV. Please note that energy output distributions span from the input energy 45 keV to 3 MeV.

1. In order to determine the RF operation curve, and based on the nominal configuration for LEBT solenoids, a measurement of the transmission should be performed. The fraction of the particles that gets accelerated to the nominal energy, can be used to characterise the RFQ, and also to infer the inter-vane voltage (see Figure 15.1).

The measurement of the current at the end of the RFQ is biased with the fraction of particles that get transported to the end of the RFQ with insufficient acceleration; therefore, the energy of the particles should be discriminated in this measurement.

2. Once the nominal RF operation conditions have been established; a 6D  $\{B_1, H_1, V_1, B_2, H_2, V_2\}$  scans of the solenoids and steerers along the LEBT should be performed again to fine tune the optimum transmission.

This optimisation should not achieve only the highest transmission, but it should analyse the *Courant-Snyder* parameters of the beam and the test that the beam is centred in the transverse phase space.

### 15.3 RFQ additional characterisation

Once the transmission curve has been characterised, additional features related to the beam quality at the exit of the RFQ could be measured: Transverse profile, halo and emittance, both transverse and longitudinal.

### 15.4 Beam diagnostic techniques and devices

Chapter 8 shows the initially intended Test Stand to use in the RFQ commissioning. The change of the scope of ESS Bilbao in 2014, implies that a new strategy should be used for the RFQ commissioning. The maximum energy of the beam to be measured will be reduced from 12 MeV (the energy of the first tank of the planned DTL) to 3 MeV. This circumstance will relax the working conditions of the diagnostic instrumentation.

We foreseen two scenarios in the diagnosis of the RFQ output beam (Figure 15.2):

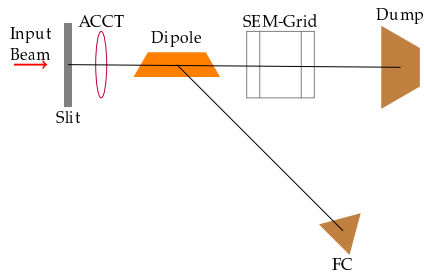
- We can build a more compact Test Stand built to measure properties needed for the fundamental characterisation; i.e, current, beam energy spectra and transverse emittance.
- We can use the set of diagnostic instrument in the MEBT<sup>1</sup> that will be installed downstream the RFQ. The MEBT will be equipped with current transformers, beam position monitors, wire scanners, non-invasive profile monitors, an emittance meter unit and a beam shape monitor. This makes the MEBT a valid baseline for the RFQ commissioning.

We will revise the usual techniques [63] to measure the main beam parameters and see which parameters could be measured using the compact Test Stand and which ones with the MEBT:

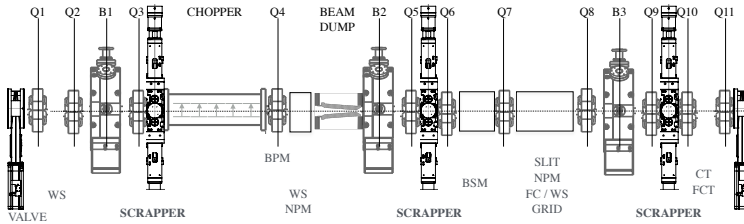
**Current** The comment about the current measurement diagnostics in Chapter 8 is still valid. Current should be measured by current transformers in both scenarios. To calculate the RFQ transmission

---

<sup>1</sup> The MEBT is part of the ESS-Bilbao contribution to the ESS project.



(a) Compact Test Stand for the RFQ fundamental parameters' characterisation.



(b) Present layout of diagnostic instrumentation in the ESS MEBT.

Figure 15.2: RFQ commissioning diagnostic instrumentation options.

the current transformers should be cross-calibrated with the one used at the input of the RFQ.

The compact Test Stand should be equipped with a current transformer. The MEBT will have several of them.

**Beam energy** The mean beam energy could be measured by this two techniques:

**Sector Magnet:** The ions with the same mass-to-charge ratio  $m/q$  are separated according to their kinetic energy. If an ion moves into a magnetic field with direction perpendicular to the field, it will follow a circular path according to the formula  $r = mv/qB$ , where  $B$  is the uniform magnetic field and  $m$ ,  $q$  stand for mass and charge of each specimen. This technique allows not only to measure the mean energy, but also the energy distribution of the particles.

**Time of flight:** The measurement of the velocity of a non-relativistic particle is related to the kinetic energy  $W$  as  $W = m(\beta c)^2/2$ . Thus, the equation  $\Delta W/W = 2\Delta\beta/\beta$  links the accuracy in energy with the accuracy in the reduced velocity  $\beta$ . The velocity is calculated by measuring the time-of-flight (TOF) of a beam bunch over a know distance  $L$ . We can measure this time  $t_f$  by means of two synchronised diagnostic devices located in the two ends of  $L$ . For a pulsed beam, we can infer the beam energy by measuring the time difference measured. The velocity for a flight length  $L$  is  $\beta c = L/t_f$ .

The TOF technique could be implemented in the MEBT by 3 BPMs, but it only give us the mean energy of the beam. To optimise the RFQ based on the current of particles with the proper energy, the beam energy distribution should be measured. Thus, we believe that the use of a sector magnet is necessary.

**Transverse emittance** This emittance can be measured in the following two methods:

**Slit-Grid** In this method the position  $x$  is fixed for one direction with a thin slit having an opening of typically 0.1 to 0.5 mm.

In the perpendicular direction the full beam is transmitted to get a large signal. The angle  $\chi'$  is determined with a SEM-grid having a distance from the slit of 10 cm to 1 m depending on the ion velocity. The slit is then scanned through the beam to get all positions and, thus, reconstructing the phase space. At the moment of writing, it is foreseen that the ESS MEBT will be equipped with such an emittance-meter unit.

**Quadrupole scans** The emittance can be determined from a series of profile measurements, either by changing the focusing strength of a quadrupole, or by measuring the profile at three or more positions along a transfer line. Linear transformation of the phase space across the optical elements can be computed. Starting with a given emittance at the input of a transport line, the beam profile is calculated along the line. If the profile is measured, one can calculate the emittance at the input of the line by using the inverse transformation.

This method is based on linear transformations and conservation of the emittance during the manipulation. Moreover, an elliptical shape of the emittance is assumed. This is a good assumption as long as non-linear effects, like space charge forces, are low. If the calculations are done with intense beams, an emittance blow-up may occur, depending on the particle density, i.e., on the In this case self-consistent algorithms have to be applied to get an estimation of the emittance at the quadrupole entrance.

The MEBT will have different means to measure the beam profile and can complement the slit-grid method described above.

This two methods could be used with the MEBT. In the case of the compact test stand it seems easier to implement the slit-grid method, because there is no need for any magnetic element.

**Beam position** The position of a beam is usually determined with pick-up plates. The idea is to measure on an insulated metal plate the charges induced by the electric field of the beam particles. The application is to determine the beam position (centroid). For this, four

pick-up plates are installed and the difference of the signals yields the centre-of-mass in both transverse axes. This device is known as Beam Position Monitor (BPM).

As opposed to the compact Test Stand, the MEBT will be equipped with various BPMs along the line.

**Transverse profile** It is important to measure the beam profile to control the beam size. Thus, it should be measured not only in the commissioning phase, but also in operation. Therefore interceptive (Wire Scanners) and non-interceptive techniques (Beam Induced Fluorescence) will be implemented in the MEBT.

In the case of a compact Test Stand equipped with a SEM grid, it is possible to use it to measure the beam profile; even if its resolution is worse than of a wire scanner.

**Longitudinal emittance** The longitudinal emittance can be measured in a similar way as the 'quadrupole scan' used to measure the transverse emittance. In this case, the amplitude of a buncher is varied and the bunches are measured by pick-ups.

The ESS MEBT has the necessary elements to implement this technique, but the compact Test Stand will not be adequate.

**Halo** Transverse halo development could be measured by comparing the remaining current for different penetration of the scrapers ( $\sigma_x, y$ ) allocated in three different positions along the MEBT.

The ESS MEBT has the necessary elements to implement this technique, but the compact Test Stand will not be adequate.

In summary, the ESS MEBT will be able to measure almost all the essential beam parameters and others. But it still could not be able to measure the current of the particles at the targeted energy; and we believe this is a mandatory need to properly optimise the RFQ.

Table 15.2 shows different techniques for measuring beam characteristics, along with the estimated resolution required for a 3 MeV  $H^+$  base on the requirements of LINAC4 [64, 65].

Table 15.2: Measuring options and resolutions.

Beam characteristic	Technique	Resolution
Beam position	BPM	0.1 mm
Beam intensity	Current transformers	1 % of peak
Transmission & Energy	Time of Flight Spectrometer	1/10 <sup>3</sup>
Transverse Emittance	Slit and Grid Tomographic reconstruc. Quadrupole scan	0.5 mm/0.5 mrad
Long. bunch shape	Bunch Shape Monitor	1°
Energy Spread	Spectrometer	5 KeV/mm

## 15.5 LEBT: a preparatory phase

Before the RFQ is installed, the beam behaviour along the LEBT should be understood and reasonably explained by particle tracking codes. An output of the RFQ that is not as expected and can not be tracked down has to be avoided at all costs. According to other colleagues' experience, all the time invested in the LEBT commissioning stage is a must, because: 'once the RFQ is installed, it becomes impossible to check the input beam and we must avoid the situation where output beam from RFQ is not as expected or losses are too high and finally we aren't able to know where the problem come from.' ([66])

The foreseen plan is to create a cartography map for LEBT in order to highlight nominal settings. For such endeavour, the following three intermediate steps (see Figure 15.3) are considered:

**LEBT #0** (from Oct 2013 to May 2013) Ion source characterisation with first diagnostic vessel. No solenoids.

**LEBT #1** (present configuration) One solenoid, two diagnostics vessels before and after the solenoid.

**LEBT #2** Complete set-up: two solenoids, three diagnostics vessels before and after solenoid each solenoid.

In the following sections we will describe the steps we already done and the planned ones.

### 15.5.1 LEBT #0

Along this stage some important parameters related to the ECR ion source were measured: among others, correct pressure levels in the plasma chamber, hydrogen flow levels, and plasma chamber magnetic profiles. This functioning map is essential to guarantee the required pulse stability in terms of current and time structure. In the first diagnostic vessel, extracted beam current was measured by means of a current transformer. Transverse beam profile was also characterised by means of a wire scanner. A residual gas luminescence profile monitor was also set up and compared with the wire scanner (see Figure 15.4).

The residual gas luminescence profile monitor relies on the proton beam's excitation of the residual gas particles, which then emit light while de-exciting. This light can be gathered and processed. The key advantage of this method is that no components have to be installed inside the vacuum system. The disadvantages are the rather low cross section and collection efficiency. For this reason, residual gas pressures above  $10^{-7}$  mbar are recommended.

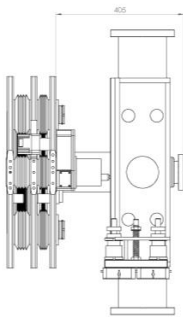
The luminescence light from the interaction is imaged with a PI-MAX:1K high speed camera with  $1024 \times 1024$  pixels, a 16-bit monochrome sensor and a Nikon 45 mm f/2.8 lens. *Reliability estimation* can be obtained taking into account that this type of counting problem will be governed by Poisson distribution  $\text{prob}(N|D) = D^N e^{-D}/N!$ .

### 15.5.2 LEBT #1

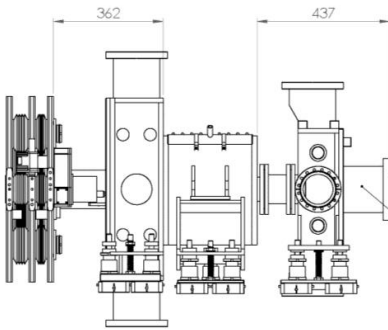
LEBT #1 stage is determinant to characterise the beam quality by the ECR ion source to the LEBT, in terms of emittance and transverse profile.

In order to improve the input distribution, a campaign to find the optimum accelerating gap distance<sup>2</sup> was carried out. For each gap distance, the right configuration settings for the ion source must be also found.

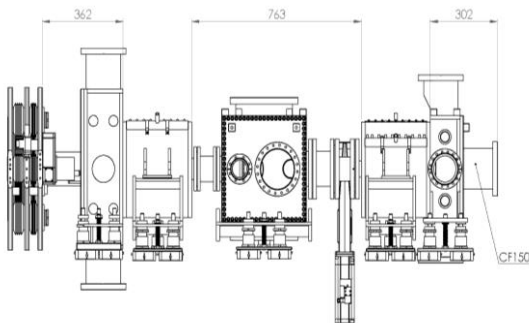
<sup>2</sup> This particular ECR ions source column extraction is movable and can be adapted for the extraction voltage.



(a) LEBT #0



(b) LEBT #1



(c) LEBT #2

Figure 15.3: LEBT Commissioning stages.

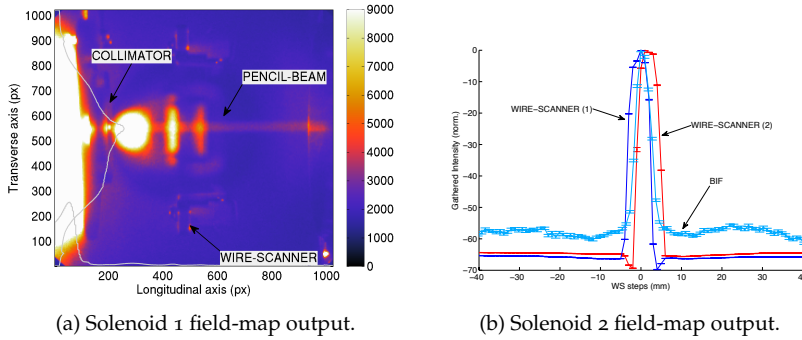


Figure 15.4: **Left:** Image produced by the fluorescence of the residual Hydrogen in the first diagnostics vessel of LEBT. **Right:** Cross section of the beam measured with both wire-scanner and non interceptive fluorescence methods.

Considering a 45 kV extraction voltage, an input RF power of 600 W that feeds the plasma chamber, a repetition rate of 10 Hz, 1.5 ms pulse length, a  $-1.25$  kV voltage for the suppressor electrode, and a regular Hydrogen gas flow to obtain a  $\sim 10^{-5}$  mbar pressure in the first diagnostic vessel.

This campaign showed that the shorter the gap the higher the beam current was; but the optimum transmission of the LEBT was around 9 to 10 mm.

Once the accelerating gap distance is fixed different campaigns to optimise beam quality along the LEBT will be carried out:

**Neutralisation Gas.** Space charge compensation (SCC) with extra gas injection is a high-efficiency method to reduce space charge effect (SCE), this increases with the increase of ion beam intensity and with the decrease of the ion beam energy. Kr and Ar gases have larger ionisation transverse cross section respect to  $H_2$  [67], this characteristic is directly related to  $H^+$  beam space charge compensation. Other gases are usually discarded for safety reasons. This additional neutralisation gas injection is expected to improve both beam quality and loss rate along the linac [68]. Gas injection location should be the source extraction region where the beam intensity and density are the highest [69, 70].

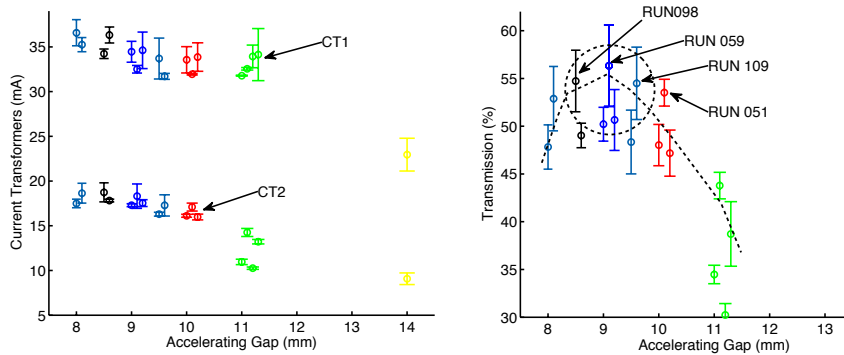


Figure 15.5: beam current in the first (CT1) and second (CT2) current transformers (left) and calculated transmission (right) for various acceleration gaps and plasma configurations with LEBT solenoid at 10 A.

Along this process, an equivalent numerical model that is in good agreement with actual beam measurements must be found. Moreover, the transverse emittance values will be measured at the end of the LEBT, at the last diagnostic vessel by means of a pepper-pot system. Depending on the results obtained here, vessel #1 might be removed; in order to shorten the distance from the plasma electrode to the first solenoid. This is a known way to improve both transmission and beam quality along the LEBT. Unfortunately, removing the first diagnostic vessel implies the renounce to the best possible location for neutralisation gas inlet, among other diagnostics.

**Suppressor voltage.** Once the gap distance is fixed, a similar procedure, measuring the beam waist size in the first vessel must be found for different combinations of repeller and residual gas (Kr). The function of the *middle* electrode between the two grounded electrodes is to inhibit the back-flow of electrons into the ion source from the downstream region. This *suppressor* electrode is held at a fixed negative voltage at the order to 5% of the extraction voltage. The suppression electrode also reduces X-ray radiation caused by back streaming secondary electrons that get accelerated and collide with the source.

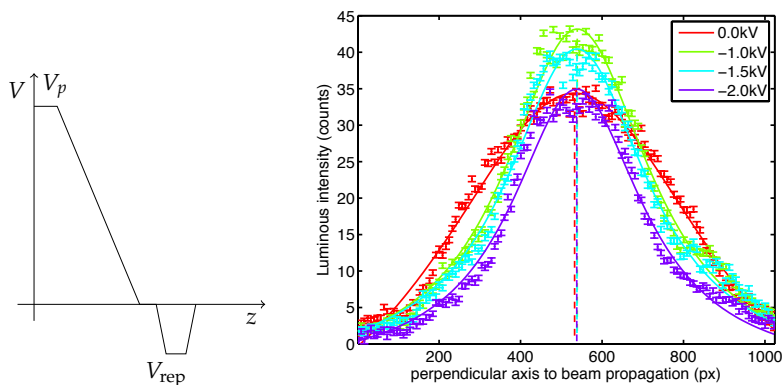


Figure 15.6: **Right:** Extraction potential diagram. **Left:** transverse cuts in the *beam region* measured at 50 Hz by the PI-MAX high speed camera.

This *Accel-decel* system —where positive hydrogen ions are accelerated in the first and decelerated in the second gap; preserves the space charge compensation of the extracted beam after this second electrode. Lining the plasma chamber with the boron nitride disks discourage the recombination of hydrogen atoms into molecules, enhancing thus, the proton fraction of the ion source [71].

An initial measurement of the beam profile with suppressor voltages varied from 0 to  $-1500$  V is shown in Figure 15.6.

**Transverse Emittance measurements.** In the last step of this LEBT configuration a pepperpot system will be installed in last diagnostic box. Measuring the transverse emittance of the beam is, probably, the most important beam benchmark.

Given the importance of the measured parameter, there is much controversy when processing and analysing transverse emittance. In order to prove that the employed algorithm lacks of any bias. A specific well known beam has been generated, and analysed by means of the data gathered with this virtual pepper-pot. The layout of this pepper-pot is made of a 2 mm block of Cu ( $\phi 2$  mm) followed

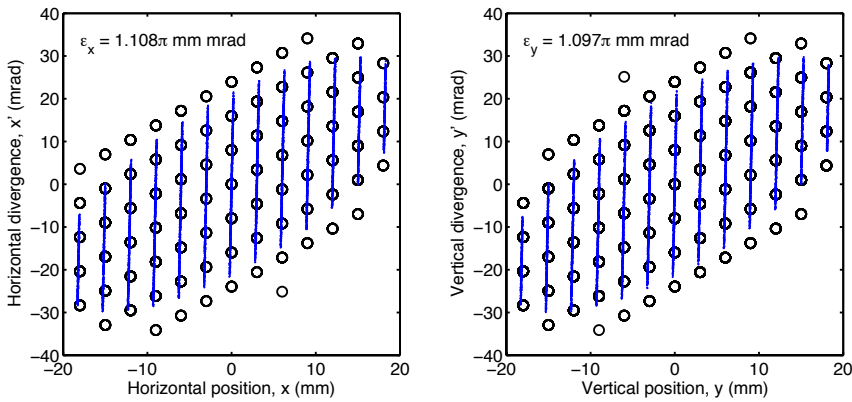


Figure 15.7: Reconstructed beam characteristics (black circles) compared with the originating beam source (blue dots).

Table 15.3: Beam parameters ( $\mathbf{x}/\mathbf{y}$ ).

Parameter	generated	reconstructed
Emittance <sub>n</sub>	1	1.107/1.097
CS <sub>α</sub>	-1	-0.777/ -0.780
CS <sub>β</sub>	1	0.909/0.913

by a 0.5 mm tungsten layer ( $\phi 0.1$  mm) and finally collimated by a 10 mm long Cu block  $\phi 2$  mm. In all cases the  $13 \times 13$  grid is separated by 3 mm.

Figure 15.7 represents the reconstructed beam by the algorithm. The slight discrepancies on the root-mean square parameters are within the precision one can obtain with this experimental setups ( $\sigma_x \approx 10$  mm and  $\sigma'_x \approx 10$ ). Reconstructed parameters compared to the actual ones are summarised in Table 15.3.

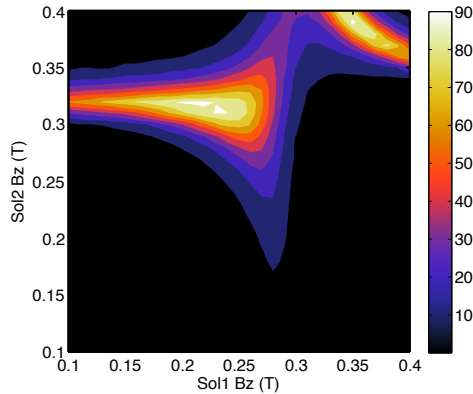


Figure 15.8: Transmission at the end of the RFQ represented as a colour map, where axis represent the employed on-axis magnetic longitudinal component.

### 15.5.3 LEBT #2

Once arrived to the last stage, and with the acquired knowledge; it is our intention to create a cartography map for LEBT under nominal settings, and compare it with numerical codes, as represented in Figure 15.8.

The last stage of the LEBT will be crucial to obtain a well aligned beam at the entrance of the RFQ. Here, the required combination of steerer power supplies for each combination of  $B_{z1}$ ,  $B_{z2}$  will be determined, defining thus the 6D solution space:  $B_{z1}$ ,  $H_1$ ,  $V_1$ ,  $B_{z2}$ ,  $H_2$ ,  $V_2$ . In order to find the right combinations of pair of steerers, a beam collimator at the entrance of the LEBT will be employed in order to produce a pencil beam to assure the perpendicularity of the beam at the entrance of the RFQ.

In each stage, the number of diagnostics elements, as well as the number of solenoids is increasing, as indicated in the suffix. This contributes to an appropriate learning curve. Allows to identify each diagnostic electronic behaviour; data acquisition system to EPICS, and from there to the HyperTable database by means of the HyperArchiver software. In particular, except the diagnostics related to the PIMAX camera; the rest of the information can be easily traced back and correlated by means of a set of python scripts that extract the information to be cross-processed.

## Chapter 16

# Open questions and future steps

The discussion and all the work done following the comments and recommendations of the Technical Advisory Committee have improve a lot the know-how of the ESS-Bilbao team on the subject of RFQ designing, building and future operation. This document has intended to summarise the work done and the results obtained but it is clear that in many aspects what is presented is only a direction arrow pointing us in the right way. As mentioned in the introduction, this report represent just a milestone and much work still has to be done to improve our understanding of the RFQ. This work will proceed in the following months or years.

Some of the aspects where we have to continue working are:

- Errors study. Many work has been done on this subject, but has not been considered for this document. Anyway, a lot of work on beam dynamics in connection with mechanical errors, thermal expansion of vanes, perturbed field maps, etc.; has yet to be done.
- Extend FEM models to the whole length of the RFQ. This will complement the work done on the mathematical model of the RFQ
- Further development of the mathematical model. The model has

to be improved to consider more realistic voltage baselines and to validate it with FEM simulations and the experimental work done with the already built cold model.

- Continue the work done on the thermal tuning of the cavity, to better understand its effects on fields and to define the characteristics of the control loops during operation and during power on transitorities.
- Define a more precise tuning procedure strategy making use of all the above tools. This includes also the design of tests (bead pull tests, tuned covers for segments ends to measure individual segments, ...) and the procedure or protocol for the cavity tuning.
- Continue the practical work on the cavity assembly and vacuum and RF gaskets, improving our confidence on this assembly method. The aluminium models already built (cold model and vacuum tests model) will be used for this purpose.

## Chapter 17

# Overall conclusions

The RFQ design presented in July 2013 has undergone a strong redesign process following the recommendations of the Technical Advisory Committee. The results of the activities done to implement the recommendations are presented in this report. Some recommendations (shorter RFQ, 2-term modulation, cavity frequency, tuning scheme, ...) have been implemented in design, that has consequently changed strongly. Other design options, like the round shaped quadrants and the bolted assembly strategy, have remained as in the previous design, but the reviewers recommendations have been taken into account and the design decisions are more documented.

All in all, the work done following the recommendations and comments of the reviewers have improved very much the knowledge and confidence of the ESS-Bilbao team on the RFQ design, fabrication and future operation.



**Part VI**

**Appendices**



# Appendix A

## Budget (2013)

### A.1 Schedule

The design stage (see Figure A.1) can now be considered as complete, exception made of some relatively minor issues which, as referred to within the text, will be settled once the pending measurements carried out on the cold models, are finished. The work carried out on cold models and other prototypes which was started in 2010, has been essential for scrutinising the results obtained from computer codes against real, manufactured components. It also has allowed to develop skills on manufacturing, metrology and RF measurements. We are fully aware of the role that high precision machining process plays in the building process, and on such grounds, a close collaboration with local manufacturers has been established. On our side, preparations to build a stand for high power RF conditioning as well as to develop a consistent set of diagnostics,<sup>1</sup> are now underway.

---

<sup>1</sup> Beam current, position, average energy and dispersion, emittance, species composition

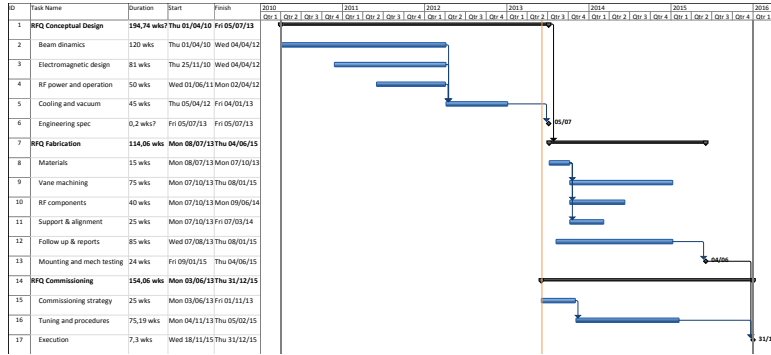


Figure A.1: Gantt diagram for the RFQ project.

Table A.1: RFQ budget

Concept	Estimated
<b>Conceptual Design</b>	<b>700 000 €</b>
Electro Magnetic and Thermo-mechanic design	600 000 €
Prototypes: Weld-Test Models, Cold-Model	100 000 €
<b>Fabrication</b>	<b>982 000 €</b>
Material	30 000 €
Machining	500 000 €
Alignment and assembly	200 000 €
Structure	100 000 €
Cooling	60 000 €
Vacuum	90 000 €
Shielding (commissioning)	2 000 €
<b>RF</b>	<b>2 093 000 €</b>
Control and Diagnostics	250 000 €
Tuners and Pickups	75 000 €
Coupler	250 000 €
RF power	1 400 000 €
RF Transmission	118 000 €
<b>Total</b>	<b>3 775 000 €</b>

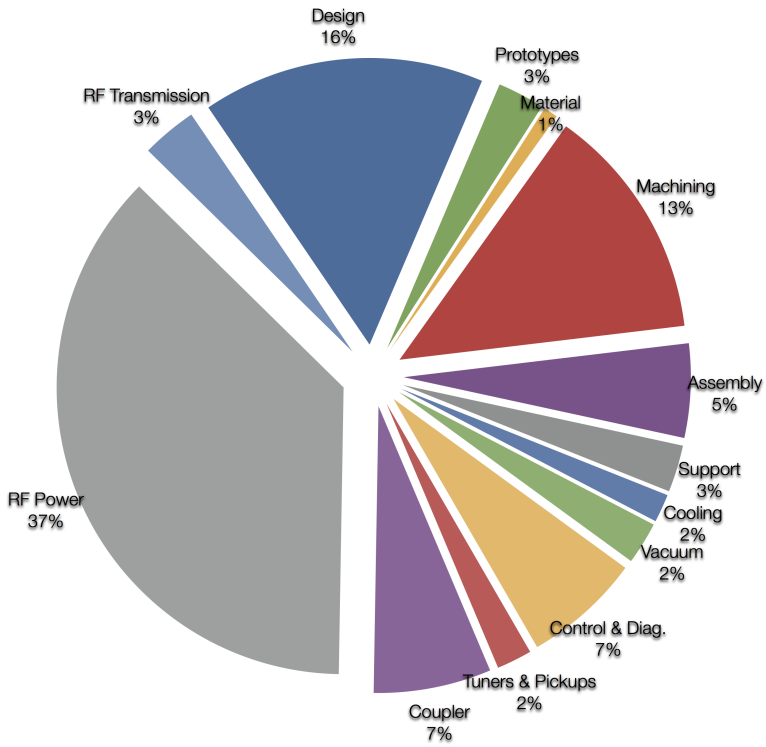


Figure A.2: Budget estimated for the RFQ project, broken down as percentages.

## A.2 Budget

Table A.1 and Figure A.2 show the cost estimation for the RFQ design and construction, three units stand above the rest: RF, which includes klystron, modulator, coupler and RF tuning of the structure. High precision machining and assembly. Finally, engineering design and prototyping.



## **Appendix B**

# **ESS-Bilbao RFQ Technical Design Review Report (2015)**

### **Introduction**

As a member of the European Spallation Source Collaboration the main goal of the Bilbao RFQ project is to drive and channel the Spanish contribution to ESS. The Bilbao team is in the process of negotiating a work package which will bring added value to Spain and the Basque Region and their respective industrial base as well as develop local expertise in accelerator technology. The team's primary objective is to complete an RFQ that can deliver a representative proton beam to test beam-line components that Bilbao has contracted to deliver to ESS.

The Technical Advisory Committee (TAC) heard several presentations in Bilbao on September 29, 2014, summarizing the work of the RFQ design team in response to comments provided by the TAC following last year's review. These presentations covered all aspects of the design effort including the beam dynamics design, the design of the resonant structure, and the mechanical design of the cavity. Also included in the review were discussions of supporting subsystems including vacuum, cooling, resonant control, support and alignment. The primary charge to the committee was

to review the technical aspects of the linac design and to assess its overall maturity.

## Specific charge to the committee

The committee was asked to submit a written report addressing the following questions.

1. Is the RFQ design, as described in the technical documentation, technically sound and mature enough to proceed towards an engineering detail phase and subsequent construction?
2. For the forthcoming engineering detail, manufacturing and commissioning steps, is there any particular item that, according to past experience, could become a bottleneck and therefore require some special attention?

## Executive Summary

Following last year's review, the TAC made a number of specific recommendations for modifications to the RFQ design. We are positively impressed by team's response to our recommendations and the work subsequently carried out in a difficult situation (change in management). We observe a significant improvement in the present design, reflecting a constructive response to the TAC's comments and the professional attitude of the team.

The new design has been described to the TAC members from various approaches: beam dynamics, electromagnetic cavity design, mechanical, cooling, vacuum and alignment plans. The team was also responsive to the various questions posed during the meeting.

The TAC concurs that the 2014 RFQ design is mature enough to proceed to the next phase, engineering detail and construction. It has not identified any particular items in the present design that would compromise its performance as a part of a beam-line test bed.

## B.1 Modulation and Beam Dynamics

**Findings:** Last year's TAC made the following specific recommendations:

- Reduce the injection energy
- Shorten the RFQ by 20 %
- Use the 2-term potential function to define the longitudinal vane tip profile

Design studies revealed that lowering the injection energy does not significantly reduce the overall length of the RFQ however it does make the injector more reliable and easier to operate. The injection energy has been reduced from 75 to 45 keV.

To shorten the RFQ required reducing the aperture of the structure while maintaining a flat field. This required a 'trade-off' study comparing length, peak surface electric field,  $E_{\text{peak}}$ , and transmission. The overall length has been shortened by deriving a 3rd order function of longitudinal position to define the aperture while avoiding 'bottlenecks' at either end of the accelerating section. Following this prescription the overall length has been reduced from 3.9 to 3.12 m, a 20 % reduction. The design assumes a flat axial electric field distribution. To achieve a flat field requires a uniform capacitance per unit length between adjacent vanes which translates into a flat frequency distribution. Using a sinusoidal shape for the vane-tip modulation, used in the previous design, resulted in a frequency 'excursion' as the modulations increased that would exceed the range of the slug tuners to correct. As a result the design has been modified to follow the 2-term potential function with a constant  $\rho/R_0$ .

To support this design approach the RFQSIM codes were modified to support the 2-term potential modulation in both generating the vane geometry and the resulting fields applied in beam simulations. As a result, a new RFQ design has been defined based on the 2-term potential.

To verify the rigor of the new design it has been examined using 4 different but complimentary computer codes. The figures of merit;

transmission, emittance growth and  $E_{\text{peak}}$ , calculated by the 4 codes are not only within acceptable ranges but are in good agreement with each other. The results for 3 codes are in excellent agreement.

The transverse focusing factor,  $B$ , is flat and is not ramped at either end of the RFQ. The exit transition cell creates a circular beam that is matched to the ESS MEBT.

Transmission (accelerated to 3 MeV) has been simulated as a function of input beam current, input beam match, vane voltage, input energy and initial emittance. All are within reasonable operational expectations. The zero-current transverse acceptance was calculated and compared with the matched input beam emittance at full current.

**Comments:** The rigor of the new RFQ design appears to be adequate by virtue of testing it with multiple codes. The transmission study indicates that the beam performance should be adequate. Using acceptance as a figure of merit for the design is probably misleading because both the design and beam performance are typically dominated by space-charge effects.

The designers should investigate the feasibility and benefits of introducing a small ramp in  $B$  at both ends of the RFQ. This will ease both the input and output matching but have minimal impact on the overall design, affecting only the 3-D end regions. While the design approach follows the committee's recommendations, further error studies will be necessary to define the fabrication tolerances required for the detailed drawings.

The output parameters of the beam from this RFQ, including the output emittances, are remarkably close to those of the ESS (Sweden) design (but for a much shorter RFQ). This is a significant advantage to the Bilbao team for testing any MEBT components and one could argue that it would serve as a valuable test facility for the entire ESS MEBT.

The new design has been optimized to operate at a peak surface electric field 1.85 times the 'Kilpatrick' limit ( $E_{\text{peak}} = 1.85E_k$ ). This value exceeds the classical design value of  $1.80E_k$  which is nominally the limit for CW operation in furnace-brazed structures. In the present

case, with a duty factor of  $\leq 4\%$  this value is acceptable. During detail design of the cavity, care must be taken to avoid any local increase in this value, especially at longitudinal interface between vane segments. While operation at such a high field levels has been demonstrated in furnace-brazed structures and special care must be taken to assure clean smooth surfaces in the high field regions. Surface preparation procedures must be clearly defined in the technical specification of the call for tender.

It is common to operate RFQs at fields higher than the design field levels to compensate for fabrication errors. It is therefore not wise to assume that operating at a lower field level to avoid sparking is an option.

**Recommendations:** The committee concurs that the RFQ physics design is now mature and well optimised. The RFQ is shorter in length, the effect of the modulation on field flatness has been minimised and the expected beam transmission is consistent with similar RFQ projects. The additional simulations performed in the last year have allowed an in-depth analysis of the beam dynamics issues that appear now to be well under control. The lower transmission predicted by one very particular tracking code should not be viewed as a shortcoming of the design.

While the physics design is now mature enough to begin the detailed mechanical design and fabrication, more simulations would be useful, to verify the stability of the design for various fabrication or tuning errors or different input beam parameters. Transporting a 'realistic' particle distribution, derived from LEBT beam measurements, should be given high priority.

The committee recommends operating the injector as soon as possible to test the feasibility of providing a matched beam to the RFQ. In addition running as many hours as possible will help

minimize the potential for difficulties arising once the beam commissioning begins (e.g. energy, focusing and steering stability).

## B.2 Electromagnetic Cavity Design

**Findings:** Last year's TAC made the following specific recommendations:

- Review the mechanical, operational and cost benefits of the round-quadrant cavity vs. a more conventional octagonal design
- Review the dynamic frequency control options, i.e. mechanical tuners vs. temperature/flow control
- Develop a mathematical model of the cavity to better understand the effects of perturbations and tuners and to develop a tuning scheme
- Pursue a single power coupler prototype
- Extend the cold model to at least 2 segments

While the team carefully reviewed the benefits of an octagonal cavity cross section they have decided to retain the circular quadrant design with some modifications. The primary reasons for retaining the circular design were based on the investment already made, not only the mechanical design details, but the fact that the Copper had already been purchased. The detailed quadrant design was modified to have parallel sides on the vanes to facilitate machining and provide convenient alignment references.

The resonant frequency of the cavity was changed from 351 to 346 MHz with the tuners flush with the walls to ensure tunability along its entire length. The frequency would be 350 MHz with the slug tuners inserted half way (in frequency) at 25 C.

A 3-D electrodynamic model of the RFQ has been created by 'extruding' the 2-D cross section and adding the radial matching and output sections. The model has been used to access the effects of tuners and other cavity perturbations. The vacuum grid was modified to compensate its perturbation on the local frequency.

The current design has abandoned dynamic mechanical tuners which have the drawback of effecting the field distribution. Fixed slug tuners will be used for static tuning to compensate for fabrication and

assembly inaccuracies. The cavity frequency will be maintained in operation using a dynamic frequency control loop on the temperature of the cavity coolant.

A mathematical model, based on classical transmission line theory, has been created. It takes into account the perturbations coming from the frequency profile and tuners, but as yet does not include the dipolar modes.

The team is now concentrating on the 'drum' type power coupler while further development of the 'nose-cone' design has been deferred.

**Comments:** The new design simplifies the machining and alignment while keeping the original round quadrant design. We understand that this choice preserves the experience already invested in the circular quadrant design.

The mathematical model will need to be further developed in order to support the RFQ tuning. In addition it should be used to provide realistic field errors for the beam dynamics error studies needed to derive the mechanical fabrication tolerances.

**Recommendations:** The committee finds that retaining the circular quadrant design acceptable when compared with the effort and potential benefits of an alternative shape.

Both the tuning strategy and the new design frequency are correct and should permit the tuning of this RFQ. Dynamic frequency control using temperature control of the cavity coolant will result in a much more stable operation.

The mathematical model must be extended to include all 4 segments to simulate the frequencies of the modes that lie close to the operating mode. In addition it should include the effect of the dipole rods that will have a strong impact on dipole modes. With the exception of the dipole rods that impact only the end cells, the electromagnetic design is ready to launch the construction of the RFQ. The model will be a crucial tool in simulating complex tuning conditions and developing tuning strategies.

During the tuning process remember to make the bead-pull measurements at the operating temperature (26° C) in 'dry' air. Final tuning should be made using the Copper end walls.

A difference often observed between the field distribution using Aluminium 'dummy' tuners and the final Copper tuners is frequently attributed to the difference in conductivity of the metal. It is more likely due to a difference in their electrical length as defined by the method of contact between the tuner and the RFQ body. Care should be taken to make the contact in the two cases as similar as possible.

The committee believes that a one-segment long cold model is too short to get an empirical feeling for the complex mode structures in an RFQ and to adequately develop and test tuning schemes. However we understand that within a fixed budget other activities must take priority and that supplementing the current cold model with full length numerical models offers an adequate alternative at an acceptable risk.

### B.3 Mechanical Design

**Findings:** Last year's TAC made the following specific recommendations:

- Vacuum relief channels are required to be able to qualify the polymeric vacuum seals.
- A relief (gap) of  $\sim 0.2$  mm between all adjacent conducting segments should be added to limit the risk of creating a poor rf contact everywhere a RF join is foreseen.
- The design of the end plates is not mature, and does not take into account the possible requirement for quadrupolar or dipolar corrections. They should accommodate bead-pull measurement in the final assembly.
- The two cooling channels seem too close to each other and could be optimised to provide an automatic frequency cancelling effect has a function of the duty cycle. The water flow seems a little too high.

- The key point for the entire project is the use of polymeric gaskets. This unconventional and innovative joining scheme constitutes a risk for the project, however the schedule leaves margin for testing and validating the scheme.
- This RFQ does not have a well-defined long-term use, indicating that the unavoidable deterioration of the polymer with time is not a concern.

The cavity cooling and frequency control as described above will be based on dual deep-drilled coolant channels in each vane. Water-cooled slug tuners will be used solely for static tuning as discussed above. The cavity will be designed and tuned to operate at a nominal temperature of 25 C.

FEM simulations have been carried out to map the expected temperature and deformation of a single cavity segment. The model shows a linear dependence of frequency on duty factor at constant coolant temperature.

The RFQ will be mounted using a kinematic (3-point) support system with CERN type jacks. Deformations due to vacuum and gravity, taking into account the weight of both the cavity and vacuum pumps, have been calculated to be  $< 10 \mu\text{m}$ .

A vacuum test model has been built to test the polymeric vacuum sealing scheme. A vacuum of  $3 \times 10^{-7}$  has been achieved with a leak rate of  $5 \times 10^{-8}$  mbar l/s. All vacuum pumps will be 'dry.'

A scheme using fiducials on the segments, a CMM, dial indicators and a laser tracker will be used to align the segments relative to each other during final assembly.

A system using a 'sling' supporting the complete RFQ assembly at multiple points ( $\sim 16$ ) is proposed for moving the RFQ from the alignment lab to the beam line where it will rest on 3 points.

**Comments & Recommendations:** The conventional limit on water velocity in Copper cooling channels is 5 m/s. High velocities at corners in the coolant channels causes cavitation and erosion. The design team

should make a technical argument that exceeding this conservative value is justified.

While the cooling scheme appears to provide thermal stability its design has not been integrated with the resonance control scheme. The committee stands by its recommendation for relocating the cooling channels to facilitate a more passive dynamic tuning scheme. The thermal/deformation maps should be used to create voltage distributions for beam dynamics error studies.

The philosophies for supporting the structure during transport and after installation seem inconsistent. If there is concern about shock during transport there should be some sort of energy absorption.

The committee remains concerned about the rf contact scheme. Conventional wisdom says that no contact is better than a poor rf joint. In particular our recommendation to provide an rf gap to prevent metal-to-metal contact has not been implemented.

The committee remains concerned about the vacuum. In particular our recommendations regarding a vacuum relief between the rf and vacuum gaskets have not been implemented. The vacuum test cavity should be leak checked using an RGA. It should also be tested with Helium to saturation to find its true ultimate leak rate. A procedure should be defined to qualify the polymer vacuum gaskets.

It is clear how the relative alignment of the segments will be measured and how transverse errors can be corrected. It is not clear how fabrication errors affecting their vertical positioning will be compensated.

The purpose and application of the Bilbao RFQ project is now clearer to the committee. We understand that its primary use will be in the development, testing and qualification of MEBT components (magnets, cavities and diagnostics) for ESS. As such, requirement for its flawless, continuous performance for many years is significantly relaxed. With this understanding the committee feels somewhat more relaxed about some of its previous concerns regarding its mechanical design.

The committee assumes that it is no coincidence that the redesigned RFQ will provide an output beam having properties that are remarkably close to those expected from the ESS design (but from a much shorter structure). This will be a significant advantage to the Bilbao team for testing any MEBT components and one could argue that it would serve as a valuable test facility for the entire ESS MEBT.



## Appendix C

# ESS-Bilbao RFQ Technical Design Review Report (2013)

J. Stovall, R. Ferdinand, M. Vretenar and A. Letchford 5 November, 2014

### Introduction

ESS-Bilbao plans to build a ‘regional-scale’ neutron research facility in Spain. To that end they will design, build and test a 352.2 MHz RFQ to deliver a  $\sim 75$  mA beam of protons at 3 MeV to eventually inject a 100 MeV drift tube linac that would illuminate a neutron production target.

The Technical Advisory Committee (TAC) heard 8 presentations in Bilbao on July 16 & 17, 2013, which summarized the efforts of the RFQ design team to date. These presentations covered all aspects of the design effort including the beam dynamics design, the design of the resonant structure supported by cold model measurements, and the mechanical design of the cavity supported by fabrication tests and the experience and recommendations of their collaborators. They also addressed supporting subsystems including vacuum, cooling, resonant control, support and alignment, the RF power coupler and transport, and beam diagnostics as well as budget and schedule. The primary assignment to the committee

was to review the technical aspects of the linac design and to access the choices adopted in its final design

## Specific charge to the committee

The committee was asked to submit a written report addressing the following questions.

- Is the RFQ design, as described in the technical documentation, technically sound and mature enough to proceed towards an engineering detail phase and subsequent construction?
- To what extent does the proposed accelerator contain significant innovative features, if any?
- Is the budget realistic and cost effective?
- Is the timeline realistic?
- Are the scientists and engineers in charge of the project development sufficiently mature to take responsibility of the engineering detail and manufacturing steps?

## Executive Summary

In general, the overall design of the RFQ appears to meet the specified performance requirements. It is reasonably thought-out and each subsystem has been addressed. The committee believes that some aspects of the design need further thought and that proceeding with detailed engineering, while possible, carries some risk. To a large extent the design stage has been completed with some physics and engineering aspects yet to be worked through before entering the construction stage. The committee recommends that the team address the recommendations detailed below.

The design does indeed contain innovative features. In general however the majority of the committee, based on our experience, prefers conservative designs that will assure long-term, problem-free operation. Some

of the 'unique' features of this design would be appropriate for an R&D project but present a definite risk for an accelerator required to be operationally reliable.

The RFQ team is clearly well trained, technically competent and motivated. They have carried out a lot of work in a reasonably short time, considering that there is little or no accelerator experience and limited resources. It is admirable that the project has solicited advice and collaborations. All of the work presented was very professional.

The project appears to be in capable technical hands. The attention to detail and breadth of investigations to date indicates that, while the leadership is relatively inexperienced, it is well informed and responsive to constructive advice.

The committee concurs that the beam dynamics design should to be modified in some respects. In its present state, the design is conservative and presents a low risk but it should be improved to benefit from lessons learned from RFQs already in service.

The committee concentrated primarily on the technical aspects of the design and to this end we make the following recommendations:

- Reduce the injection energy.
- Shorten the RFQ by 20 %.
- Use the 2-term potential function to define longitudinal the vane tip profile.
- Review the mechanical, operational and cost benefits of the round-quadrant cavity versus a more conventional octagonal design.
- Independently prove the viability of the proposed vacuum and RF gasket designs
- Review the dynamic frequency control options, i.e. mechanical tuners versus temperature/flow control.
- Develop a mathematical model of the cavity to better understand the effects of perturbations and tuners; and to develop a tuning scheme.
- Extend the cold model to at least 2 segments.

- Pursue a single power coupler prototype.
- Generate a commissioning plan from which you can derive the required diagnostics.

Reducing the injection energy in particular will shorten the RFQ making it cheaper and easier to tune while preserving the final energy, beam quality and transmission.

ESS-Bilbao has been a very gracious host to the TAC and it is a pleasure working with this team. Our comments are intended to be tough and critical and we hope that they are accepted in a constructive light. We wish the project our best.

## C.1 Conceptual Design

**Findings:** The team has completed a detailed beam dynamics design of the RFQ using RFQSIM. The design constraints included (a) a 75 keV injection energy, (b) a flat field distribution, (c) a constant radius of curvature vane tip ( $\rho$ ), (d) a constant cavity cross section, (e) a peak surface electric field  $\leq 1.8E_K$ , and (f) a total length  $\leq 3.9$  m. In addition the input and output radial matching sections assume a 'circular' longitudinal profile. Figures of merit for evaluating candidate designs included transmission and emittance growth.

Particle tracking simulations were carried out using 3 different codes; RFQSIM, Toutatis and GPT using both an analytical field calculation and field maps generated by COMSOL, a finite element electromagnetic code. Each code gave reasonably consistent results for transmission ( $\pm 2.5\%$ ) and emittance growth ( $\pm 14\%$ ). All design constraints were met.

Static error studies were carried out to determine the fabrication and assembly tolerances required to have minimal impact on transmission and emittance growth.

**Comments:** We would expect this beam dynamics design to perform nominally as predicted by the simulations. It is admirable that the design has been validated using multiple codes. Until RFQSIM and

COMSOL are calibrated against a variety of operating RFQs, Toutatis or Parmteq are probably the gold standard with which to evaluate design variants.

There are, however, other recently commissioned RFQs having nominally the same performance requirements (eg. CERN & THU) that are shorter, have higher transmission and less emittance growth. Any new design should strive to at least meet the performance characteristics of such existing machines. The CERN RFQ has the same design constraints with the exception of the injection energy. Some aspects of the design therefor deserve further thought.

Simulated acceptance and transmission as a function of vane voltage, emittance, beam current and injection energy are consistent with the measured performance in operating RFQs. It would be safe to increase  $E_{\text{peak}}$  to  $1.8E_{\kappa}$  throughout.

The RFQ requires a highly convergent input beam which, in turn, requires a very large aperture solenoid located close to the RFQ. Filling too much of the solenoid aperture introduces unrecoverable distortion of the emittance. The RFQ should deliver a circular beam to facilitate matching both  $H^+$  &  $H^-$  into a DTL.

The error studies carried out to date show that, with easily attainable fabrication tolerances, the beam quality should experience little or no degradation. The manufacturing tolerances, however, should be specified in terms of the geometry required to provide the required RF fields. The RF constraints are typically tighter than the mechanical requirements.

**Recommendations:** The committee believes that the injection energy of 75 keV is unnecessarily high and difficult to defend. It is not needed to provide the required beam current from the ion source for either ion species and results in an excessively long accelerating structure. The long structure will be unnecessarily expensive and, at  $\sim 4.5\lambda$ , it will be difficult to tune. We recommend lowering the injection energy to  $\sim 45$  keV, consistent with CERN & THU.

Investigate increasing  $m$ , the modulation parameter and  $E_{\text{peak}}$  to  $1.8E_{\kappa}$  in the accelerator section. Investigate lowering the transverse

focusing in the initial cells and add a 'Crandall cell' at the exit.

Carry out end-to-end simulations, from the plasma surface, through a representative MEBT using  $\sim 500\,000$  particles.

Error studies should be carried out to determine the fabrication tolerances required to achieve the required resonant frequency and field distribution.

## C.2 Electromagnetic Design

**Findings:** The basic EM design replicates the round-quadrant geometry used in the ISIS-FETS RFQ now in fabrication. The cavity cross section was designed using SuperFish, while the geometries of the end regions were designed using COMSOL in 3-D mode. Frequencies of individual cross sections were calculated in 3-D, including the effect of vane-tip modulations, vacuum grills and tuners. Particular care has been given to the meshing and to the design of the input and output matching sections.

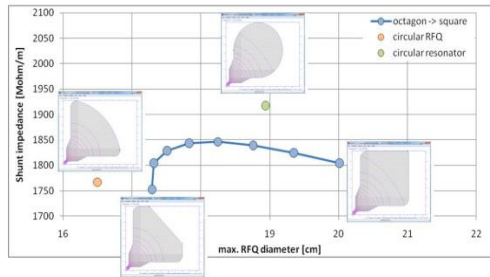
The cavity geometry was constrained by the parameters  $\rho$ , the vane tip radius,  $r_0$ , the distance from the vane tip to the axis at the cell midpoint, and  $m$ , the vane tip modulation as a function of  $z$ , the longitudinal coordinate. All 3 of these parameters are defined by the beam dynamics design. Because the width of the vane skirt is constrained by the diameter of the coolant channel closest to the vane tip, essentially the only remaining free parameters are  $y_{p1}$ , the height of the vane tip above the skirt, and  $r_{\text{-lobe}}$ , the radius of the quadrant or lobe. By searching these parameters, the cavity geometry was optimized by maximizing the cavity  $Q$  within the constraints.

The 3-D cavity simulations revealed a strong frequency correlation with  $z$ . This effect was mistakenly attributed to the changing vane tip modulation.

The RFQ field will be statically tuned by means of 6 fixed slug tuners. The frequency will be dynamically maintained using 2 movable tuners per segment for a total of 40 tuners in all. The target frequency

of the cavity, with all tuners flush, is 351 MHz, 1.2 MHz below nominal value and will be compensated by an 11 mm penetration of all tuners.

**Comments:** The round shape of the quadrants is intended to increase the shunt impedance, however, the gain looks marginal compared to more traditional ‘flat surface’ quadrant designs. This shape makes the machining more difficult and expensive. Moreover, the gain in shunt impedance is probably lost because of the cross large section of the vanes.



The constant radius of curvature vane tip has traditionally been chosen to facilitate machining using a shaped cutting tool on a 2-axis milling machine. Since these vane tips will be machined with a ball-end mill in a 3-axis machine, there is no advantage to constrain the vane tip to have a constant  $\rho$  and it eliminates a useful design variable. If you were to introduce a variable  $\rho$ , the quadrant cross section would have to be modified to maintain resonance. Since this is impractical in a circular-quadrant design it may be a moot point.

The cavity shape should be designed to resonate at the design frequency of 352.2 MHz with the slug tuners inserted to their mid-position (in frequency) to guarantee maximum tuning flexibility. The effect of the modulations on the frequencies of the RFQ ‘slices’ is probably too large to be compensated by the tuners and, it does not make sense to waste precious tuning range on known and predictable effects.

A calculation of the effect on frequency of all tuners at their mid-position should allow defining a new target frequency that provides

an equal tuning range in both directions.

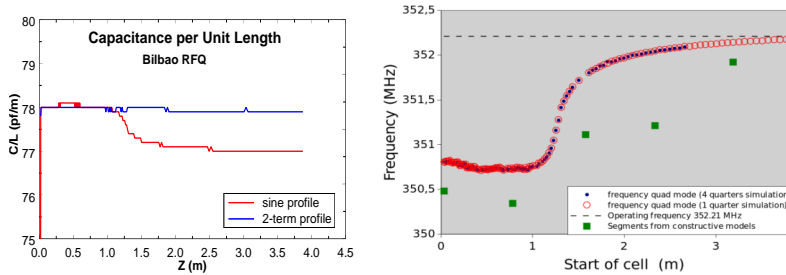
In general terms, the electromagnetic design is missing a mathematical model or a model based on equivalent circuits or more extensive 3D simulations, to describe the effect of perturbations to the frequencies of the slices (mechanical errors or introduction of the tuners) on the field profile. Such a model will allow dimensioning the tuning system (number and penetration depth of the tuners) to compensate for the expected errors and it will be an essential tool for the tuning phase (flattening the field and eliminating the dipole components acted on by the tuners).

Typically, tuning an RFQ that is very long with respect to the RF wavelength ( $4.5\lambda$ ), is very challenging and requires a large number of tuners as well as sophisticated measurements and analysis tools. Using dynamic tuners to maintain resonance raises concerns because the field profile will be drastically changed by the movement of the tuners. This effect can be mitigated only by increasing the number of movable tuners with respect to the fixed ones, adding significant complexity to the system. Compared with the CERN, SNS & THU RFQs, whose resonance is maintained thermally, there are already too few tuners.

The vacuum ports have an important effect on the frequency that is not compensated. The pumping ports should have ridges to compensate the perturbations introduced by the grill.

The sine-like longitudinal vane tip profile results in  $\sim 1.5$  MHz end-to-end frequency excursion that cannot be corrected by the slug tuners which are designed to compensate fabrication errors. The sine-like profile provides no practical benefit and should be changed to follow the 2-term potential function which will produce a flat frequency & field distribution and otherwise have a negligible effect on the beam dynamics. Otherwise the cavity cross section must be modified so that the inductance will compensate the change in capacitance.

In the 2-term profile,  $r_0$  is not defined as the average of  $a$  and  $ma$ , as it is for a sine-wave profile. It is the value of the displacements of both horizontal and vertical vane tips at mid cell. As the RFQ gets longer (higher energy),  $r_0$  approaches  $a$  rather than  $ma$ .



**Recommendations:** Reconsider the RFQ cross-section and compare the ‘round quadrant’ design with a ‘flat quadrant’ design, keeping in mind that the plunger insertion has a ‘simpler’ effect in the ‘flat quadrant’ design. Calculate the gain in Q-value and ask the workshop for an estimate of the difference in fabrication cost to motivate the final choice.

The Cu bars that have been procured to accommodate the circular quadrant design would probably be large enough to provide a proper braze joint in a flat-quadrant design having a smaller overall diameter. In addition, a flat-quadrant design would accommodate a variable vane tip radius giving the designer an additional degree of flexibility to improve the beam performance.

To avoid using the tuners to compensate for the modulation, either change the modulation to a 2-term design, that has only a negligible effect on the slice frequencies, or change the cross-section along the RFQ to compensate for the sine-like profile (inconvenient to do in a circular quadrant design). The first option is preferable because it avoids adding an additional complication to the RFQ design and has no impact on its manufacture.

Develop a model, in the form a computer tool based on a mathematical or electrical model of the entire RFQ length, and use it to: (a) define the number of tuners required, (b) calculate the field deformation induced by different numbers and insertion depth of movable tuners, (c) adjust the fields in the cold model, and (d) achieve field flatness on the final RFQ. Perhaps a more productive solution

would be to establish a collaboration on this point with an existing team e.g. Saclay, Legnaro, CERN, RAL, etc.

Carefully consider all possible options to reduce the length of the RFQ to stay within a more conservative electrical length (e.g.  $3.8\lambda$ , corresponding to 4 segments of 800 mm).

Compensate locally for the frequency shift induced by the vacuum ports and redefine the target frequency to accommodate equal slug tuning range about their design mid-point (frequency) position.

### C.3 Modulation & Segmentation

**Findings:** The RFQ is subdivided into longitudinal segments separated by a  $\sim 200\ \mu\text{m}$  gap. Two options were compared, (a) 4 segments each 1 m long and (b) 5 segments each 0.8 m long. The manufacturer has a clear preference for the 0.8 m segments that fit in his high-precision milling machine. The corner at the end of the vane tip can have a square, rounded or elliptical shape.

**Comments:** The manufacturing argument gives a clear preference to the 0.8 m segments; the only drawback would be that there is one more segment to align with respect to the others (i.e. achieving the required precision moves a bit more from machining to survey). Nevertheless the TAC committee endorses the proposed solution which seems to be a good compromise between cost and risk.

The elliptical segment ends have a clear advantage in terms of peak surface field and the potential for sparking.

**Recommendations:** No particular recommendations

### C.4 Coupler Design & RF Transmission

**Findings:** Two power couplers have been designed (nose-cone and drum-like) and evaluated in detail. In addition to their mechanical design, the structural and thermal properties of both have been analyzed

as well as their potential for multipacting. The two couplers show comparable performance and will be tested in a cavity designed specifically for the purpose at full power.

Both designs are very detailed and represent the state-of-the-art for these items. In particular, all precautions have been correctly taken to avoid multipacting.

The performance of the two is equivalent, while the smaller size of the drum-like coupler is an advantage in that it will require a smaller and less expensive support system when installed on the RFQ.

Ti coating of the ceramic window is a critical element of the design that should be carefully analyzed (thickness of the deposition).

The RF transmitter is based on commercial items (modulator, klystron, circulator, etc.) of proven design (apart the modulator which is a new development). While the ESS pulse repetition frequency (PRF) is 14 Hz, the PRF specified for the Bilbao RF system is the 50 Hz, which has a clear impact on the system cost. A high-power RF test stand is being prepared. Test and conditioning of couplers will be carried out using a dedicated cavity. The RF power transmission system of the RFQ has been designed with waveguide-coaxial transitions and trombones to match the phase. RF seals were presented.

**Comments:** Because the coupler designs are similar and have similar performance characteristics, the management should consider the relative benefits of pursuing the construction of prototypes of both couplers vs. concentrating the resources on a single option (keeping the second as back-up). In this respect, the drum-like design presents some advantages because of its smaller size. Instead of building two different coupler prototypes, it could be more interesting to test different ceramic coatings on the same prototype.

The design of the RF system is well advanced; all components have been delivered or will be soon. The RF test stand is going to be an excellent tool to gain experience in high-power RF and to test accelerator components at high-power.

The quantity and quality of the RF seals will dominate the final Q-value of the RFQ (more than the design details). Having separate

gaskets for RF and vacuum between the longitudinal vane segments is a quick and cheap solution, but may result in a virtual leak from of the volume around the RF seal.

**Recommendations:** Concentrate all further development efforts on the drum-like coupler.

Leave a gap between the longitudinal segments for pumping of the RF seal groove to avoid a virtual leak and for avoiding any metal-to-metal contact which has the potential to considerably reduce the Q-value.

## C.5 RFQ Cold Model

**Findings:** A 1-m long Al ‘cold’ model with modulated vanes has been produced and RF measurements have begun. It is equipped with 12 fixed and 4 movable tuners and 8 ports for couplers and pick-ups. Field flatness is expected to be hampered by the effect of vane modulation. Dipole suppressors have been foreseen on the two end covers. Measurements show some deviations in the position of the dipole modes with respect to simulations. There is also a major discrepancy between bead-pull measurements of the E and H fields. The Q-value is measured to be ~60% of the theoretical value for Al. The behavior of the dipole suppressors is within expectations.

**Comments:** The cold model is well designed mechanically and apparently has been well made (the field measurements do not reflect any mechanical problems). It will become an invaluable tool to develop measurement and tuning strategies. It can be used to test mechanical and RF solutions, and to train the team. However, it is only one meter long and the effect of longitudinal modes will be one sixteenth of the effect expected in the ‘real’ RFQ.

The higher than simulated frequencies measured for the quadrupole and dipole modes indicate some mechanical errors that are concentrated in the diagonal quadrants containing the power couplers. The

increased frequency is a result of an error in either the capacitance or the inductance. This could be the effect of the coupler volume.

Bead-pull measurements on the E-field are not reliable when the bead is only suspended and does not slide on a support. This will become even more important if a design is adopted that has a variable vane tips radius. Although the E-field measurements seem to agree with simulations, they do not agree with the measured dipole frequencies. The H-field measurements present a more consistent profile (consistent with a strong positive perturbation at one end).

Using a large bead is possible because of the low Q-value but is not recommended because of the higher sensitivity to field variation.

**Recommendations:** Rely on the H-field measurement and use a smaller bead that provides better accuracy (up to the limit of the phase noise).

Consider doubling the length of this model with a second 1 m segment or building a new longer model.

The committee recommends using Cu tuners (slugs & rods) in the cold model and putting apertures in the final Cu end walls to accommodate bead-pull measurements of the final assembly.

## C.6 Cooling Design

**Findings:** Two types of cooling methods have been evaluated; one derived from ISIS experience (baffles) and one more classical approach using deep-drilled channels.

The analysis uses 3-D calculations in which the heat flux, derived from the electromagnetic calculation is applied to the cavity geometry. The thermal deformations resulting from RF heating and cooling are returned to the electromagnetic simulation in the form of a deformed mesh to derive the resulting frequency error. This loop is repeated until the system comes to thermal equilibrium.

Water flow has been limited to  $< 2.5$  m/s to avoid cavitation. The inlet temperature is held constant at 15 °C and both models have

been evaluated for a nominal RF heat flux of up to twice the expected value.

The derived thermal maps are neither symmetric nor homogeneous although maximum deformations are within 10  $\mu\text{m}$ .

Although the maximum local temperature is higher for the drilled option, the temperature map is more homogeneous. The expected frequency excursion per watt of RF power in the drilled option is approximately  $\frac{1}{3}$  of that in the baffled option. The drilled option is therefore the preferred option.

Frequency variation can be as high as  $-65$  kHz which lies within the specified  $\pm 250$  kHz limit.

Cooling experiments have been carried out to validate the CFD simulations.

Two cooling schemes are being considered. In the first, each segment of the RFQ has its own chiller while in the second, all 5 segments are fed from a common manifold which, in turn, is fed from a single chiller. In both schemes the plan is to actively control the inlet temperature and mass flow rate in each channel (8 channels per segment equals 40 parallel channels).

**Comments:** A coolant flow rate of 2.5 m/s is conservative.

The effect of the frequency variation has not been applied to the voltage law.

The 3  $^{\circ}\text{C}$  temperature variation in the drilled option may result in a frequency 'slope' in the individual segments. No estimation of this effect on voltage was calculated.

No thermal calculations were shown for the end flanges and their dipole rods where the highest current densities occur.

Slug tuner cooling, which relies on thermal contact with the RFQ body is not reliable. The tuner temperature should be maintained within  $\pm 10$   $^{\circ}\text{C}$  of the body temperature.

The proposed 15  $^{\circ}\text{C}$  coolant temperature at the chiller exit will induce water condensation on the RFQ and all associated hardware. A

more classical value would be 25 °C. The operating temperature and pressure, being different than ambient, must be taken into account during machining and subsequent tuning.

One chiller is the cheapest solution.

No explanation of how to control the flow rate was showed or how such a thermal control loop would be closed. Controlling the flow rate in each of 40 channels would be expensive.

There is no discussion on closing a control loop on either the cavity temperature or its resonant frequency. Because of the drawbacks of controlling the frequency mechanically, the team should consider using the cooling system to control the cavity frequency. There are at least two proven approaches to achieve this. The more common approach is to fix the temperature of the body of the RFQ which, to first order, fixes its diameter (inductance), using one chiller. The resonant frequency is then maintained dynamically by adjusting the temperature (or mass flow rate) in the channels cooling in the vanes, essentially controlling the vane tip gap dimension (capacitance). This scheme requires 2 chillers if temperature is used as the control variable.

A second scheme requires that the coolant channels be placed in such a way that any change in capacitance is just balanced by a corresponding change in inductance. In this case, the cavity temperature is initially adjusted isothermally with the power 'off' to give the correct resonant frequency. The RF power is then applied and the cavity allowed to reach thermal equilibrium. The mass flow rate in the vanes is then adjusted again to achieve resonance. The RFQ frequency can be stabilized by fixing the cooling water temperature and the steady-state frequency can be made constant, independent of RF power level, at constant flow. The frequency of the RFQ can be adjusted by changing the cooling water temperature. In the event of a spark, the frequency will drop temporarily when RF power is turned back on, but will quickly return to its steady state value.

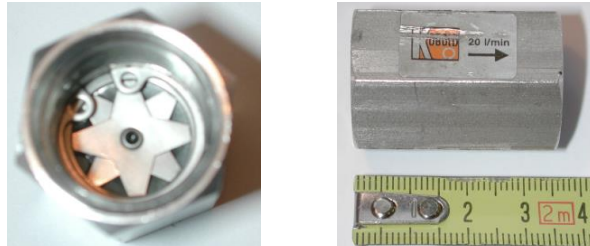
**Recommendations:** It is necessary to calculate the expected temperature of the end flanges and dipole rods. Both should be cooled.

Be sure that the thermal distortion at the ends of the vanes, shown with the 3-D calculation, does not deform the field distribution.

Tuners must be water cooled, in a simple way, at least to remove any uncertainty.

It is important to evaluate the dynamic effects that will occur during operation. For example how will the system recover from a spark in which the RF is turned off long enough for the cavity to go cold and isothermal.

Consider fixing the flow rates with simple and cheap flow limiters, and just control the temperature.



Consider controlling the cavity resonant frequency using the coolant temperature or mass flow and only using the dynamic tuners for tuning the static field distribution.

## C.7 Mechanical & Vacuum

**Mechanical Findings** The RFQ is a single continuous cavity comprised of 5 longitudinal segments bolted together. The segments are each ~800 mm long to facilitate the manufacturing process, achieve the required tolerances and minimize the surface roughness.

The vane assembly and vacuum seal design is based on the ISIS FETS design, an R&D project, that has presumably been thoroughly tested. Testing results were not presented.

Two types of support systems were evaluated, the ISIS and LINAC4 systems. Very small mechanical deformations were seen in both cases. The ISIS type design is estimated to be the cheapest approach. EB welding and furnace brazing solutions were briefly evaluated in terms of mechanics and difficulties. No advantages for either were shown based on cost, availability, shunt impedance, vacuum or thermal properties.

Mechanical tolerances are based on beam performance as evaluated by the beam dynamics group. The tolerance budget specifies  $\pm 100 \mu\text{m}$  between segments,  $\pm 50 \mu\text{m}$  absolute position of the vane tips, and  $\pm 100 \mu\text{m}$  on global vane positions (tilt, parallelism & longitudinal displacement).

All prototypes were used to validate the manufacturing procedure and the resulting tolerance. The machining steps were tested successfully on short Cu prototypes.

**Mechanical Comments:** The reference support design has 3 adjustable feet per segment. The committee doubts that this is the cheapest solution and it complicates the segments connection one to the other. As the support of the structure will be over determined the RFQ will be subject to stress.

The transverse shape of the cavity was carefully optimized using a round-shaped (Montgolfier) quadrant design, leading to a larger than usual outer diameter and a sophisticated cross section. No flat surfaces exist in the magnetic region for device insertion.

EB welding can typically penetrate no more than 5 mm and cannot hold the required tolerances.

The vacuum & RF seals are highly unconventional and represent the highest risk.

Brazing tests were inconclusive, probably because adequate intermediate annealing was not performed.

**Mechanical Recommendations:** The round-shaped quadrant shape, which has the highest shunt impedance, is wasted by thick vanes and other

mechanical features such as RF gaskets and moveable tuners. Because this will be an expensive fabrication project, having no operational benefits, the team should consider a simpler, more classical shape.

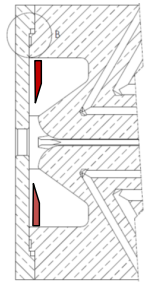
Establish the best method to compensate the RF perturbation introduced by the vacuum port. This is usually compensated by adding material to the inside of the bars of the grill. Do not rely on adjacent tuners as they will be needed to compensate for manufacturing errors.

All of the RF joints should be designed to avoid any copper-to-copper contact. No contact is better than a poor contact. A 0.2 mm–0.5 mm gap is recommended on all joints using mechanical gaskets.

All critical Cu parts should be machined in a temperature controlled environment.

The joining of the 4 quadrants (bolted, brazed or EB welded) is a fundamental decision. It requires different types of tests on short models to prove the viability and reliability of the candidate techniques. Because the Bilbao design is so unconventional, a short model should be built to prove the sealing (RF & vacuum) features of the design and allow the measurement of the leak rate and Q-factor.

Think about how to correct manufacturing errors in the 3-D extremity (under-cut area). You may need a thick flange that you can cut to the right frequency. A careful thermal analysis of the 3-D extremities, including the dipole rods, is required.



To a large extent today one can rely on 3-D numerical modeling. However a 2 m long or even a full length cold model is recommended to verify the tuning procedure, especially for an inexperienced team.

**Vacuum Findings:** The vacuum required during operation has been specified to be  $\leq 10 \times 10^{-7}$  mbar.

The system is comprised of one 550 l/s turbo pumps per segments (5 pumps total), with the possibility to insert a second one. The accessibility for later insertion of the second pump has not been checked.

The assembly is vacuum sealed using glued O-rings (RAL design).

**Vacuum Comments:** The glued O-ring solution is very unconventional and of questionable reliability and feasibility (repeatability).

A maximum leak rate to be controlled during the manufacturing process and assembly process should be defined ( $\sim 1.1 \times 10^{-10}$  Pa m<sup>3</sup>/s). It will allow you to calculate the ultimate expected pressure.

It is not clear what wall outgassing rate was assumed for the vacuum calculation. Hydrogen typically represents a significant vacuum load in RFQs. It is not clear what hydrogen load and pumping rate were assumed for the vacuum calculation

**Vacuum Recommendations:** The glued O-ring scheme must be thoroughly tested to validate the performance and reliability of the concept and to provide a reference leak rate.

## C.8 Test Stand

**Findings:** A Mobile Test Stand (MOTS) will be built for installation downstream of the RFQ for the purpose of commissioning the RFQ, to measure its beam properties and support tuning a MEBT for injection into the DTL. The beam parameters to be measured include the following:

- Beam current

- Transmission
- Energy
- Energy spread
- Bunch shape
- Transverse emittance
- Position
- Phase

The MOTS will include the following instrumentation:

- An AC current transformer (ACCT) to measure beam current
- A Faraday cup (FC) to measure beam current
- A fast current transformer (FCT) to enable TOF measurements
- Slit and magnetic spectrometer for energy measurements
- Quadrupole magnets and secondary emission monitor (SEM) grids for measuring beam profiles and emittance
- Beam position monitors (BPMs) to measure absolute beam position
- Feschenko type monitor to measure longitudinal bunch shape

The RFQ commissioning scheme has yet to be defined.

The performance requirements for each diagnostic device have yet to be defined.

A detailed layout of the MOTS has yet to be defined.

**Comments:** Beam measurements fall into three categories: essential, desirable and interesting. Essential measurements are those that have to be performed to enable commissioning of the RFQ (or subsequent accelerators). Desirable measurements are those that aren't essential but which might help commissioning or understanding why the performance differs from expected, e.g. code validation. Interesting measurements are not necessary but are of academic interest and

might reveal new beam physics. The diagnostics described have elements from all 3 categories.

ACCTs are the usual and sensible way to measure the pulsed current. At least one ACCT in the MOTS should be identical to and cross calibrated with one before the RFQ for accurate transmission measurements

A FC for low current measurements below the range of the ACCT makes sense. It can also act as a beam stop although at 3 MeV, it will produce neutrons if made from copper as suggested.

Although BPMs will be a part of the diagnostic suite there is apparently no way to steer the beam after the RFQ until a MEBT is installed.

A FCT will resolve the bunch structure and allow TOF measurements although the same could be achieved with the BPM signal.

It is not clear what the purpose of the phase measurement is.

A magnetic spectrometer is proposed. Mean energy can be determined from TOF so this is a rather expensive way to measure energy spread which nothing can be done about anyway. There are other cheaper (but not necessarily easier) ways to measure energy spread.

A buncher cavity in the line would allow the measurement of the longitudinal emittance using the 3 gradients method. Developing this diagnostic would be useful in matching the MEBT beam to the following accelerator.

The bunch shape monitor is an interesting measurement but we are not convinced that it helps commissioning.

The slit and grid will allow transverse emittance measurements but it looks like the drift distance between them is too long for accurate measurements at high current. Determining the emittance requires a good model of the space charge.

Measured performance is given in some cases but no required performance has been specified.

**Recommendations:** Develop a commissioning plan.

Produce a functional specification for all diagnostic devices.

Consider if magnetic spectrometer is necessary or justified.

Consider if FCT and BPMs are both necessary.

Evaluate material options for intercepting diagnostics. The expected radiation and activation levels produced in the beam stop at full duty factor should be calculated.

Consider adding a buncher to measure longitudinal emittance.

To a large degree the MOT will be used to develop and test beam diagnostic devices that may be used in the rest of the linac.

## C.9 Budget & Schedule

Overall, the total budget for the RFQ project looks reasonable and consistent with similar prior RFQ projects.

The budget is dominated by the RF power system costs which include the development and construction of a 50 Hz modulator which exceeds the present requirements of the project but will be compatible with other high-duty linac projects.

The machining costs for the RFQ appear surprisingly low, but the committee takes note that they are based on budgetary estimates from local companies.

The cost of Copper looks extremely low in comparison with similar projects. Is the copper quality adequate for the mechanical requirements of this RFQ? Does it meet the specifications required if you choose a brazed assembly?

The assembly and alignment costs are based on the bolted solution for the RFQ construction. If a brazed or welded assembly is selected, this budget line will increase.

It is not clear whether some components (end plates, support, assembly system) are included or not in the budget.

The budget for shielding appears extremely low. At 3 MeV we should not expect appreciable radiation levels however some basic shielding (and radiation monitoring!) should be implemented. The cost of diagnostics

(and of the measurement line) is not included. Does it appear in a separate budget (test stand), or should it be included in the RFQ budget?

It would be prudent to add a spare Cu segment to the cost as a contingency.

The schedule submitted to the committee consists of a (small) Gantt chart with only 7 tasks between now and end 2015. The level of detail is not sufficient to give precise comments or recommendations. Hopefully it is a summary of a much more detailed analysis.

Machining the vanes is foreseen to start at the beginning of Q4, 2013. This objective looks very ambitious, because: (a), the mechanical design is not yet frozen and (b), after freezing the design an important time (several months) will be required to prepare the fabrication drawings. The overall duration of the task (about 1.5 years) looks realistic. We do not recommend concurrent design and fabrication.

The administrative procedures for placing large contracts could add considerable delay to the schedule.

It is not clear what the task 'reports' means.

It is not clear how the final part of the project is organized (there is a gap of 1 year in the schedule between end of vane machining and execution).

15 August, 2013



# Bibliography

- [1] I. M. Kapchinsky and V. A. Tepliakov. *A Linear Ion Accelerator with Spatially Uniform Hard Focusing*. Tech. rep. SLAC-TRANS-0099. Stanford Linear Accelerator Center, 1969 (cit. on p. 4).
- [2] J. E. Stovall, K. R. Crandall and R. W. Hamm. *Performance Characteristics of a 425 MHz RFQ LINAC*. Tech. rep. LA-UR-80-3140. Los Alamos Scientific Laboratory, 1980 (cit. on p. 4).
- [3] J. Delayen and F. Gerigk. *Summary of the working group on Accelerator Components*. Multi-MW Spallation Neutron Sources: Current Challenges and Future Prospects. Tech. rep. Bilbao: ESS-Bilbao, Mar. 2009, pp. 16–19 (cit. on p. 21).
- [4] A. Letchford. ‘RFQ design codes RFQCURLIM, RFQGEN, and RFQSIM’. Apr. 2010 (cit. on p. 21).
- [5] K. R. Crandall. ‘Ending RFQ Vane tips with Quadrupole Symmetry’. In: *Proceedings of 14 LINAC Conference*. Tsukuba, Japan, Aug. 1994, pp. 227–229 (cit. on p. 29).
- [6] K. R. Crandall and D. P. Rusthoi. *Trace 3-D Documentation*. LA-UR-97-886. Los Alamos National Laboratory (cit. on p. 30).
- [7] R. Duperrier. ‘Intense beam dynamics in RFQs linacs’. PhD thesis. Orsay: University of Orsay, July 2000 (cit. on p. 31).
- [8] R. Ferdinand, R. Duperrier, J.-M. Lagniel, P. Mattei and S. Nath. ‘Field Description In An RFQ And Its Effect On Beam Dynamics’. In: *Proceedings of LINAC98*. Chicago, USA, 1998, pp. 115–117 (cit. on p. 31).

- [9] *General Particle Tracer User Manual (v. 2.82)*. Pulsar Physics (cit. on p. 31).
- [10] W. E. Shoupp, B. Jennings and W. Jones. 'Threshold for the Proton-Neutron Reaction in Copper'. In: *Phys. Rev.* 73 (5 Mar. 1948), pp. 421–423. doi: [10.1103/PhysRev.73.421](https://doi.org/10.1103/PhysRev.73.421). url: <http://link.aps.org/doi/10.1103/PhysRev.73.421> (cit. on p. 34).
- [11] D. C. Faircloth, J. W. G. Thomason, M. Haigh, I. H.-c. Yiu, J. Morrison and G. Doucas. 'Energy Distribution of H<sup>-</sup> Ions from the ISIS Ion Source'. In: *Proceedings of EPAC 2006*. TUPLSo88. Edinburgh, Scotland, 2006, pp. 1708–1710 (cit. on p. 36).
- [12] R. Duperrier, J. Payet and D. Uriot. *The IFMIF High Energy Beam Transport line - Error studies*. Tech. rep. CEA Saclay, 2004 (cit. on p. 40).
- [13] M. J. Browman and L. Young. 'Coupled RadioFrequency Quadrupoles as Compensated Structures'. In: *Proceedings of LINAC1990*. A-12004-C. Albuquerque, USA, Sept. 1990, p. 70 (cit. on pp. 45, 48).
- [14] L. M. Young. 'Private communication' (cit. on p. 47).
- [15] P. Balleyguier. '3D Design of the IPHI RFQ Cavity'. In: *XX International Linac Conference*. Monterey, California, 2000 (cit. on pp. 47, 48, 50).
- [16] L. M. Young. 'Private communication' (cit. on p. 47).
- [17] K. Cummings, D. Rees, W. Roybal, S. Lenci, S. Risbud, C. Shang and D. Wilcox. 'Experimental evaluation of 350 MHz RF accelerator windows for the Low Energy Demonstration Accelerator'. In: *Proceedings of PAC1997*. Vol. 3. 1997, 3183–3185 vol.3. doi: [10.1109/PAC.1997.753149](https://doi.org/10.1109/PAC.1997.753149) (cit. on p. 80).
- [18] S. Michizono, Y. Saito, S. Yamaguchi, S. Anami, N. Matuda and A. Kinbara. 'Dielectric materials for use as output window in high-power klystrons'. In: *Electrical Insulation, IEEE Transactions on* 28.4 (1993), pp. 692–699. issn: 0018-9367. doi: [10.1109/14.231552](https://doi.org/10.1109/14.231552) (cit. on p. 80).

- [19] Y. W. Kang, A. Vassioutchenko, A. V. Aleksandrov, D. Anderson, M. S. Champion, M. Crofford, P. Gibson, T. Hardek, P. Ladd, M. P. McCarthy and D. Stout. 'Design and high power processing of RFQ input power couplers'. In: *Particle Accelerator Conference, 2007. PAC. IEEE*. 2007, pp. 2505–2507. doi: [10.1109/PAC.2007.4441298](https://doi.org/10.1109/PAC.2007.4441298) (cit. on pp. 81, 86).
- [20] Y. W. Kang, A. Vassioutchenko, A. V. Aleksandrov, M. M. Champion, M. S. Champion, M. Crofford, P. Gibson, H. L. Haenichen, T. Hardek, P. Ladd, M. P. McCarthy and D. Stout. 'Development of an RFQ Input Power Coupling System'. In: *Proceedings of LINAC 2006*. Knoxville, Tennessee, USA, 2006 (cit. on pp. 81, 86).
- [21] *Preliminary study of the power coupler for ESS-Bilbao*. Tech. rep. ESS-Bilbao, 2010 (cit. on p. 86).
- [22] A. Vélez, O. Gonzalez, J. L. Muñoz, D. de Cos, I. Madariaga, N. Garmendia, J. Feuchtwanger, I. Bustinduy, F. J. Bermejo, J. Portilla and V. Etxebarria. 'Complete Electromagnetic Design of the ESS-Bilbao RFQ Cold Model'. In: (2012), pp. 2991–2993 (cit. on p. 107).
- [23] T. P. Wangler. *RF Linear Accelerators*. Wiley-VCH Verlag GmbH & Co. KGaA, 2010. isbn: 9783527623426. doi: [10.1002/9783527623426.ch1](https://doi.org/10.1002/9783527623426.ch1). url: <http://dx.doi.org/10.1002/9783527623426.ch1> (cit. on p. 113).
- [24] R. Bailey, ed. *RF for Accelerators*. Comments: 20 lectures, 460 pages. CERN. Geneva: CERN, 2011 (cit. on p. 114).
- [25] D. Kajfez. 'Linear fractional curve fitting for measurement of high Q factors'. In: *Microwave Theory and Techniques, IEEE Transactions on* 42.7 (1994), pp. 1149–1153. issn: 0018-9480. doi: [10.1109/22.299749](https://doi.org/10.1109/22.299749) (cit. on p. 114).
- [26] D. Kajfez. *Q Factor*. Oxford, MS: Vector Forum, 1994. 174 pp. isbn: 0-930071-06-9 (cit. on p. 114).
- [27] D. Kajfez and E. J. Hwan. 'Q-Factor Measurement with Network Analyzer'. In: *Microwave Theory and Techniques, IEEE Transactions on* 32.7 (1984), pp. 666–670. issn: 0018-9480. doi: [10.1109/TMTT.1984.1132751](https://doi.org/10.1109/TMTT.1984.1132751) (cit. on p. 114).

- [28] D. Kajfez. *Q factor measurements, analog and digital*. 1999. url: <http://www.ee.olemiss.edu/darko/rfqmeas2b.pdf> (cit. on p. 114).
- [29] K. Leong, J. Mazierska, M. V. Jacob and D. Ledenyov. ‘Comparing unloaded Q-factor of a high-Q dielectric resonator measured using the transmission mode and reflection mode methods involving S-parameter circle fitting’. In: *Microwave Symposium Digest, 2002 IEEE MTT-S International*. Vol. 3. 2002, 1665–1668 vol.3. doi: [10.1109/MWSYM.2002.1012178](https://doi.org/10.1109/MWSYM.2002.1012178) (cit. on p. 114).
- [30] R. Pasquinelli and D. McGinnis. ‘Microwave Measurements and Beam Instrumentation Laboratory’. In: *U.S. Particle Accelerator School (USPAS)*. 2012 (cit. on p. 114).
- [31] A. Ratti, R. DiGennaro, R. A. Gough, M. Hoff, R. Keller, K. Kennedy, R. MacGill, J. Staples, S. Virostek and R. Yourd. ‘The design of a high current high duty factor RFQ for the SNS’. In: *Proceedings of EPAC 2000*. Vienna, pp. 495–497 (cit. on p. 115).
- [32] F. Simoens, A. France and J. Gaiffier. ‘Electromagnetic Characterization of the First IPHI RFQ Section’. In: *Proceedings of EPAC 2002*. Paris, 2002, pp. 1049–1051 (cit. on p. 115).
- [33] J. C. Slater. ‘Microwave Electronics’. In: *Reviews of Modern Physics* 18 (Oct. 1946), pp. 441–512. doi: [10.1103/RevModPhys.18.441](https://doi.org/10.1103/RevModPhys.18.441) (cit. on pp. 116, 118).
- [34] H. Hassanzadegan and N. Garmendia. *Technical Report of the ISIS LLRF System*. Tech. rep. ESS-Bilbao, Sept. 2010 (cit. on p. 119).
- [35] T. Poggi. *Klystron Modeling and LLRF System*. Tech. rep. ESS-Bilbao, May 2012 (cit. on p. 119).
- [36] A. Kaftoosian. *Klystron driver technical specifications*. Tech. rep. ESS-Bilbao, Dec. 2011 (cit. on p. 120).
- [37] M. Huerta, R. Martínez and E. Abad. *Water Cooling and Copper Corrosion*. Internal report. ESS-Bilbao, 2012 (cit. on p. 129).
- [38] S. Turner, ed. *Vacuum Technology*. CERN Accelerator School. CERN-99-05. Snekersten, Denmark: CERN, Aug. 1999. isbn: 92-9083-149-9. doi: [10.5170/CERN-1999-005](https://doi.org/10.5170/CERN-1999-005) (cit. on p. 166).

- [39] V. A. Lisovskiy, S. D. Yakovin and V. D. Yegorenkov. 'Low-pressure gas breakdown in uniform dc electric field'. In: *Journal of Physics D: Applied Physics* 33.21 (2000), p. 2722. url: <http://stacks.iop.org/0022-3727/33/i=21/a=310> (cit. on p. 167).
- [40] R. Kersevan and J.-L. Pons. 'Introduction to MOLFLOW+: New graphical processing unit-based Monte Carlo code for simulating molecular flows and for calculating angular coefficients in the compute unified device architecture environment'. In: *55th International Symposium of AVS*. Vol. 27. 4. AVS, 2009, pp. 1017–1023. doi: [10.1116/1.3153280](https://doi.org/10.1116/1.3153280). url: <http://link.aip.org/link/?JVA/27/1017/1> (cit. on p. 167).
- [41] R. Kersevan and M. Szakacs. url: <https://test-molflow.web.cern.ch/> (cit. on p. 167).
- [42] *Vacuum Seals Design Criteria*. Practice no. PD-ED-1223. url: <http://www.nasa.gov/offices/oce/llis/0674.html> (cit. on p. 170).
- [43] I. Bustinduy. *From envelope dynamics to multi-particles*. Tech. rep. DTLS-LD-IR11-V2-MultipartDynamics-Bustinduy. ESS-Bilbao, 2011 (cit. on p. 176).
- [44] Z. Izaola. *Energy measurement by time-of-flight measurement*. Tech. rep. DIAG-CD-IR12-VF-ResolucionTOF-Izaola. ESS-Bilbao, 2012 (cit. on p. 176).
- [45] B. Cheymol, E. Bravin, D. Gerard, U. Raich and F. Roncarolo. 'Design of the Emittance Meter for the 3 and 12 MeV LINAC4 H<sup>-</sup> Beam'. In: *Proceedings of IPAC'10*, Kyoto, Japan, 2010, MOPE052 (cit. on p. 176).
- [46] F. Roncarolo, G. Bellodi, E. Bravin, B. Dehning, M. Duraffourg, D. Gerard, E. B. Holzer, F. Lenardon, G. Focker, U. Raich, L. Soby, M. Sordet, J. Tan, G. Tranquille, C. Vuitton, C. Zamantzas and B. Cheymol. 'Overview of the CERN Linac4 beam instrumentation'. In: *Proceedings of Linear Accelerator Conference LINAC2010*, Linear Accelerator Conference LINAC2010. 2010, pp. 770–772 (cit. on p. 177).

- [47] L. Muguira, D. Belver, V. Etxebarria, S. Varnasseri, I. Arredondo, M. del Campo, P. Echevarria, N. Garmendia, J. Feuchtwanger, J. Jugo and J. Portilla. 'A configurable electronics system for the ESS-Bilbao beam position monitors'. In: *Nuclear Instruments and Methods in Physics Research Section A: Accelerators, Spectrometers, Detectors and Associated Equipment* 721 (2013), pp. 50–59. issn: 0168-9002. doi: <http://dx.doi.org/10.1016/j.nima.2013.03.058>. url: <http://www.sciencedirect.com/science/article/pii/S0168900213003689> (cit. on p. 179).
- [48] ACCT from Bergoz. [http://www.bergoz.com/index.php?option=com\\_content&view=article&id=9&Itemid=466](http://www.bergoz.com/index.php?option=com_content&view=article&id=9&Itemid=466) (cit. on p. 181).
- [49] S. Varnasseri, D. Belver and I. Arredondo. *ACCT Characteristics Measurements for Carro-Movil Preparation*. Tech. rep. DIAG-ND-CToo-ESS-oo-DOC. ESS-Bilbao, Dec. 2012 (cit. on p. 181).
- [50] *Faraday Cup from NTG*. <http://www.ntg.de/index.php?id=182&L=1> (cit. on p. 181).
- [51] FCT from Bergoz. [http://www.bergoz.com/index.php?option=com\\_content&view=article&id=23&Itemid=28](http://www.bergoz.com/index.php?option=com_content&view=article&id=23&Itemid=28) (cit. on p. 181).
- [52] S. Varnasseri and D. Belver. *Test bench measurements of FCTs for Time-of-Flight (TOF) technique*. Tech. rep. DIAG-DS-MT01-ESS.oo-DOC. ESS-Bilbao, Dec. 2012 (cit. on p. 182).
- [53] D. Belver, F.J. Bermejo, J. Feuchtwanger, P.J. Gonzalez, V. Etxebarria and J. Jugo. 'Design and Measurements of a Test Stand for the SEM-Grid System of the ESS-Bilbao'. In: *Proceedings of IPAC2012, MOPPR040*. New Orleans, Louisiana, USA, May 2012, pp. 867–869 (cit. on p. 183).
- [54] A. V. Feschenko. 'Methods and instrumentation for bunch shape measurements'. In: *Proceedings of the PAC2001*. Vol. 1. 2001, 517–521 vol.1. doi: [10.1109/PAC.2001.987557](https://doi.org/10.1109/PAC.2001.987557) (cit. on p. 183).
- [55] K. R. Crandall. *Effect of RFQ vane-tip modulation on local resonant frequency*. Internal Report. 1982 (cit. on p. 198).

- [56] I. Bustinduy. *Required inputs for MEBT*. Presentation. 2014 (cit. on p. 201).
- [57] *Commissioning of the LINAC4 RFQ at the 3 MeV Test Stand*. Shanghai, China, 2013, pp. 3951–3953 (cit. on p. 201).
- [58] L. M. Young et al. ‘High Power Operations of LEDA’. In: arXiv:physics/0008158. 2000 (cit. on p. 202).
- [59] F. J. Bermejo and I. Bustinduy, eds. *Technical Design Report: ESS-BILBAO RFQ*. 1st ed. Aug. 2013. isbn: 978-84-616-5445-1 (cit. on p. 203).
- [60] A. Ponton. ‘The ESS RFQ Beam Dynamics Design’. In: Tel-Aviv, Israel, 2012, pp. 915–917 (cit. on p. 203).
- [61] *Tuning and stabilization of RFQ’s*. Albuquerque, New Mexico, 1990, pp. 530–534 (cit. on p. 230).
- [62] T. Wangler. *RF Linear Accelerators*. Physics textbook. Wiley, 2008. isbn: 9783527406807. url: [http://books.google.es/books?id=5E04%5C\\_nyndUMC](http://books.google.es/books?id=5E04%5C_nyndUMC) (cit. on p. 230).
- [63] P. Forck. *Lecture Notes on Beam Instrumentation and Diagnostics*. English. Tech. rep. Gesellschaft für Schwerionenforschung (GSI), Darmstadt, Germany, Jan.–Mar. 2010. 152 pp. (cit. on p. 264).
- [64] J.-B. Lallement, G. Bellodi, M. Eshraqi, M. G. Tudela, A. Lombardi, P. Posocco, E. Sargsyan and J. Stovall. ‘Linac4 Commissioning Strategy’. In: *Proceedings of HB2010*. 46th ICFA Advanced Beam Dynamics Workshop on High-Intensity and High-Brightness Hadron Beams. Morschach, Switzerland, 2010, pp. 405–409. url: <http://epaper.kek.jp/HB2010/papers/tuo1d01.pdf> (cit. on p. 268).
- [65] Z. Izaola. *Energy measurement by time-of-flight measurement*. Internal Report. ESS-Bilbao, 2011 (cit. on p. 268).
- [66] D. Uriot. ‘Injector beam commissioning’. Workshop ESS (Lund). 2014 (cit. on p. 269).

- [67] M. E. Rudd, R. D. DuBois, L. H. Toburen, C. A. Ratcliffe and T. V. Goffe. 'Cross sections for ionization of gases by 5–4000-keV protons and for electron capture by 5–150-keV protons'. In: *Phys. Rev. A* 28 (6 Dec. 1983), pp. 3244–3257. doi: [10.1103/PhysRevA.28.3244](https://doi.org/10.1103/PhysRevA.28.3244). url: <http://link.aps.org/doi/10.1103/PhysRevA.28.3244> (cit. on p. 272).
- [68] P.-Y. Beauvais, R. Ferdinand, R. Gobin, J. M. Lagniel, P.-A. Leroy, L. Celona, G. Ciavola, S. Gammino, B. Pottin and J. Sherman. 'Emittance improvement of the electron cyclotron resonance high intensity light ion source proton beam by gas injection in the low energy beam transport'. In: *Review of Scientific Instruments* 71.3 (2000), pp. 1413–1416. doi: <http://dx.doi.org/10.1063/1.1150448>. url: <http://scitation.aip.org/content/aip/journal/rsi/71/3/10.1063/1.1150448> (cit. on p. 272).
- [69] N. Chauvin, O. Delferrière, R. D. Duperrier, R. Gobin, P. A. P. Nghiem and D. Uriot. 'Beam Dynamics Simulation of the Low Energy Beam Transport Line for IFMIF/EVEDA'. In: *Proceedings of LINACo8. MOPo72*. Victoria (Canada), 2008, pp. 242–244 (cit. on p. 272).
- [70] S. Peng, P. Lu, H. Ren, J. Zhao, J. Chen, Y. Xu, Z. Guo, J. Chen, H. Zhao and L. Sun. 'Key elements of space charge compensation on a low energy high intensity beam injector'. In: *Review of Scientific Instruments* 84, 033304 (2013), p. 033304. doi: <http://dx.doi.org/10.1063/1.4794966>. url: <http://scitation.aip.org/content/aip/journal/rsi/84/3/10.1063/1.4794966> (cit. on p. 272).
- [71] T. Taylor and J. S. Wills. 'A high-current low-emittance dc ECR proton source'. In: *Nuclear Instruments and Methods in Physics Research Section A: Accelerators, Spectrometers, Detectors and Associated Equipment* 309.1–2 (1991), pp. 37–42. issn: 0168-9002. doi: [http://dx.doi.org/10.1016/0168-9002\(91\)90090-D](http://dx.doi.org/10.1016/0168-9002(91)90090-D). url: <http://www.sciencedirect.com/science/article/pii/S016890029190090D> (cit. on p. 274).





This document was typeset  
using the  $\text{\LaTeX}$  system, with  
Palatino, Optima and Euler  
fonts by Hermann Zapf; and  
Inconsolata by Raph Levien.

